Toward Enhancement of Evolutionary Multi- and Many-objective Optimization: Algorithms, Performance Metrics, and Visualization Techniques

by

Amin Ibrahim

A Thesis Submitted in Partial Fulfillment
of the Requirements for the Degree of

Doctor of Philosophy in Electrical and Computer Engineering

in

The Department of Electrical, Computer, and Software Engineering

Faculty of Engineering and Applied Science

University of Ontario Institute of Technology

December, 2017

Abstract

In the last three decades, the focus of multi-criteria optimization has been solving problems containing two or three objectives. However, real-world problems generally involve multiple stakeholders and functionalities requiring relatively large number of objectives and decision variables to model these sophisticated problems. In the optimization field, multi-objective problems with four or more objectives are called many-objective problems. Although there are a number of highly successful multi-objective algorithms capable of solving complex two- or three-objective problems, the majority of these algorithms experience significant performance deterioration due-to an increase in the number of solutions required for approximating the entire Pareto-front and the loss of selection pressure required to move non-dominated candidate solutions towards the optimal Pareto-front. Moreover, as the number of objectives increases, visualization of the solution set becomes progressively challenging as well as the applicability of quantitative performance metrics capable of measuring the convergence and diversity of solution become computationally too expensive or unreliable.

This thesis explores the challenges associated with solving many-objective optimization problems and proposes novel algorithms, performance measures, and visualization techniques to mitigate these challenges. Firstly, three multi- and many-objective visualization techniques are proposed. These visualization techniques are capable of showing the convergence and distribution of solutions on the Pareto-optimal front, the distribution of solutions along each objective, and relationship among decision variables and objective function values. Secondly, two novel performance measures capable of assessing the distribution and spread of solutions along each objective are proposed.

Thirdly, a new reference-based hybrid optimization framework is proposed to allow multiple optimization algorithms to work together to take advantage of their combined benefits. This framework is also capable of extracting a subset of well-distributed solutions from thousands of non-dominated solutions collected during the optimization process of several algorithms. Lastly, the proposed optimization algorithms, visualization techniques, and performance measures are applied to multi-objective renewable energy systems to assess their efficacy when dealing with real-world problems. Experimental results on widely used benchmark and real-world optimization problems indicate that the proposed optimization algorithms, visualization techniques, and performance measures can significantly enhance the solving and decision-making processes involved in multi- or many-objective optimization.

Acknowledgments

I would like to thank my supervisors Dr. Shahryar Rahnamayan and Dr. Miguel Vargas Martin for being my guides along my journey, inspiring and challenging me, and providing me with valuable lessons. Without their help and guidance this work wouldn't have been possible.

Special thanks to Dr. Kalyanmoy Deb for sharing his wealth of expertise in the optimization field.

I would like to also thank Dr. Bekir Sami Yilbas and Dr. Farid Bourennani for their collaboration in applying my work to real world problems.

My gratitude to the committee members who provided valuable feedback. This includes committee members Dr. Masoud Makrehchi and Dr. Jing Ren; university examiner Dr. Ken Pu and external examiner Dr. Erik Goodman for his invaluable comments.

I would like to thank my friend Hamid Semeralul who spent many hours editing and proofreading this thesis and several research articles published during my PhD study; my brother Omer Aliso who immensely helped me in the preparation of my PhD defense artwork as well as editing this manuscript.

Finally, I would like to thank the various members of the research community who have reviewed my work and gave me valuable feedback.

Dedication

This thesis is dedicated to the memory of my late father, Abdulrahman Ibrahim, who instilled in me a desire to learn and the value of hard work and good education. To my mother, Fathia Yonis, for her ongoing prayers, love, and support. To my beautiful wife, Inas Yusuf, you have been the greatest source of support and encouragement throughout this education journey. To my wonderful children, Aleena and Haadi, you are my pride and joy. To my extended family, your encouraging words gave me the strength to make this dream a reality.

Table of Contents

List of Figures

List of Tables

List of Algorithms

Nomenclature

A_{max}	maximum collector height above ground
a_s	relative shaded area
D	distance between collector rows
D_{min}	minimum distance between collector rows
d	normalized distance between collector rows
F_d	configuration factor for unshaded collectors
F_d^{sh}	configuration factor for shaded collectors
G_b	direct beam irradiance on the collector perpendicular to solar rays
G_{dh}	horizontal diffuse irradiance
H	collector height
H_s	shadow height
h_s	relative shadow height
H_{max}	maximum collector height
K	number of solar collector rows
L	solar field length
L_s	shadow length
l	normalized collector length
l_s	relative shadow length
Q	yearly energy

q_b	yearly beam irradiation per unit area of an un-shaded collector (first row)
q_d	yearly diffuse irradiation per unit area of an un-shaded collector (first row)
q_b^{sh}	average yearly beam irradiation per unit area of shaded collector ($(K-1)$ rows)
q_d^{sh}	average yearly diffuse irradiation per unit area of shaded collector ($(K-1)$ rows)
T_R	sun rise on the collector for the beam irradiance
T_S	sun set on the collector for the beam irradiance
T_{SR}	sun rise for the diffuse irradiance
T_{SS}	sun set for the diffuse irradiance
W	solar field width
W_{max}	maximum solar field width
Z^+	natural number set
α	sun elevation angle
β	collector inclination angle
γ	difference between the sun and collector azimuth
γ_C	collector azimuth with respect to south
γ_S	sun azimuth with respect to south
θ	angle between the solar beam and the normal to the collector
ΔT	time interval
A_o	average (mid-height) cross-sectional area

I	electrical current
K	thermal conductance of the thermoelectric generator
K_0	the reference thermal conductance
$K_{e,p}$	p-type electrical conductivity
$K_{e,n}$	n-type electrical conductivity
K_{leg}	overall thermal conductance of the pin
K_n	n-type thermal conductivity
K_p	p-type thermal conductivities
L	height of the pin
L_R	external load parameter
$\dot{Q}$	the rate of heat transfer along the x-axis in the pin
R	overall electrical resistivity of the thermoelectric generator
R_0	the reference electrical resistivity
r_k	thermal conductivity ratio
r_{ke}	electrical conductivity ratio
R_L	external load resistance
R_{leg}	overall electrical resistance of the pin
S	shape factor of the pin
T_{ave}	average temperature
T_R or T_H	hot side temperature of the thermoelectric generator

T_2 or T_L	cold side temperature of the thermoelectric generator
$\dot{W}$	electrical power output from the thermoelectric generator
Z	figure of merit = α^2/KR
α	the difference between the Seebeck coefficients of *p* and *n* junctions
α_n	n-junction Seebeck coefficient
α_p	p-junction Seebeck coefficient
δ	the thickness of the pin
θ	Temperature ratio = T_2/T_1
η	efficiency of the thermoelectric generator
μ	dimensionless slope parameter

Chapter 1

INTRODUCTION

Nowadays, real-world applications are becoming more complex. These complex applications are being modeled by an increasing number of decision variables. Additionally, more parameters, input data and other metrics are available to get a quantitative understanding of a problem's complexity. Despite recent advances in computer technology, finding exact solutions for these applications remains a challenge. However, there are numerous metaheuristics capable of finding preferable solutions in a practical time. Due to the inherent complexities and dynamics found in nature, and its ability to address its own problems, nature is the main source of inspiration for solving our complex problems in science and engineering [1].

Metaheuristics are general strategies used for search space exploration by using variant search methods. Their main goal is efficiently exploring the search space in order to find optimal (or near to optimal) solutions in a reasonable time. They solve problems which are "hard" to solve by an exhaustive exploration of the search space. Metaheuristics have been used in many applications, including software engineering, energy systems design, bioinformatics, telecommunication, finance, and others. A description of well-known metaheuristics can be found in [2, 3].

Metaheuristics can be divided into two main categories, namely, population-based metaheuristics (P-metaheuristics) and single solution-based metaheuristics (S-metaheuristics). Basically, they differ by the number of tentative candidate solutions which are involved in every iteration. S-metaheuristics start with a single initial solution which is replaced by a more accurate solution at every iteration. These types of optimization methods offer strong local search properties known as exploitation properties - however,

they get trapped by local optima. Examples of such optimization algorithms are Simulated Annealing (SA) [4] and Tabu Search (TS) [5].

In contrast, P-metaheuristics use an entire set of candidate solutions, called a population, which are improved during optimization process. The first step in P-metaheuristics is the initialization of the population, P. Next, new individuals are generated using some operations (e.g. evolutionary operations) P'. Then, the best fitting individuals are selected from $P \cup P'$ based on domination and/or density of the population. This process iterates until the stopping criteria (e.g. maximum number of function calls) are met. The main advantage of P-metaheuristics is that the diversification of the population aids the search properties known as exploitation properties. Algorithm 1.1 shows a high-level template of P-metaheuristics.

Algorithm 1.1 High-level template of P-metaheuristic

1: P = Generate initial population (uniform randomly);
2: Evaluate objective values for the population members
3: **while** stopping criteria not satisfied **do**
4: P' = Generate new population from P (e.g., using recombination and mutation in evolutionary optimization)
5: P = Select new population from $P \cup P'$ (based on dominance, density or reference)
6: **end while**
7: **Output:** Best solution(s)

Although there have been several advancements in the field of optimization, visualization, and decision-making techniques, there are still a number of challenges when the number of objective is three or greater. Some of these challenges are as follows:

- **Optimization algorithms:** When solving problems involving a higher number of objectives (usually more than three objectives, known as many-objective optimization (MaOO)), evolutionary algorithms fail to find well-converged, well-diversified, non-dominated solutions due to the loss of selection pressure in fitness evaluation [6]. In a high-dimensional space, the proportion of non-dominated individuals in a randomly generated initial population is often higher than 90% [7-11] and this will diminish the selection pressure considerably during the evolutionary process. Moreover, when the distance between nearly converged parent solutions is high, they will likely produce offspring solutions that are far from the true Pareto-front (PF) [10, 11].
- **Visualization techniques:** almost all visualization techniques are not effective when the number of objective is more than three [12-14]. A proper visualization tool must be able to show the location, range, shape, and distribution of obtained non-dominated solutions (both Pareto-surface and objective-wise distribution). Moreover, there does not exist a novel multi- or many-objective optimization visualization method capable of visualizing the relationship among decision variables and objective functions.
- **Performance metrics:** Another significant issue is the lack of efficient and effective quantitative metrics capable of measuring the convergence and diversity of a solution set when the number of objectives is high. For example, the hypervolume (HV) [15] measure is a widely used performance metric in MaOO. It captures the convergence and diversity of a solution set even when the optimal PF (PF) is unknown. However, the high computational complexity (i.e., exponential) of the HV metric makes it impractical to be used when the number objectives is high [16-18]. Also, Pareto-surface metrics such as generational distance (GD), inverted generational distance

(IGD), and spread are simple and provide knowledge about the overall performance of the solution set [19-21]. However, these measures do not provide any insight into the distribution or spread of a solution set with respect to each objective. Furthermore, studies have shown that these performance metrics can contradict one another in the presence of extreme cases [22].

- **Solution selection:** Although there are number of state-of-the-art multi- and many-objective optimization algorithms capable of finding trade-off solutions, effective decision making techniques are needed to select one or more solutions among many candidate solutions [23-26]. Normally, an optimizer generates hundred or thousands of candidate solutions during several runs of the algorithm and hence the challenge is to provide the decision maker with a tool to easily select a well-distributed subset of solutions for further consideration in order to end-up a single optimal solution.

1.1 Motivation

The motivation for this thesis stems from several challenges faced by experts in the field of optimization. The first challenge is the fact that several real-world applications involve a large number of objectives (typically more than three) which leads to solutions becoming difficult to visualize. However, visualization is necessary as it is an effective decision making tool and allows decision makers to understand the algorithms used and also their generated trade-off solutions. There are many two- or three-dimensional data visualization methods that are used for many-objective optimization. However, such methods are often difficult to interpret due to solutions being superimposed or arbitrarily ordered. There are other methods that show the distribution and inter-relationship among objectives, yet they do not illustrate the shape and convergence trend of the solution sets. Fortunately, there are

recent advances in visualization methods to cope with visualizing high-dimensional objective spaces while attempting to preserve the distribution, shape, and dominance relationship among approximate PF members.

Second, there is no visualization scheme currently capable of showing the relationship between the decision variables and objective values (even when the number of objectives is two). Typically, current visualization tools are designed to assess the distribution and convergence of solution sets without any regard for the decision variables used to obtain the solution set [27-30]. These methods fail to identify the relationship between the decision variables and objective values that perhaps strongly correlate which may improve the search process, or decision variables those have nearly no correlation, whose elimination may also improve the search process.

Third, the focus of almost all multi- or many-objective performance metrics has so far been the convergence and distribution of solutions in the objective space (Pareto-surface). These are simple and provide knowledge about the overall performance of the solution set. Nonetheless, as the number of objectives increase, most of these measures fail to properly measure the performance of the solution set or become computational expensive. Also, these measures do not provide any insight into the distribution or spread of solution sets with respect to each objective.

Last, there is a fact so-called “No-Free-Lunch” theorem [31], which stipulates that an algorithm, that may have proven to give good performance on a particular class of problems, may not provide the same level of performance on other classes of problems. In response, some researchers shifted their focus from developing powerful algorithms that are more problem-specific or instance-specific toward hybridization. This task can be

accomplished through the hybridization of optimization algorithms which means developing new algorithms by combining two or more optimization algorithms.

1.2 Thesis Scope

In general optimization involves four main steps. The first step is formulating and modelling the problem. Once the problem is modeled, an appropriate optimization algorithm is selected/designed to solve the problem. Then, the quality of the obtained solutions through the optimization algorithms are assessed. In this step, one can use different visualization techniques and/or performance metrics to visually asses or quantify the performance of each algorithm involved in the optimization process. The last step involves selecting the preferred solution(s) among many solutions obtained during the optimization process; generally, it is required for multi-modal or multi-objective optimization. If the solution is deemed unacceptable by the decision maker, the model and/or the optimization algorithm can be improved and the decision-making process is repeated. Figure 1-1 illustrates the steps involved in the decision making process.

The scope of the thesis focuses on the improvement of each of the optimization steps when the problem contains multi or many objectives; which includes: 1) the introducing of new visualization techniques to deal with high dimensional search spaces and/or objective spaces, 2) the introducing of novel complimentary performance measures to assess the quality of obtained solutions based on their objective-wise spread, convergence, and distribution, 3) the improvement of current state-of-the-art MOEAs through hybridization and utilizing elite population archive, 4) the application of reference points to select one of more preferred solutions (decision making), and 5) applying the

proposed algorithms and visualization techniques to solve multi-objective real-world renewable energy systems to assess their efficacy when dealing with practical problems.

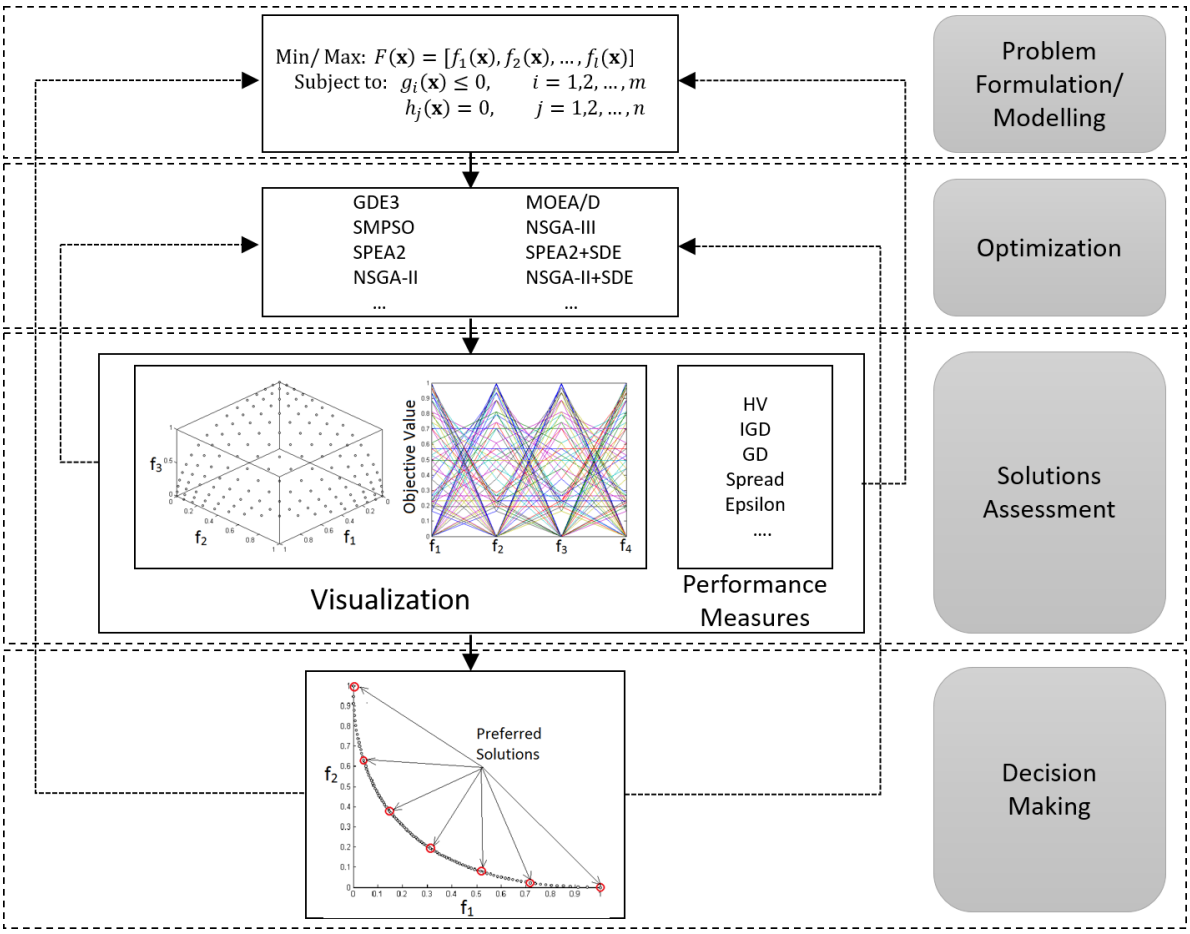

FIGURE 1-1 An optimization process: problem formulation and modelling, problem solving/ optimization, solution assessment, and decision-making.

1.3 Thesis Objective

This thesis targets several objectives. Firstly, it aims to introduce a powerful visualization method that allows MaOO researchers, decision makers, and any other interested parties to better understand the optimization process along with intermediate and final results of population-based optimization algorithm. Particularly, decision makers should be able to visually explore many-objective solution sets and identify one or more preferred optimal

solutions. This should not only be based on the convergence and distribution of solutions on the Pareto-optimal front but also distribution of solutions along each objective.

Additionally, a simple visualization scheme should show not only the relationship among objective functions but also the relationship among objective functions and decision variables. Similarly, decision makers should be provided with well-distributed solutions and be able to quantitatively assess the distribution of solutions along an objective regardless of other objectives.

Another objective guiding this work is the need for a framework to help decision makers easily select a subset of well-distributed solutions from a large set of non-dominated solutions using predefined structured reference points or user-defined reference points. This framework should be able to integrate solutions from multiple optimization algorithms during, or after, several runs of one or many algorithms and then extract well-distributed solutions from thousands of non-dominated solutions using predefined structured reference points or user-defined reference points. Furthermore, there is a need for a hybridization technique capable of utilizing a number of algorithms during the optimization process to improve the quality of solutions achieved without the burden of selecting or parameter tuning one or more algorithms to solve a specific problem.

1.4 Organization of Thesis

The remainder of this thesis is organized as follows:

Chapter 2 introduces definition and the concepts behind of multi-objective optimization, performance measures, and benchmark test problems used in MOEAs.

Chapter 3 provides a technical description of three proposed visualization methods, namely, 3D-RadVis, 3D-RadVis Antenna, and Enhanced Correlation Matrix (ECM) plot.

3D-RadVis is capable of mapping M-dimensional objective space to a three-dimensional radial coordinate plot while seeking to preserve the relative location of solutions, shape of the PF, distribution of solutions, and convergence trend of an optimization process on the Pareto-optimal surface. 3D-RAdVis Antenna is an extension of 3D-RadVis where it incorporates poles for each objective to show objective-wise distribution of solutions. An ECM plot is designed to show the relationship between decision variables and objective functions.

Chapter 4 presents two proposed performance measures called objective-wise inverse generational distance (ObjIGD) and line distribution (Δ_{Line}). These measures are designed to assess the convergence, spread and diversity of MOEA solutions along each objective with or without the presence of a reference solution set.

Chapter 5 presents a novel preferred solution(s) extraction mechanism called, Fusion of Non-dominated Fronts using Reference points (FNFR) to assist decision makers to extract a subset of well-distributed solutions from a large set of solutions collected after many runs of an optimization algorithm.

Chapter 6 provides a detailed description of the proposed hybridization of multi- and many-objective optimization algorithms called Fusion. The Fusion algorithm gains the combined benefit of several algorithms and eliminates the challenge associated with choosing one optimization algorithm to solve complex problems.

Chapter 7 presents the proposed extension of the NSGA-III algorithm called EliteNSGA-III to improve the diversity and accuracy of solutions obtained by the NSGA-III algorithm. The EliteNSGA-III algorithm maintains an elite population archive to

preserve previously generated elite solutions that would probably be eliminated by NSGA-III's selection procedure.

Chapters 8 and 9 investigate how the proposed visualization techniques and algorithms can be utilized to solve two real-world problems. The first problem is the multi-objective design of a photovoltaic farm in Ontario, Canada, and the second problem deals with the multi-objective optimal configuration of thermoelectric devices. In these case studies, the Fusion algorithm is used to solve the optimization problem. The ECM plot is used to visualize and identify relationships among decision and objective variables, the ObjIGD measure is used as a complement of existing performance measures by quantifying the convergence and distribution of solutions along each objective, and finally the FNFR method is utilized to help decision makers select few preferred solutions among thousands of possible solutions.

Chapter 10 provides a summary of this thesis's contribution, recommendation, and future directions.

Appendix A provides 30 years of climate information for the Toronto, Ontario, Canada area used in the case study described in Chapter 8. This data include monthly averaged hourly direct normal beam irradiance and horizontal diffuse irradiance in KWh/m^2.

Appendix B presents the best non-dominated solution sets found by the Fusion and other state-of-the-art optimization algorithms involved in solving the photovoltaic farm design discussed in Chapter 8.

Appendix C provides a list of uniformly distributed non-dominated solutions extracted from the thermoelectric problem (with and without the shape factor) described in

Chapter 9 using the FNFR scheme. These solutions are extracted from thousands of non-dominated solutions assembled during 25 runs of the Fusion algorithm as well as other algorithms.

Chapter 2

MULTI-OBJECTIVE OPTIMIZATION

This chapter provides 1) the background concept of multi-objective optimization such as non-dominance, Pareto optimality, diversity, elitism, and ranking; 2) performance metrics used in multi-objective optimization (MOO) such as the hypervolume (HV) measure and the inverted generational distance (IGD); and 3) the mathematical and the landscape characteristics of benchmark test problems used in MOO, such as the DTLZ and WFG test problems.

2.1 Multi-objective Optimization: Background Review

Almost all real-world problems are concerned with complex and often problems with many objectives. Moreover in many cases these objectives are in conflict with each other. For example, when designing a photovoltaic farm, we would like to maximize the energy absorbed by the photovoltaic panels while minimizing its installation and maintenance costs. In order to buildup a good understanding of MOOs, this section provides a formal definition of MOO as well as the corresponding concepts required to identify and select "optimal" solutions.

2.1.1 Definition

Multi-objective optimization is the process of simultaneously optimizing two or more conflicting objectives subject to certain constraints. A multi-objective optimization problem may be defined as:

$$\begin{aligned} &\text{Minimize/ Maximize: } F(\mathbf{x}) = (f_1(\mathbf{x}), f_2(\mathbf{x}), \dots, f_l(\mathbf{x})) \\ &\text{Subject to: } g_i(\mathbf{x}) \leq 0, \qquad i = 1,2, \dots, m \\ &\qquad\qquad\quad h_j(\mathbf{x}) = 0, \qquad j = 1,2, \dots, n \end{aligned} \tag{2.1}$$

where l ($l \geq 2$) is the number of objectives, $\mathbf{x} = (x_1, \ldots, x_k)$ is the vector representing the decision variables (decision vector) in the decision space, $g_i(\mathbf{x})$ are inequality constraints and $h_j(\mathbf{x})$ are the equality constraints. $F(\mathbf{x}) = (f_1(\mathbf{x}), f_2(\mathbf{x}), \ldots, f_l(\mathbf{x}))$ is the vector of objectives (objective vector in the objective space) to be optimized.

Generally, multi-objective optimization problems having more than three objectives are called many-objective optimization problems. Hence, the above definition holds true for both multi- and many-objective problems with the exception that when l = 2 or 3 we refer to the problem as multi-objective and many-objective when l > 3. The optimal solution for MOOs is not a single solution as for single objective problems, but a set of solutions defined as Pareto-optimal solutions. A solution is Pareto-optimal if it is not possible to improve a given objective without deteriorating the value of another objective. The main goal of the resolution of a multi-objective problem (MOP) is to obtain the Pareto-optimal set and consequently non-dominated solutions known as the Pareto front (PF). A good PF consists of solutions that are well-distributed, well-spread and close to the true Pareto-optimal front. Figure 2-1 shows an example of five solution sets representing several approximate fronts. Figure 2-1 (a) and (b) illustrate the difference between distribution and spread. The remaining three sub-figures show the difference between convergence and distribution. The first solution set depicted in Figure 2-1 (a) show five solutions that are well-distributed but does not contain the two extreme solutions. However, Figure 2-1 (b) illustrates five solutions with good spread but bad distribution. Similarly the solution set depicted in Figure 2-1 (c) show good spread and distribution but failed to converge to the true Pareto-optimal front. Figure 2-1 (d) show solutions close to the true

Pareto-optimal front but failed to cover the entire front. Figure 2-1 (e) illustrates the three desirable properties of good convergence, spread, and distribution.

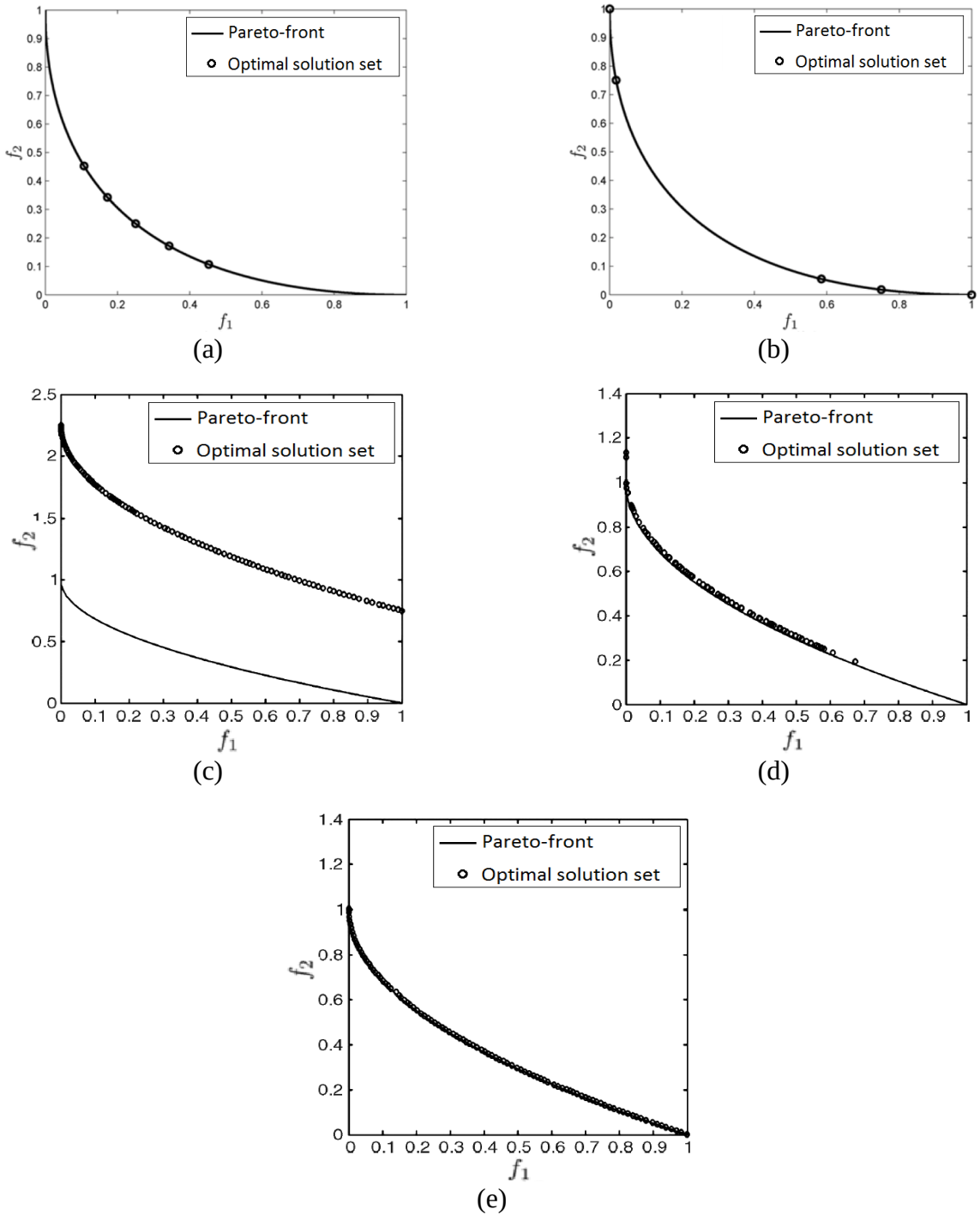

FIGURE 2-1 Example of approximate PFs: (a) Good distribution but bad spread. (b) Good spread but bad distribution. (c) Good distribution but bad convergence. (d) Good convergence bad distribution. (e) Good distribution, spread, and convergence [2, 22].

2.1.2 Dominance

An objective vector $\mathbf{u} = (u_1, \ldots, u_n)$ is said to $dominate$ $\mathbf{v} = (v_1, \ldots, v_n)$ (denoted by $\mathbf{u} \prec \mathbf{v}$) if and only if no component of v is smaller than the corresponding component of u and at least one component of u is strictly smaller, assuming a minimization problem; that is,

$$\forall\, i \in \{1, \ldots, n\}: u_i \leq v_i \wedge \exists\, i \in \{1, \ldots, n\} :\ u_i < v_i. \tag{2.2}$$

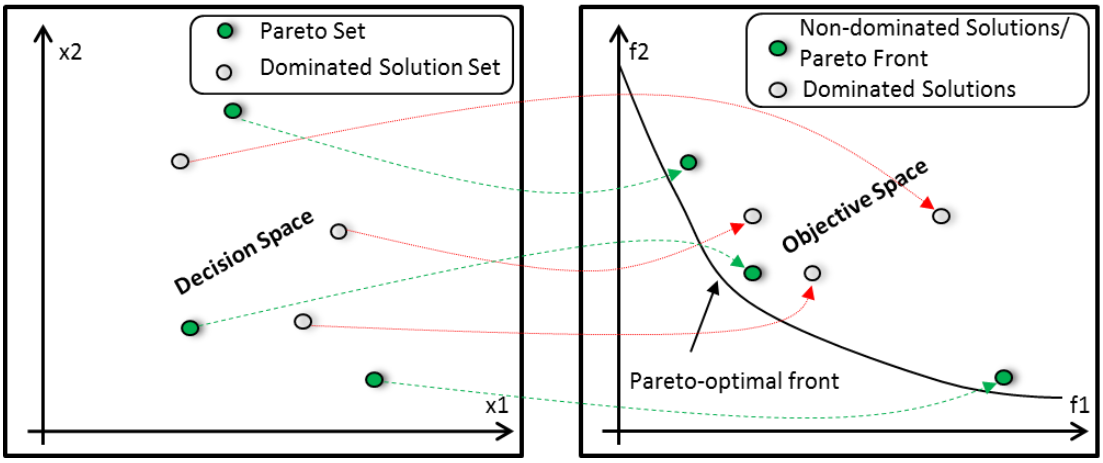

FIGURE 2-2 Illustration of a general multi-objective optimization problem space (including variable and objective spaces).

2.1.3 Pareto Optimality

A solution $\mathbf{x}$ is said to be Pareto-optimal if and only if there is no $\mathbf{x}'$ for which $\mathbf{v} \Rightarrow F(\mathbf{x}') = (f_1(\mathbf{x}'), f_2(\mathbf{x}') \ldots, f_k(\mathbf{x}'))$ dominates $\mathbf{u} \Rightarrow F(\mathbf{x}) = (f_1(\mathbf{x}), f_2(\mathbf{x}) \ldots, f_k(\mathbf{x}))$. The set of all feasible non-dominated solutions in $\mathbf{x}$ is referred to as the *Pareto-optimal set*, and for a given Pareto-optimal set, the corresponding objective function values in the objective space are called the *PF*. Here we are saying if $\mathbf{x}$ is the Pareto-optimal set, then there is no feasible vector $\mathbf{x}'$ that can improve any of the objectives simultaneously without

degrading at least one other objective. Figure 2-2 illustrates a general MOO problem's decision and objective spaces.

2.1.4 Diversity

In MOO, finding the PF is not the only task – a good multi-objective algorithm should provide solutions that span the boundaries of the objective space as well as uniformly diverse [32]. A good diversity can provide better choices to decision makers. Several techniques are available for maintaining diversity in a MOO. These techniques include the fitness sharing/niching [33, 34], the weight vector approach [35, 36], restricted mating [37, 38], crowding/clustering [21, 39], and relaxed forms of dominance [40, 41].

2.1.5 Elitism

Using elitism in MOO has been addressed by several researchers in the past. In elitist selection, the best n individuals ($n \geq 1$) from the current generation to the next one are retained intact - without applying any operators to them. The significance of elitism in single objective genetic algorithms is very high [42]. The use of elitism in MOEAs, however, is still subject of research [43]. The premise here is to retain a subset of individuals with the highest rank in the population. Then the rest of the population is filled using other techniques.

2.1.6 Ranking

In MOO, ranking is mainly based on the concept of dominance. The main goal for ranking is to get a population closer to the PF. In other words, the set of individuals in the population that are Pareto non-dominated by the rest of the population is found. Usually, rankings are

assigned based on the classical Non-dominating Sorting (NDS) procedure. In NDS, a set of non-dominated solutions are determined and assigned a rank of 1 (or 0), then eliminated. Next, the non-dominated solutions are determined from the remaining population and assigned a rank of 2 (or 1). This process continues until the population is appropriately ranked. A noteworthy point here is the fact that ranking assigns selection probabilities only on an individual's rank; absolute fitness values are ignored.

2.2 MOO Performance Metrics (Quality Indicators)

Unlike single-objective optimization, where the assessment of the performance of a metaheuristic requires observing the best value given by an algorithm, this is not applicable in multi-objective optimization. An approximation set to the optimal PF of the problem is rather computed. Here, the required properties are convergence (i.e., how close the solution is to the true PF) and uniform diversity (i.e., solutions that exhibit uniform distribution). Ideally, we are interested in quality indicators that do not require the true Pareto-optimal front but are capable of measuring the convergence and diversity of a known solution set. Because, these metrics are applicable for real-world problems with unknown optimal PF. Several indicators for measuring the aforementioned properties have been proposed in the literature. These include: Generational Distance (GD) [44], Inverse Generational Distance (IGD), Error Ratio (ER) [19], Hypervolume (HV) [15], Epsilon [45], Spread [8] and others. Some of these indicators are meant to only measure either convergence or diversity; other indicators, however, take into account both criteria. Table 2.1 below lists some MOO performance indicators and their intended measure.

2.2.1 Hypervolume (HV)

Means of comparing Pareto sets is a core area of MOO research. One such mean that has attracted recent attention in MOO is the hypervolume indicator (HV). The HV indicator is a very popular and widely used measure of fitness of a Pareto set [15]. This indicator measures the volume of the dominated portion of the objective space. The interest in this indicator stems from the fact that it contains the strict Pareto compliance which is a highly desirable feature. In other words, if A strictly dominates B, then the HV value of A is higher than the HV value of B. The HV metric takes into consideration both the accuracy of a solution set and the diversity of a solution set.

TABLE 2.1 Summary of MOO performance metrics.

Quality Indicator	Intended measure		Optimal PF Required
	Convergence	Diversity	
Hypervolume (HV)	Yes	Yes	No
Error Ratio (ER)	Yes	No	Yes
Spread	No	Yes	Yes
Inverted Generational Distance (IGD)	Yes	Yes	Yes
R2	No	Yes	Yes/No
Epsilon (ϵ)	Yes	No	No

The HV is obtained by computing the volume of the non-dominated set of solutions Q for minimization MOO problems. For every solution Q, a hypercube v_i is generated with a reference point W and the solution i as its diagonal corner (see Figure 2-3). The reference point W can be generated by building a vector of the worst possible objective function values. Then, the HV is computed as a union of all the found hypercubes as follows:

$$HV = volume\left(\bigcup_{i=1}^{|Q|} v_i\right). \tag{2.3}$$

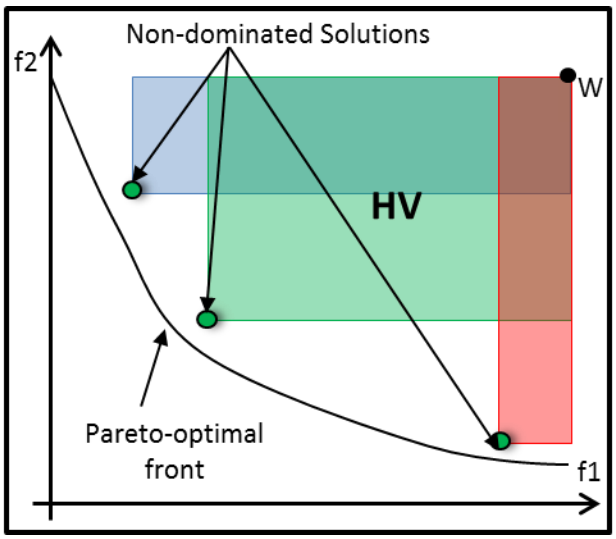

FIGURE 2-3 Hypervolume enclosed by non-dominated solutions

2.2.2 Error Ratio (ER)

ER is one of the simplest indicators and measures the ratio of the number of solutions that are elements of the true PF to the total number of solutions [19]. ER is defined as

$$ER = \frac{\sum_{i=1}^{n} e_i}{n}, \tag{2.4}$$

where n is the number of vectors in PF_{known} and e_i is zero when the i^{th} solution is an element of PF_{true}, otherwise e_i is one. An ER value of one indicates that all solutions are in PF_{true}, whereas an ER value of zero indicates that none of the solutions are in PF_{true}.

2.2.3 Spread

This indicator measures the distribution of solutions using the extreme points of Pareto PF_{true} [8]; and is defined as:

$$\Delta = \frac{d_f + d_l + \sum_{i=1}^{N-1} \left| d_i - \bar{d} \right|}{d_f + d_l + \bar{d}(N-1)}, \tag{2.5}$$

where d_f and d_l are the Euclidean distances to the extreme solutions of the optimal PF in the objective space; d_i is the Euclidean distance between consecutive solutions and $\bar{d}$ is the mean of these distances. The Spread value of zero indicates an ideal distribution (i.e., uniformly distributed solutions in the PF).

Nonetheless, the Spread indicator is based on calculating the distance between two consecutive solutions which only works for 2-objective problems. This indicator can further be extended by calculating the distance from a given point to its nearest neighbours; this is based on the metric proposed in [46]:

$$\Delta = \frac{\sum_{i=1}^{m} d(e_i, S) + \sum_{X \in S} |d(X, S) - \bar{d}|}{\sum_{i=1}^{m} d(e_i, S) + |S| * \bar{d}}, \tag{2.6}$$

where $e_1, \ldots, e_m$ are m extreme solutions in S^*, m is the number of objectives, S is a set of solutions, S^* is the set of Pareto-optimal solutions and

$$d(X, S) = \min_{Y \in S, Y \neq X} \|F(X) - F(Y)\|^2 \tag{2.7}$$

$$\bar{d} = \frac{1}{|S^*|} \sum_{X \in S^*} d(X, S). \tag{2.8}$$

2.2.4 Generational Distance (GD)

The Generational Distance (GD) indicator measures the average distance between the approximated solutions, PF_{known}, to the nearest solution in the Pareto optimal set, PF_{true}. The GD indicated is defined as:

$$GD = \frac{\sqrt{\sum_{i=1}^{n} d_i^2}}{n}, \tag{2.9}$$

where n is the number of solutions in the PF_{known} and d_i is the Euclidean distance between each solution in PF_{known} and the nearest solution, PF_{true}. A value of $GD = 0$ indicates that all solutions in PF_{known} are in PF_{true}.

2.2.5 Inverted Generational Distance (IGD)

The Inverted Generational Distance (IGD) indicator is similar to the GD indicator; however, IGD measures the distances between each solution composing the Pareto-optimal front, PF_{true} and the approximated solution set, PF_{known}. The IGD metric is defined as follows:

$$IGD = \frac{\sqrt{\sum_{i=1}^{n} d_i^2}}{n}, \tag{2.10}$$

where n is the number of solutions in the PF_{true} and d_i is the Euclidean distance between each solution in PF_{true} and the nearest solution PF_{known}.

2.2.6 R2

R2 is a subset of the R indicator for assessing the quality of two PF approximation sets based on utility functions that a vector and a scalar utility value [47] [48]. The R2 indicator mathematically defined as:

$$R_2 = \frac{\sum_{\lambda \in A} u(\lambda, B) - u(\lambda, A)}{|\lambda|}, \tag{2.11}$$

where $u(A, \lambda)$ is the minimum distance of a point in a set A from the reference point. A and B are approximation sets, λ is the scalarizing vector and u is a utility function. Usually B is replaced with a reference set composed of points in PF_{true}.

The utility functions u requires a reference point and a scalarizing vector λ specified by the user. Vectors are distributed uniformly across the objective space. The distance of the point in each set that is closest to the reference point is measured. Then, the differences in these distances are added up. To obtain an indicator from these two indicators, the set B is replaced by a reference set containing R - the true PF points. Next, these indicator functions measure the difference in the mean distance of the attainment surfaces A and R (from a user-defined reference point).

2.2.7 Epsilon

Given two approximate sets, A and B, Epsilon (the ε-indicator) measures the minimal amount, ε, that must be used to translate the set A so that every point in B is dominated [45].

Given $A, B \subseteq X$, $\varepsilon(A, B)$ is the minimum $\varepsilon \in \mathbb{R}$ such that any solution $b \in B$ is ε-dominated by at least one solution $a \in A$:

$$\varepsilon(A, B) = min\{\varepsilon \in \mathbb{R} | \forall b \in B \exists a \in A : b \prec_\varepsilon a\}$$

Therefore, when $\varepsilon(A, B) < 1$, all solutions in B are dominated by a solution in A. If $\varepsilon(A, B) = \varepsilon(B, A) = 1$, then A and B represent the same PF approximation. Also, if $\varepsilon(A, B) > 1$ and $\varepsilon(B, A) > 1$, then A and B are not comparable since they both contain solutions not dominated by the other set.

2.3 Benchmark Test Problems

Pareto-optimal fronts for multi-objective problems can have a variety of geometries – unlike single objective problems where the fronts are a single point. By definition, a set is convex if and only if it is covered by its convex hull. In other words, if we take two points

in a set A, $A \subset \mathbb{R}^n$, the line segment that connects these points is entirely contained in A. It is concave if we take two points in a set A, $A \subset \mathbb{R}^n$, the line segment that connects these points is not entirely contained in A. Also, a set is said to be strictly convex (respectively, strictly concave) if it is convex (respectively, concave) and not concave (respectively, convex). Finally, a set is linear if it is both concave and convex.

Extending this definition, a mixed front is defined as one with connected subsets that are each strictly concave, strictly convex, or linear but not all of the same type. A front is said to be degenerate when it is of lower dimension than the objective space in which the front is embedded less one. Pareto-optimal fronts that are degenerate can cause potential problems for some algorithms. Of particular interest is the question of whether a front is a connected set or not. A front that is a disconnected set is typically referred to as discontinuous (see Figure 2-4 for clarification).

Convergence velocity relative to various Pareto-optimal geometries and bias conditions can be tested using unimodal test problems. There are three main types of Pareto-optimal geometries that have to be covered by any testing, Pareto-optimal fronts, disconnected Pareto-optimal sets, and disconnected Pareto-optimal fronts. These test problems should mainly be a multimodal and non-separable but also include few deceptive PFs. Furthermore, there should be problems that are multimodal and non-separable at the same time.

In multi-objective evolutionary algorithms, and in order to draw accurate conclusions, it is essential to understand the employed test problems very well. Additionally, the measures and statistical methods that are used must be proper. These two requirements have received much attention in the literature and have been rigorously

analyzed. Among several test sets ZDT, DTLZ, WFG, and LZ09 are widely utilized benchmark problems to test the efficiency of MOO algorithms [21], [49], [50], [51], [52], [53], [54], [55] , and [56].

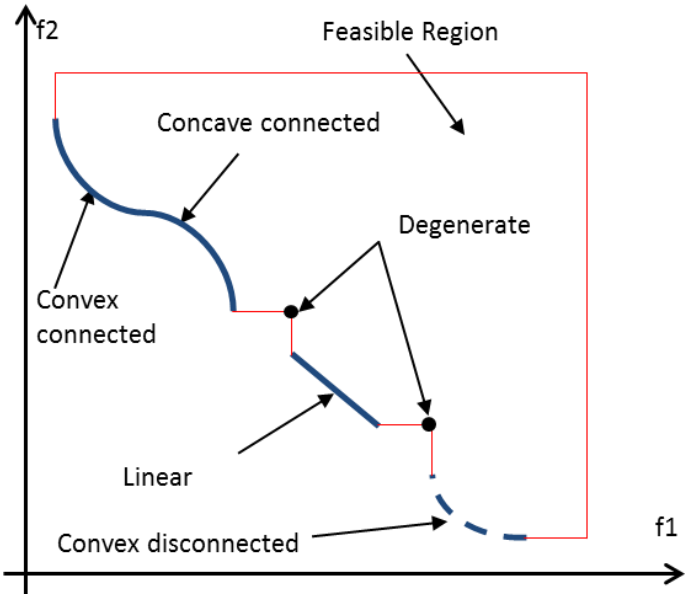

FIGURE 2-4 Example of PF geometry

2.3.1 Classical problems: Kursawe, Fonseca, Schaffer

In the past, the test problems which were the focus of MOEA studies were either non-scalable or simple. Furthermore, other problems were too complicated which lead to the exact shape and location of the resulting Pareto-optimal front being hard to visualize. Two test problems that have been widely used are SCH1 and SCH2 which are both single-variable test problems introduced by Schaffer [57]. Other test problems include KUR [58], introduced by Kursawe, that was scalable in terms of decision variables but not in terms of the number of objectives. Similar to this is the FON test problems introduced by Fonseca and Fleming [59]. Another test problem, POL, introduced by Poloni, only uses two decision variables. Table 2.2 lists these classical test problems utilized in MOEAs. Figure 2-5 shows the PF geometry of these classical problems.

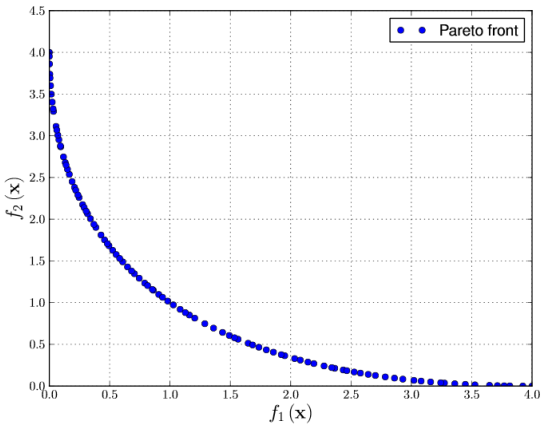

(a)

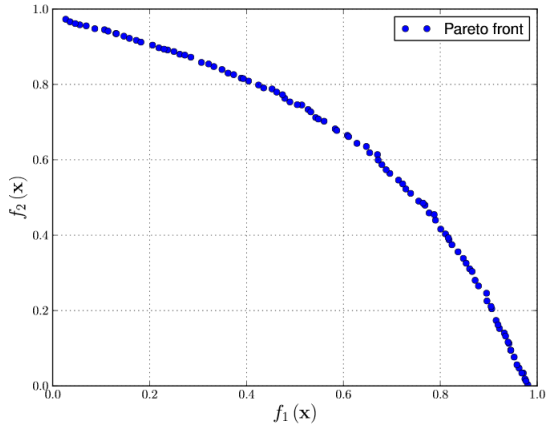

(b)

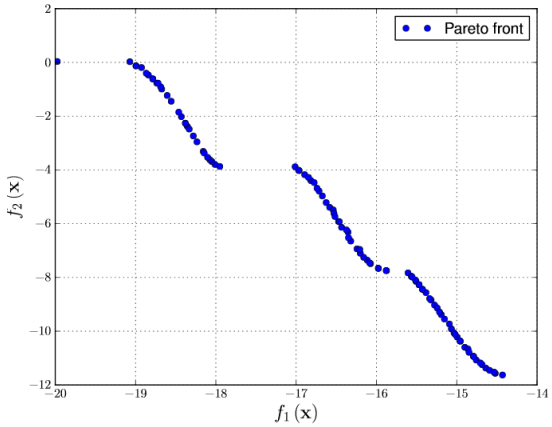

(c)

FIGURE 2-5 Classical test problems: (a) Schaffer, (b) Fonseca, and (c) Kursawe

TABLE 2.2 Classical test problems

Problem	n	Variable Bounds	Objective Functions	Optimal Solutions	General Description
Schaffer	1	$x_i \in [10^5, 10^5]$	$f_1(\mathbf{x}) = x_i^2$ $f_2(\mathbf{x}) = (x_i - 2)^2$	$x_i \in [0,1]$ $i = 1, \ldots, n$	Convex
Fonseca	3	$x_i \in [-4,4]$	$f_1(\mathbf{x}) = e^{-1.0\sum_{i=1}^{n}(x_i - \frac{1}{\sqrt{n}})^2}$ $f_2(\mathbf{x}) = e^{-1.0\sum_{i=1}^{n}(x_i + \frac{1}{\sqrt{n}})^2}$	$x_i \in [0,1]$ $i = 1, \ldots, n$	Concave
Kursawe	3	$x_i \in [-5,5]$	$f_1(\mathbf{x}) = \sum_{i=1}^{n}(-10e^{-0.2}\sqrt{x_i^2 + x_{i+1}^2})$ $f_2(\mathbf{x}) = \sum_{i=1}^{n}(\lvert x_i\rvert^{0.8} + 5\sin(x_i)^3)$	$x_i \in [-5,5]$ $i = 1, \ldots, n$	Disconnected, mixed, degenerate

TABLE 2.3 The ZDT family test problems

Problem	n	Variable Bounds	Objective Functions	Optimal Solutions	General Description
ZDT1	30	$x_i \in [0,1]$	$f_1(\mathbf{x}) = x_1$ $f_2(\mathbf{x}) = g(\mathbf{x})\left[1 - \sqrt{\frac{x_1}{g(\mathbf{x})}}\right]$ $g(\mathbf{x}) = 1 + \frac{9}{n-1}\left(\sum_{i=2}^{n} x_i\right)$	$x_1 \in [0,1]$ $x_i = 0$ $i = 2, \ldots, n$	Convex
ZDT2	30	$x_i \in [0,1]$	$f_1(\mathbf{x}) = x_1$ $f_2(\mathbf{x}) = g(\mathbf{x})\left[1 - \left(\frac{x_1}{g(\mathbf{x})}\right)^2\right]$ $g(\mathbf{x}) = 1 + \frac{9}{n-1}\left(\sum_{i=2}^{n} x_i\right)$	$x_1 \in [0,1]$ $x_i = 0$ $i = 2, \ldots, n$	Non-convex
ZDT3	30	$x_i \in [0,1]$	$f_1(\boldsymbol{X}) = x_1$ $f_2(\mathbf{x}) = g(\mathbf{x})\left[1 - \sqrt{\frac{x_1}{g(\mathbf{x})}} - \frac{x_1}{g(\mathbf{x})}\sin(10\pi x_1)\right]$ $g(\mathbf{x}) = 1 + \frac{9}{n-1}\left(\sum_{i=2}^{n} x_i\right)$	$x_1 \in [0,1]$ $x_i = 0$ $i = 2, \ldots, n$	Convex, disconnected
ZDT4	10	$x_1 \in [0,1]$ $x_i \in [-5,5]$, $i = 2, \ldots, n$	$f_1(\mathbf{x}) = x_1$ $f_2(\mathbf{x}) = g(\mathbf{x})\left[1 - \sqrt{\frac{x_1}{g(\mathbf{x})}}\right]$ $g(\mathbf{x}) = 1 + 10(n-1) + \sum_{i=2}^{n}[x_i^2 - 10\cos(4\pi x_i)]$	$x_1 \in [0,1]$ $x_i = 0$ $i = 2, \ldots, n$	Nonconvex
ZDT6	10	$x_i \in [0,1]$	$f_1(\mathbf{x}) = 1 - e^{-4x_1}\sin^6(6\pi x_1)$ $f_2(\mathbf{x}) = g(\mathbf{x})\left[1 - \left(\frac{x_1}{g(\mathbf{x})}\right)^2\right]$ $g(\mathbf{x}) = 1 + 9\left[\left(\sum_{i=2}^{n} x_i\right)/(n-1)\right]^{0.25}$	$x_1 \in [0,1]$ $x_i = 0$ $i = 2, \ldots, n$	Nonconvex, non-uniformly spaced

2.3.2 ZDT Test Suite

The ZDT family of problems are one of the simplest MOPs and the most commonly utilized for benchmark purposes [60]. The ZDT1 function is composed of a convex Pareto-optimal front. The ZDT2 function is composed of a non-convex Pareto-optimal front. The ZDT3 function is a convex discontinuous Pareto-optimal front caused by a *sine* function in this objective space but not in the parameter space. The ZDT4 function is highly multimodal

by being composed of 21 local Pareto-optimal fronts. The ZDT6 function has an irregular search space: the Pareto-optimal solutions have non-uniform distribution along the global PF and their density is the highest away from the Pareto-optimal front and is the lowest near the front. The ZDT family of problems suffers from certain deficiencies such as none of its problems has fitness landscapes with flat regions, none of its problems has a degenerate Pareto-optimal front, none of its problems are non-separable, and only the number of distance parameters is scalable. Table 2.3 presents the ZDT test problems utilized in MOEAs. Figure 2-6 shows the PF geometry of ZDT1, ZDT3, and ZDT4 test problems.

2.3.3 DTLZ Test Suite

Another test problem set is the DTZL family introduced by Deb et al. [61] which has the advantages of being simple to construct and scalable to a number of objectives and decision variables. Additionally, in this set of test problems the exact shape and location of the resulting Pareto-optimal front is known. In the DTLZ test problems, the objective function values lie on the linear hyper-plane. However, the difficulty that is faced in this problem is when it comes to hyper-plane convergence. Table 2.4 presents the DTLZ test problems utilized in MOEAs. Figure 2-7 shows the PF geometry of DTLZ1, and DTLZ7 test problems. Below is a summary of some of the available DTLZ test problems:

- DTLZ1 is linear whereas DTZL2 concave.
- DTLZ3: since the global Pareto-optimal front is parallel to the local Pareto-optimal fronts, this function can be used to investigate MOEAs ability to scape these local Pareto-optimal fronts.

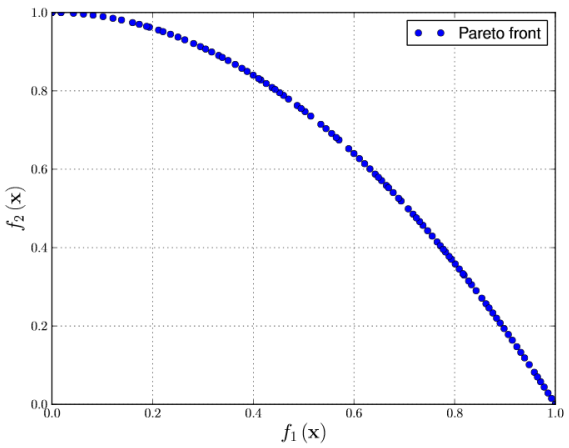

(a)

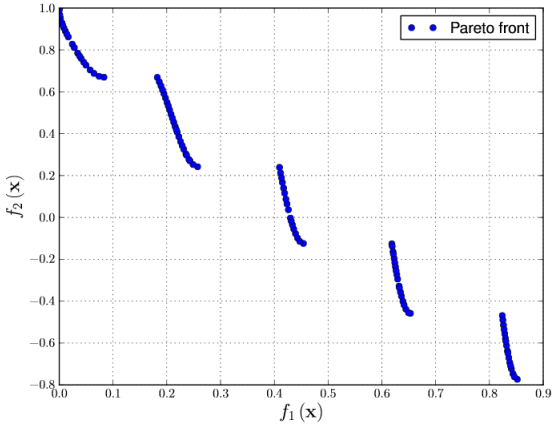

(b)

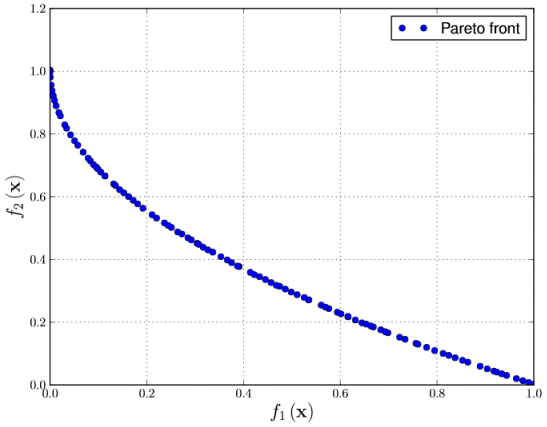

(c)

FIGURE 2-6 The ZDT family test problems: (a) ZDT1, (b) ZDT3, and (c) ZDT4

- DTLZ4: this version allows a dense set of solutions to exist around the $f_M - f_1$ objective plane, where M is the number of objectives. However, these problems may impede MOEAs in achieving a well-distributed set of solutions due to the fact that MOEAs try to find multiple and well-distributed Pareto-optimal solutions in one simulation run.

- DTLZ5 and DTLZ6: in this modification, an MOEA's ability to converge to a curve is tested. Due to its simplicity it can be used to examine the computational time complexity of a higher-objective version. The g function used in DTLZ6 makes it difficult for MOEAs to converge to the true Pareto-optimal front.
- DTLZ7: in this modification, a disconnected set of Pareto-optimal regions exist in the search space. In this case, the ability of an algorithm to maintain distributed subpopulation in different Pareto-optimal regions is tested.

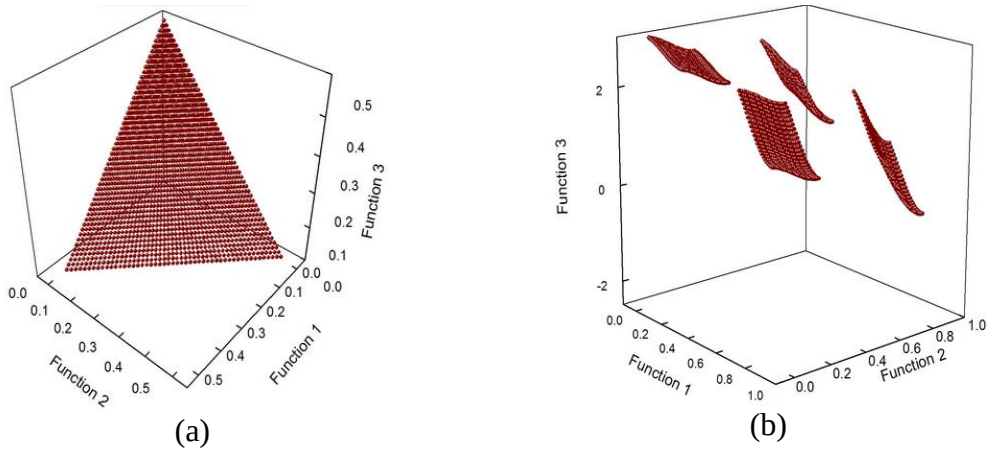

(a) (b)

FIGURE 2-7 The DTLZ family test problems: (a) DTLZ1 and (b) DTLZ7

2.3.4 WFG Test Suite

Unlike the above-mentioned test problems which are hard-wired, the WFG test suite offers framework that is easily modifiable and which gives users the ability to test different features by plugging in different forms of transformations [62]. This way, the WFG suite offers a set of problems that show a variety of different characteristics such as shape, complexity, and dimensionality.

The nature of the Pareto-optimal front is determined by shape functions, parameters with domain [0, 1] are mapped (using transformation functions) onto the range [0, 1].

Examples include linear, concave, convex, mixed, or disconnected. Transformation functions take a vector of parameters which is referred to as the primary parameters. These parameters are then mapped to a single value. In general, transformation functions come in three types: shift, bias, and reduction functions. Bias transformations bias the fitness landscape and therefore have a natural impact on the search process. On the other hand, shift transformations move the location of optima and can be used to set the location of parameter optima. Tables 2.5 to 2.7 present the shape functions, transformation functions and properties of the WFG family test problems respectively. Figure 2-8 and Figure 2-9 show the PF geometry and transformation geometries of the WFG test problems.

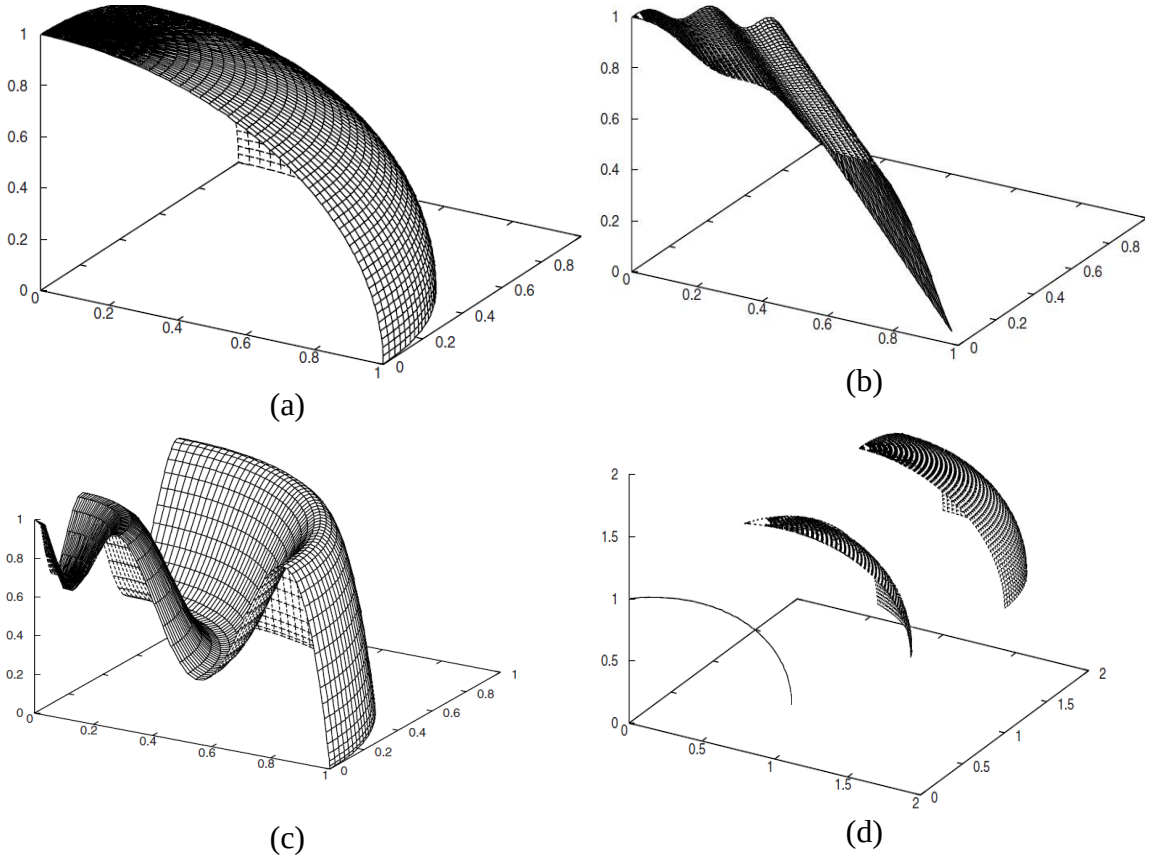

FIGURE 2-8 Example of three-objective WFG Pareto-optimal fronts (a) $h_{m=1:3}$ = concave, (b) $h_{m=1:2}$ = linear$_m$, h_3 = mixed$_3$ (α = 0.4, A = 3), (c) $h_{m=1:2}$ = concave$_m$, h_3 = disc$_3$ (dominated regions not removed, α = 0.4, β = 0.4, A = 3) and (d) $h_{m=1:3}$ = concave$_m$, degenerate on x_2, shown for distances 0, 0.5, and 1.

TABLE 2.4 The DTLZ family test problems.

Problem	n	Variable Bounds	Objective Functions	No. Objectives	General Description
DTLZ1	7	$x_i \in [0,1]$	$f_1(\mathbf{x}) = 0.5(1 + g(\mathbf{x}))\prod_{i=1}^{M-1} x_i$ $f_{m=2:M-1}(\mathbf{x}) = 0.5(1 + g(\mathbf{x}))\prod_{i=1}^{M-m} x_i\,(1 - x_{M-m+1})$ $f_M(\mathbf{x}) = 0.5[1 + g(\mathbf{x})](1 - x_1)$ $g(\mathbf{x}) = 100\left[k + \sum_{i=1}^{k}\left((x_i - 0.5)^2 - \cos(20\pi(x_i - 0.5))\right)\right]$	2/3	Linear
DTLZ2	12	$x_i \in [0,1]$	$f_1(\mathbf{x}) = (1 + g(\mathbf{x}))\prod_{i=1}^{M-1} cos(x_i\,\pi/2)$ $f_{m=2:M-1}(\mathbf{x}) = (1 + g(\mathbf{x}))\left(\prod_{i=1}^{M-m}\cos(x_i\pi/2)\right)\sin(x_{M-m+1}\pi/2)$ $f_M(\mathbf{x}) = (1 + g(\mathbf{x}))\,sin(x_1\pi/2)$ $g(\mathbf{x}) = \sum_{i=1}^{k}(x_i - 0.5)^2$	2/3	Concave
DTLZ3	12	$x_i \in [0,1]$	$f_1(\mathbf{x}), f_m(\mathbf{x})$ and $f_M(\mathbf{x})$ idem DTLZ2 $g(\mathbf{x}) = 100\left[k + \sum_{i=1}^{k}\left((x_i - 0.5)^2 - \cos(20\pi(x_i - 0.5))\right)\right]$	2/3	Concave
DTLZ4	12	$x_1 \in [0,1]$ $\alpha = 100$	$f_1(\mathbf{x}) = (1 + g(\mathbf{x}))\prod_{i=1}^{M-1}\cos(x_i^{\alpha}\,\pi/2)$ $f_{m=2:M-1}(\mathbf{x}) = (1 + g(\mathbf{x}))\left(\prod_{i=1}^{M-m}\cos(x_i^{\alpha}\pi/2)\right)\sin(x_{M-m+1}^{\alpha}\pi/2)$ $f_M(\mathbf{x}) = (1 + g(\mathbf{x}))\sin(x_1^{\alpha}\pi/2)$ $g(\mathbf{x}) = \sum_{i=1}^{k}(x_i - 0.5)^2$	2/3	Concave, degenerate when (M > 2)
DTLZ5	12	$x_i \in [0,1]$	Idem DTLZ2, except $\forall\, x_2,\ldots, x_{M-1} \in \mathbf{x}$ are replaced by $\frac{1+2g(\mathbf{x})x_i}{2(1+g(\mathbf{x}))}$	2/3	Concave, degenerate when (M > 2)

DTLZ6	12	$x_i \in [0,1]$	Idem DTLZ5, except $g(\mathbf{x}) = \sum_{i=1}^{k} x_i^{0.1}$	2/3	Concave, Degenerate
DTLZ7	22	$x_i \in [0,1]$	$f_{m=1:M-1}(\mathbf{x}) = x_m$ $f_M(\mathbf{x}) = [1 + g(\mathbf{x})]\left(M - \sum_{i=1}^{M-1}\left(\frac{f_i}{1+g}(1 + \sin(3\pi f_i)\right)\right)$ $g(\mathbf{x}) = \sum_{i=1}^{k}(x_i - 0.5)^2$	2/3	Disconnected

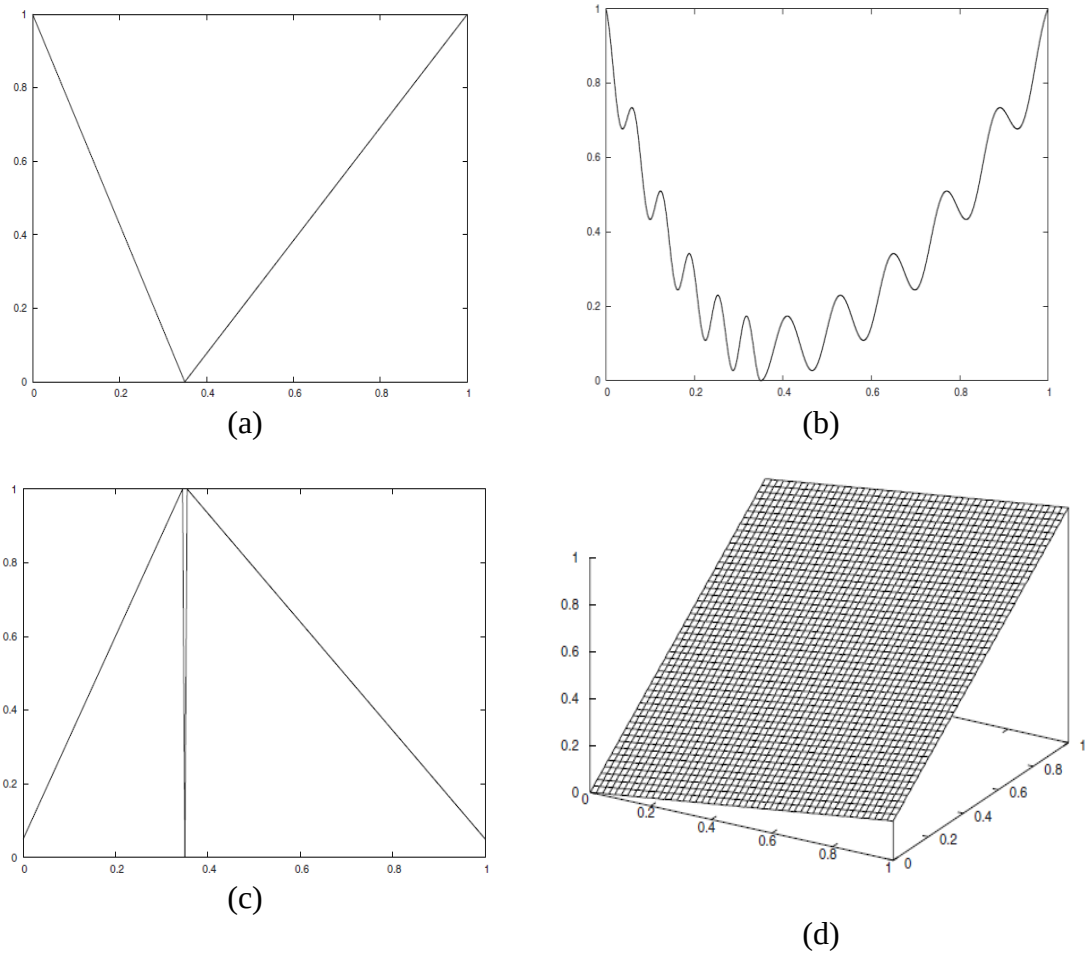

FIGURE 2-9 Example of WFG transformations based on primary parameter(s) versus the result of the transformation: (a) s linear (A = 0.35), (b) s_multi (A = 5, B = 10, C = 0.35), (c) s_decept (A = 0.35, B = 0.005, C = 0.05) and (d) r sum for two parameters (w_1 = 1, w_2 = 5).

TABLE 2.5 The WFG shape functions in all cases, $x_1, \ldots, x_{M-1} \in [0,1]$. A, α, and β are constants.

Linear

$$\text{linear}_1(x_1, \ldots, x_{M-1}) = \prod_{i=1}^{M-1} x_i$$

$$\text{linear}_{m=2:M-1}(x_1, \ldots x_{M-1}) = \left(\prod_{i=1}^{M-m} x_i\right)(1 - x_{M-m+1})$$

$$\text{linear}_{\text{M}}(x_1, \ldots, x_{M-1}) = 1 - x_1$$

When $h_{m=1:M} = linear_m$, the Pareto-optimal front is a linear hyper-plane, where $\sum_{m=1}^{M} h_m = 1$.

Convex

$$\text{convex}_1(x_1, \ldots, x_{M-1}) = \prod_{i=1}^{M-1} (1 - \cos(x_i \pi/2))$$

$$\text{convex}_{m=2:M-1}(x_1, \ldots x_{M-1}) = \left(\prod_{i=1}^{M-m} (1 - \cos(x_i \pi/2))\right)(1 - \sin(x_{M-m+1} \pi/2))$$

$$\text{convex}_{\text{M}}(x_1, \ldots, x_{M-1}) = 1 - \sin(x_1 \pi/2)$$

When $h_{m=1:M} = convex_m$,the Pareto-optimal front is purely convex.

Concave

$$\text{concave}_1(x_1, \ldots, x_{M-1}) = \prod_{i=1}^{M-1} sin(x_i \pi/2))$$

$$\text{concave}_{m=2:M-1}(x_1, \ldots x_{M-1}) = \left(\prod_{i=1}^{M-m} sin(x_i \pi/2)\right)(\cos(x_{M-m+1} \pi/2))$$

$$\text{concave}_{\text{M}}(x_1, \ldots, x_{M-1}) = \cos(x_1 \pi/2)$$

When $h_{m=1:M} = concave_m$, the Pareto-optimal front is purely concave, and a region of the hyper-sphere of radius one centered at the origin, where $\sum_{m=1}^{M} h_m^2 = 1$.

Mixed convex/concave ($\alpha > 0,\ A \in \{1,2, \ldots\}$)

$$\text{mixed}_{\text{M}}(x_1, \ldots, x_{M-1}) = \left(1 - x_1 - \frac{\cos(2A\pi x_1 + \pi/2}{2A\pi}\right)^{\alpha}$$

Causes the Pareto-optimal front to contain both convex and concave segments, the number of which is controlled by *A*. The overall shape is controlled by α: when $\alpha > 1$ or when $\alpha < 1$, the overall shape is convex or concave respectively. When $\alpha = 1$, the overall shape is linear.

Disconnected ($\alpha, \beta > 0,\ A \in \{1,2, \ldots\}$)

$$\text{disc}_{\text{M}}(x_1, \ldots, x_{M-1}) = 1 | - (x_1)^{\alpha} \cos^2(A(x_1)^{\beta} \pi)$$

Causes the Pareto-optimal front to have disconnected regions, the number of which is controlled by *A*. The overall shape is controlled by α (when $\alpha > 1$ or when $\alpha < 1$, the overall shape is concave or convex respectively, and when $\alpha = 1$, the overall shape is linear), and β influences the location of the disconnected regions (larger values push the location of disconnected regions towards larger values of x_1, and vice versa).

TABLE 2.6 The WFG transformation functions. Primary parameters, $y_1, \ldots, y_{|y|} \in [0,1]$; A, B, C, α, and β are constants for b_{param}; the vector $\mathbf{y}' \in [0,1]$ is a vector of the secondary parameters; and u is a redirection function.

Bias: Polynomial $(\alpha > 0, \alpha \neq 1)$ b_poly $(y, \alpha) = y^{\alpha}$ When $\alpha > 1$ or when $\alpha < 1$, y is biased towards zero or towards one respectively.
Bias: Flat Region $(A, B, C \in [0,1], B < C, B = 0 \Longrightarrow A = 0 \wedge C \neq 1, C = 1 \Longrightarrow A = 1 \wedge B \neq 0)$ $\mathrm{b}_{\mathrm{flat}}(y, A, B, C) = A + \min(0, \lvert y - B \rvert)\frac{A(B-y)}{B} - \min(0, \lvert C - y \rvert)\frac{(1-A)(y-C)}{1-C}$ Values of *y* between *B* and *C* (the area of the flat region) are all mapped to the value *A*.
Bias: Parameter Dependant $(A \in (0,1), 0 < B < C)$ $\mathrm{b}_{\mathrm{param}}(y, \boldsymbol{y}', A, B, C) = y^{B+(C-B)_{v(u(\mathbf{y}'))}}$ $v(u(\mathbf{y}')) = A - (1 - 2u(\boldsymbol{y}'))\lvert \lfloor 0.5 - u(\mathbf{y}') \rfloor + A \rvert$ *A,B,C* and the secondary parameter vector $\boldsymbol{y}'$ together determine the degree to which y is biased by being raised to an associated power: values of $u(\boldsymbol{y}') \in [0, 0.5]$ are mapped linearly onto $[B, B + (C-B)A]$, and values of $u(\boldsymbol{y}') \in [\,0.5,1]$ are mapped linearly onto$[\,B + (C-B)A, C]$
Shift: Linear $(A \in (0,1))$ s_linear$(y, A) = \frac{\lvert y - A \rvert}{\lvert \lfloor A - y \rfloor + A \rvert}$ *A* is the value for which *y* is mapped to zero.
Shift: Deceptive $(A \in (0,1), 0 < B \ll 1, 0 < C \ll 1, A - B > 0, A + B < 1)$ s_decept $(y, A, B, C) = 1 + (\lvert y - A \rvert - B) \times$ $\left(\frac{\lfloor y - A + B \rfloor (1 - C + \frac{A-B}{B})}{A-B} + \frac{\lfloor A + B - y \rfloor (1 - C + \frac{1-A-B}{B})}{1-A-B} + \frac{1}{B} \right)$ *A* is the value at which *y* is mapped to zero, and the global minimum of the transformation. *B* is the "aperture" size of the well/basin leading to the global minimum at *A*, and *C* is the value of the deceptive minima (there are always two deceptive minima).
Shift:Multi-modal $A \in \{1, 2, \ldots\}, B \geq 0, (4A+2)\pi \geq 4B,\ C \in (0,1))$ s_multi$(y, A, B, C) = \frac{1 + \cos\left[(4A+2)\pi\left(0.5 - \frac{\lvert y - C \rvert}{2(\lfloor C - y \rfloor + C)}\right)\right] + 4B\left(\frac{\lvert y - C \rvert}{2(\lfloor C - y \rfloor + C)}\right)^2}{B+2}$ *A* controls the number of minima, *B* controls the magnitude of the "hill sizes" of the multi-modality, and *C* is the value for which y is mapped to zero. When *B = 0, 2A + 1* values of *y* (one at *C*) are mapped to zero, and when B ≠ 0, there are 2A local minima, and one global minimum at *C*. Larger values of *A* and smaller values of *B* create more difficult problems.
Reduction: Weighted Sum$(\lvert w \rvert = \lvert y \rvert, w_1, \ldots, w_{\lvert y \rvert} > 0)$ r_sum (y,w) $= \left(\sum_{i=1}^{\lvert y \rvert} w_i y_i\right) / \sum_{i=1}^{\lvert y \rvert} w_i$

By varying the constants of the weight vector w, EAs can be forced to treat parameters differently.
Reduction: Non-separable$(A \in \{1, \dots, \lvert y\rvert\}, \lvert y\rvert mod\ A = 0$ r_nonsep $(y, A) = \frac{\left(\sum_{j=1}^{\lvert y\rvert}\left(y_j + \sum_{k=0}^{A-2}\lvert y_j - y_{1+(j+k) mod\ \lvert y\rvert}\rvert\right)\right)}{\frac{\lvert y\rvert}{A}\lceil A/2\rceil(1+2A-2\lceil A/2\rceil)}$ *A* controls the degree of non-separability (noting that r_nonsep$(y, 1) = r\ sum(y, \{1, \dots, 1\})$).

TABLE 2.7 Properties of the WFG functions. For detailed definitions, see [60] and [62].

Problem	Objective	Separability	Modality	Bias	Geometry
WFG1	$f_{1:M}$	Separable	Uni	Polynomial	Convex, mixed
WFG2	$f_{1:M-1}$ f_M	Non-separable Non-separable	Uni Multi	—	Convex, disconnected
WFG3	$f_{1:M}$	Non-separable	Uni	—	Linear, degenerate
WFG4	$f_{1:M}$	Separable	Multi	—	Concave
WFG5	$f_{1:M}$	Separable	Deceptive	—	Concave
WFG6	$f_{1:M}$	Non-separable	Uni	—	Concave
WFG7	$f_{1:M}$	Separable	Uni	Parameter dependent	Concave
WFG8	$f_{1:M}$	Non-separable	Uni	Parameter dependent	Concave
WFG9	$f_{1:M}$	Non-separable	Multi, Deceptive	Parameter dependent	Concave

2.3.5 Z09 Test Suite

Other test problems include the LZ family which was introduced by Li and Zhang [49]. Here, a general class of continuous MO optimization test instances was introduced with arbitrary prescribed Pareto set shapes. This class could be used for studying the ability of MOE algorithms to deal with complicated Pareto set shapes. Similar to DTLZ and WFG test problems, in LZ the proposed test problem utilizes component functions to define its Pareto set and introduce multimodality. Table 2.8 presents the LZ_09 test problems utilized in MOEAs.

TABLE 2.8 LZ_09 family test problems.

Problem	n	Variable Bounds	Objective Functions	No. Objectives	General Description
LZ_F1	30	$x_i \in [0,1]$	$f_1(\mathbf{x}) = x_1 + \frac{2}{\lvert J_1\rvert}\sum_{j\epsilon J_1}\left(x_j - x_1^{0.5\left(1.0+\frac{3(j-2)}{n-2}\right)^2}\right)$ $f_2(\mathbf{x}) = 1-\sqrt{x_1} + \frac{2}{\lvert J_2\rvert}\sum_{j\epsilon J_2}\left(x_j - x_1^{0.5\left(1.0+\frac{3(j-2)}{n-2}\right)^2}\right)$ $J_1 = \{j \mid j \text{ is odd and } 2 \le j \le n\}$ and $J_2 = \{j \mid j$ is even and $2 \le j \le n\}$	2	Convex
LZ_F2	30	$x_1 \in [0,1]$ $x_i \in [-1,1]$ $i = 2, \dots, n$	$f_1(\mathbf{x}) = x_1 + \frac{2}{\lvert J_1\rvert}\sum_{j\epsilon J_1}\left[x_j - \sin\left(6\pi x_1 + \frac{j\pi}{n}\right)\right]^2$ $f_2(\mathbf{x}) = 1-\sqrt{x_1} + \frac{2}{\lvert J_2\rvert}\sum_{j\epsilon J_2}\left[x_j - \sin\left(6\pi x_1 + \frac{j\pi}{n}\right)\right]^2$ J_1 and J_2 idem LZ_F1	2	Convex
LZ_F3	30	$x_1 \in [0,1]$ $x_i \in [-1,1]$ $i = 2, \dots, n$	$f_1(\mathbf{x}) = x_1 + \frac{2}{\lvert J_1\rvert}\sum_{j\epsilon J_1}\left[x_j - 0.8x_1\cos\left(6\pi x_1 + \frac{j\pi}{n}\right)\right]^2$ $f_2(\mathbf{x}) = 1-\sqrt{x_1} + \frac{2}{\lvert J_2\rvert}\sum_{j\epsilon J_2}\left(\left[x_j - 0.8x_1\sin\left(6\pi x_1 + \frac{j\pi}{n}\right)\right]\right)^2$ J_1 and J_2 idem LZ_F1	2	Convex
LZ_F4	30	$x_1 \in [0,1]$ $x_i \in [-1,1]$ $i = 2, \dots, n$	$f_1(\mathbf{x}) = x_1 + \frac{2}{\lvert J_1\rvert}\sum_{j\epsilon J_1}\left[x_j - 0.8x_1\cos\left(\frac{6\pi x_1 + \frac{j\pi}{n}}{3}\right)\right]^2$	2	Convex

			$f_2(\mathbf{x}) = 1 - \sqrt{x_1} + \frac{2}{\lvert J_2\rvert}\sum_{j\epsilon J_2}\left(\left[x_j - 0.8x_1 sin\left(6\pi x_1 + \frac{j\pi}{n}\right)\right]\right)^2$ J_1 *and* J_2 idem LZ_F1		
LZ_F5	30	$x_1 \in [0,1]$ $x_i \in [-1,1]$ $i = 2, \dots, n$	$f_1(\mathbf{x}) = x_1 + \frac{2}{\lvert J_1\rvert}\sum_{j\epsilon J_1}\left[x_j - \left(0.3x_1^2 cos\left(24\pi x_1 + \frac{4j\pi}{n}\right) + 0.6x_1\right)\cos\left(6\pi x_1 + \frac{j\pi}{n}\right)\right]^2$ $f_2(\mathbf{x}) = 1 - \sqrt{x_1} + \frac{2}{\lvert J_2\rvert}\sum_{j\epsilon J_1}\left[x_j - \left(0.3x_1^2 cos\left(24\pi x_1 + \frac{4j\pi}{n}\right) + 0.6x_1\right)\sin\left(6\pi x_1 + \frac{j\pi}{n}\right)\right]^2$ J_1 *and* J_2 idem LZ_F1	2	Convex
LZ_F6	10	$x_1 \in [0,1]$ $x_2 \in [0,1]$ $x_i \in [-1,1]$ $i = 3, \dots, n$	$f_1(\mathbf{x}) = \cos(0.5x_1\pi)\cos(0.5x_2\pi) + \frac{2}{\lvert J_1\rvert}\sum_{j\epsilon J_1}\left[x_j - 2x_2 sin\left(2\pi x_1 + \frac{j\pi}{n}\right)\right]^2$ $f_2(\mathbf{x}) = \cos(0.5x_1\pi)\cos(0.5x_2\pi) + \frac{2}{\lvert J_2\rvert}\sum_{j\epsilon J_2}\left[x_j - 2x_2 sin\left(2\pi x_1 + \frac{j\pi}{n}\right)\right]^2$ $f_3(\mathbf{x}) = \sin(0.5x_1\pi) + \frac{2}{\lvert J_3\rvert}\sum_{j\epsilon J_3}\left[x_j - 2x_2 sin\left(2\pi x_1 + \frac{j\pi}{n}\right)\right]^2$ $J_1 = \{j \mid 3 \le j \le n,$ and is even and $j-1$ is a multiple of 3 $\}$ $J_2 = \{j \mid 3 \le j \le n,$ and is even and $j-2$ is a multiple of 3 $\}$ $J_3 = \{j \mid 3 \le j \le n,$ and is even and j is a multiple of 3 $\}$	3	Convex
LZ_F7	10	$x_i \in [0,1]$	$f_1(\mathbf{x}) = x_1 + \frac{2}{\lvert J_1\rvert}\sum_{j\epsilon J_1}\left[4y_j^2 - cos\left(8y_j\pi + 1.0\right)\right]$	2	Convex

			$f_2(\mathbf{x}) = 1 - \sqrt{x_1} + \frac{2}{\lvert J_2\rvert}\sum_{j\epsilon J_2}\left[4y_j^2 - cos\left(8y_j\pi + 1.0\right)\right]$ $J_1\ and\ J_2$ idem LZ_F1 and $y_j = x_j - x_1^{0.5\left(1.0+\frac{3(j-2)}{n-2}\right)}, J = 2,\ldots,n$		
LZ_F8	10	$x_i \in [0,1]$	$f_1(\mathbf{x}) = x_1 + \frac{2}{\lvert J_1\rvert}\left[4\sum_{j\epsilon J_1} y_j^2 - 2\prod_{j\epsilon J_1}\cos\left(\frac{20y_j^\pi}{\sqrt{j}}\right) + 2\right]$ $f_2(\mathbf{x}) = 1 - \sqrt{x_1} + \frac{2}{\lvert J_2\rvert}\left[4\sum_{j\epsilon J_2} y_j^2 - 2\prod_{j\epsilon J_1}\cos\left(\frac{20y_j^\pi}{\sqrt{j}}\right) + 2\right]$ $J_1\ and\ J_2$ idem LZ_F1 and $y_j = x_j - x_1^{0.5\left(1.0+\frac{3(j-2)}{n-2}\right)}, J = 2,\ldots,n$	2	Convex
LZ_F9	30	$x_1 \in [0,1]$ $x_i \in [-1,1]$ $i = 2,\ldots,n$	$f_1(\mathbf{x}) = x_1 + \frac{2}{\lvert J_1\rvert}\sum_{j\epsilon J_1}\left[x_j - sin\left(6\pi x_1 + \frac{j\pi}{n}\right)\right]^2$ $f_2(\mathbf{x}) = 1 - x_1^2 + \frac{2}{\lvert J_2\rvert}\sum_{j\epsilon J_2}\left[x_j - sin\left(6\pi x_1 + \frac{j\pi}{n}\right)\right]^2$ $J_1\ and\ J_2$ idem LZ_F1 and $y_j = x_j - x_1^{0.5\left(1.0+\frac{3(j-2)}{n-2}\right)}, J = 2,\ldots,n$	2	Concave

2.3.6 Constrained problems: Srinivas, Tanaka, Osyczka, and Golinski

When it comes to constrained test problems, there are several that are available in literature; however the focus here are on the three most commonly used ones: Osyczka [63], Tanaka [64], and Srinivas [65]. In multi-objective optimization, constraints can hamper the Pareto-optimal region convergence of multi-objective EA. Furthermore, constraints can cause difficulty in maintaining a diverse set of Pareto-optimal solutions. Whether MOEA is

successful or not in dealing with these two issues will depend, in large, on the constraint handling technique used. The aforementioned test problems attempt to test an MOEA's ability to deal with constrained multi-objective optimization problems. Nonetheless, they have few difficulties such as: the scarcity of decision variables, the inadequate non-linearity of most objective functions and constraints, and the fact that they're not tunable for introducing varying degrees of complexity when it comes to constrained optimization. Table 2.9 presents the LZ_09 test problems utilized in MOEAs. Figure 2-10 show projections of LZ Pareto sets of F1–F9 onto a three-dimensional space.

TABLE 2.9 Constrained problems test problems.

Problem	***n***	**Variable Bounds**	**Objective Function**	**Constraints**
Osyczka	6	$x_1, x_2, x_6 \in [0,10]$ $x_3, x_5 \in [1,5]$ $x_4 \in [0,6]$	$f_1(\mathbf{x}) = -[25(x_1-2)^2 + (x_2-2)^2 + (x_3-1)^2(x_4-4)^2]$ $f_2(\mathbf{x}) = -[25(x_1-2)^2 + (x_2-2)^2 + (x_3-1)^2(x_4-4)^2]$	$g_1(\mathbf{x}) \equiv 0 \leq x_1 + x_2 - 2$ $g_2(\mathbf{x}) \equiv 0 \leq -x_1 - x_2 + 6$ $g_3(\mathbf{x}) \equiv 0 \leq x_1 - x_2 + 2$ $g_4(\mathbf{x}) \equiv 0 \leq -x_1 + 3x_2 + 2$ $g_5(\mathbf{x}) \equiv 0 \leq -(x_3-3)^2 - x_4 + 4$ $g_6(\mathbf{x}) \equiv 0 \leq (x_5-3)^3 + x_6 - 4$
Tanaka	2	$x_1, x_2 \in [-\pi, \pi]$	$f_1(\mathbf{x}) = x_1$ $f_2(\mathbf{x}) = x_2$	$g_1(\mathbf{x}) \equiv 0 \geq -x_1^2 - x_2^2 + 0.1cos\left[16\, arctan\left(\frac{x_1}{x_2}\right)\right] + 1$ $g_2(\mathbf{x}) \equiv 0.5 \geq (x_1-0.5)^2 + (x_2-0.5)^2$
Srinivas	2	$x_1, x_2 \in [-20,20]$	$f_1(\mathbf{x}) = 2 + (x_1-2)^2 + (x_2-1)^2$ $f_2(\mathbf{x}) = 9x_1 + (x_2-1)^2$	$g_1(\mathbf{x}) \equiv 0 \leq -x_1^2 - x_2^2 + 225$ $g_2(\mathbf{x}) \equiv 0 \leq -x_1 + 3x_2 - 10$

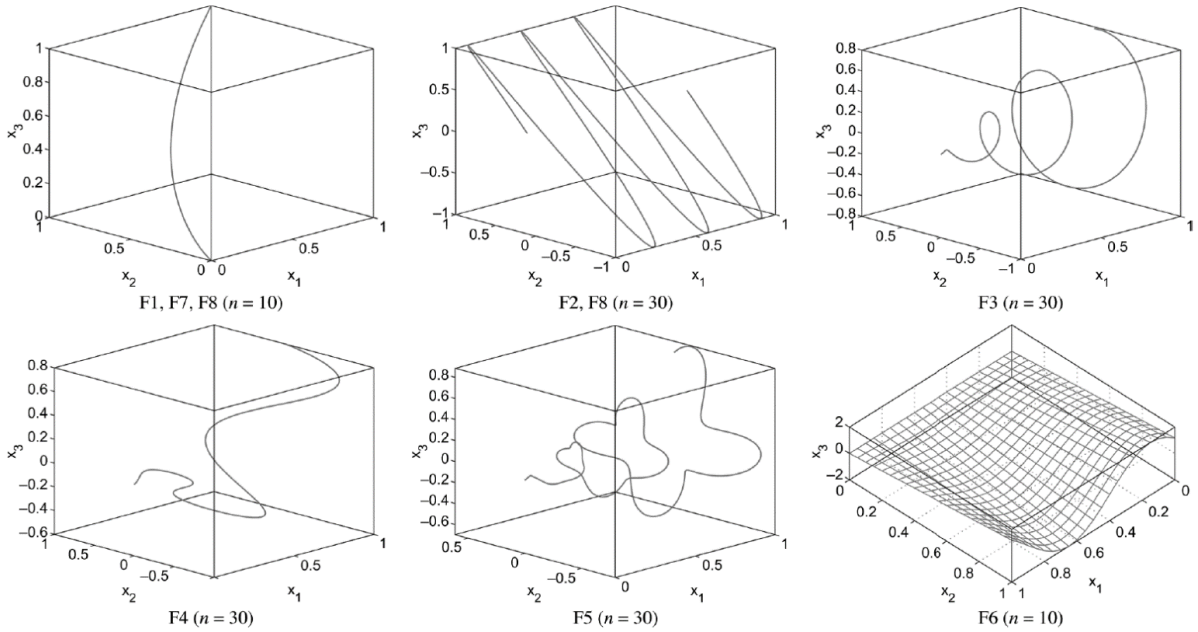

FIGURE 2-10 Projections of LZ Pareto sets of F1–F9 onto the x_1, x_2, and x_3 space [49].

Chapter 3

3D-RADVIS, 3D-RADVIS ANTENNA, AND ECM PLOTS: NOVEL VISUALIZATION METHODS FOR MANY-OBJECTIVE OPTIMIZATION DATA SET

In many-objective optimization, visualization of optimal PFs or obtained non-dominated solutions is a challenging task. A proper visualization tool must be able to show the location, range, shape, and distribution of obtained non-dominated solutions. Existing commonly used visualization tools in many-objective optimization (e.g., parallel coordinates) fail to show the shape of the PF or distribution of solutions along each objective. This chapter presents three proposed multi- and many-objective visualization methods, namely, 3D-RadVis, 3D-RadVis Antenna, and Enhanced Correlation Matrix (ECM) plot for visualizing the distribution, convergence, and relationship between decision variables and objective functions. The 3D-RadVis plot is capable of mapping M-dimensional objective space to a three-dimensional radial coordinate plot while seeking to preserve the relative location of solutions, shape of the PF, and distribution of solutions on the Pareto-optimal surface. On the other hand, the 3D-RadVis Antenna plot incorporates additional dimension to the 3D-RadVis plot to visualize the distribution of solutions as along each objective. These plots can be used by decision makers to visually navigate large many-objective solution sets, to observe behavior of a population-based optimization process, to visualize the relative location of a solution, to evaluate trade-offs among objectives, and to select preferred solutions. The effectiveness of the proposed methods are demonstrated on widely used many-objective benchmark problems containing a variety of PFs (linear, concave, convex, mixed, and disconnected). Experimental results show that the proposed visualization method can effectively be used to compare and track the performance of many-objective algorithms.

3.1 Introduction

Real-world optimization applications are ever more encompassing and increasingly complex these days. Particularly, more input data and parameters are available to capture the complexity of a problem leading to more decision variables being used to model complex situations. Additionally, optimizing a high number of objectives is involved in these situations, leading to further complexity.

Many real-world applications involve a high number of objectives (typically more than three). Visualization of solutions hence becomes difficult. However, visualization is necessary as it is a proper decision-making tool leading to a better understanding of algorithms used and trade-off solutions. As the number of objectives exceeds three, the visualization of approximation sets is more challenging [66]. There exists several two- or three-dimensional data visualization methods that are used for many-objective optimization (MaOO). Parallel coordinates [27] and Heatmap plots [29] are two examples that can be used to visualize distribution, range, and trade-off among solutions of multi-dimensional objectives. Nonetheless, such methods are often difficult to interpret due to solutions being superimposed or arbitrarily ordered [12]. There are other methods, such as self-organizing maps [29] and radial coordinate visualization [30], that show the distribution and inter-relationship among objectives, yet they do not illustrate the shape and convergence trend of the solution sets. Fortunately, there are recent advances in visualization methods to cope with visualizing high-dimensional search space while attempting to preserve the distribution, shape, and dominance relationship among approximate PF members. Some of these visualization methods include the extension of radial coordinate visualization and Heatmap [12, 67-69].

The objective of this chapter is to introduce three powerful visualization methods, namely, three-dimensional radial coordinate (3D-RadVis), three-dimensional radial coordinate with antenna (3D-RadVis Antenna), and enhanced correlation matrix plots which allow MaOO researchers, decision makers and any interested party to better understand the optimization process along with intermediate and final results of an algorithm. The 3D-RadVis and 3D-RadVis Antenna plots permit a decision maker to visually explore many-objective solution sets and identify one or more preferred optimal solutions (not solely based on the convergence and distribution of solutions on the Pareto-optimal front but also distribution of solutions along each objective). Moreover, decision makers can use these visualization methods in conjunction with immersive virtual reality (VR) technologies, such as the CAVE [70] to visualize high-dimensional decision and solution space and select preferred solutions with ease. VR tools have been widely used in several disciplines where past visualization technologies are limited when analyzing and interacting with data [71-74]. In the optimization field, decision makers can use VR tools to visualize and interactively select the ideal solution according to their specific situation (set of requirements, budget, etc.). In the same fashion, researchers can utilize the proposed visualization techniques in conjunction with VR tools to investigate aspects of many-objective optimization algorithm's (MaOOA) behaviour such as, performance comparison, parameter specifications, and maybe even develop efficient algorithms to tackle MaOO problems. Also, a proper visualization tool can potentially lead to the development of effective interactive optimization methods.

3.2 Visualization Methods Used in Many-objective Optimization: A Survey

As the number of objectives increases, visualization of the approximation set becomes progressively challenging. Moreover, the applicability of quantitative metrics capable of measuring the convergence and diversity of solution sets are problematic due to inconsistencies among them [22]. In this section we describe the classical and recent advances in visualization techniques.

3.2.1 Classical Visualization Methods

In MaOO, when the number of objectives are two or three, many effective visualization tools are available. The issue arises when the number of objectives are four or more leading to very challenging visualization of approximation sets. For instance, parallel coordinates [27] Heatmap plots [28], self-organizing maps [29] and radial coordinate visualization [30] are classical visualization tools that can be used to visualize the distribution, range, and trade-off among solutions of many-objective solution sets. Nonetheless, these tools usually fail to preserve the shape or dominance relationship and are not capable of showing the convergence trend of the solution set.

Parallel coordinates plot is a popular way to visualize the distribution, range, and trade-off among solutions of multi-objectives [75, 76]. Here, an objective is represented by a polyline with vertices on parallel axes placed along the x-axis. The parallel axes are equidistant vertical bars along the x-axis for each of the objectives. The y-axis corresponds to the range of possible values for each of the objectives. Despite the inability of parallel coordinate plots of showing the shape of the PF, they are simple to construct, scale well to larger numbers of objectives, and are a great visualization tool to illustrate dependencies

among objectives without the loss of data in the representation [77]. Figure Figure 3-1 (a) depicts a parallel coordinates plot of four-dimensional concave data points constructed from symmetric and continuous PFs using the equation $f_1^2 + f_2^2 + f_3^2 + f_4^2 = 1$.

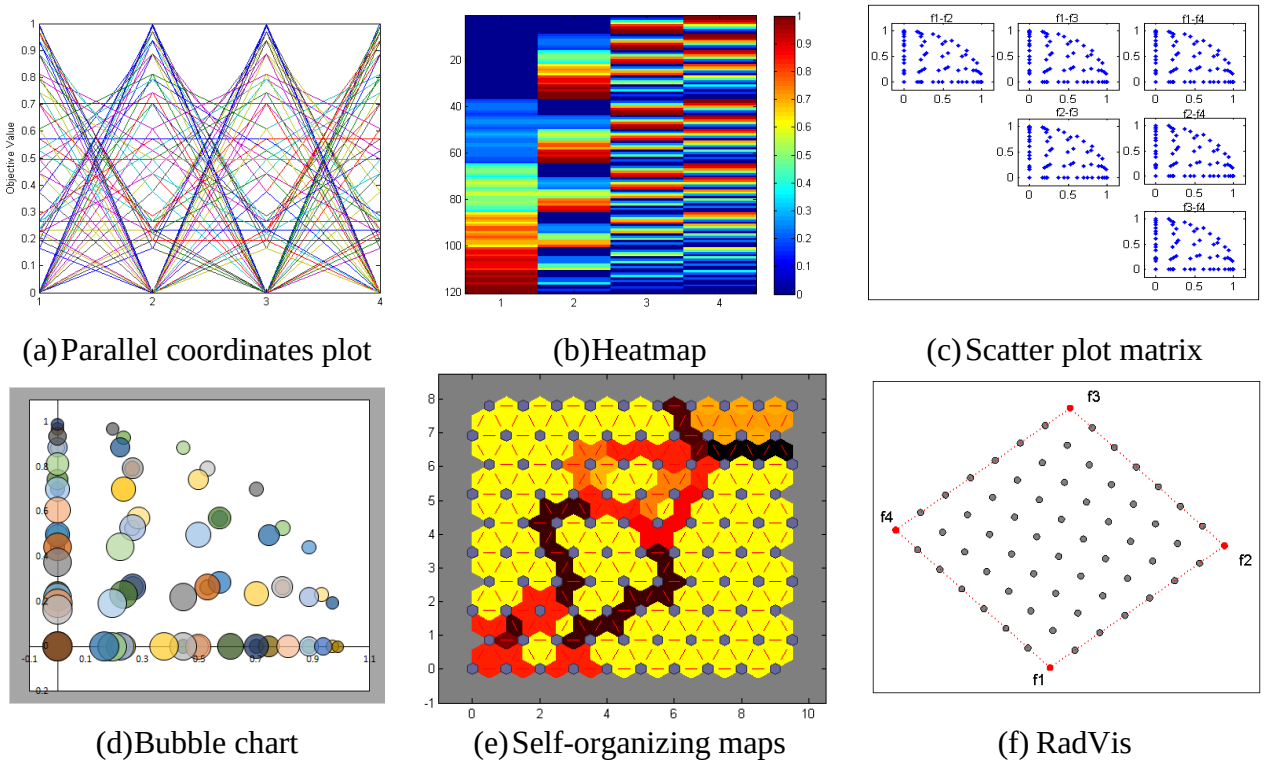

(a) Parallel coordinates plot (b) Heatmap (c) Scatter plot matrix

(d) Bubble chart (e) Self-organizing maps (f) RadVis

FIGURE 3-1 Visualization schemes used in MaOO problems showing well-distributed four-dimensional concave PF generated using the equation $f_1^2 + f_2^2 + f_3^2 + f_4^2 = 1$

Similar to the parallel coordinates plot, Heatmap [28] plots represents objective values using colors as opposed to polylines with vertices. These plots are very easy to construct and can scale well to visualize higher dimensional objectives. Additionally, heat maps can show dependencies among objectives without the loss of data in the representation. However, these plots do not scale well when the number of solutions are large because the number of colors used to represent each solution is also large. Furthermore, they cannot show the shape of the PF. Figure 3-1 (b) depicts a Heatmap plot of four-dimensional concave data points.

A scatter plot matrix is a simple visualization method capable of showing the pair-wise relationship of objectives while also preserving some information on the shape of the PF. Given an M-objective data set, a scatter plot matrix plots all objective pairs [8, 78]. However, as the number of objectives increases, the scatter plot matrix does not scale well because it requires a large space to show the relationship among pairs of objectives. Figure 3-1 (c) depicts a scatter plot matrix of four-dimensional concave data points.

Bubble chart is another classical visualization method where the first and second objective values are represented using bubbles along the x- and y-axis and the third objective is represented by varying the size of the bubbles. There exists also a variation of bubble chart that utilizes the z-axis and colored bubbles to represent the 4^{th} and 5^{th} dimension [79, 80]. Figure 3-1 (d) depicts bubble chart representing four-dimensional concave data points.

Self-organizing maps (SOM) [29] are one type of artificial neural networks (ANN) trained using unsupervised learning in order to provide a mapping from M-dimensional objective to a lower dimensional space (typically two-dimensional) [30]. These maps consist of nodes (neurons) associated with a weight vector of the same dimension as the input data vectors or neurons. These nodes are arranged in a 2D space using a hexagonal or rectangular grid. Typically, SOMs use the unified distance matrix (U-Matrix) [81] to store each node's average distance to its closest neighbours (different colors are used to represent each node's distance to adjacent nodes). Clusters of similar neurons are represented with light areas while dark areas indicate cluster boundaries. Figure 3-1 (e) depicts a self-organizing map plot of four-dimensional concave data points.

Radial coordinate visualization (RadVis) [30] is an alternative high-dimensional visualization method mainly used to visualize hierarchical density clusters by mapping M-dimensional data set to a 2-dimensional space using a nonlinear mapping. To better understand RadVis, consider a point in 2-dimensional space connected to M equally spaced points on a circle with springs, where each dimension value is equal to the spring constant for the corresponding spring. Now, imagine that the 2-dimensional point is allowed to move and reach equilibrium, the location of this point will be the mapping of M-dimensional data points onto a 2-dimensional space. Figure 3-1 (f) depicts RadVis plot of well-distributed four-dimensional concave data points. Despite RadVis plots incapability of showing the shape and convergence of the PF, RadVis plots are simple to construct, scale well to large numbers of objectives, and are a great visualization tool to show the distribution of solutions.

3.2.2 Recently Proposed Visualization Methods

Recently a number of visualization methods have been proposed to deal with higher dimensional data sets. The following paragraphs will introduce the main ones.

Tusar and Filipic [69] proposed a visualization method that uses projection of a chosen subsection of the solution set to visualize 4-D approximation. This method allows researchers and decision makers to view the shape, range and distribution of large approximation sets. In some cases, it preserves the Pareto dominance relation and the convergence of the Pareto-optimal front. The drawback of this method is that it cannot scale for higher dimensions (greater than four objectives).

He and Yen [68] proposed another method for visualizing high dimensional objectives by mapping them onto a two-dimensional polar coordinate. Their visualization

method takes each individual high-dimensional Cartesian point and assigns a radial and angular coordinate value. The radial coordinate value represents the convergence and shape of the PF and the angular coordinate represents the distribution among the individuals. However, their method fails to show the relative location of a solution with respect to each objective.

Walker et al. [12] proposed visualization for mutually non-dominating solution sets by using the rank solutions on each objective. As a result, they enhanced the Heatmap plot by spectral seriation of both the objectives and the solutions in order to place similar objectives and similar solutions together. However, even though their scheme is able to enhance the Heatmap plot, the visualization of dominance relationships between solutions was not geometrically apparent.

3.3 Proposed Methods

This section presents three proposed visualization techniques, called, three-dimensional radial coordinate (3D-RadVis), three-dimensional radial coordinate with antenna (3D-RadVis Antenna), and enhanced correlation matrix (ECM) plots which is applicable in MaOO. The 3D-RadVis plot is designed to visualize the convergence, shape, and distribution of many-objective solutions. Whereas the 3D-RadVis Antenna integrates additional dimension to visualize the distribution of solutions along each objective. The ECM is designed for visualizing the distribution, convergence and relationship between decision variables and objective functions.

3.3.1 Proposed 3D-RadVis Plot

The framework of the proposed 3D-RadVis scheme is similar to RadVis; however, 3D-RadVis incorporates a third dimension to visualize the shape and convergence of an M-dimensional solution set. Consider $N \times M$ non-dominated solutions where N is the number of solutions and M is the dimension of the solution set. 3D-RadVis involves two main steps: first, mapping the location of M-dimensional solutions to a 2-dimensional xy plane, and second, determining the distance of each solution from a reference hyper-plane.

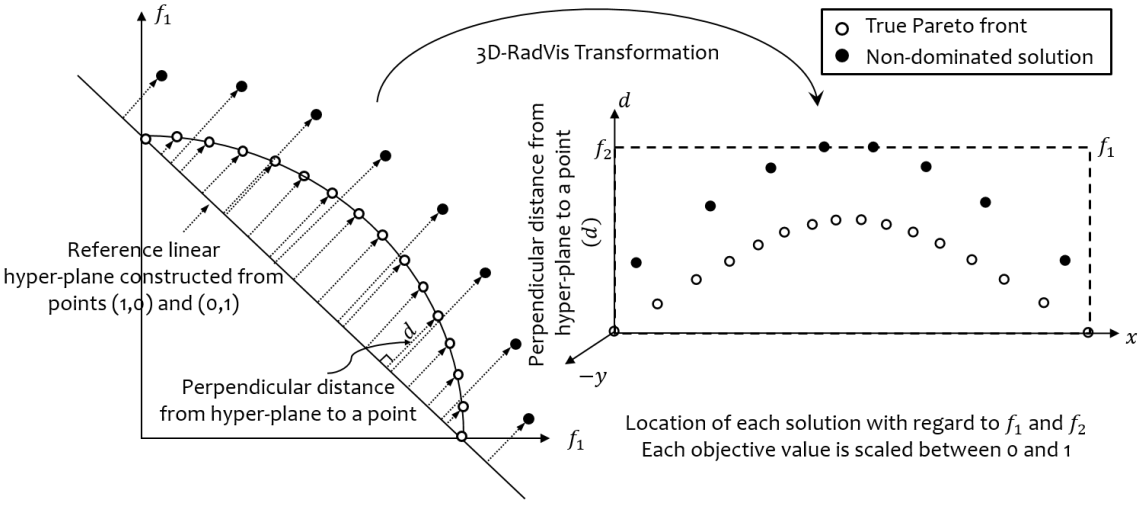

FIGURE 3-2 Illustration of 3D-RadVis transformation

The 3D-RadVis plot utilizes the RadVis [30] scheme to determine the location of an M-dimensional solution onto a 2-dimensional xy plane (u_x, u_y). Given $N \times M$ non-dominated solutions, the first step is to normalize each solution per objective between 0 and 1 ($f^{Norm} = \forall\, i \in 1..M\ [f_i(\mathbf{x}) - \min(f_i(\mathbf{x}))/(\max(f_i(\mathbf{x}) - \min(f_i(\mathbf{x}))]$), where N is the number of solutions and M is the number of objectives. Now, consider the normalized M-dimensional solutions in a 2-dimensional space are connected to M equally spaced points on a circle with springs, where each dimension value is the spring constant (K) for

the corresponding spring. Then, the 2-dimensional points are allowed to move and reach equilibrium. The location of these points are the mapping of M-dimensional data points to a 2-dimensional space. Thus, given $N \times M$ normalized non-dominated solutions (f^{Norm}), solution i can be mapped to a 2D radial space as follows:

$$x_i = \frac{\sum_{j=1}^{M} f_{i,j}^{Norm} \cos(\theta_j)}{\sum_{j=1}^{M} f_{i,j}^{Norm}}, \tag{3.1}$$

and

$$y_i = \frac{\sum_{j=1}^{M} f_{i,j}^{Norm} \sin(\theta_j)}{\sum_{j=1}^{M} f_{i,j}^{Norm}}, \tag{3.2}$$

where θ_j is the angular position on the circle corresponding to dimension j. The RadVis mapping procedure is described in Algorithm 3.1 and Algorithm 3.2 lines 6 to 8.

Next, before calculating the distance of each solution to the reference hyper-plane, a reference hyper-plane must be constructed. The reference hyper-plane for M-dimensional problem is constructed using M points containing $\{z_1 = (1,0,0,\dots,0), z_2 = (0,1,0,\dots,0), \dots, z_M = (0,0,\dots,1)\}$. The choice of these points are to standardize the 3D-RadVis plots so that the same reference hyper-plane is used for computing the orthogonal distance (d) between a point (solution) and the reference hyper-plane. Next, a linear hyper-plane passing through these points is constructed. Then, the perpendicular distance (d) from the reference hyper-plane for each point is computed, thereby preserving the shape and accuracy of the solution set. The values of d are used as the altitude (height or z-axis) of the solution in the 3D-RadVis. Figure 3-2 illustrates 3D-RadVis transformation.

Algorithm 3.1 RadVis (f^{Norm}) Procedure

Input: f^{Norm}: $N \times M$ normalized non-dominated solutions, where M is the number of objectives and N is the number of solutions.

Output: $[u_x, u_y]$ non-linear radial coordinates mapping of f^{Norm}

1: **for** $i = 1$ to N
2: Calculate 2D radial location/mapping of normalized objective: $[x_i, y_i]$ //Eqs.(3.1) and (3.2)
3: **end for**
4: $[u_x, u_y] = [x, y]$

Algorithm 3.2 3D-RadVis Procedure

Input: f: $N \times M$ matrix formed by N non-dominated solutions, where M is the number of objectives.

Output: R: $N \times 3$ transformation matrix for 3D-RadVis visualization.

// 3D-RadVis transformation

1: //Construct a reference hyper-plane
Z = `eye(M)` //$\{z_1 = (1,0,0,\dots,0), z_2 = (0,1,0,\dots,0), \dots, z_M = (0,0,\dots,1)\}$
2: //Calculate the normal vector for the reference hyper-plane with boundary points, Z:
n = `norm`(Z)
3: Calculate the hyper-plane equation constant, c for this plane: $c = (n \cdot z_i)$
4: **for** $i = 1$ to N
5: //Calculate the perpendicular distance from *n* to solution i:
$d = \frac{abs((f_i \cdot n) - c))}{\|n\|}$
6: **end for**
7: Normalize f by each objective: f^{Norm} = `normalize`(f)
8: Map f^{Norm} to 2D radial coordinates $[u_x, u_y]$ = `RadVis` (f^{Norm})
9: $R = [u_x, u_y, d]$

3.3.2 Proposed 3D-RadVis Antenna Plot

The framework of the proposed 3D-RadVis Antenna visualization scheme is similar to 3D-RadVis (the bottom portion of the plot); however, 3D-RadVis Antenna incorporates poles for each objective to show objective-wise distribution of solutions (shown in the top portion of the plot).

The top portion of 3D-RadVis Antenna plot consists of M poles (antenna) to show the distribution of solutions along each objective. The first step to plot the antenna is to find the location of antenna poles (vertical lines). The location of these vertical lines are computed using the boundary points. The length of these vertical lines are kept at the maximum perpendicular distance of points from the reference hyper-plane (z_{max}). This strategy will keep the top and the bottom portions of the plot with equal height. The next step is to compute the location of antenna directors (tick marks) along the vertical poles. The location of the antenna directors along each objective calculated by multiplying f^{Norm} by z_{max} and shifting these points by z_{max} to place them on the top portion of the plot. Algorithm 3.3, lines 1 to 8 show the 3D-RadVis transformation and lines 10 to 15 describe the Antenna extension to the 3D-RadVis Antenna plot. Figure 3-3 illustrates the 3D-RadVis Antenna transformation process.

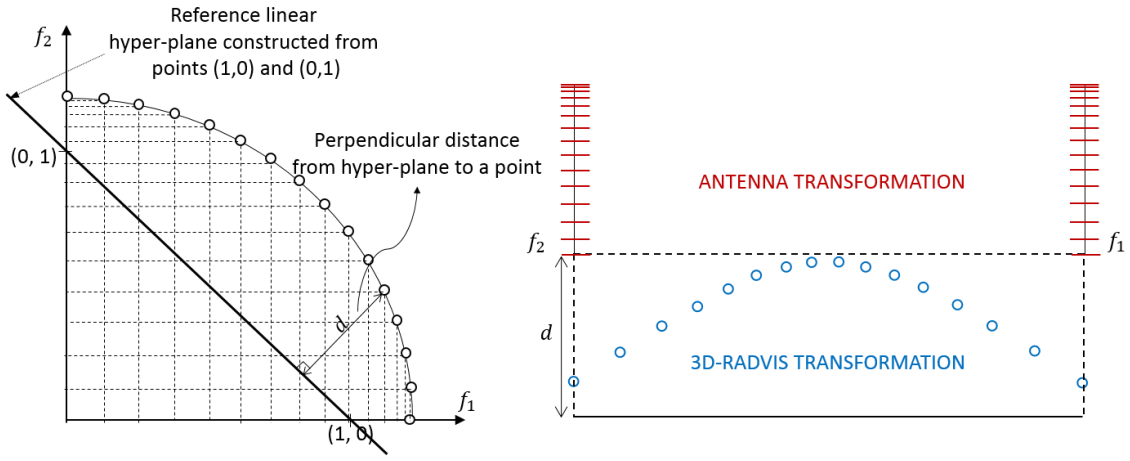

FIGURE 3-3 Illustration of 3D-RadVis Antenna transformation

3.3.3 Proposed ECM Plot

To date, there is no visualization method in optimization field capable of showing the relationships among the decision variables and objective functions when the number of

decision variables and the number of objective functions are more than three. This section presents a novel visualization technique called, Enhanced Correlation Matrix (ECM) plot applicable for multi-and many-objective optimization. The main features of an ECM plot are the following:

1. It provides information on the domain and range of a Pareto-optimal front
2. It provides visual correlation information between each decision variable and objective function as well as objective-wise relationship for different regions of the optimal PF
3. It provides visual distribution of solutions along each objective.

Before we dive into the proposed ECM method, we first give a definition of the correlation coefficient between two variables. The Pearson correlation coefficient of two random variables (say A and B) is a measure of their extent of interdependence of variable quantities. If A and B each has N scalar observations, then the linear (Pearson) correlation coefficient is defined as:

$$\rho(A,B) = \frac{1}{N-1}\sum_{i=1}^{N}\left(\frac{A_i-\mu_A}{\sigma_A}\right)\left(\frac{B_i-\mu_B}{\sigma_B}\right), \tag{3.3}$$

where $\mu_A$and σ_A are the mean and standard deviation of A, and $\mu_B$and σ_B are the mean and standard deviation of B. A correlation value of +1 indicates a perfect increasing linear relationship where a value of −1 indicates a perfect decreasing linear relationship. A correlation value of zero implies there is no direct relationship between the two variables. Depending on the data set, the above correlation coefficient formula can be influenced by outliers, unequal variances, non-normality, and non-linearities. One way of dealing with this problem is through Spearman-rank correlation coefficient. Spearman-rank correlation coefficient is a nonparametric measure of rank correlation, (i.e. statistical dependency

between the ranks of two variables). The Spearman-rank correlation coefficient is defined as:

$$\rho_r(rgA, rgB) = \frac{1}{N-1}\sum_{i=1}^{N}\left(\frac{rgA_i-\mu_{rgA}}{\sigma_{rgA}}\right)\left(\frac{rgB_i-\mu_{rgB}}{\sigma_{rgB}}\right), \quad (3.4)$$

where rgA and rgB are the ranks of A and B, respectively. The ranks of rgA and rgB can be computed by sorting A and B independently and assigning the rank values from $\{1\ldots n\}$. The Spearman correlation assesses the relationship of the two variables regardless of outliers, unequal variances, non-normality, and non-linearities.

Given $f: N \times M$ non-dominated solutions and $x: N \times S$ corresponding decision variables values, the ECM plot starts by sorting the non-dominated solutions in ascending order independently (f_{Sorted}). The index location f_{Sorted} is recorded ($f_{SortIndex}$) for plotting purposes. Then, the sorted data set is divided into d parts (in this study $d = 4$ is used) and the correlation for each region computed. The reason to divide the solution set into d parts has three folds: 1) anomalies in the data set only affect the correlation value of a specific region not the entire data set, 2) it identifies the range and distribution of solutions along each objective, and 3) it allows us to identify the relationship between two variables on specific region. After the correlation values between the decision variables and the objective functions are computed, the relationship between objective values are computed in a similar way. Algorithm 3.4 presents the ECM plot procedure.

Algorithm 3.3 3D-RadVis Antenna Procedure

Input: f: $N \times M$ matrix formed by N non-dominated solutions, where M is the number of objectives.

Output: R: $N \times 3$ transformation matrix for 3D-RadVis visualization and P: $N \times M$ transformation matrix for Antenna plot.

// 3D-RadVis transformation

1: //Construct a reference hyper-plane
Z = `eye(M)` //$\{z_1 = (1,0,0,\dots,0), z_2 = (0,1,0,\dots,0), \dots, z_M = (0,0,\dots,1)\}$
2: //Calculate the normal vector for the reference hyper-plane with boundary points, Z:
n = `norm`(Z)
3: //Calculate the hyper-plane equation constant, c for this plane:
$c = (n \cdot z_i)$
4: **for** $i = 1$ to N
5: Calculate the perpendicular distance from n to solution i:
$$d = \frac{abs((f_i \cdot n) - c))}{\|n\|}$$
6: **end for**
7: //Normalize f by each objective:
f^{Norm} = `normalize`(f)
8: //Map f^{Norm} to 2D radial coordinates
$[u_x, u_y]$ = `RadVis` (f^{Norm})
9: $R = [u_x, u_y, d]$ //The value of ranges from 0 to `max`(d).

// Antenna transformation

10: //Compute the highest value
d: z_{max} = `max`(d).
11: //Compute x and y location of the boundary points:
$[b_x, b_y]$ = `RadVis` (Z)
//Compute the location of antenna directors (tick marks) along each objective:
12: **for** $i = 1$ to N
13: **for** $j = 1$ to M
14: $P(i,j) = z_{max} + z_{max} \times f^{Norm}(i,j)$
15: **end for**
16: **end for**

Algorithm 3.4 ECM Plot Procedure

Input: f: $N \times M$ matrix formed by N non-dominated solutions, where M is the number of objectives, x : $N \times S$ matrix formed by N decision variables associated with f, where S is the number dimension of the decision variable, d: data division, corrType: correlation type Pearson or Spearman rank

1: $d_{Size} = N/d$ //number solutions in each division
2: // Sort m^{th} objective in ascending order
3: **for** $i = 1$ to M
    $[f_{Sorted}(1{:}\,N, i)\ \ f_{SortIndex}(1{:}\,N, i)]$ = Sort $(f(1{:}\,N, i))$
   end for
4: //Calculate the correlation between objective functions and decision variables for each division
5: **for** $i = 1$ to M
6: **for** $j = 1$ to S
7: **for** $k = 1$ to d
8: $d_{start} = (k-1) * d_{Size}$
9: $d_{end} = k * d_{Size}$
10: $corr(k) = correlation(f_{Sorted}(d_{start}{:}\,d_{end}, i), x(f_{SortedIndex}(d_{start}{:}\,d_{end}), j), corrType)$
11: **end for**
12: Scatterplot($f_{Sorted}(1{:}\,N, i), x(f_{SortIndex}(1{:}\,N, i), j)$)
13: Mark the location of the end of each division
14: Apply color map that corresponds to the correlation value
15: **end for**
16: **end for**
17: //Calculate the correlation between objective functions
18: **for** $i = 1$ to M
19: **for** $j = 1$ to M
20: **for** $k = 1$ to d
21: $d_{start} = (k-1) * d_{Size}$
22: $d_{end} = k * d_{Size}$
23: $corr(k) = correlation(f_{Sorted}(d_{start}{:}\,d_{end}, i), x(f_{SortedIndex}(d_{start}{:}\,d_{end}), j), corrType)$
24: **end for**
25: Scatterplot($f_{Sorted}(1{:}\,N, i)\ f(f_{SortIndex}(1{:}\,N, i), j)$
26: Mark the location of the end of each division
27: Apply color map corresponds to the correlation value
28: **end for**
29: **end for**

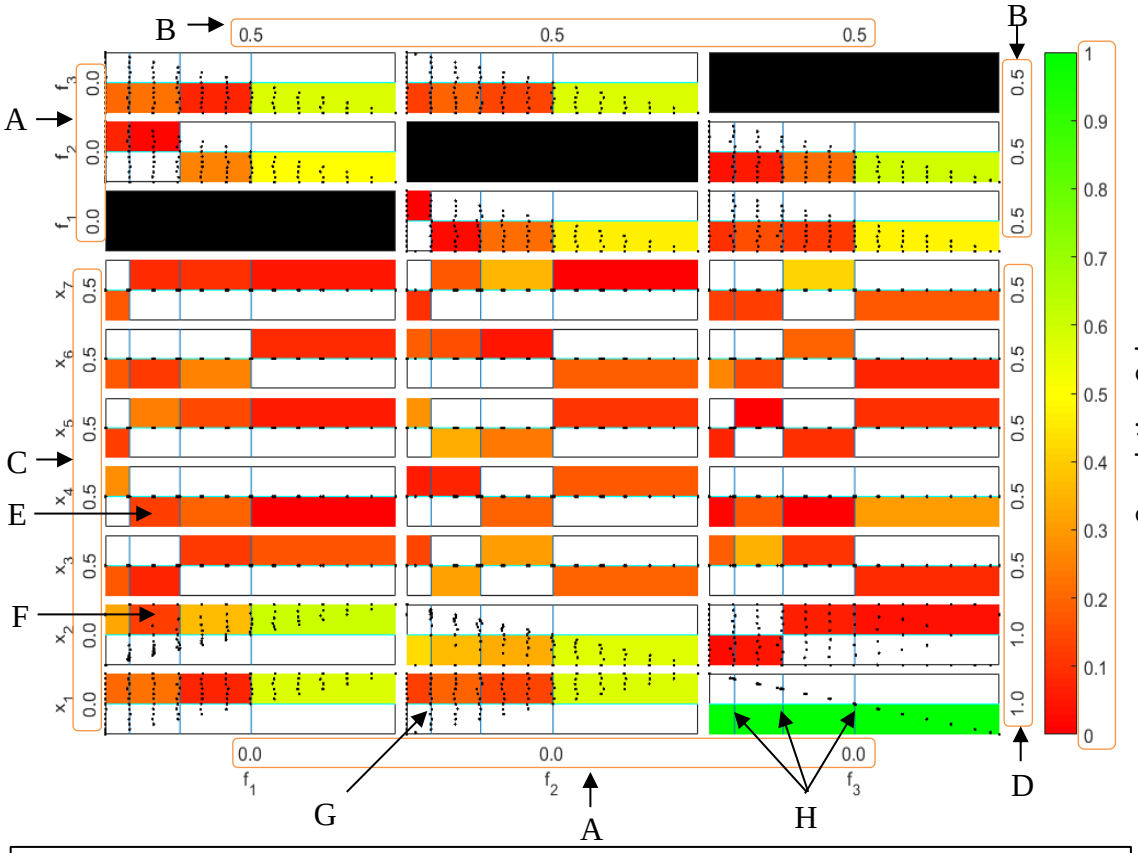

FIGURE 3-4 An ECM plot of approximated non-dominated solutions found by an optimizer for three-objective DTLZ1 test problem.

Figure 3-4 shows an ECM plot generated using Eq. 3.3 for approximated non-dominated solutions found by an optimizer for three-objective DTLZ1 test problem. In the right side of the ECM plot, the heat map color shows the correlation coefficients and the corresponding colors. The ranges of each objective function is shown at the bottom (min value) and top portions (max value) of the ECM plot (see Figure 3-4 A and B). Negative correlation values are displayed on the bottom portion of each cell (see Figure 3-4 E) and

positive correlations are displayed on the top portion of the each cell (see Figure 3-4 F). From this figure we see that the Pareto-optimal front for DTLZ1 problem is in $f_i \in [0, 0.5]$.The domain of each decision variable is located at the left (min value) and the right (max value) of the ECM plot (see Figure 3-4 C and D). From this plot we see that the first $M-1$ variables (x_1 and x_2) is in $[0, 1]$ and k variables (x_3 to x_7) have a value of 0.5. The color map for the correlation values between the decision variables (x_3 to x_7) and objective functions is shown in red shade indicating that no direct relationship is found between these variables. From the bottom right cell of the ECM plot we see that $x_1$and f_3 have very strong inverse correlation. Consequently, as $x_1$values linearly decrease from 1 to 0 the f_3 values linearly increase from 0 to 0.5. On the other hand, $f_1 - x_1$, $f_2 - x_1$, $f_1 - x_2$, , $f_2 - x_2$, $f_1 - f_2$, $f_1 - f_3$, and $f_2 - f_3$ shown strong positive or negative correlation only in the fourth quarter of the data set. The scatter plots and the quarterly interval lines in each cell (see Figure 3-4 H) indicate that 75% of the solution set lie in the first half of the solutions' range and the remaining lie in the second half of the solution range. This indicates that either there are a number of many-to-one relationships or dense distribution for the first 75% of solutions and sparse distribution for the remaining 25% of solutions. Chapters 8 and 9 further investigates how an ECM plot can be used in the decision-making process when solving real-world multi-objective optimization problems.

3.4 Experimental Investigation

In this section, we describe selected test benchmark problems, algorithms and their parameter settings used in this study.

3.4.1 Test Problems

In order to investigate the visualization capability of 3D-RadVis, 3D-RadVis Antenna and ECM plots we have used five scalable MaOO benchmark problems with linear, concave, and convex shapes and two benchmark problems with complicated PFs. The benchmark problems are: DTLZ1, DTLZ2, Convex DTLZ2, DTLZ7, WFG1 and WFG2 [61, 62]. The number of variables are $(M + k - 1)$, where M is the number of objectives and $k = 5$ for DTLZ1, $k = 10$ for DTLZ2 and Convex DTLZ2, and $k = 20$ for DTLZ7 test problems. The corresponding Pareto-optimal fronts lie in $f_i \in [0, 0.5]$ for the DTLZ1 problem and in $f_i \in [0, 1]$ for DTLZ2 and DTLZ7 test problems. The DTLZ7 test problem has disconnected Pareto-optimal fronts, where the Pareto-optimal front consists of convex and some mixed concavity. The WFG1 has a mixed Pareto-optimal front and the Pareto-optimal fronts is in $f_i \in [0, 2i]$. Table 3.1 presents detailed characteristics of the test problems utilized in this study.

In addition, to investigate the visualization capability of (mainly the distribution of solutions along each objective) the proposed 3D-RadVis Antenna plot, we have constructed symmetric and continuous PFs as described in [22]. The true PFs for these experiments are constructed using:

$$f_1^p + f_2^p + \cdots + f_M^p = 1, \tag{3.5}$$

where the objectives are normalized in the range [0, 1], and $p \in (0,3]$ is the parameter to control the geometrical shapes of PFs. To obtain the reference PFs (P) required by the IGD and spread metrics, first we systematically generate weight vectors using the λ method or also known as the simplex lattice design [82, 83], where $\lambda = (\lambda_1, \cdots, \lambda_m)^T$, $\lambda_i \geq 0$ are

weight vectors and $\sum_{i=1}^{M} \lambda_i = 1$. The weight vectors are values taken from $\left\{\frac{0}{H}, \frac{1}{H}, \ldots, \frac{H}{H}\right\}$ where H is the number of divisions along each objectives. The number of weight vectors for M objectives is then given by C_{H+M-1}^{M-1}. Finally, the intersection point between λ line and (3.5) denotes a reference solution. We also constructed two optimal solution sets (S_1 and S_2) with different diversities, where S_1 is generated based on the simplex lattice design and S_2 is generated using the Pareto-adaptive weight vectors ($pa\lambda$ method) [84] to maximize the HV value of S_2. The reference set R for HV metric is generated as R = {(1, 1)}, {(1, 1, 1)}, {(1, 1, 1, 1), (1, 1, 1, 1, 1)} on 2-, 3-, 4-, and 5-D PFs, respectively. Table 3.2 presents the number of solutions in the reference PFs (P) and optimal PFs (S_1 and S_2) used in this study.

TABLE 3.1 Benchmark test problems

Problem	Characteristics
DTLZ1	Linear, multimodal
DTLZ2	Concave
Convex DTLZ2	Convex
DTLZ7	Disconnected, convex and mixed convexity
WFG1	Convex, mixed, biased
WFG2	Convex, Disconnected, Multimodal

3.4.2 Experimental Results: 3D-RadVis

In this section, we investigate how well 3D-RadVis maps 2-, 3-, 4-, 5-, and 8-objective linear, concave, convex, mixed, and disconnected PFs to a 3-dimensioanl space. Further, it investigates how 3D-RadVis can be utilized to track the progress of an optimizer during the optimization process.

TABLE 3.2 Test number of solutions in the reference PFs and optimal PFs. M is the number of objectives and D is number of divisions along each objective.

M	Reference PFs		Optimal PFs		
	D	|P|	D	$\|S_1\|$	$\|S_2\|$
2	10000	10001	24 49 99	25 50 100	25 50 100
3	140	10011	8 12 16	45 91 153	45 91 153
4	38	10660	5 7 9	56 120 220	56 120 220
5	20	10626	4 6 7	70 210 330	70 210 330

3.4.2.1 Visualization of Benchmark Test Problems

Here, we investigate how well 3D-RadVis maps 2-, 3-, 4-, 5-, and 8-objective PFs to a three-dimensional space. Note that since we can map two-dimensional data points onto the x-axis, the u_y value always set to zero. Figure 3-5 (a) depicts the mapping of two-dimensional DTLZ1 onto a three-dimensional space. Since all the points lie on the reference hyper-plane, the value of d is zero. Figure 3-5 (b) shows the mapping of 2-objective DTLZ2 onto a three-dimensional space.

Here we see that the shape of DTLZ2 is similar to a quarter circle centered at (0, 0), where the largest distant point from the reference hyper-plane is located at the center of the arc. Figure 3-5 (c) shows the mapping of 2-objective convex DTLZ2 onto a three-dimensional space. Here we can see that the lowest point on the 3D-RadVis plot is located close to f_1, and this is because the Pareto-optimal surface of the convex DTLZ2 problem

has sharp decent close to the intermediate f_1 region. Figure 3-5 (d) shows the mapping of the 2-objective WFG1 test problem onto a three-dimensional space RadVis. It can be seen that 3D-RadVis is able to map the mixed Pareto-optimal surface to a three-dimensional space. Figure 3-5 (e) shows the mapping of the WFG2 test problem. Similar to the previous

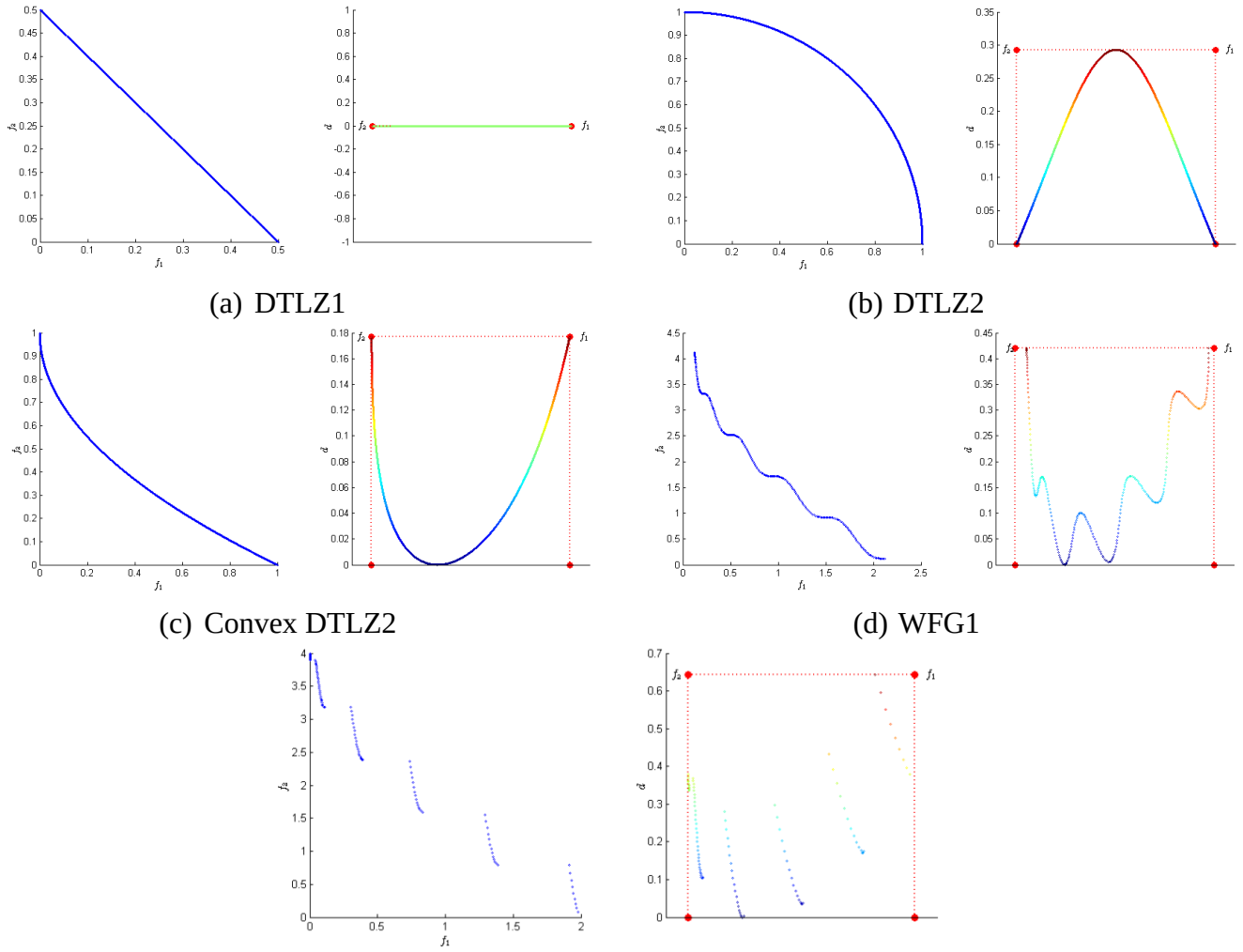

(a) DTLZ1 (b) DTLZ2

(c) Convex DTLZ2 (d) WFG1

(e) WFG2

FIGURE 3-5 3D-RadVis plots of 2-objective linear (DTLZ1), concave (DTLZ2), convex (convex DTLZ2), mixed (WFG1) disconnected (WFG2) PFs.

test problems, 3D-RadVis is able to capture the shape of relative locations of disconnected Pareto-optimal fronts of the WFG2 problem. In all test problems, 3D-RadVis is able to capture all features of the test problems regardless of shape or sharp/slow changes in the Pareto-optimal front.

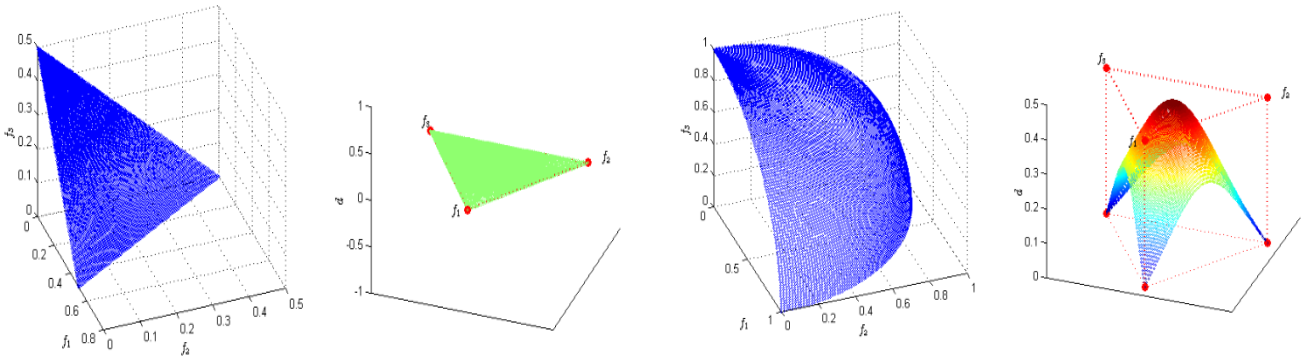

(a) DTLZ1 (b) DTLZ2

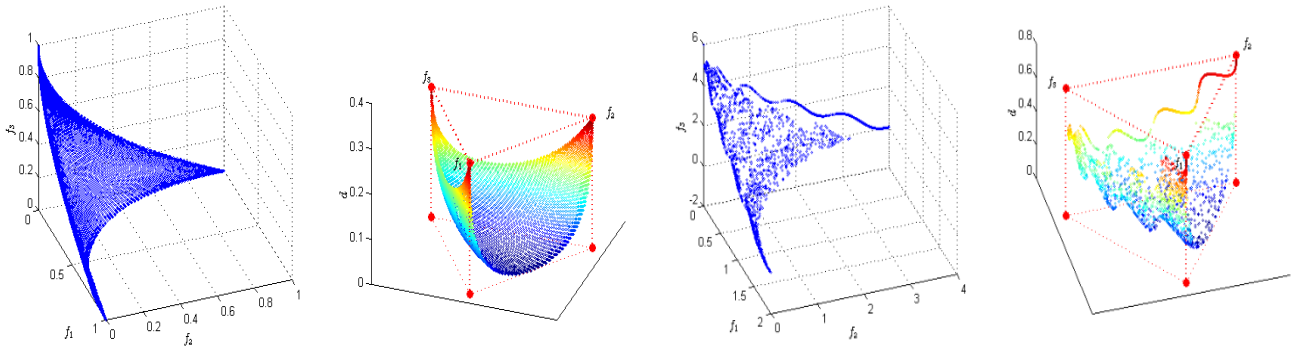

(c) Convex DTLZ2 (d) WFG1

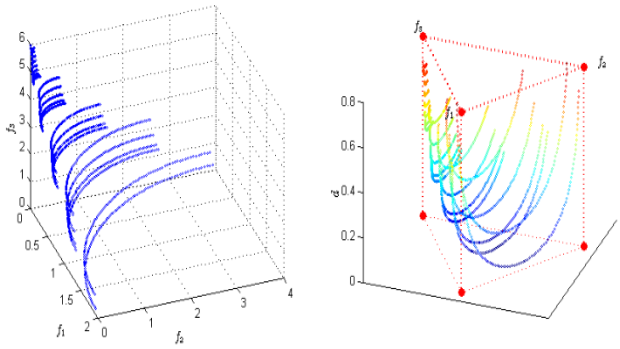

(e) WFG2

FIGURE 3-6 3D-RadVis plots of 3-objective linear (DTLZ1), concave (DTLZ2), convex (convex DTLZ2), mixed (WFG1) disconnected (WFG2) PFs.

Figure 3-6 demonstrates the effectiveness of 3D-RadVis in mapping 3-objective test problems to three-dimensional space while preserving all characteristics of the test problems. Figure 3-6 shows the mapping of 4-, 5- and 8-objective DTLZ2 and convex DTLZ2 test problem onto three-dimensional spaces. As it can be seen from these diagrams, 3D-RadVis is able to precisely map and visualize all aspects of higher dimensional problems.

3.4.2.2 Visualization of Approximate Pareto Fronts

The previous section has shown the effectiveness of 3D-RadVis to visualize the true Pareto-optimal fronts when the number of objectives are three or more. In this section, we show how researchers can utilize 3D-RadVis to investigate the performance of an algorithm. In the current experiment, we have used the NSGA-III algorithm to solve 5- and 8-objective DTLZ1, DTLZ2, and convex DTLZ3 test problems. Table 3.3 shows parameter settings, population size, number of reference points and maximum number of generations used in these experiments.

TABLE 3.3 Number of reference points, population size, and the maximum number of generations used for solving 3- and 5-objective DTLZ1, DTLZ2 and convex DTLZ2 test problems.

Problem	M	Divisions		Reference Points (H)	Population Size (N)	Max Gen
		Outer	Inner			
DTLZ1	5	6	0	210	212	750
	8	3	2	156	156	2000
DTLZ2	5	6	0	210	212	750
	8	3	2	156	156	2000
Convex DTLZ2	5	6	0	210	212	750
	8	3	2	156	156	2000

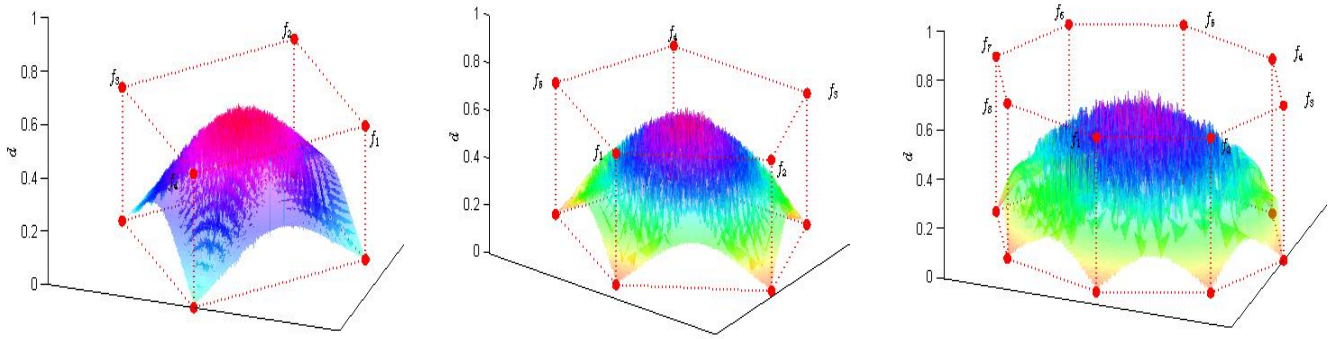

(a) DTLZ2

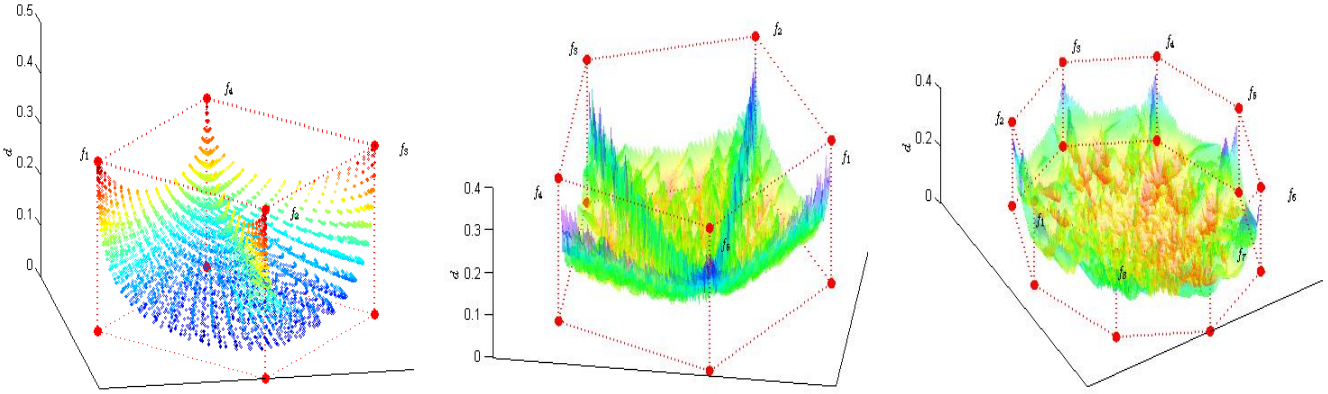

(b) Convex DTLZ2

FIGURE 3-7 3D-RadVis plots of 4-, 5- and 8-objective linear (DTLZ1), concave (DTLZ2), and convex (convex DTLZ2) PFs.

Figure 3-8 shows the performance of NSGA-III for 5- and 8-objective DTLZ1 test problems. From the 3D-RadVis plot, we can precisely see how close the obtained solutions are to the true PF. For example, Figure 3-8 (b) shows that the worst (based on distance) solution is $d = 10^{-3}$ far from the true front. The top view of 3D-RadVis plot shows that NSGA-III is able to uniformly distribute the solutions on the entire front. Figure 3-9 shows the performance of NSGA-III for 5- and 8-objective DTLZ2 test problems. While the convergence and distribution of the obtained solutions are close to the true PF, when examining the performance of NSGA-III on 8-objective convex DTLZ2 problem, NSGA-III is not able to find well-distributed solutions on the entire PF (see Figure 3-10).

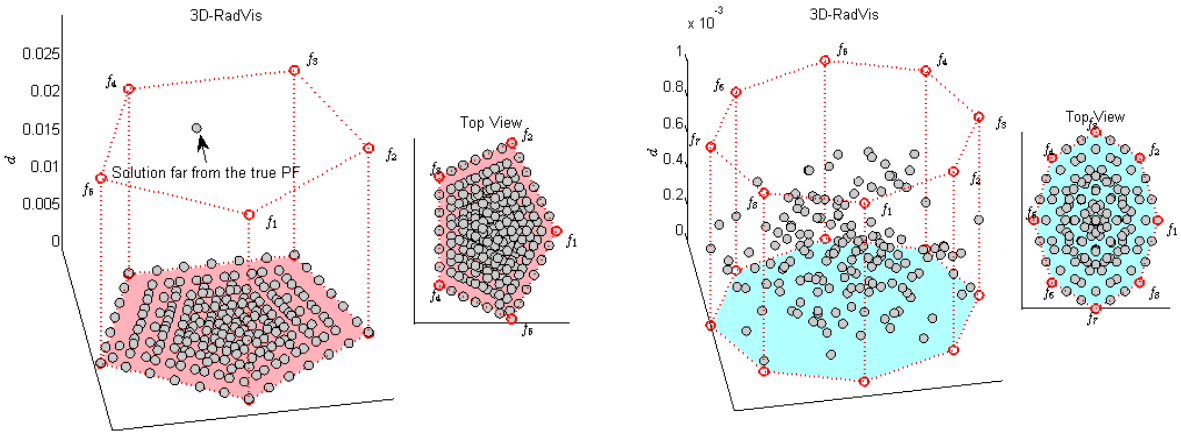

(a) 5- objective DTLZ1 (b) 8- objective DTLZ1

FIGURE 3-8 3D-RadVis plots showing obtained solutions by NSGA-III for 5- and 8-objective DTLZ1 test problems.

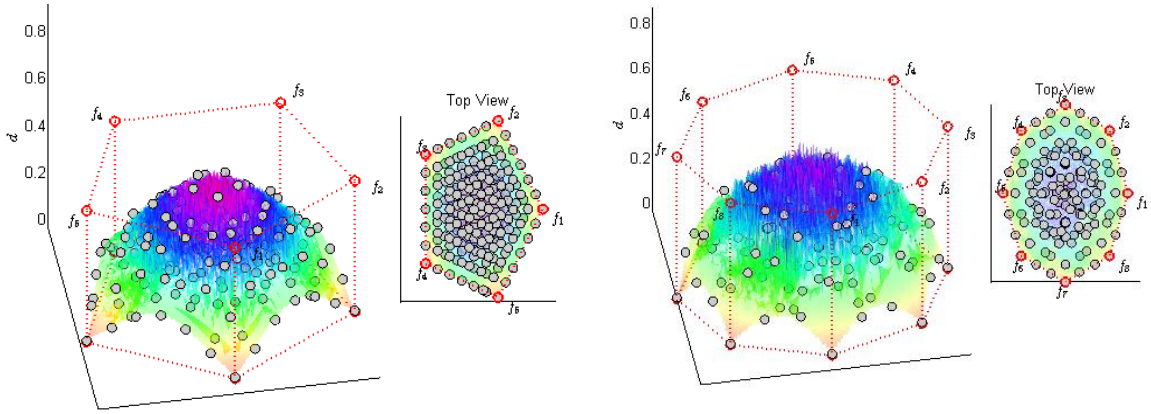

(a) 5- objective DTLZ2 (b) 8- objective DTLZ2

FIGURE 3-9 3D-RadVis plots showing obtained solutions by NSGA-III for 5- and 8-objective DTLZ2 test problems.

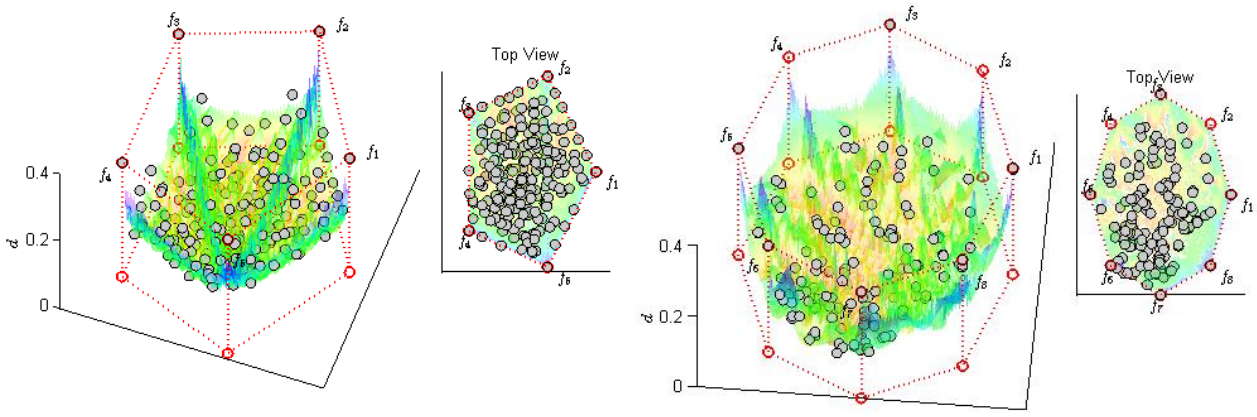

(a) 5- objective DTLZ2 (b) 8- objective DTLZ2

FIGURE 3-10 3D-RadVis plots showing obtained solutions by NSGA-III for 5- and 8-objective convex DTLZ2 test problems.

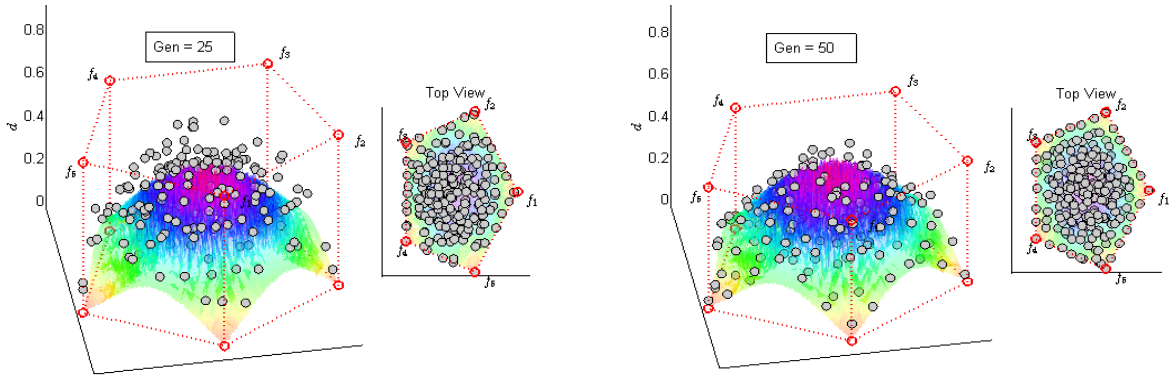

(a) 25 generations (b) 50 generations

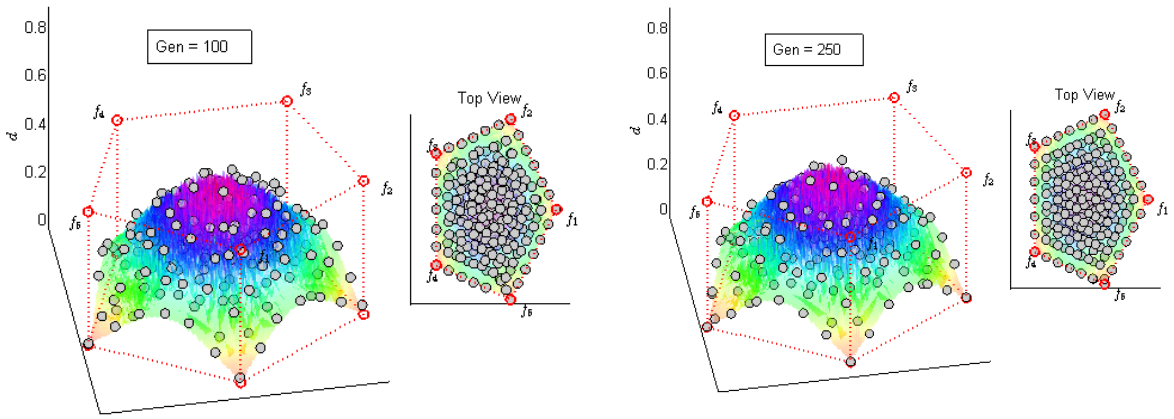

(c) 100 generations (d) 250 generations

FIGURE 3-11 3D-RadVis plots showing the progress of obtained solutions by NSGA-III for 5-objective DTLZ2 test problems after 25, 50, 100, and 250 generations.

3D-RadVis can also effectively be used by researchers and decision makers to explore and understand the search behaviour of an algorithm at each generation. They can take advantage of the visualization power of 3D-RadVis to gain useful information regarding an algorithm and improve their search ability and ultimately develop new optimization algorithms. Furthermore, in an interactive environment it is possible to rotate and visualize solutions from different perspectives to better understand the relationships among solutions. Figure 3-11 shows the performance of NSGA-III for 5-objective DTLZ2 test problem after 25, 50, 100 and 250 generations. For the 3D-RadVis plots, we can see that NSGA-III is able to converge while maintaining well a distributed solutions through generations.

3.4.3 Experimental Results: 3D-RadVis Antenna

Here, we investigate how well 3D-RadVis Antenna maps to 2-, 3-, 4-, and 5-objective PFs to a 3-dimensioanl space. Note that since 2-objective data points are mapped to only the *x*-axis, the u_y value is set to zero.

3.4.3.1 Visualization of Concave and Convex PFs

Experimental series 1 – these experiments investigate how well 3D-RadVis Antenna maps optimal solution sets (S_1 and S_2) having different diversities to a 3D space. The number of solutions in S_1 and S_2 are set to 100, 153, 220, 330 for 2-, 3-, 4- and 5-objective, respectively. Figure 3-12 (a) to (d) show 2D scatter plots of S_1 and S_2 points for 2D concave ($f_1^2 + f_2^2 = 1$) and convex ($f_1^{0.5} + f_2^{0.5} = 1$) PFs. From these figures we see that S_1 has better spread on concave PF than S_2 and worse spread on convex PF. The 3D-RadVis Antenna in Figure 3-12 (e) to (h) also show similar distribution of S_1 and S_2 solutions on

concave and convex PF surfaces. Moreover the 3D-RadVis Antenna shows the distribution of S_1 and S_2 solutions along each individual objectives. From Figure 3-12 (a) and (b) we see that the shape of the PF is similar to a quarter circle with radius = 1, centered at (0, 0). The largest distant point from the reference hyper-plane is located at the center of the arc. From the 3D-RadVis Antenna plots in Figure 3-12 (g) and (f), we also see that the shape and the relative location of solutions are well-preserved. Similarly, from Figure 3-12 (c) and (d) we see that the lowest distant point from the reference hyper-plane is located at the center of the arc and from the 3D-RadVis Antenna plots (Figure 3-12 (g) and (h)) we see that the shape and distribution of solutions are well preserved.

Experimental series 2 – these experiments investigate how well 3D-RadVis Antenna maps 3-objective optimal solution sets (S_1 and S_2) with different diversities onto 3D space. Figure 3-13 (a) to (d) show 3D scatter plots of S_1 and S_2 points for 3D concave ($f_1^2 + f_2^2 + f_3^2 = 1$) and convex ($f_1^{0.5} + f_2^{0.5} + f_3^{0.5} = 1$) PFs. Similar to the previous experiment 3D-RadVis Antenna is able to capture the shape and distribution of 3D PFs. Moreover, 3D-RadVis Antenna is clearly able to show the distribution of solutions along each objective which would not be possible using other types of visualization tools. For example, in Figure 3-13 (g), for the S_1 solution set, we see sparse region at the top portion of the antenna and high dense values at the bottom of the antenna. In other words, many of the solutions are concentrated on the interval of [0, 0.5] along each objective and leaving much of the interval [0.5, 1] unrepresented. However in Figure 3-13 (h), for S_2 solution set, we see that the distribution of solutions along each objective is much better than that of S_1. This is because the S_2 solution set is generated using the Pareto-adaptive weight vectors ($pa\lambda$ method) with highest possible HV value.

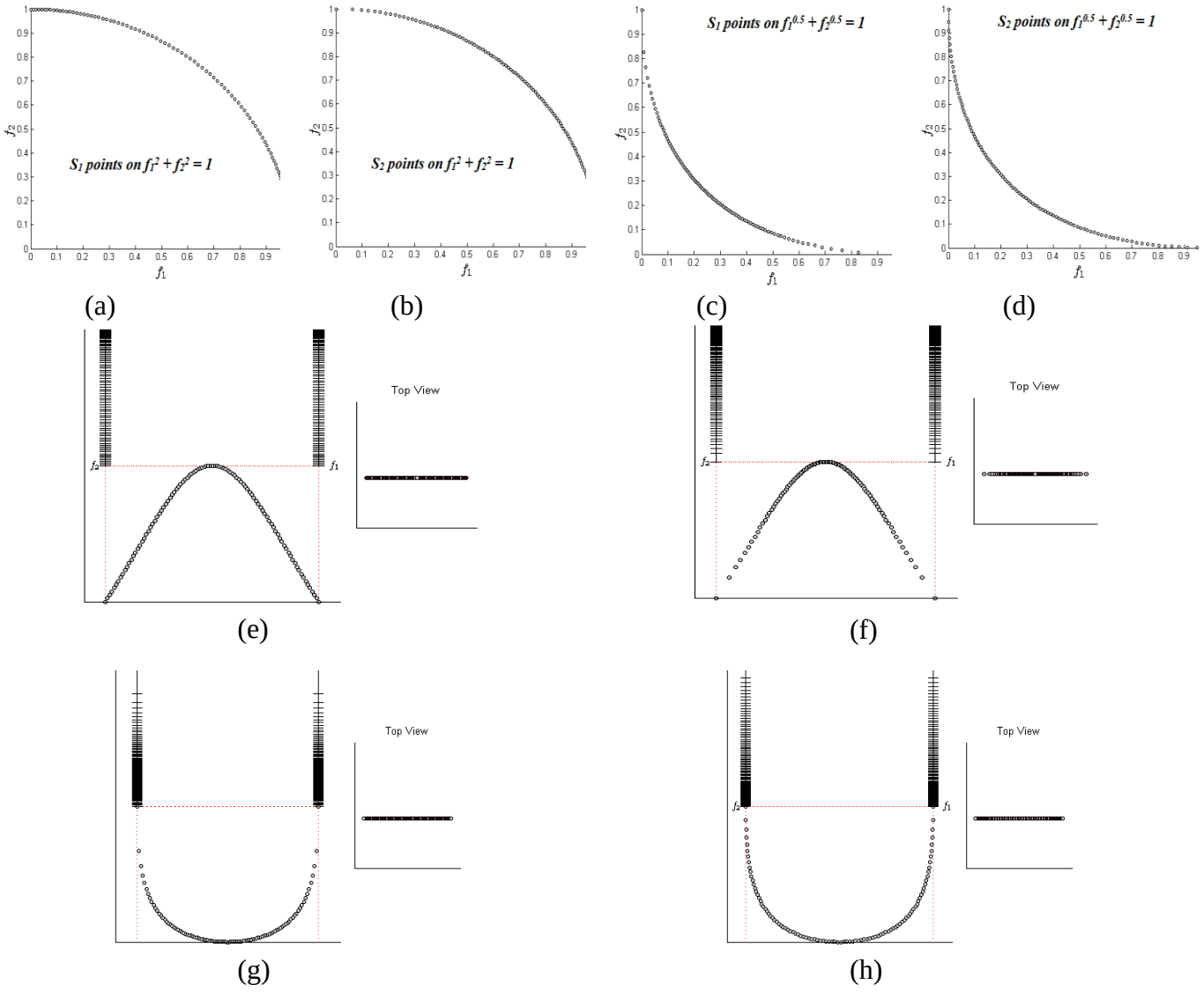

FIGURE 3-12 Scatter and 3D-RadVis Antenna plots for two-objective PFs. S_1 and S_2 points are generated using the simplex lattice design and $pa\lambda$ methods respectively. (a) Scatter plot of S_1 points for concave PF $f_1^2 + f_2^2 = 1$. (b) Scatter plot of S_2 points for concave PF $f_1^2 + f_2^2 = 1$. (c) Scatter plot of S_1 points for convex PF $f_1^{0.5} + f_2^{0.5} = 1$. (d) Scatter plot of S_2 points for convex PF $f_1^{0.5} + f_2^{0.5} = 1$. (e) 3D-RadVis Antenna plot of S_1 points for concave PF $f_1^2 + f_2^2 = 1$. (f) 3D-RadVis Antenna plot of S_2 points for concave PF $f_1^2 + f_2^2 = 1$. (g) 3D-RadVis Antenna plot of S_1 points for convex PF $f_1^{0.5} + f_2^{0.5} = 1$. (h) 3D-RadVis Antenna plot of S_2 points for convex PF $f_1^{0.5} + f_2^{0.5} = 1$.

Experimental series 3 – these experiments investigate how well 3D-RadVis Antenna maps 4-objective optimal solution sets (S_1 and S_2) with different diversities onto 3D space. Figure 3-14 (a) to (d) show 3D-RadVis Antenna plots of S_1 and S_2 points for 4D concave

$(f_1^2 + f_2^2 + f_3^2 + f_4^2 = 1)$ and convex $(f_1^{0.5} + f_2^{0.5} + f_3^{0.5} + f_4^{0.5} = 1)$ PFs. One interesting observation from these plots is that the distribution of the S_1solution set along each individual objective (Figure 3-14 (a)) is better than the S_2 solution set (Figure 3-14 (b)) even though the S_2 solution set has higher HV value. Thus, we can conclude that a solution set with higher HV value does not necessarily exhibit better distribution of solutions along each objective. More discussion on this point is provided in subsection D.

Experimental series 4 – these experiments investigate how well 3D-RadVis Antenna maps 5-objective optimal solution sets (S_1 and S_2) with different diversities onto 3D space. Figure 3-15 (a) to (d) show 3D-RadVis Antenna plots of S_1 and S_2 points for 5D concave $(f_1^2 + f_2^2 + f_3^2 + f_4^2 + f_5^2 = 1)$ and convex $(f_1^{0.5} + f_2^{0.5} + f_3^{0.5} + f_4^{0.5} + f_5^{0.5} = 1)$ PFs. Similar to the previous three experiments we can see that 3D-RadVis Antenna not only is able to capture the shape and distribution of solutions in higher dimension but also provide us valuable information regarding the quality of approximate solutions.

Experimental series 5 – these experiments investigate how well 3D-RadVis Antenna maps 3- to 5-objective solutions with complicated PFs, namely DTLZ7 and WFG1. The DTLZ7 test problem has disconnected convex and some mixed convexity Pareto-optimal fronts. On the other hand, the WFG1 has a mixed and biased Pareto-optimal front. Figure 3-16 (a), (c) and (e) depicts 3D-RadVis Antenna transformation of the DTLZ7 problem. As the number of dimension increases, the bottom portion of the 3D-RadVis Antenna plot is able to capture shape and distribution of solutions on the Pareto-optimal front. Similarly, the top portion of the plot (Antenna) is also able to capture the distribution of solutions along each objective. From this plot, we see that the DTLZ7 test problem has good distribution of solutions along the M_{th} (the last) objective and very sparse distribution along the

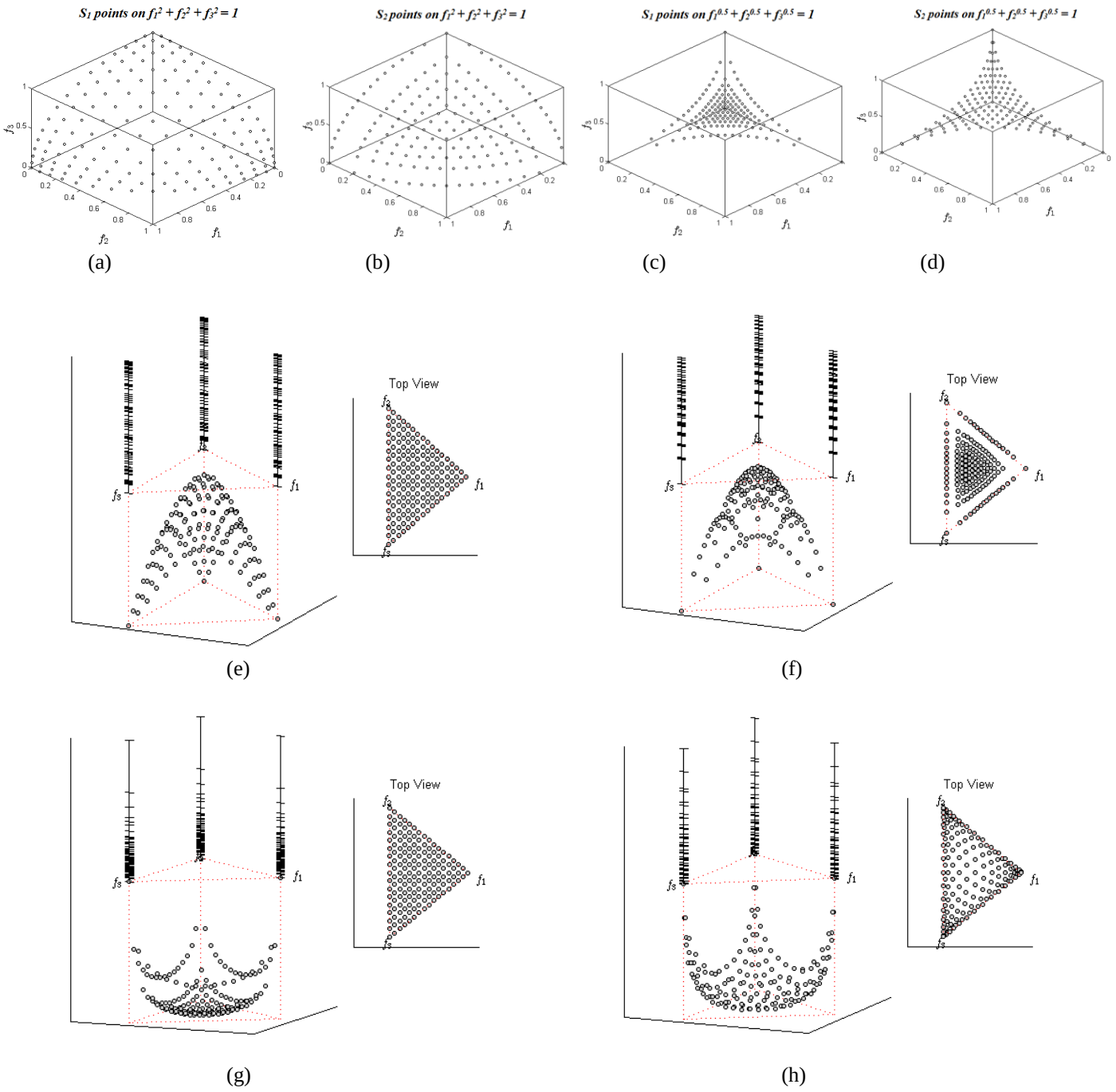

FIGURE 3-13 Scatter and 3D-RadVis Antenna plots for three-objective PFs. S_1 and S_2 points are generated using the simplex lattice design and $pa\lambda$ methods respectively. (a) Scatter plot of S_1 points for concave PF $f_1^2 + f_2^2 + f_3^2 = 1$. (b) Scatter plot of S_2 points for concave PF $f_1^2 + f_2^2 + f_3^2 = 1$. (c) Scatter plot of S_1 points for convex PF $f_1^{0.5} + f_2^{0.5} + f_3^{0.5} = 1$. (d) Scatter plot of S_2 points for convex PF $f_1^{0.5} + f_2^{0.5} + f_3^{0.5} = 1$. (e) 3D-RadVis Antenna plot of S_1 points for concave PF $f_1^2 + f_2^2 + f_3^2 = 1$. (f) 3D-RadVis Antenna plot of S_2 points for concave PF $f_1^2 + f_2^2 + f_3^2 = 1$. (g) 3D-RadVis Antenna plot of S_1 points for convex PF $f_1^{0.5} + f_2^{0.5} + f_3^{0.5} = 1$. (h) 3D-RadVis Antenna plot of S_2 points for convex PF $f_1^{0.5} + f_2^{0.5} + f_3^{0.5} = 1$.

remaining $(M-1)$ objectives. Furthermore, as the number of objectives increase the sparseness of solutions along these $(M-1)$ objectives also increases. Similarly Figure 3-16 (b), (d) and (e) depict 3D-RadVis Antenna transformation of the WFG1 test problem. From these figures, we see that 3-RadVis Antenna is able to capture the shape (mixed type) and the distribution of solutions along each objectives and on the Pareto-optimal surface.

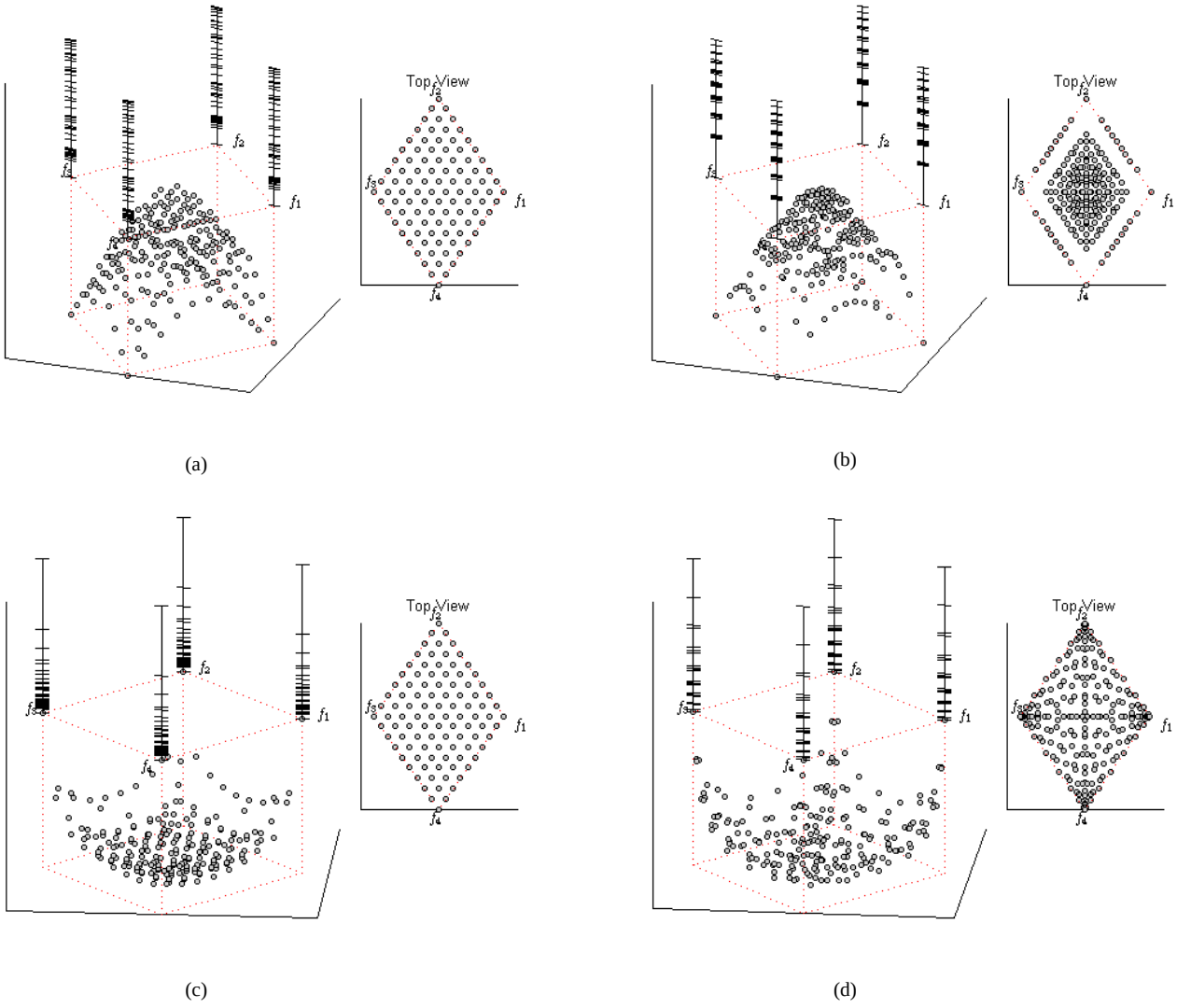

FIGURE 3-14 3D-RadVis Antenna plots for four-objective PFs. S_1 and S_2 points are generated using the simplex lattice design and $pa\lambda$ methods respectively. (a) S_1 points for concave PF $f_1^2 + f_2^2 + f_3^2 + f_4^2 = 1$. (b) S_2 points for concave PF $f_1^2 + f_2^2 + f_3^2 + f_4^2 = 1$. (c) S_1 points for convex PF $f_1^{0.5} + f_2^{0.5} + f_3^{0.5} + f_4^{0.5} = 1$. (d) S_2 points for convex PF $f_1^{0.5} + f_2^{0.5} + f_3^{0.5} + f_4^{0.5} = 1$.

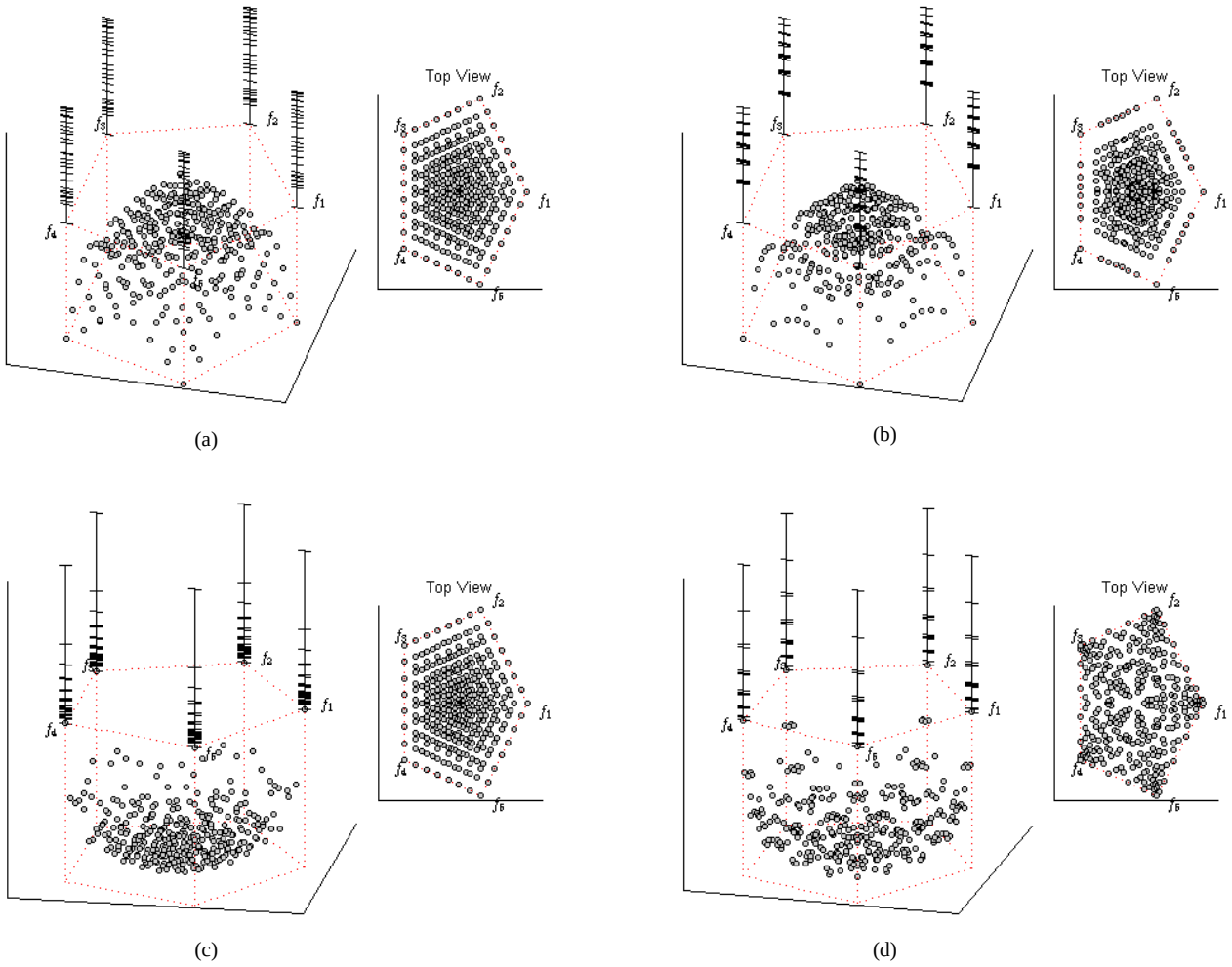

FIGURE 3-15 3D-RadVis Antenna plots for four-objective PFs. S_1 and S_2 points are generated using the simplex lattice design and $pa\lambda$ methods respectively. (a) S_1 points for concave PF $f_1^2 + f_2^2 + f_3^2 + f_4^2 + f_5^2 = 1$. (b) S_2 points for concave PF $f_1^2 + f_2^2 + f_3^2 + f_4^2 + f_5^2 = 1$. (c) S_1 points for convex PF $f_1^{0.5} + f_2^{0.5} + f_3^{0.5} + f_4^{0.5} + f_5^{0.5} = 1$. (d) S_2 points for convex PF $f_1^{0.5} + f_2^{0.5} + f_3^{0.5} + f_4^{0.5} + f_5^{0.5} = 1$.

3.4.3.2 Tracking the Progress of an Optimizer Using 3D-RadVis Antenna

The previous section has shown the effectiveness of 3D-RadVis Antenna to visualize and assess the quality of different solution sets when the number of objectives are two or more. In this section, we investigate how 3D-RadVis Antenna can be used to plot approximate

PFs or monitor the progress of an algorithm when the PF_{true} is known. The 3D-RadVis Antenna plots in Figure 3-17 show the performance of NSGA-III algorithm for 5-objective DTLZ2 test problem after 25, 50, 200 and 400 generations. From these plots, we can see that NSGA-III is able to converge to the PF_{true} while maintaining well-distributed solutions. However, as the generation progressed, the distribution of solutions along each objective deteriorated due to reference points utilized in the NSGA-III algorithm. This phenomenon was expected as NSGA-III tries to guide solutions towards well-spread reference points on the Pareto-surface but ignoring the distribution of solutions along each objective. From this experiment, we can see that 3D-RadVis Antenna can effectively be used by researchers and decision makers to explore, understand and ultimately improve the search behaviour of an algorithm. Furthermore, in an interactive environment it is possible to rotate and visualize solutions from different viewpoints to better understand the relationships among solutions and selectively guide solutions towards the optimal PF.

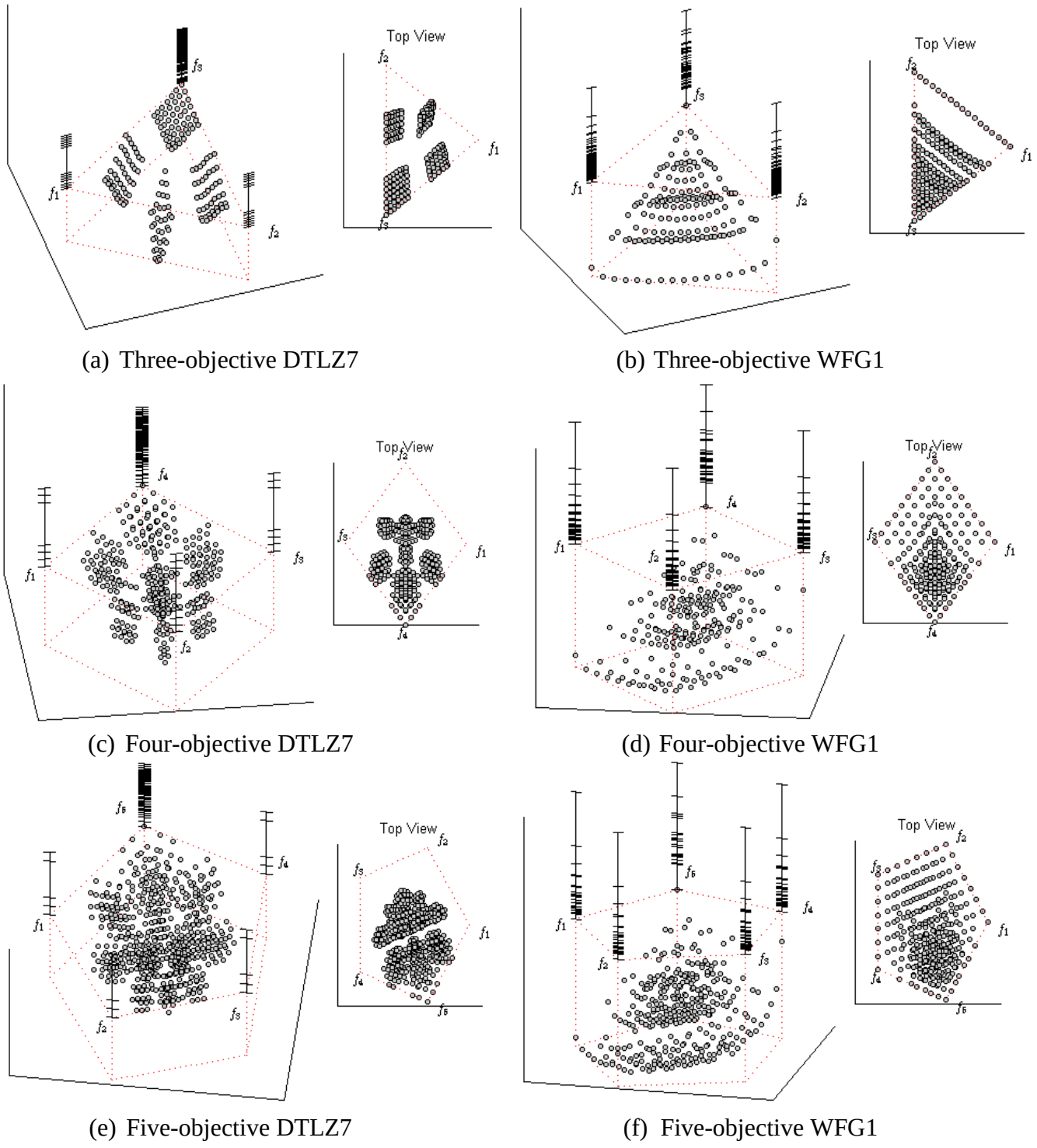

(a) Three-objective DTLZ7 (b) Three-objective WFG1

(c) Four-objective DTLZ7 (d) Four-objective WFG1

(e) Five-objective DTLZ7 (f) Five-objective WFG1

FIGURE 3-16 3D-RadVis Antenna plots of three- to five-objective DTLZ7 and WFG1 test problems. The DTLZ7 test problem has disconnected, convex and mixed convexity PF and the WFG1 test problem has convex, mixed and biased PF.

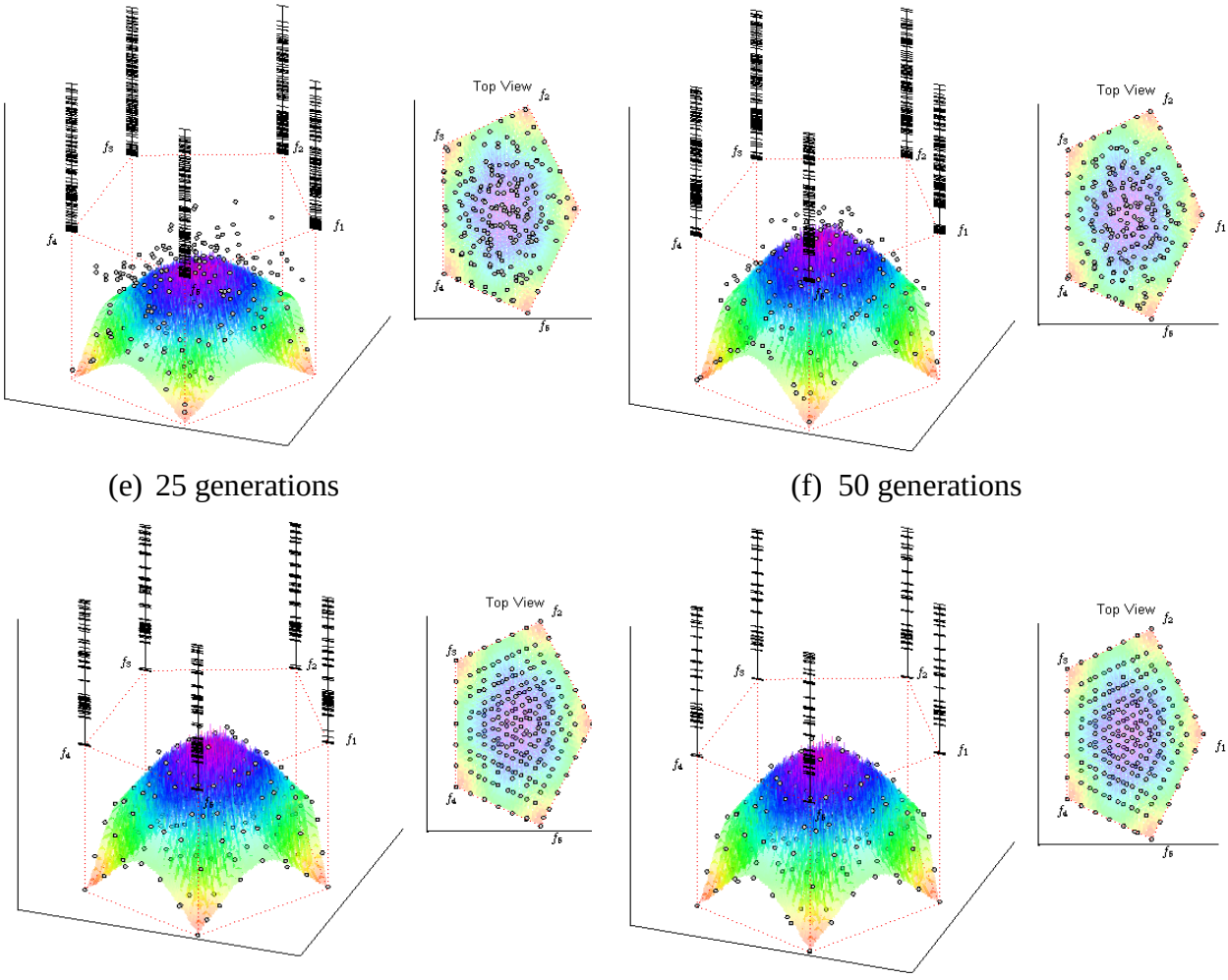

(e) 25 generations (f) 50 generations

(g) 200 generations (h) 400 generations

FIGURE 3-17 3D-RadVis Antenna plots showing the progress of obtained solutions by NSGA-III for 5-objective DTLZ2 test problem after 25, 50, 200, and 400 generations.

3.5 Concluding Remarks

This chapter presented three proposed multi- and many-objective visualization methods namely, 3D-RadVis, 3D-RadVis Antenna, and Enhanced Correlation Matrix (ECM) plot for visualizing the distribution, convergence and relationship between decision variables and objective functions. The 3D-RadVis and 3D-RadVis Antenna plots use a radial coordinate system to map M-dimensional objectives space to a two-dimensional space (u_x, u_y) and a distance (d) to maintain the location of each non-dominated solution from

TABLE 3.4 Summary of visualization methods and their capabilities

Method	PF Shape	Distribution of Solutions on the PF	Distribution of Solutions along Each Objective	Objective Range/ Variable Range	Relationship between Decision Variables and Objective Functions	Simultaneous Visualization	Scalability
Parallel Coordinates	×	×	×	✓ / ×	×	×	✓
Scatter Plot Matrix	≈	≈	×	✓ / ×	×	✓	≈
Heatmap	×	≈	×	✓ / ×	×	✓	✓
Bubble Chart	≈	≈	×	✓ / ×	×	✓	×
Self-Organizing Maps	×	×	×	× / ×	×	×	×
RadVis	×	≈	×	× / ×	×	✓	✓
3D-RadVis	✓	≈	×	× / ×	×	✓	✓
3D-RadVis Antenna	✓	≈	✓	× / ×	×	✓	✓
Enhanced Correlation Matrix	≈	≈	✓	✓ / ✓	✓	✓	✓

a reference hyper-plane constructed using the extreme points. The radial coordinates, (u_x, u_y), show the distribution of the solutions and the combination of these radial coordinates with the distance metric d, show the shape and accuracy of the solutions. The 3D-RadVis Antenna plot incorporates additional dimension to the 3D-RadVis plot to visualize the distribution of solutions as along each objective. The 3D-RadVis plot is capable of mapping M-dimensional objective space to a three-dimensional radial coordinate plot while seeking to preserve the relative location of solutions, shape of the PF, and distribution of solutions on the Pareto-optimal surface. On the hand, the 3D-RadVis Antenna plot incorporates additional dimension to the 3D-RadVis plot to visualize the

distribution of solutions as along each objective. These plots can be used by decision makers to visually navigate large many-objective solution sets, to observe the evolutionary process, to visualize the relative location of a solution, to evaluate trade-offs among objectives, and to select preferred solutions. Table 3.4 summarizes the capabilities of the proposed visualization methods and classical visualization methods presented in this chapter.

From the experimental tests on widely used MaOO test problems, 3D-RadVis Antenna is able to precisely show the shape, distribution, and convergence of approximate solutions on the PF surface as well as distribution of these solutions along each objective. 3D-RadVis Antenna can be scaled to higher dimensions and capable of showing multiple PFs simultaneously (e.g. true PF and approximate solutions). This visualization tool can effectively be used by researchers and decision makers to explore and understand the search behaviour of an algorithm at each generation whereby gaining useful information regarding an algorithm to improve their search ability and ultimately, we hope, the development of new optimization algorithms. 3D-RadVis Antenna can also be utilized by decision makers to observe the relative location of a solution, evaluate trade-offs among objectives, and select preferred solutions. For an improved navigation, decision makers can use immersive virtual technologies, such as the CAVE, to easily visualize the entire PF from the 3D-RadVis plot and select the ideal solution according to their requirements and budget restrictions.

Chapter 4

OBJECTIVE-WISE INVERTED GENERATIONAL DISTANCE AND SPREAD MEASURES FOR MANY-OBJECTIVE OPTIMIZATION ALGORITHMS

So far the focus of almost all multi- or many-objective performance metrics has been the convergence and distribution of solutions in the objective space (Pareto-surface). Pareto-surface metrics such as IGD, HV, and Spread are simple and provide knowledge about the overall performance of the solution set. However, these measures do not provide any insight into the distribution or spread of a solution set with respect to each objective. This chapter presents two novel performance measures, named objective-wise inverse generational distance (ObjIGD) and line distribution (Δ_{Line}), capable of measuring the convergence and distribution of solutions along each objective as well as the overall performance of approximate solutions. The effectiveness of the proposed methods are demonstrated on widely used many-objective benchmark problems containing a variety of PFs (linear, concave, and convex). In addition, a case study demonstrates the capability of previously proposed visualization method, 3D-RadVis Antenna (Chapter 3) combined with the proposed performance measures to visually and quantitatively track the progress of the NSGA-III algorithm through generations. Experimental results show that the proposed performance measures can be used as reliable complementary measures along with other widely used performance measures to compare many-objective solution sets.

4.1 Introduction

Many real-world applications involve a high number of objectives. As the number of objective increase, many of currently used performance metrics are not able to adequately measure the convergence and diversity of a solution set and/or they are computationally "expensive". For example, the hypervolume (HV) [15] measure is a widely used performance metric in MaOO. It captures the convergence and diversity of a solution set even when the optimal PF (PF) is unknown. However, the high computational complexity

of the HV metric makes it impractical to be used when the number objectives are high [16-18, 85]. Furthermore, Pareto-surface metrics such as generational distance (GD), inverted generational distance (IGD), and Spread are simple and provide knowledge about the overall performance of the solution set [19-21]. However, these measures do not provide any insight into the distribution or spread of solution sets with respect to each objective. For example, a decision maker might mainly be interested in knowing real-estate properties in the range of $500,000 to $800,000. As an optimization tool provider, we need to provide the decision maker with well-distributed solutions in this price range and be able to quantitatively measure the distribution of solutions along this objective regardless of other objectives. Here, we are not implying the distribution of solutions over the Pareto-optimal surface is not important but we are suggesting the distribution of solutions along each objective is equally important. Furthermore, studies have shown that these performance metrics contradict one another in the presence of extreme cases [22]. Hence, there is room for introducing more performance metrics (in conjunction with widely used performance metrics) suited for measuring the distribution of solutions along each objective.

This chapter presents two performance measures, called objective-wise inverse generational distance (ObjIGD) and line distribution (Δ_{Line}). The ObjIGD and Δ_{Line} measures are designed to quantitatively assess the objective-wise convergence, spread, and diversity of solution sets obtained by multi- or many-objective population-based algorithms. The ObjIGD measure is used when the Pareto-optimal set is known, whereas, the Δ_{Line} measure is used when it is unknown.

4.2 Classical Performance Metrics

Unlike single-objective optimization, where the assessment of the performance of a metaheuristic requires observing the best value given by an algorithm, this is not applicable in multi-objective optimization. For multi-objective optimization problem, an approximation set to the optimal PF of the problem is computed. Here, the required properties are convergence (i.e., how close the solution set is to the true PF) and uniform diversity (i.e., solutions that exhibit uniform distribution). Ideally, we are interested in quality indicators that do not require the true Pareto-optimal front, but are however capable of measuring the convergence and diversity of a known solution set. Several indicators for measuring the aforementioned properties have been proposed in the literature. These include: capacity metrics such as the overall non-dominated vector generation (ONVG) [86] and error ratio (ER) [87], convergence metrics such as metric GD [19] and ϵ-indicator [15], diversity metrics such as the overall Pareto spread (OS) [88] and spread/diversity (Δ) [21] and finally convergence-diversity metrics such as IGD [19, 20] and HV. For detailed list of performance metrics used in multi- or many-objective optimization readers are encourage to visit Section 2.2.

4.3 Proposed Performance Metrics

In multi- or many-objective optimization evaluating the superiority of a solution set is complex due to the presence of conflicting objectives and the number of obtained optimal solutions. So far, a number of performance metrics have been proposed in multi-objective and none of them provide any insight into the distribution or spread of solution sets with respect to each objective function. Further, studies have shown that these performance

metrics contradict one another in the presence of extreme cases. To the best of our knowledge, there is no performance measure capable of evaluating solution superiority based on the accuracy and distribution of solution along each objective. Therefore, we propose two new performance measures called objective-wise inverse generational distance (ObjIGD) and line distribution () to specifically assess the convergence, spread and diversity of MaOEAs along each objective.

For example, consider a convex Pareto-surface $f_1^{0.5} + f_2^{0.5} + f_3^{0.5} = 1$ containing 91 solutions as depicted in Figure 4-1. From the scatter plot Figure 4-1 (a), we see that the solution set is well-distributed on the optimal PF surface. However, when we look at the 3D-RadVis Antenna plot in Figure 4-1 (b) we see that the distribution of solutions along each objective is very poor. In fact, there is no solution containing $f_i \in [0.5903, 1]$, which means more than 40% of possible solutions are not accounted for by each objective. Therefore, we need to shift our research focus to find algorithms that not only provide accurate and well-distributed solutions on the PF surface but also well-distributed solutions along each objective and are able to measure the performance of these algorithms quantitatively. Now, let us define two such measures capable of measuring the convergence and distribution of solutions along the i^{th} objective.

4.3.1 Objective-wise Inverse Generational Distance (ObjIGD)

The ObjIGD measure evaluates the convergence and distribution performance of MaOOA specifically along each objective. The main idea of ObjIGD is similar to the IGD metric, however ObjIGD measures the distance between the PF_{true} and the closest solution based on individual objectives. The ObjIGD for the i^{th} objective is defined as follows:

$$ObjIGD_i(S,P) = \frac{\sum_{j=1}^{|P|} \min_{s \in S} |F_i(p_j) - F_i(s)|}{|P|} \quad (4.1)$$

where P is the reference (PF_{true}), S is the approximate PF, $F_i(p_j)$ is the j^{th} PF_{true} solution of the i^{th} objective and $F_i(s)$ is an approximate solution of the i^{th} objective. The overall ObjIGD measure is defined as:

$$ObjIGD(S,P) = \frac{\sum_{i=1}^{M} ObjIGD_i(S,P)}{M}, \quad (4.2)$$

where $ObjIGD_i$ is the i^{th}objective ObjIGD value and M is the number of objectives. A lower value of the $ObjIGD_i$ measure implies better convergence and distribution along the i^{th} objective.

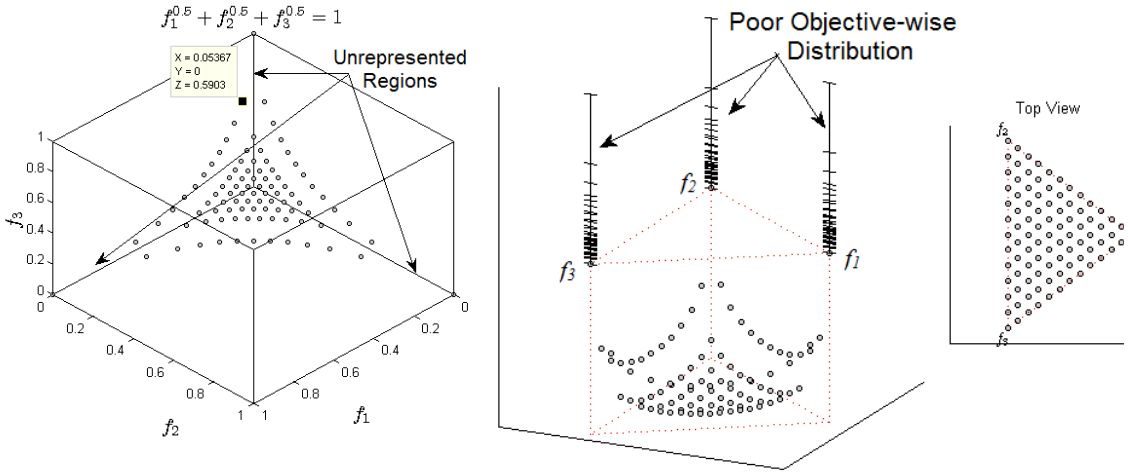

FIGURE 4-1 Scatter and 3D-RadVis Antenna plots of three-objective convex PF containing 91 solutions. (a) Scatter plot showing more than 40% of f_i with no associated values. (b) 3D-RadVis Antenna showing poor objective-wise distribution.

4.3.2 Line Distribution (Δ_{Line})

The Δ_{Line}metric measures the diversity and spread of approximate solutions without the need for the PF_{true}. Let β be the mid-points of N equally divided intervals in the range of

[0, 1] $\left(\left[0,\frac{1}{N}\right],\left[\frac{1}{N},\frac{2}{N}\right],\ldots,\left[\frac{N-1}{N},1\right]\right)$, where N is the number of solutions in approximate the PF, then the i^{th} objective line distribution (Δ_{Line}^{i}) is defined as:

$$\Delta_{Line}^{i}(S,\beta)=\frac{\sum_{j=1}^{|\beta|}\min_{s\in S}\left|\beta_j-F_i(s)\right|}{|\beta|}, \tag{4.3}$$

where $F_i(s)$ is a normalized approximate solution of i^{th} objective. A zero value of the i^{th} objective line distribution signifies uniform distribution of the approximate PF along the i^{th} objective. The overall line distribution measure is defined as:

$$\Delta_{Line}(S,\beta)=\frac{\sum_{i=1}^{M}\Delta_{Line}^{i}(S,\beta)}{M}, \tag{4.4}$$

where Δ_{Line}^{i} is the i^{th}objective ObjIGD value and M is the number of objectives.

4.4 Experimental investigation

This section presents test benchmark problems, algorithms and their parameter settings used to assess the efficacy of the proposed performance measures. Also, it investigates the relationships among HV, IGD and the two proposed measures on systematically constructed symmetric and continuous PFs.

4.4.1 Test Problems

In order to investigate the consistencies and contradiction of the proposed performance measures and other well-known performance metrics (spread, IGD, and HV), we have constructed symmetric and continuous PFs as described in [22]. The true PFs for these experiments are constructed using:

$$f_1^p + f_2^p + \cdots + f_M^p = 1, \tag{4.5}$$

where the objectives are normalized in the range [0, 1], and $p \in (0,3]$ is the parameter to control the geometrical shapes of PFs. To obtain the reference PFs (P) required by the IGD and spread metrics, first we systematically generate weight vectors using the λ method or also known as the simplex lattice design [82, 83], where $\lambda = (\lambda_1, \cdots, \lambda_m)^T$, $\lambda_i \geq 0$ are weight vectors and $\sum_{i=1}^{M} \lambda_i = 1$. The weight vectors are taken values from $\left\{\frac{0}{H}, \frac{1}{H}, \ldots, \frac{H}{H}\right\}$ where H is the number of divisions along each objectives. The number of weight vectors for M objectives is then given by C_{H+M-1}^{M-1}. Finally, the intersection point between the λ line and Equation (4.5) denotes a reference solution. We also constructed two optimal solution sets (S_1 and S_2) with different diversities, where S_1 is generated based on the simplex lattice design and S_2 is generated using the Pareto-adaptive weight vectors ($pa\lambda$ method) [84] to maximize the HV value of S_2. The reference set R for HV metric is generated as R = {(1, 1)}, {(1, 1, 1)}, {(1, 1, 1, 1), (1, 1, 1, 1, 1)} on 2-, 3-, 4-, and 5-D PFs, respectively. Table 4.1 presents the number of solutions in the reference PFs (P) and optimal PFs (S_1 and S_2) used in this study.

Furthermore, in order to investigate the efficacy of the proposed performance measures, we have used five scalable MaOO benchmark problems with linear, concave, and convex shapes. The benchmark problems are: DTLZ1, DTLZ2, convex DTLZ2, DTLZ3 and DTLZ4 [61, 62]. The number of variables are $(M + k - 1)$, where M is the number of objectives and $k = 5$ for DTLZ1 and $k = 10$ for the remaining DTLZ test problems. The corresponding Pareto-optimal fronts lie in $f_i \in [0, 0.5]$ for the DTLZ1 problem and in $f_i \in [0, 1]$ for DTLZ2 – DTLZ4 problems.

TABLE 4.1 Test number of solutions in the reference PFs and optimal PFs. M is the number of objectives and D is number of divisions along each objective.

M	Reference PFs		Optimal PFs		
	D	$\|P\|$	D	$\|S_1\|$	$\|S_2\|$
2	10000	10001	24 49 99	25 50 100	25 50 100
3	140	10011	8 12 16	45 91 153	45 91 153
4	38	10660	5 7 9	56 120 220	56 120 220
5	20	10626	4 6 7	70 210 330	70 210 330

4.4.2 Comparison of Proposed Performance Measures with Spread, IGD, and HV on 2-, 3-, 4-, and 5-D PFs

In this section, we investigate the similarities and differences of the proposed measures and three widely used MaOO performance metrics on various PF shapes and dimensions. Table 4.1 shows the number of solutions in the reference PFs and optimal PFs used in this experiment. The optimal PF, S_1, is generated using the simplex lattice design, and S_2 is generated using the $pa\lambda$ method by restructuring S_2 points so that they attain the maximum HV value. Figure 4-2 to Figure 4-5 show differences in metrics (diversity$\Delta(S_1, P) - \Delta(S_2, P)$, objective-wise diversity $\Delta_{line}(S_1, P) - \Delta_{Line}(S_2, P)$, convergence and diversity $HV(S_2, R) - HV(S_1, R)$, convergence and diversity $IGD(S_1, P) - IGD(S_2, P)$, and objective-wise convergence and diversity $ObjIGD(S_1, P) - ObjIGD(S_2, P)$) on 2- to 4-objective PFs. A negative difference value indicates the superiority of S_1 over S_2 while a positive difference value indicates the superiority of S_2 over S_1 according to the assessed metric. A difference value of zero indicates no superiority between S_1 and S_2.

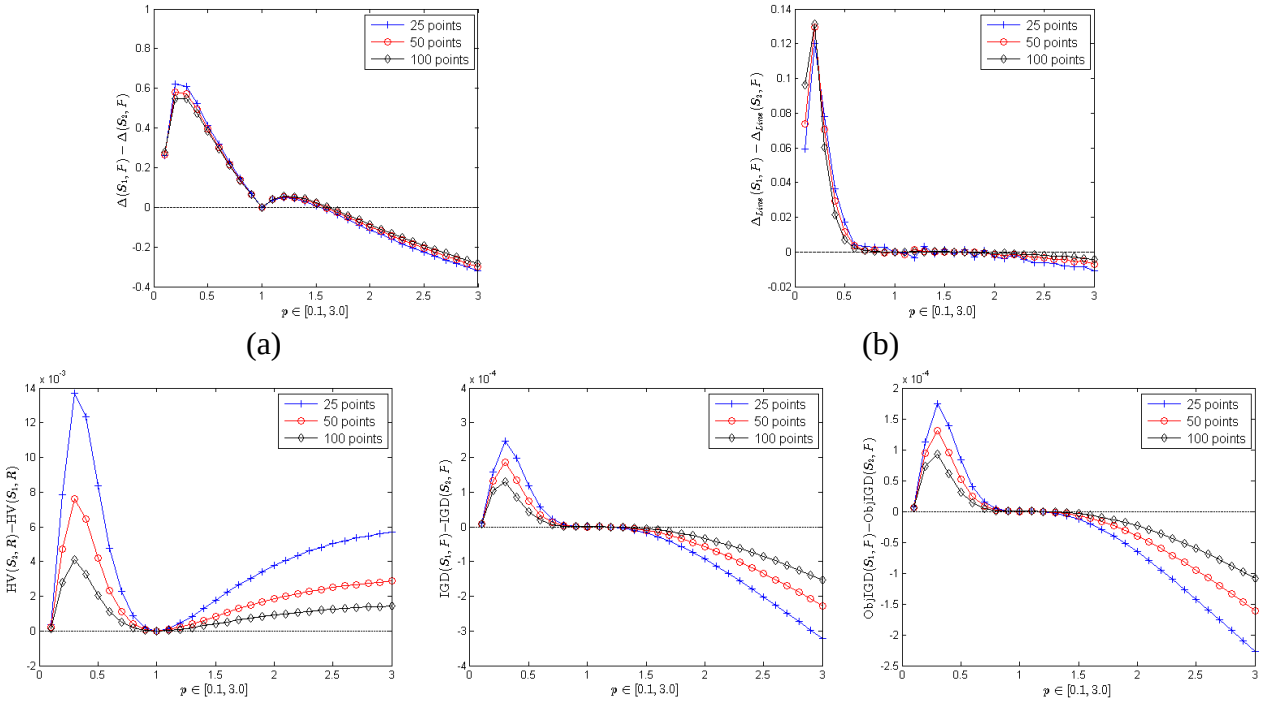

FIGURE 4-2 Differences in metrics of two-objective S_1 and S_2 solutions containing 25, 50, and 100 points. S_1 and S_2 points are generated using the simplex lattice design and $pa\lambda$ methods respectively and $p \in [0.1, 3]$. A positive value indicates S_2 is superior to S_1. (a) Diversity $\Delta(S_1, P) - \Delta(S_2, P)$. (b) Objective-wise diversity $\Delta_{line}(S_1, P) - \Delta_{Line}(S_2, P)$. (c) Convergence and diversity $HV(S_2, R) - HV(S_1, R)$. (d) Convergence and diversity $IGD(S_1, P) - IGD(S_2, P)$. (e) Objective-wise convergence and diversity $ObjIGD(S_1, P) - ObjIGD(S_2, P)$.

Experimental series 1 – examines the relationship of five performance metrics on 2D PFs. Figure 4-2 shows the difference values of each metric on PFs $f_1^p + f_2^p = 1$, where $p \in [0.1, 3.0]$. When comparing the diversity metrics (Δ and Δ_{Line}), in Figure 4-2 (a) and (b), both metrics exhibit similar results when $p \in [0.1, 1.5]$. However when $p \in (1.0, 2.5]$ Δ_{Line} is not able to distinguish the difference between the two optimal sets. Figure 4-2 (c) to (e) show the difference values for convergence-diversity measures (HV, IGD and ObjIGD). The difference values for IGD are similar to ObjIGD, however both measures contradicting difference values with the HV metrics on concave PFs, $p \in (1.0, 3.0]$.

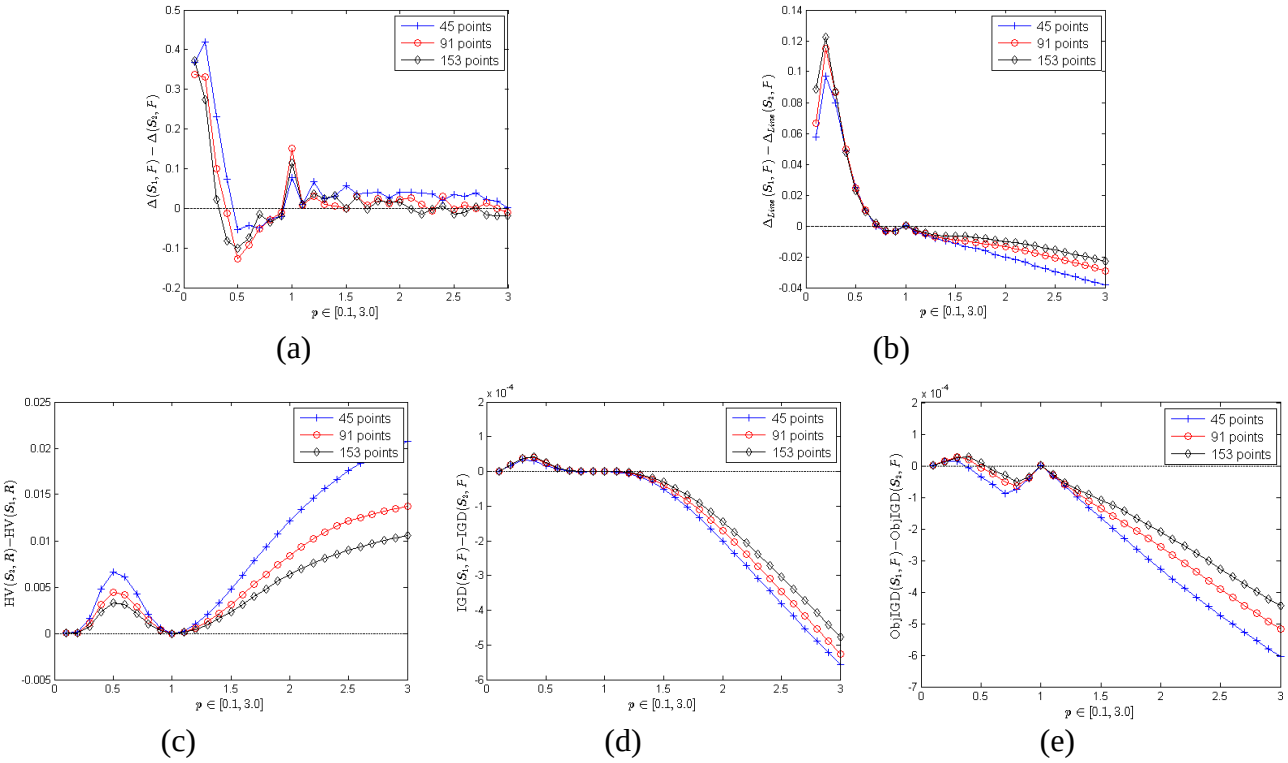

FIGURE 4-3 Differences in metrics of three-objective S_1 and S_2 solutions containing 45, 91, and 153 points. S_1 and S_2 points are generated using the simplex lattice design and $pa\lambda$ methods respectively and $p \in [0.1, 3]$. A positive value indicates S_2 is superior to S_1. (a) Diversity $\Delta(S_1, P) - \Delta(S_2, P)$. (b) Objective-wise diversity $\Delta_{line}(S_1, P) - \Delta_{Line}(S_2, P)$. (c) Convergence and diversity $HV(S_2, R) - HV(S_1, R)$. (d) Convergence and diversity $IGD(S_1, P) - IGD(S_2, P)$. (e) Objective-wise convergence and diversity $ObjIGD(S_1, P) - ObjIGD(S_2, P)$.

Experimental series 2 – examines the relationship of performance measures on 3D PFs. Figure 4-3 shows the difference values of each measure on PFs $f_1^p + f_2^p + f_3^p = 1$, where $p \in [0.1, 3.0]$. When comparing the diversity measures (Δ and Δ_{Line}), in Figure 4-3 (a) and (b), the Δ metric was unable to decisively distinguish the difference between the two optimal PFs for $p \in (1.0, 3.0]$. On the other hand, the Δ_{Line} measure was able to distinguish S_2's superiority on $p \in [0.1, 0.6]$ and inferiority on $p \in (1.0, 3.0]$. Figure 4-3 (c) to (e) show the difference values for convergence-diversity measures (HV, IGD and ObjIGD).

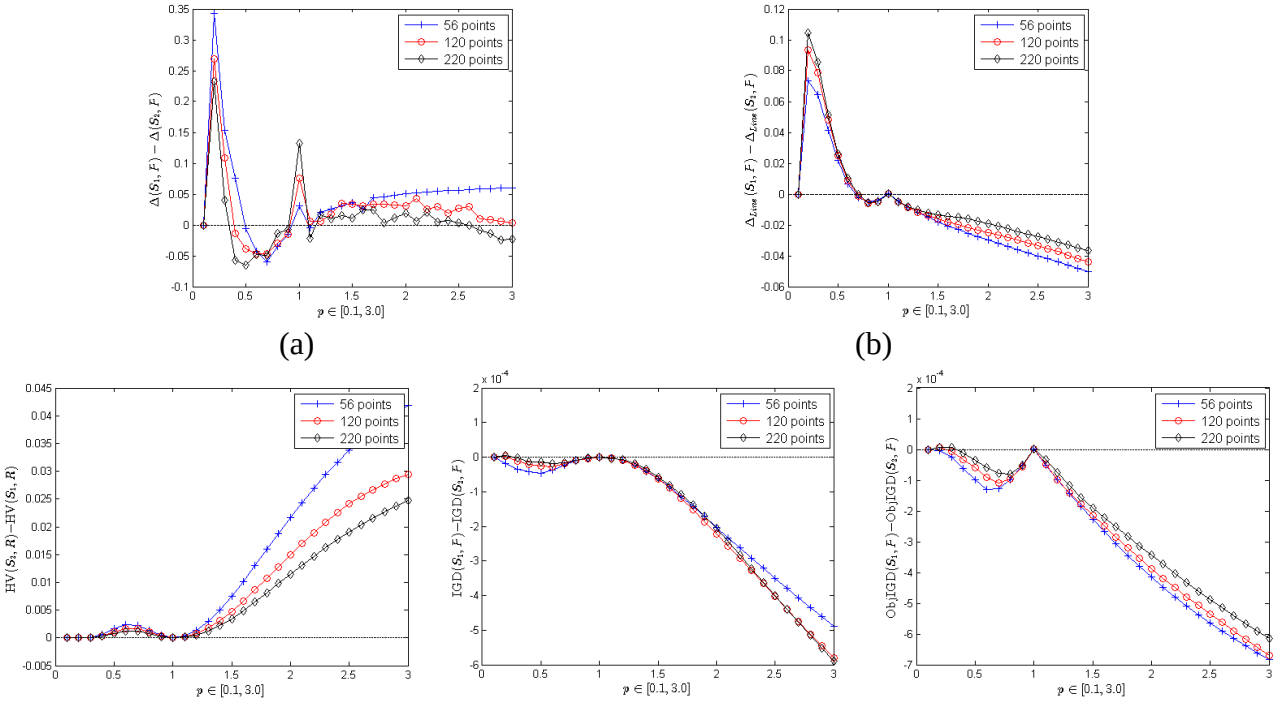

FIGURE 4-4 Differences in metrics of four-objective S_1 and S_2 solutions containing 56, 120, and 220 points. S_1 and S_2 points are generated using the simplex lattice design and $pa\lambda$ methods respectively and $p \in [0.1, 3]$. A positive value indicates S_2 is superior to S_1. (a) Diversity $\Delta(S_1, P) - \Delta(S_2, P)$. (b) Objective-wise diversity $\Delta_{line}(S_1, P) - \Delta_{Line}(S_2, P)$. (c) Convergence and diversity $HV(S_2, R) - HV(S_1, R)$. (d) Convergence and diversity $IGD(S_1, P) - IGD(S_2, P)$. (e) Objective-wise convergence and diversity $ObjIGD(S_1, P) - ObjIGD(S_2, P)$.

Experimental series 3 – examines the relationship of performance metrics on 4D PFs. Figure 4-4 shows the difference values of each metric on PFs $f_1^p + f_2^p + f_3^p + f_4^p = 1$, where $p \in [0.1, 3.0]$. As it can be seen in Figure 4-4 (a) and (b), the diversity measures (Δ and Δ_{Line}) exhibit similar results for the convex portion of the PF $p \in (0.1, 1.0)$ and contradictory results for the concave portion of the PF $p \in (1.0, 3.0)$. When comparing the convergence-diversity measures (HV, IGD, and ObjIGD) in Figure 4-4 (c) to (e), the IGD and ObjIGD measures show identical trend on $p \in (0.1, 3.0]$, however the HV metric shows contradictory results for all shapes.

Experimental series 4 – examines the relationship of performance metrics on 3D PFs. Figure 4-5 shows the difference values of each metric on PFs $f_1^p + f_2^p + f_3^p + f_4^p + f_5^p = 1$, where $p \in [0.1, 3.0]$. When comparing the diversity measures (Δ and Δ_{Line}), in Figure 4-5 (a) and (b), the Δ and Δ_{Line} measures show consistent trend as the previous experiment (4D PFs). Similarly, the convergence-diversity metrics (see. Figure 4-5 (c) to (e)) also show the same trend as the previous experiment. However, the HV metric difference values for $p \in (0.1, 1{,}0]$ is close to zero and thus unable to clearly distinguish the superiority of a solution set for convex PFs.

From our experiments on 2- to 5-objective PFs for the two optimal solution sets on different shapes of PFs, we summarize our observations as follows:

- The IGD and ObjIGD performance measures showed similar trend for all test cases, however the ObjIGD results curves were smoother than the IGD metric. Therefore, the ObjIGD measure can be used as complementary measure to IGD as a tiebreaker.
- As the number of objectives increases, the difference HV values on convex PF, $p \in (0.1, 1.0]$ approaches zero. This means, in the presence of extreme cases, the HV metrics cannot distinguish the superiority of a solution set for high dimension on convex PFs. Therefore, in such cases the ObjIGD measure can be used to determine the superior solution set.
- In almost all experiments the difference Δ values on concave PFs $p \in (1.0, 3.0]$ were unstable (the difference Δ values fluctuated throughout this interval). On the other hand, the Δ_{Line} measure was stable for all PFs and as a result this characteristics make it a desirable performance measure when we need to determine a solution set with greater diversity.

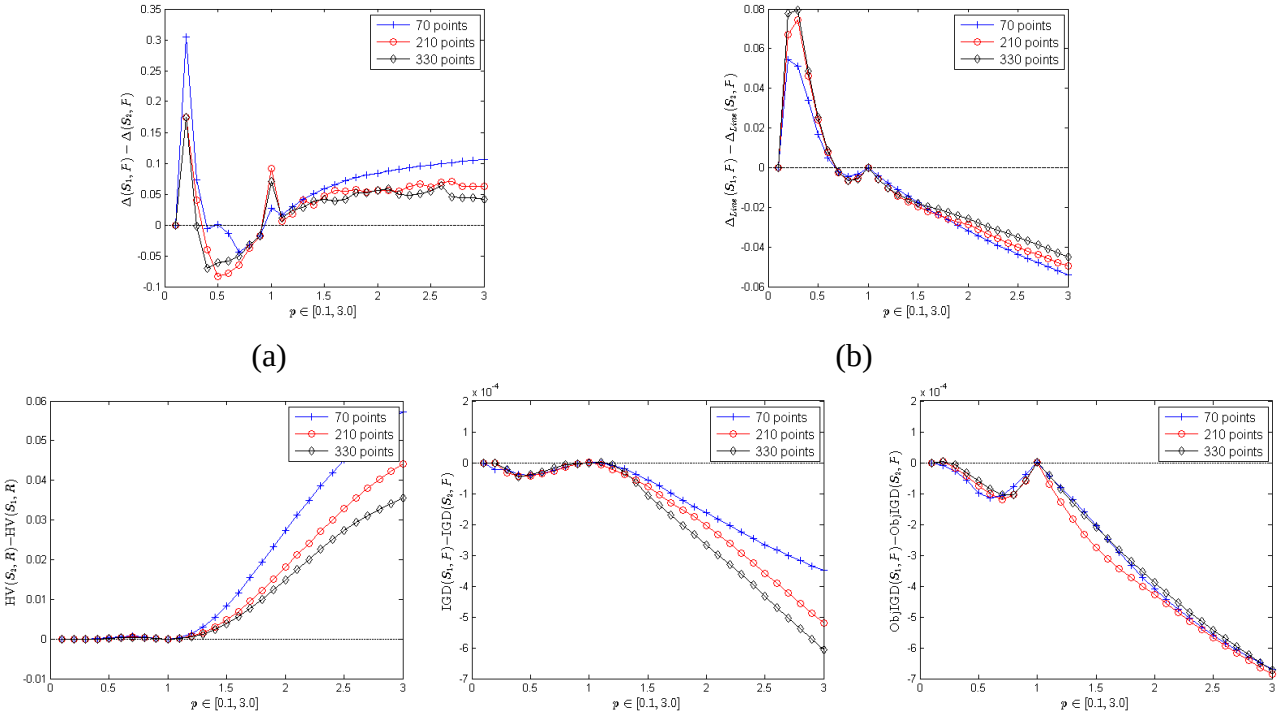

FIGURE 4-5 Differences in metrics of five-objective S_1 and S_2 solutions containing 70, 210, and 330 points. S_1 and S_2 points are generated using the simplex lattice design and $pa\lambda$ methods respectively and $p \in [0.1, 3]$. A positive value indicates S_2 is superior to S_1. (a) Diversity $\Delta(S_1, P) - \Delta(S_2, P)$. (b) Objective-wise diversity $\Delta_{line}(S_1, P) - \Delta_{Line}(S_2, P)$. (c) Convergence and diversity $HV(S_2, R) - HV(S_1, R)$. (d) Convergence and diversity $IGD(S_1, P) - IGD(S_2, P)$. (e) Objective-wise convergence and diversity $ObjIGD(S_1, P) - ObjIGD(S_2, P)$.

TABLE 4.2 Parameter settings for GDE3, NSGA-II, and NSGA-III. n is the number of variables

Parameters	GDE3	NSGA-II	NSGA-III
SBX probability (p_c)	-	0.9	0.9
Polynomial mutation (p_m)	-	$1/n$	$1/n$
Crossover Distribution Index (η_c)	-	20	30
Mutation Distribution Index (η_m)	-	20	20
Mutation probability	0.5	-	-
Crossover probability	0.9	-	-

4.4.3 Performance Assessment of MaOOAs using 3D-RadVis Antenna and Proposed Performance Measures

In Chapter 3, we have shown how the proposed 3D-RadVis Antenna and the proposed performance measures can be used separately. In this section, we will show how these two ideas can be combined to assess and investigate the performance of a MaOOA visually and quantitatively. The algorithms and their parameter settings used is shown in Table 4.2.

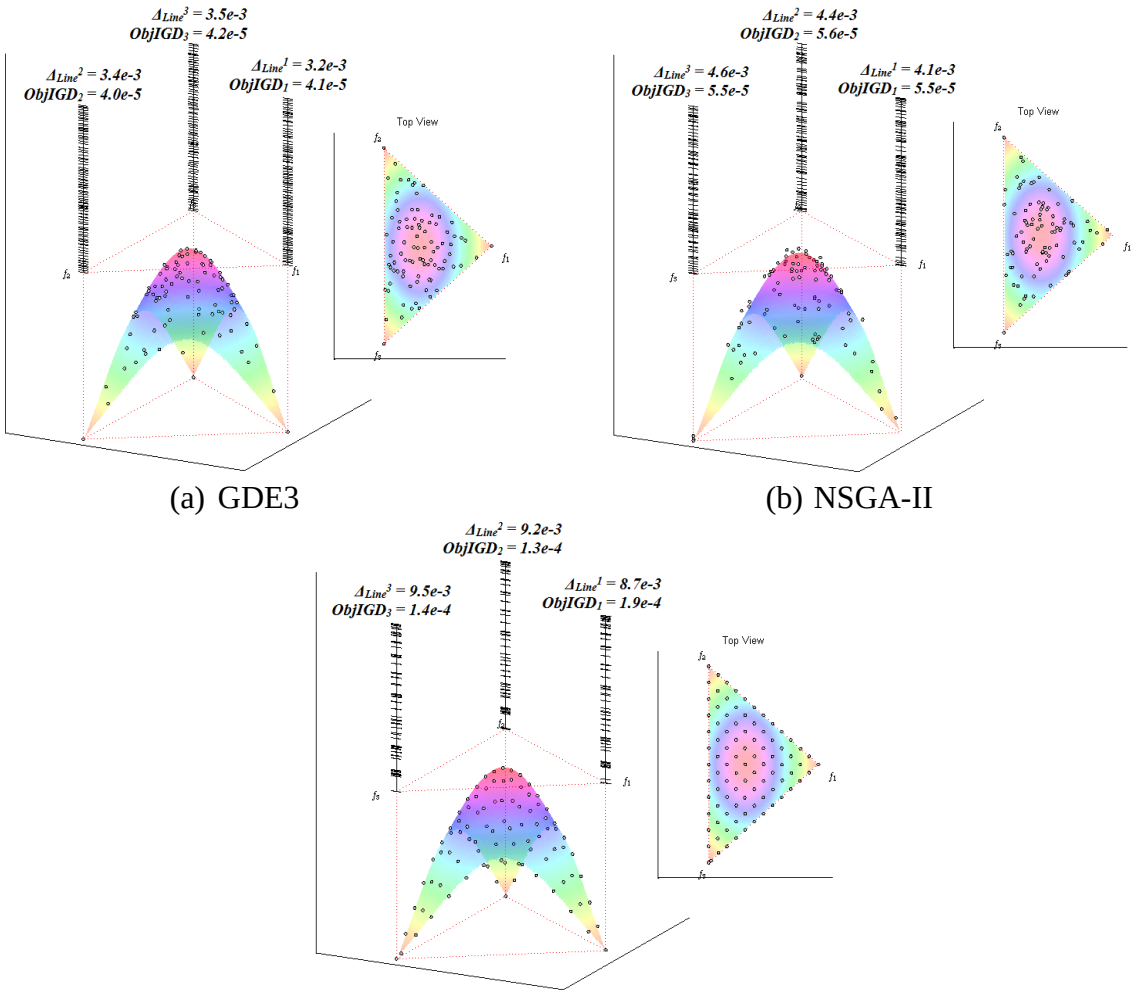

(a) GDE3 (b) NSGA-II

(c) NSGA-III

FIGURE 4-6 3D-RadVis Antenna plots of three-objective DTLZ2 problem showing the convergence and diversity of obtained solutions onto the Pareto-optimal surface and the convergence and diversity of obtained solutions along each objective. A small value of Δ_{line}^{i} and $ObjIGD_i$ indicates the superiority of solutions along the i^{th} objective.

Figure 4-6 to Figure 4-9 show 3D-RadVis Antenna plots with Δ_{Line} and ObjIGD values along each objective for GDE3, NSGA-II and NSGA-III algorithms on 3- and 5-objective DTLZ2 and convex DTLZ2 test problems. In 3-dimesional DTLZ2 (Figure 4-6), we see that GDE3 has slightly better distribution of solutions along each objective than NSGA-II. However, both NSGA-II and GDE3 have significantly better distribution in all objectives than NSGA-III. The poor performance of NSGA-III along each objective is attributed to the fact that NSGA-III tries to guide solutions towards well-spread reference points onto the optimal Pareto-surface while disregarding the distribution of solutions along each objective. When comparing the IGD values for these algorithms (1.32×10^{-3}, 1.53×10^{-3}, 3.14×10^{-4} for GDE3, NSGA-II and NSGA-III respectively), NSGA-III exhibited superior performance than the NSGA-II and GDE3 as the IGD metric measures the convergence and distribution of solutions on the optimal PF surface.

In 3-objective convex DTLZ2, from Figure 4-7 (a) and (b), GDE3 and NSGA-II show very poor distribution on the optimal Pareto-surface while attaining far better distribution of solutions along each objective. On the other hand, NSGA-III (see Figure 4-7 (c)) is able to distribute 92 solutions onto 91 uniformly placed reference points on a normalized hyper-plane. However, NSGA-III still fails to attain good distribution of solutions along each objective. The IGD values for GDE3, NSGA-II and NSGA-III are 9.90×10^{-4}, 1.16×10^{-3}, and 5.76×10^{-4} respectively.

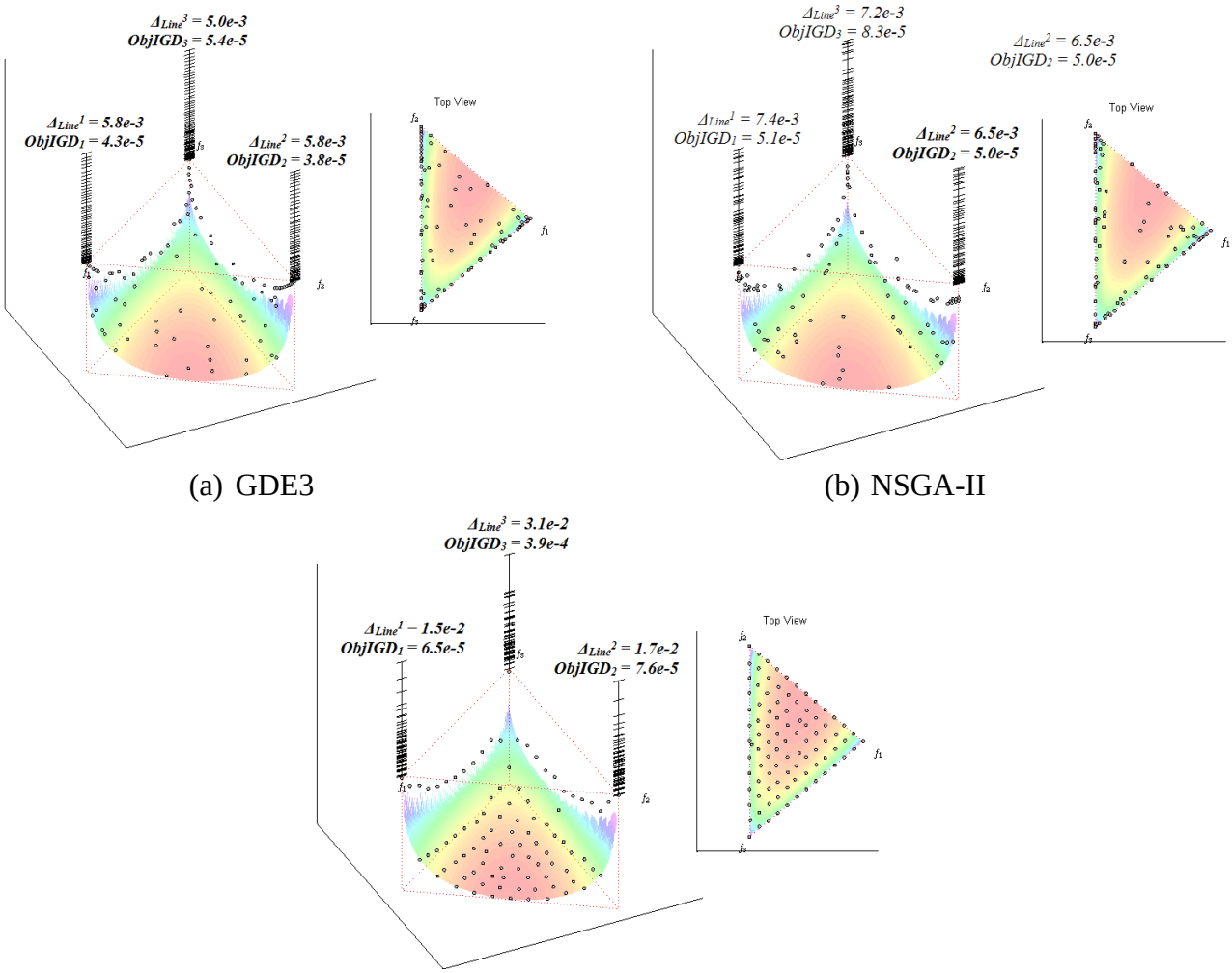

(a) GDE3

(b) NSGA-II

(c) NSGA-III

FIGURE 4-7 3D-RadVis Antenna plots of three-objective convex DTLZ2 problem showing the convergence and diversity of obtained solutions onto the Pareto-optimal surface and the convergence and diversity of obtained solutions along each objective. A small value of Δ_{line}^{i} and $ObjIGD_i$ indicates the superiority of solutions along the i^{th} objective.

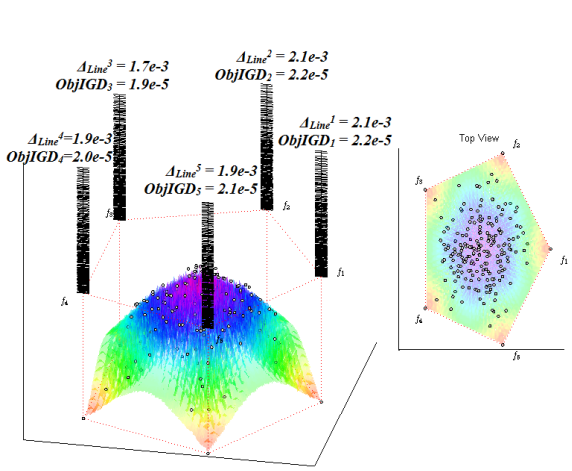

(a) GDE3

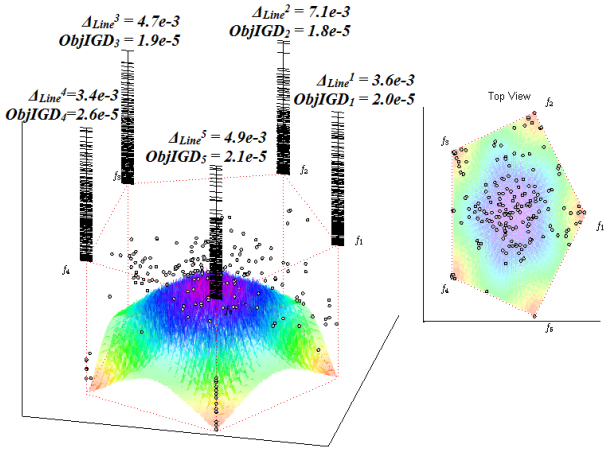

(b) NSGA-II

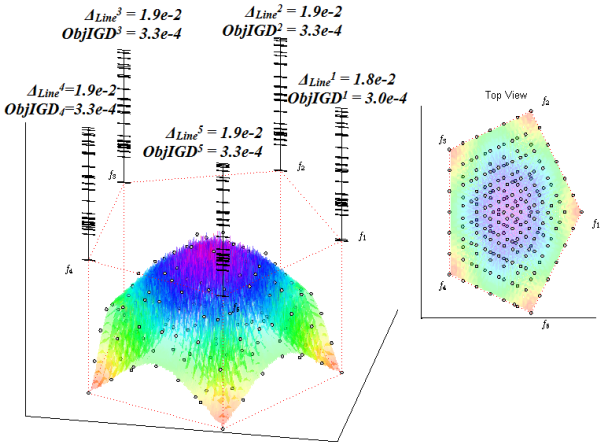

(c) NSGA-III

FIGURE 4-8 3D-RadVis Antenna plots five-objective DTLZ2 problem showing the convergence and diversity of obtained solutions onto the Pareto-optimal surface and the convergence and diversity of obtained solutions along each objective. A small value of Δ_{line}^{i} and $ObjIGD_i$ indicates the superiority of solutions along the i^{th} objective.

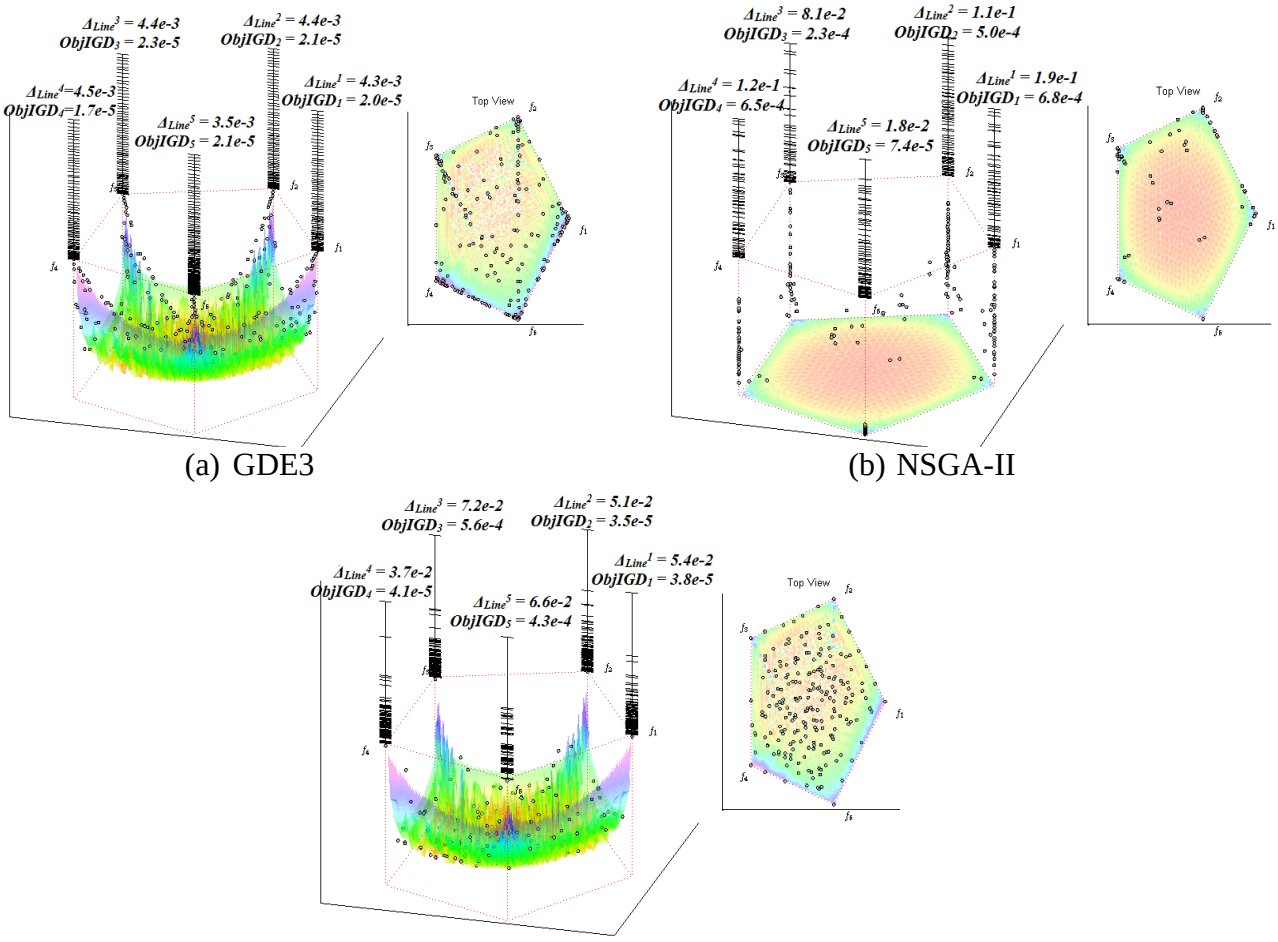

FIGURE 4-9 3D-RadVis Antenna plots five-objective convex DTLZ2 problem showing the convergence and diversity of obtained solutions onto the Pareto-optimal surface and the convergence and diversity of obtained solutions along each objective. A small value of Δ_{line}^{i} and $ObjIGD_i$ indicates the superiority of solutions along the i^{th} objective.

Figure 4-8 (a) shows obtained solutions found by the GDE3 algorithm for a 5-objective DTLZ2 test problem. It found fairly distributed solutions on the optimal Pareto-surface while attaining an excellent distribution along each objective. On the other hand, from Figure 4-8 (b), we see that NSGA-II is not able to maintain well-converged or good distribution of solutions on the optimal Pareto surface or along each objective. This shows that NSGA-II performs better on bi- and tri-objective problems and loses its power when the number of objectives is high. Figure 4-8 (c) show that the NSGA-III algorithm is able

to maintain well-converged and uniformly distributed solutions on the optimal PF surface and as a result it is able to achieve superior IGD score. The IGD scores for GDE3, NSGA-II and NSGA-III are 9.90×10^{-4}, 1.16×10^{-3}, and 5.76×10^{-4} respectively. Similar to the previous results NSGA-III still failed to show good distribution along each objective. In the 5-objective convex DTLZ2 test problem, from Figure 4-9 (b) we see that the performance of the NSGA-II algorithm continues to deteriorate and as a result it showed very poor IGD, ObjIGD and Δ_{Line} scores. However, from Figure 4-9(a) and (c) we see that GDE3 and NSGA-III are able to maintain their strength (i.e. good convergence and distribution of solutions on the optimal PF surface for NSGA-III and good convergence and well-distributed solutions along each objective for GDE3) for 5-objective convex DTLZ2 test problem. The IGD scores for GDE3, NSGA-II and NSGA-III are 5.88×10^{-3}, 1.16×10^{-3}, and 5.76×10^{-4}, respectively. An interesting observation from Figure 4-7 (c) and Figure 4-9 (c) is that even though the supplied reference points for NSGA-III are uniformly distributed on normalized hyper-plane, the distribution of solutions obtained by the NSGA-III algorithm are poor outside the intermediate region of the surface. This poor distribution of solutions also surfaced in the 3D-RadVis Antenna plots.

4.4.4 Comparison of Proposed Performance Measures with Spread, IGD, and HV on 2-, 5-, and 8-D Benchmark Test Problems

In this experiment series, we compare the performance of GDE3, NSGA-II, and NSGA-III algorithms based on the IGD [7, 89, 90], ObjIGD, and Δ_{Line} measures on 3-, 5- and 8-objective DTLZ1 to DTLZ4, and convex DTLZ2 test problems. The reference PFs used in the IGD and ObjIGD measures are mathematically computed to evaluate the efficacy of the proposed measure. Table 4.3 shows the IGD, ObjIGD and Δ_{Line} scores as well as the

best, the worst, the median, and the average results for GDE3, NSGA-II and NSGA-III. The first best performing algorithm for each measure is emphasized in grey shade and the second best is emphasized in boldface.

From Table 4.3, as expected, we see that NSGA-III has the worst score when measuring the overall distribution of solutions along each objective. This is because NSGA-III tries to guide solutions towards well-spread reference points on the Pareto-surface while discounting the distribution of solutions along each objective. When using the Δ_{Line} measure, both NSGA-II and GDE3 shown comparable performance as the Δ_{Line} measure only measures the distribution of solutions along each objective while disregarding the convergence of solutions. On the other hand, when using the ObjIGD measure, GDE3 has shown superior performance as the ObjIGD measure measures the convergence and the distribution of solutions along each objective. In overall, GDE3 was the dominant algorithm when comparing the performance of algorithms in all measures utilized in this study.

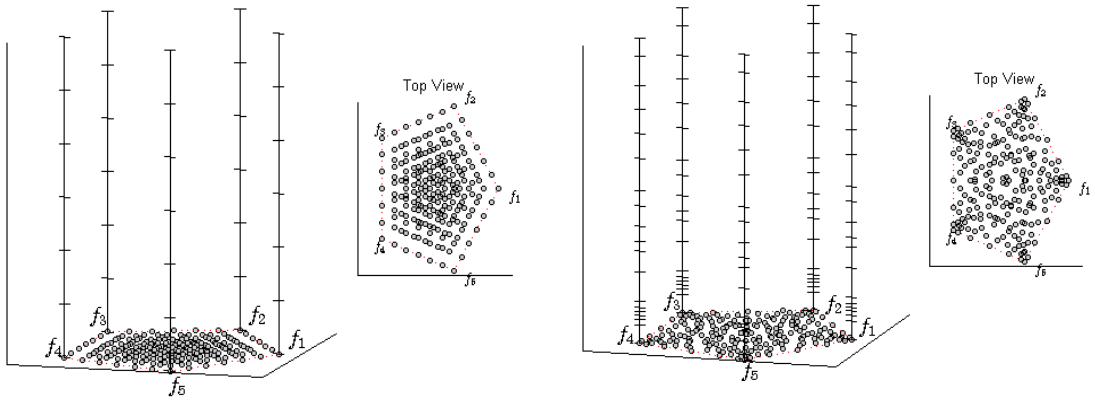

(a) (b)

FIGURE 4-10 3D-RadVis Antenna showing five-objective reference points generated using (a) Das and Dennis's method (b) $pa\lambda$ method

TABLE 4.3 Best, median, worst, and average IGD, ObjIGD and Δ_{Line} values for GDE3, NSGA-II, and NSGA-III on M-objective DTLZ test problems. First best performing algorithm is shown in grey highlight and second best is shown in boldface.

Problem	*M*	*Max Gen*	*IGD*			*ObjIGD*			Δ_{Line}		
			GDE3	*NSGA-II*	*NSGA-III*	*GDE3*	*NSGA-II*	*NSGA-III*	*GDE3*	*NSGA-II*	*NSGA-III*
DTLZ1	3	400	**5.60E-04**	5.97E-04	4.41E-04	4.39E-05	**5.12E-05**	8.72E-05	4.15E-03	**4.70E-03**	8.04E-03
			5.86E-04	6.84E-04	5.37E-04	4.56E-05	**5.68E-05**	1.11E-04	4.37E-03	**5.15E-03**	9.81E-03
			1.05E-02	9.38E-04	**2.49E-03**	**7.93E-05**	7.42E-05	6.28E-04	**7.03E-03**	7.01E-03	5.24E-02
			1.08E-03	**7.03E-04**	6.49E-04	4.72E-05	**5.92E-05**	1.58E-04	4.51E-03	**5.39E-03**	1.38E-02
	5	1000	**1.33E-03**	3.05E-02	1.15E-03	2.21E-05	1.51E-04	**8.64E-05**	3.21E-03	1.67E-02	**1.31E-02**
			1.36E-03	8.10E-02	**1.42E-03**	2.49E-05	2.25E-04	**2.04E-04**	3.27E-03	2.84E-02	**2.33E-02**
			1.41E-03	1.07E+00	**8.40E-03**	2.84E-05	**3.72E-04**	3.14E-03	3.34E-03	**4.98E-02**	3.93E-01
			1.36E-03	1.49E-01	**2.60E-03**	2.50E-05	**2.41E-04**	6.83E-04	3.28E-03	**2.92E-02**	8.42E-02
	8	1500	**5.41E-03**	1.18E-01	2.47E-03	2.33E-05	**1.36E-04**	2.17E-04	4.16E-03	**2.18E-02**	3.82E-02
			5.91E-03	4.99E-01	**1.04E-02**	2.87E-05	**2.44E-04**	2.79E-03	4.62E-03	**2.89E-02**	4.14E-01
			6.48E-03	1.51E+00	**1.16E-02**	3.79E-05	**3.43E-04**	3.18E-03	5.10E-03	**4.27E-02**	4.54E-01
			5.90E-03	6.20E-01	**8.49E-03**	2.95E-05	**2.39E-04**	2.19E-03	4.60E-03	**3.00E-02**	3.28E-01
DTLZ2	3	250	**6.99E-04**	7.69E-04	5.92E-04	4.10E-05	**5.07E-05**	1.11E-04	3.34E-03	**4.01E-03**	7.72E-03
			7.35E-04	8.19E-04	5.94E-04	4.28E-05	**5.62E-05**	1.26E-04	3.47E-03	**4.29E-03**	8.54E-03
			8.08E-04	8.84E-04	6.70E-04	4.46E-05	**5.93E-05**	1.37E-04	3.67E-03	**4.51E-03**	9.55E-03
			7.45E-04	8.17E-04	5.99E-04	4.28E-05	**5.55E-05**	1.24E-04	3.47E-03	**4.27E-03**	8.59E-03
	5	500	**1.94E-03**	3.18E-03	1.84E-03	2.23E-05	**3.99E-05**	2.86E-04	**4.23E-02**	4.14E-03	5.08E-02
			1.99E-03	3.53E-03	1.84E-03	2.29E-05	**5.03E-05**	3.35E-04	**4.24E-02**	4.57E-03	5.26E-02
			2.03E-03	4.20E-03	1.85E-03	2.36E-05	**5.58E-05**	3.70E-04	**4.24E-02**	6.92E-03	5.44E-02
			1.99E-03	3.59E-03	1.84E-03	2.29E-05	**5.03E-05**	3.31E-04	**4.24E-02**	4.69E-03	5.27E-02
	8	750	**7.55E-03**	1.73E-02	4.08E-03	4.99E-05	**6.72E-05**	3.96E-04	**1.45E-02**	5.08E-03	1.49E-01
			8.49E-03	2.10E-02	8.01E-03	5.53E-05	**8.02E-05**	8.39E-04	**2.72E-02**	5.88E-03	2.18E-01
			9.20E-03	2.50E-02	**1.05E-02**	6.96E-05	**9.04E-05**	2.21E-03	**4.20E-02**	6.80E-03	3.50E-01
			8.34E-03	2.11E-02	7.11E-03	5.63E-05	**7.94E-05**	1.01E-03	**2.63E-02**	5.95E-03	2.15E-01
Convex DTLZ2	3	250	5.15E-04	5.52E-04	**5.43E-04**	4.67E-05	**6.04E-05**	1.37E-04	5.38E-03	**6.58E-03**	1.56E-02
			5.57E-04	6.40E-04	**5.92E-04**	4.75E-05	**6.48E-05**	1.84E-04	5.51E-03	**7.01E-03**	2.13E-02
			6.19E-04	**8.37E-04**	1.27E-03	4.89E-05	**7.15E-05**	4.29E-04	5.71E-03	**7.70E-03**	4.68E-02
			5.60E-04	**6.48E-04**	6.69E-04	4.76E-05	**6.51E-05**	2.12E-04	5.51E-03	**7.06E-03**	2.45E-02
	5	750	**9.12E-04**	7.91E-03	8.25E-04	2.38E-05	4.61E-04	**1.76E-04**	**1.49E-01**	5.10E-02	1.61E-01
			9.64E-04	1.22E-02	9.29E-04	2.58E-05	6.51E-04	**2.26E-04**	**1.49E-01**	8.77E-02	1.76E-01
			1.04E-03	2.05E-02	**1.47E-03**	2.75E-05	8.12E-04	**3.50E-04**	1.49E-01	**1.62E-01**	1.88E-01
			9.74E-04	1.35E-02	**1.01E-03**	2.56E-05	6.48E-04	**2.40E-04**	**1.49E-01**	9.70E-02	1.75E-01
	8	2000	**2.66E-03**	5.89E-03	1.65E-03	1.05E-04	**3.26E-04**	3.50E-04	**7.90E-02**	4.95E-02	3.42E-01
			3.52E-03	1.21E-02	**3.84E-03**	1.35E-04	**4.98E-04**	7.92E-04	**9.07E-02**	7.51E-02	4.66E-01
			4.10E-03	2.02E-02	**6.49E-03**	1.61E-04	**6.78E-04**	1.02E-03	1.12E-01	**1.22E-01**	4.78E-01
			3.46E-03	1.27E-02	**3.61E-03**	1.34E-04	**4.92E-04**	7.35E-04	**9.26E-02**	7.70E-02	4.55E-01
DTLZ3	3	250	**7.07E-04**	1.38E-02	5.96E-04	4.08E-05	6.54E-04	**9.24E-05**	3.32E-03	4.33E-02	**6.97E-03**
			7.61E-04	6.52E-02	**8.75E-04**	4.36E-05	1.20E-03	**1.33E-04**	3.59E-03	8.45E-02	**9.31E-03**
			4.11E-02	1.40E-01	3.47E-03	2.29E-04	2.34E-03	**6.54E-04**	1.82E-02	1.88E-01	**5.34E-02**
			5.80E-03	6.68E-02	1.16E-03	6.75E-05	1.35E-03	**1.80E-04**	5.41E-03	9.47E-02	**1.33E-02**
	5	500	**1.95E-03**	9.73E-01	1.84E-03	2.21E-05	3.08E-04	**7.37E-05**	1.99E-01	1.84E-02	**1.98E-01**
			1.99E-03	1.39E+00	**4.67E-03**	2.29E-05	**4.53E-04**	7.17E-04	**1.99E-01**	2.64E-02	2.16E-01
			2.07E-03	2.48E+00	**9.46E-03**	2.42E-05	**7.82E-04**	2.87E-03	**1.99E-01**	6.00E-02	4.41E-01
			2.00E-03	1.51E+00	**5.16E-03**	2.30E-05	**4.83E-04**	1.09E-03	**1.99E-01**	2.79E-02	2.45E-01
	8	750	**9.50E-03**	9.41E-01	6.54E-03	2.62E-04	6.36E-04	**2.79E-04**	**1.94E-02**	1.73E-02	1.98E-01
			9.30E-02	2.44E+00	1.32E-02	1.80E-03	**9.92E-04**	5.74E-04	**3.26E-02**	3.16E-02	3.84E-01
			2.46E-01	5.60E+00	1.01E-01	**3.31E-03**	1.49E-03	3.99E-03	**1.17E-01**	5.50E-02	4.69E-01
			1.01E-01	2.79E+00	2.53E-02	1.77E-03	1.05E-03	**1.23E-03**	**4.16E-02**	3.42E-02	3.68E-01
DTLZ4	3	250	**6.97E-04**	7.47E-04	5.94E-04	4.12E-05	**5.31E-05**	9.95E-05	3.20E-03	**4.14E-03**	8.43E-03
			7.41E-04	**8.06E-04**	8.13E-04	4.33E-05	**5.53E-05**	1.28E-04	3.48E-03	**4.24E-03**	8.86E-03
			8.25E-04	**8.46E-04**	1.03E-02	4.51E-05	**6.20E-05**	2.98E-03	3.69E-03	**4.59E-03**	1.71E-01
			7.47E-04	**8.00E-04**	3.31E-03	4.33E-05	**5.56E-05**	9.30E-04	3.46E-03	**4.28E-03**	6.43E-02
	5	500	**1.94E-03**	2.59E-03	1.84E-03	2.21E-05	**3.60E-05**	7.79E-05	4.09E-02	3.57E-03	**4.04E-02**
			1.97E-03	2.68E-03	**1.99E-03**	2.30E-05	**3.97E-05**	1.13E-04	**4.09E-02**	4.64E-03	4.31E-02
			2.02E-03	**2.88E-03**	5.45E-03	2.36E-05	**4.87E-05**	1.00E-03	**4.09E-02**	8.75E-03	1.25E-01
			1.98E-03	2.71E-03	**2.22E-03**	2.30E-05	**4.05E-05**	1.88E-04	**4.09E-02**	4.96E-03	4.79E-02
	8	750	**5.77E-03**	2.00E-02	4.11E-03	5.61E-05	**6.80E-05**	2.18E-04	**3.24E-02**	5.17E-03	1.60E-01
			6.37E-03	2.43E-02	5.52E-03	6.35E-05	**8.40E-05**	5.77E-04	**5.41E-02**	5.71E-03	1.79E-01
			6.90E-03	2.68E-02	1.06E-02	7.52E-05	**9.78E-05**	2.29E-03	**7.73E-02**	8.06E-03	3.25E-01
			6.41E-03	2.39E-02	5.64E-03	6.32E-05	**8.42E-05**	6.48E-04	**5.50E-02**	5.82E-03	1.91E-01

To improve the distribution of solutions along each objective while preserving the convergence and distribution of solutions on the optimal PF surface, we suggest using an alternate systematic way of generating reference points used in NSGA-III. For example, NSGA-III uses Das and Dennis's [91] systematic approach to generate uniformly distributed reference points on a normalized hyper-plane. Figure 4-10 (a) shows 3D-RadVis Antenna plot of reference points generated using the Das and Dennis's approach for 5-objective with 6 divisions. From this plot we see that the distribution of these reference points along each objective is poor. Instead, we can use a method similar the $pa\lambda$ approach [84] (in our case $p = 1$ and the optimal scaling parameter l^{opt} is calculated based on the minimum Δ_{Line}) to adjust the reference points with better distribution along each objective. Figure 4-10 (b) shows 3D-RadVis Antenna plot of adjusted reference points using the $pa\lambda$ approach

From our studies on the proposed measures (ObjIGD and Δ_{Line}), we summarize our findings as follows:

1. The ObjIGD and Δ_{Line} measures are not aimed to replace popular performance metrics such as IGD and HV, but rather to complement existing performance metrics.
2. The Δ_{Line} measure should be used when solely interested in measuring the distribution of solutions along each objective.
3. The ObjIGD measure should be used when mainly interested in measuring the distribution of solutions along each objective but still require some information of convergence.

4. When measuring the overall performance of a MaOOA, the ObjIGD and Δ_{Line} measures can be used as a tiebreaker.
5. When designing reference-point based algorithms, we should also incorporate the idea of distribution of points along each objective; because it is important from decision maker perspective.

4.5 Conclusion

This chapter presented two proposed performance measures; objective-wise inverse generational distance (ObjIGD) and line distribution (Δ_{Line}) to measure the convergence and distribution of solutions along each objective. Experimental results have shown that these two measures can be used as reliable complementary measures along with other widely used performance measures to compare many-objective solution sets.

In future work, we would like to investigate how we can improve the performance (i.e. convergence and distribution along each objective) of reference-point based algorithms through the generation of well-balanced reference points – reference points with good distribution on the hyper-plane and along each objective.

Chapter 5

FUSION OF MANY-OBJECTIVE NON-DOMINATED SOLUTIONS USING REFERENCE POINTS

With recent advancements of multi- or many-objective optimization algorithms, researchers and decision makers are increasingly faced with the dilemma of choosing the best algorithm to solve their problems. This chapter proposes a simple hybridization of population-based multi- or many-objective optimization algorithms called fusion of non-dominated fronts using reference points (FNFR) to gain combined benefits of several algorithms. FNFR combines solutions from multiple optimization algorithms during or after several runs and extracts well-distributed solutions from a large set of non-dominated solutions using predefined structured reference points or user-defined reference points. The proposed FNFR is applied to non-dominated solutions obtained by the Generalized Differential Evolution Generation 3 (GDE3), Speed-constrained Multi-objective Particle Swarm Optimization (SMPSO), and the Strength Pareto Evolutionary Algorithm 2 (SPEA2) on seven unconstrained many-objective test problems with three to ten objectives. Experimental results show FNFR is an effective way for combining and extracting (fusion) of well-distributed non-dominated solutions among a large set of solutions. In fact, the proposed method is a solution-level hybridization approach. FNFR showed promising results when selecting well-distributed solutions around a specific region of interest.

5.1 Introduction

For the last three decades, there has been a number multi- and many-objective algorithms capable of solving complex problems. However, despite recent advancements, researchers and decision makers are increasingly faced with the difficulty of choosing an appropriate algorithm capable of solving their problem effectively. This is due to a well-established "no-free-lunch" theorem that no one algorithm works best for all class of problems. As a result, many researchers have shifted their focus in developing powerful problem-specific

or instance-specific algorithms. One way to accomplish this task is the hybridizations of optimization algorithms where new algorithms are developed by combining one optimization algorithm with another, by combining a standard optimization algorithm with mathematical operators, or incorporating evolutionary operators (selection, mutation, and crossover) into non-evolutionary optimization algorithms [92]. The main hope is that hybridization combines the desirable properties of different approaches so that the hybrid algorithm exhibits improved exploration and exploitation capabilities.

For example, Mirjalili and Hashim [93] proposed a hybrid population-based algorithm called PSOGSA by combining Particle Swarm Optimization (PSO) and Gravitational Search Algorithm (GSA). Their main aim was to integrate the exploitation ability of PSO with the exploration ability of GSA to synthesize both algorithms' strength. Similarly, El-hossini et al. [94] proposed three hybrid algorithms based on the PSO and the strength Pareto evolutionary algorithm 2 (SPEA2) to solve multi-objective optimization problems. In all of these algorithms, strength Pareto fitness assignment is used to maintain an external archive; and the three algorithms are developed by alternating the evolutionary and PSO processes in different order. Experimental results showed that the proposed hybrid PSO algorithms have comparable performance to SPEA2. Also, Tang and Wang [95] proposed a novel hybrid multi-objective evolutionary algorithm (HMOEA) for real-valued multi-objective problems by incorporating the concepts of personal best and global best in PSO and evolutionary operators (multiple crossovers) to improve the robustness of evolutionary algorithms to solve variant kinds of optimization problems.

Wang et al. [96] proposed a hybrid evolutionary algorithm based on different crossover and mutation strategies combined with adaptive constrained-handling technique

to deal with numerical and engineering constrained optimization problems. Zăvoianu et al. [97] proposed a hybrid and adaptive co-evolutionary optimization method that can efficiently solve a wide range of multi-objective optimization problems. Their approach combines Pareto-based selection for survival, differential evolution's crossover and mutation operators, and decomposition-based strategies. Recently, an ensemble strategy was proposed to benefit from both the availability of diverse approaches and to overcome the difficulty of fine tuning associated parameters. Some of these work include ensemble of ε parameter values and an ensemble of external archives in a multi-objective PSO algorithm [98], ensemble of constraint handling methods to tackle constrained multi-objective optimization problems [99], and ensemble of different neighborhood sizes in multi-objective evolutionary algorithm based on decomposition (MOEA/D) with online self-adaptation [100].

Tan et a1. [101] proposed a hybrid multi-objective evolutionary algorithm (HMOEA) featured with specialized genetic operators, variable-length representation and local search heuristic to find the Pareto-optimal routing solutions for the truck and trailer vehicle routing problem (TTVRP). Experimental results showed the HMOEA is effective in solving a multi-objective and multi-modal combinatorial optimization problems. Similarly, Xia and Wu [102] proposed a hybrid multi-objective algorithm by combining the PSO algorithm for its explorative power and simulated annealing (SA) for its exploitations to solve flexible job-shop scheduling problem (FJSP). Tavakkoli-Moghaddam et al. [103] also proposed a hybrid multi-objective algorithm based on the features of a biological immune system (IS) and bacterial optimization (BO) to find Pareto-optimal solutions for flow shop scheduling problem. Their algorithm uses the clonal

selection principle in IS with highest affinity antibodies and criterion distinguishing between antigens and antibodies in BO for Pareto dominance relationship among solutions. Karthikeyan et al. [104] proposed a hybrid discrete firefly algorithm (HDFA) to solve the multi-objective FJSP problem. They have combined the discrete firefly algorithm with local search (LS) method to enhance the searching accuracy and information sharing among fireflies.

In the effort of developing a powerful general-purpose hybridization framework, propose a novel hybridization of population-based multi- or many-objective optimization algorithms called fusion of non-dominated fronts using reference points (FNFR), to gain combined benefit of several algorithms in solution-level. The FNFR method uses well-structured or user supplied reference points to extract targeted solutions from thousands of non-dominated solutions gathered during several runs of multiple multi-objective algorithms. The primary goal for this framework is to assist decision makers in extracting a subset of well-distributed solutions from a large set of non-dominated solutions and ultimately arrive at one optimal solution.

5.2 Proposed Method: Fusion of Non-Dominated Solutions Using Reference Points

Generally speaking, hybridization of optimization algorithms can be grouped into two main categories. The first category includes hybridization of algorithms during the optimization process and the second category includes hybridization of algorithms after the optimization process. Hybridization during the optimization process can also further be grouped into two main categories: Algorithms created by combining multiple metaheuristic algorithms and algorithms created by combining a metaheuristic algorithm with multiple mathematical operators or evolutionary operators.

In this section, we present a novel hybridization technique called fusion of non-dominated fronts using reference points (FNFR) capable of extracting targeted solutions from a set of non-dominated solutions collected during several runs of multiple optimization algorithms. The skeleton for the FNFR hybridization procedure is shown as a flowchart in Figure 5-1. The FNFR procedure consists of three main modules:

1) Problem Formulation. In this module, the problem to be optimized is formulated and set the number of runs required by each algorithm.

2) Approximate Front Evaluation. In this module, algorithms appropriate for the problem are selected and run as many times as indicated by the user. Although any algorithm can be selected and combined together in this framework, we recommend combining algorithms complimentary to each other to get good representative solutions on the entire Pareto-optimal front. Note that each algorithm is run independently and the algorithms can run in parallel or serial. In every run, the found approximate non-dominated front is combined with previously obtained front to create new non-dominated front by removing dominated solutions from the combined front. This step is a crucial step, because we need well-represented set of solutions on the entire Pareto-optimal front before extracting preferred solutions from this set. According to the no-free-lunch theorem, it is well established that depending on the property and complexity of a problem, optimization algorithms known to provide great solutions on a particular class of problems cannot achieve same level of performance on other classes of problems.

3) Fusion and Extraction of Targeted Solutions. In this module, targeted solutions are extracted from the union of non-dominated solutions obtained from several runs of multiple algorithms using a procedure similar to reference-point-based non-dominated sorting

algorithm (NSGA-III) [105]. Given the union of M-objective non-dominated approximate front obtained from several algorithms, the first step is to combine these solutions and remove dominated solutions from the union of these solutions ($FNDS = NDS_1 \dot{\cup} NDS_2 \dot{\cup} \cdots \dot{\cup} NDS_n$, where $\dot{\cup}$ indicate the extraction of non-dominated solutions from the union of two non-dominated solution sets). Second, supply structured or target predefined set of reference points. In the case of structured reference points, one can use the Das and Dennis'[91] procedure to create well-distributed structured reference points. However, if the reference points are targeted points selected by the decision maker, then M extreme points, one at each objective axis $\{z_1 = (1,0,0,\dots,0), z_2 = (0,1,0,\dots,0), \dots, z_M = (0,0,\dots,1)\}$, are needed to determine the right normalized hyper-plane. Then, it constructs reference lines corresponding to each reference point by joining the reference point with the origin. Third, it constructs an ideal point by finding the minimum objective values of $FNDS$. Fourth, it translates each solution in $FNDS$ by the ideal point and finds M extreme points from these translated solutions. These extreme points are used to construct M-dimensional linear hyper-plane. Special care is required when finding extreme points so that we construct proper hyper-plane and are able to extract targeted solutions. We recommend verifying obtained extreme points by finding the individual optimum of each objective function to make sure proper line hyper-plane constructed before moving to the next step. Thereafter, it normalizes each objective by the intercepts each objective axis and the linear hyper-plane. Now, it associates each solution in normalized objective space to a reference line whose perpendicular distance closest to this reference point. The last step is to select one solution from each set of solutions associated with each reference lines based on the closest solution to the reference line. Note

that Algorithm 5.1 is used when the optimization problem is bi-objective.

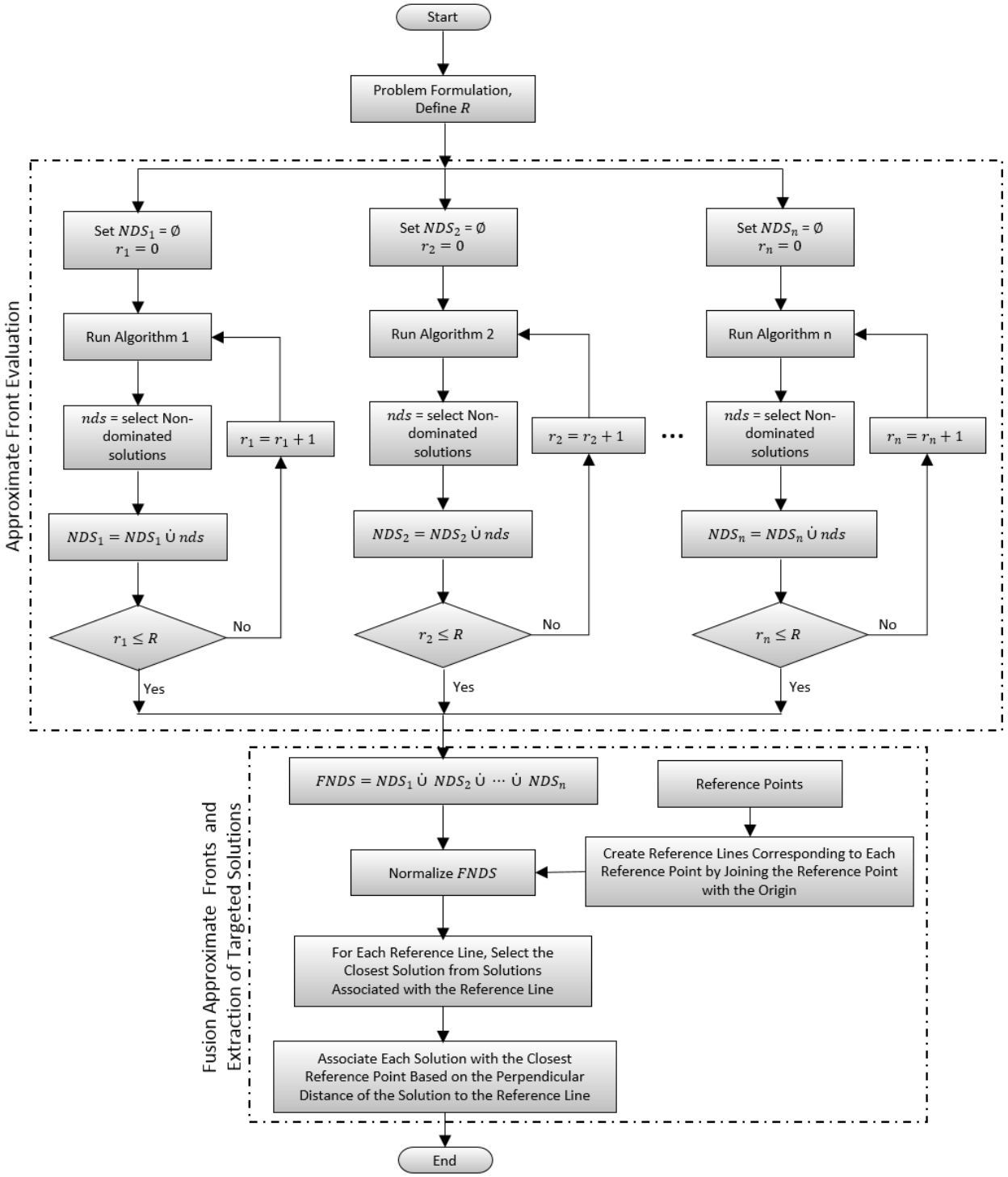

FIGURE 5-1 Flowchart illustrating the FRFR procedure, where $\dot{\cup}$ indicate the extraction of non-dominated solutions from the union of two non-dominated solution sets.

The main advantages of the FNFR framework are: (1) we get the full benefit of all algorithms involved in the optimization process, (2) we don't need to investigate how and when to combine merits of different algorithms, (3) many algorithms can be used without the need of extra parameter tuning, and (4) we can run all algorithms in the optimization process in parallel. The main disadvantage of the FNFR framework is the time required to run all algorithms in the optimization process (i.e., higher time complexity).

5.3 Experimental Setup and Results

In this section, we describe the optimization algorithms, parameter settings, used test problems, and simulation results of the proposed framework on 3- to 10-objective benchmark test problems.

5.3.1 Algorithms

In order to assess the capability of the proposed FNFR hybridization framework, we have considered algorithmic combination of three well-known evolutionary multi-objective algorithms: Generalized Differential Evolution Generation 3 (GDE3), Speed-constrained Multi-objective Particle Swarm Optimization (SMPSO), and the Strength Pareto Evolutionary Algorithm 2 (SPEA2). However, depending on the problem, it's also possible to use variants (through mathematical operators or evolutionary operators) of one algorithm in this framework.

5.3.1.1 Generalized Differential Evolution Generation 3 (GDE3)

GDE3 [106] is an extension of Differential Evolution (DE) for global optimization with an arbitrary number of objectives and constraints (Kukkonen & Lampinen, 2005). GDE3 with a single objective and without constraint is similar to the original DE. GDE3 improves earlier GDE versions in the case of multi-objective problems by giving well-distributed solutions. GDE3 uses a growing population and non-dominated sorting with pruning of non-dominated solutions to decrease the population size at the end of each generation. This improves obtained diversity and makes the method more stable for the selection of control parameter values.

5.3.1.2 Speed-constrained Multi-Objective Particle Swarm Optimization (SMPSO)

SMPSO [107] is similar to multi-objective Particle Swarm Optimization (PSO) algorithm which inspired by the social behaviour of birds flocking to find food. In PSO, particles move in the search space in a cooperative manner where movements are performed by the velocity operator. The velocity operator is guided by a local and a social behaviour of swarm. SMPSO uses the concept of crowding distance to filter out leader solutions when the leaders archive is full, mutation operator accelerates the convergence of the swarm and it incorporates a mechanism to limit the velocity of the particles which can result in erratic movements of particles towards the upper and lower position limits of particles.

5.3.1.3 Strength Pareto Evolutionary Algorithm 2 (SPEA2)

SPEA2 [39] is an extension SPEA for solving multi-objective optimization problems. Both SPEA and SPEA2 use an external archive to store previously found non-dominated

solutions. In SPEA, the external archive maintained based on each individual's strength in which the strength of an individual is measured according to the number of solutions this individual dominates. In every generation, the fitness of each member of the current population is computed according to the strengths (closeness to the true PF and distribution of solutions) of all external non-dominated solutions that dominate it. On the other hand, in SPEA2, the external archive is maintained according to each individual's strength not only by the number of individuals that dominate it but also the number of individuals by which it is dominated. Moreover, SPEA2 uses a nearest neighbor density estimation method to guide the search process efficiently and it preserves boundary solutions.

5.3.2 Test Problems

In order to test the quality of the proposed algorithm, we have used seven many-objective benchmark test problems. The first set of test problems are the DTLZ (DTLZ1 – DTLZ4, Convex DTLZ2) introduced by Deb et al. [61]. The number of variables are $(M + k - 1)$, where M is the number of objectives and $k = 5$ for DTLZ1, while $k = 10$ for DTLZ2, Convex DTLZ2, DTLZ3, and DTLZ4. The corresponding Pareto-optimal fronts is in $f_i \in [0, 0.5]$ for the DTLZ1 problem and in $f_i \in [0, 1]$ for other DTLZ problems. The DTLZ1 problem has a linear Pareto-optimal front, Convex DTLZ2 has convex Pareto-optimal front, and DTLZ2 to DTLZ4 problems have concave Pareto-optimal fronts.

The second set of test problems utilized in this study are WFG1 and WFG2 test problems introduced by Huband et al. [62]. The number of position parameters is set to $k = M - 1$, and the number of distance parameters is set to $l = 3$ for all dimensions. The WFG1 has a mixed Pareto-optimal front and WFG2 problem has a convex, disconnected

Pareto-optimal front. The Pareto-optimal fronts for WFG test problems used in this work lie in $f_i \in [0, 2i]$.

5.3.3 Parameter Settings

Here, we describe the parameter setting used in the three sample algorithms used in the FNFR method. The GDE3 algorithm has two control parameters: mutation ($F = 0.5$) and crossover ($CR = 0.1$) probabilities. The SMPSO algorithm has three control parameters: external archive size (same as population size), Polynomial mutation ($p_m = 1/n$, where n is the number of variables) and Mutation Distribution Index ($\eta_m = 20$). The SPEA2 algorithm has five control parameters: external archive size (same as population size), SBX probability ($p_c = 0.9$), Polynomial mutation ($p_m = 1/n$, where n is the number of variables), Crossover Distribution Index ($\eta_c = 20$), and Mutation Distribution Index ($\eta_m = 20$). In order to maintain a consistent and fair comparison, the optimal parameter settings reported in [39, 106, 108] are used. Table 6.3 presents the number of reference points (H), the population size (N), and the number of inner and outer divisions used for different dimensions of test problems. In this study we have utilized the Das and Dennis' [91] procedure to create structured reference points used in the FNFR method.

To evaluate the performance of the proposed fusion technique, we ran each algorithm 20 times independently and the best, the worst, and the median results of each algorithm are recorded. For the performance measure, we used the inverse generational distance (IGD) metric, which is capable of measuring the convergence and the diversity of the obtained Pareto-optimal solutions. The IGD measure has been predominantly used to evaluate the performance of evolutionary many-objective problems [21 -22]. In this study,

the reference PF utilized in the IGD metric is constructed by joining all the results from all the runs, and then selecting non-dominated solutions from this set.

5.3.4 Experimental Results and Discussion

In this section, we describe experiments carried out to investigate the effectiveness of the FNFR method. Overall, we have conducted three sets of experiments. The first experiment compares the quality of solutions obtained by each algorithm and the FNFR scheme using scatter plots (for three-objective problems) and 3D-RadVis [109] (for many-objective problems, $M > 3$). The second set of experiments involve numerical analysis to evaluate the quality of solutions obtained by each algorithm and the FNFR method. The last set of experiments involve interactively extracting preferred solutions around a specific region.

5.3.4.1 Visual Analysis of Solutions obtained by each Algorithm against the FNFR Method

Here we investigate solutions obtained by the three algorithms and solutions extracted by the FNRF method. We run each algorithm 20 times and assembled the non-dominated fronts from each run by removing dominated solutions after combining non-dominated solutions from each run. Figure 5-2 shows trade-off plots of solutions obtained by the GDE3, SMPSO, and SPEA2 for 3-objective WFG1 test problem. Figure 5-3 illustrates trade-off plots of solutions collectively obtained by the GDE3, SMPSO, and SPEA2 and solutions extracted by the FNFR procedure for 3-objective DTLZ1 and WFG1 and test problems.

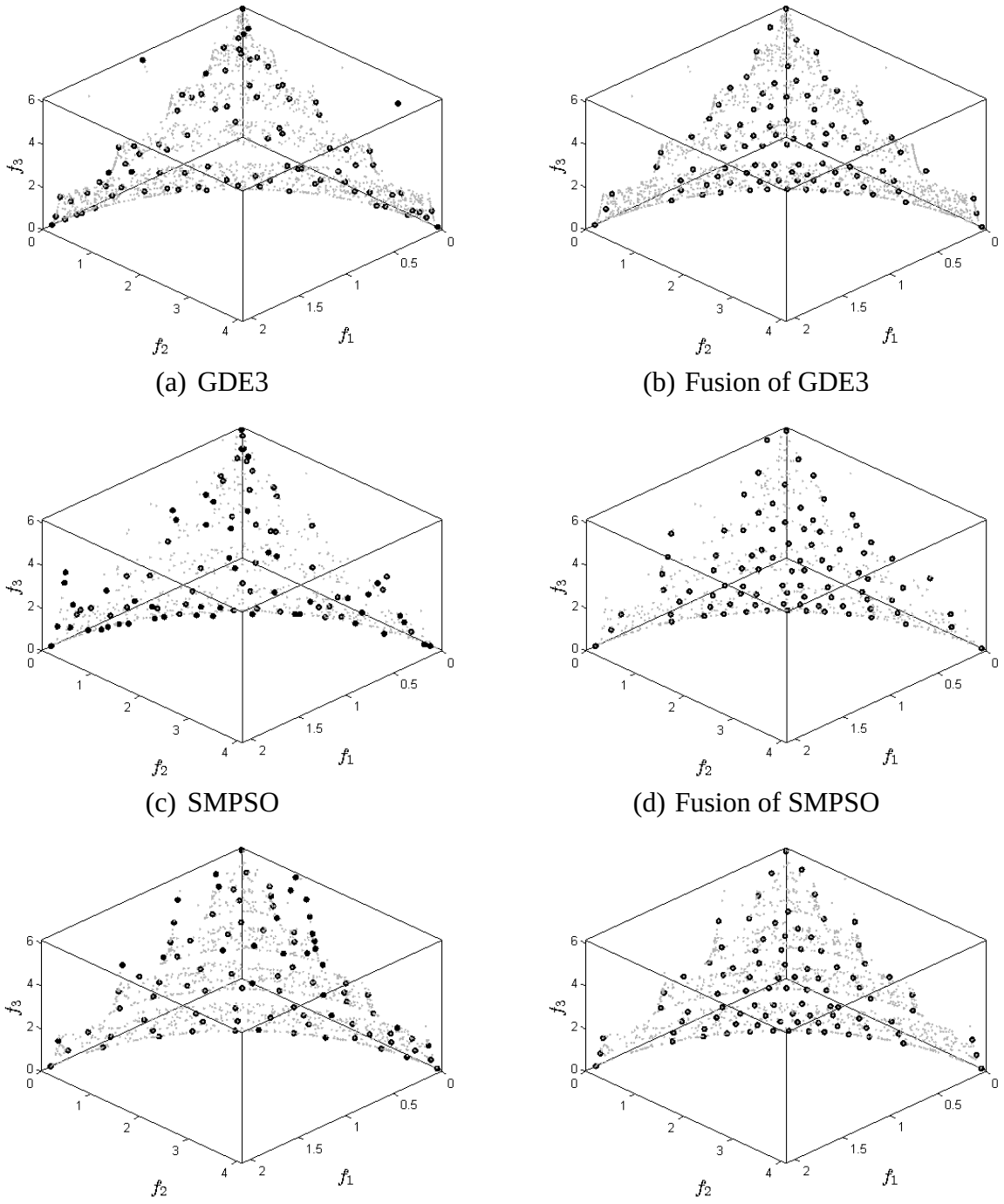

(a) GDE3 (b) Fusion of GDE3

(c) SMPSO (d) Fusion of SMPSO

(e) SPEA2 (f) Fusion of SPEA2

FIGURE 5-2 The trade-off plots of obtained solutions by the GDE3, SMPSO and SPEA2 algorithms for three-objective WFG1 test problem. The grey dotted background indicated the non-dominated solutions assembled during 20 runs of the GDE3 ((a) and (b)), SMPSO ((c) and (d)), and SPEA2. The black dots in (a), (c), and (e) indicate the best solution set obtained by each algorithm based on the IGD metric. The black dots in (b), (d), and (f) show well-distributed solutions extracted from the non-dominated solutions assembled in 20 runs of each algorithm.

The black dots in Figure 5-2 (a), (c), and (e) left plots illustrate the best solution set (based on the IGD metric) found by GDE, SMPSO, and SPEA2 in 20 runs for the 3-objective WFG1 test problem. From these plots, we can see that none of the algorithms is able to find well-converged and well-distributed solutions in a single run. However, when we consider all non-dominated solutions collected during 20 runs (grey dots) by each algorithm, we see that they are able to find "satisfactory" solutions on the Pareto-optimal front. This analysis indicate that the algorithms used in this experiment cannot consistently find well-distributed and well-converged solutions in 20 runs. This phenomenon is in agreement with the no-free-lunch theorem – which states, "for any algorithm, any elevated performance over one class of problems is offset by performance over another class".

The black dots in Figure 5-2 (b), (d) and (f) plots show well-distributed and well-converged solutions extracted using the FNFR method from the non-dominated solutions gathered by each algorithm during the 20 runs of the 3-objective WFG1 test problem. It can be seen that the FNFR method is an effective way of collecting and extracting well-distributed solutions after the optimization process is complete. We also observe that solutions extracted by the FNFR method is better than the best solution sets found by any of the algorithms in a single run. Moreover, Figure 5-3 shows trade-off plots of non-dominated solutions obtained by all algorithms for three-objective DTLZ1 and WFG1 test problems. The grey dotted background indicates the non-dominated solutions collected during 20 runs of GDE3, SMPSO, and SPEA2 algorithms. The black dots in these plots illustrate well-distributed solutions extracted from these solutions using the FNFR method. It can be observed that non-dominated solutions collected and extracted from several runs

of multiple algorithms have better coverage and accuracy than that of the solutions gathered by a single algorithm.

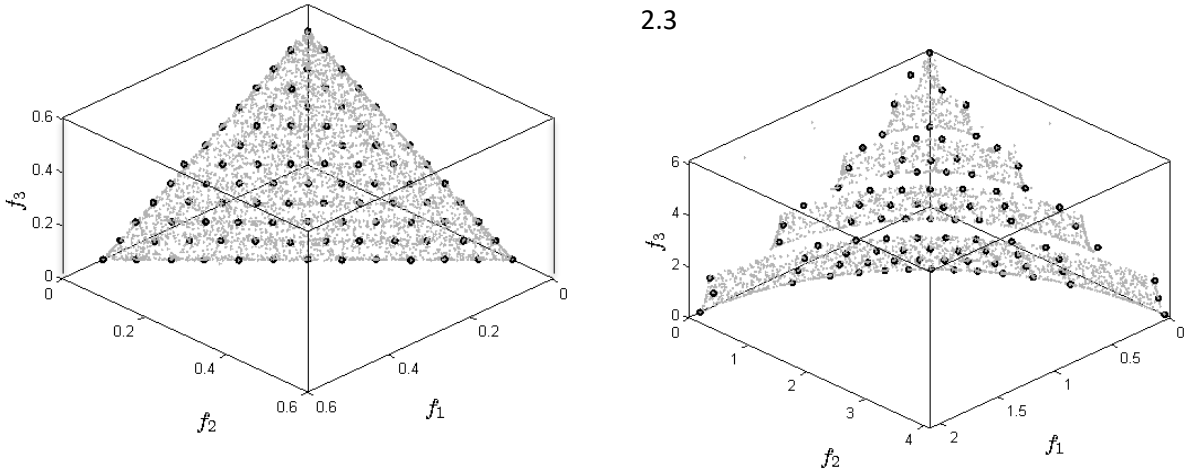

(a) DTLZ1 (b) WFG1

FIGURE 5-3 The trade-off plots of solutions obtained by all algorithms for three-objective DTLZ1 and WFG1 test problems. The grey dotted background indicates non-dominated solutions assembled during 20 runs of the GDE3, SMPSO, and SPEA2 algorithms and the black dots illustrate well-distributed solutions extracted from these solutions using the proposed FNFR scheme.

The 3D-RadVis plots in Figure 5-4 show the best non-dominated solutions obtained by GDE3, SMPSO, and SPEA2 algorithms for 5-objective convex DTLZ2 test problem. As it can be seen that as the number of objective functions increase the quality of solutions found by each algorithm start to degrade in terms of solution diversity and accuracy. However, in Figure 5-5, we see that these algorithms collectively are able to find well-distributed solutions on the entire Pareto-optimal front and we are able to extract uniformly distributed non-dominated solutions using the FNFR method among solutions gathered during 20 runs of multiple algorithms.

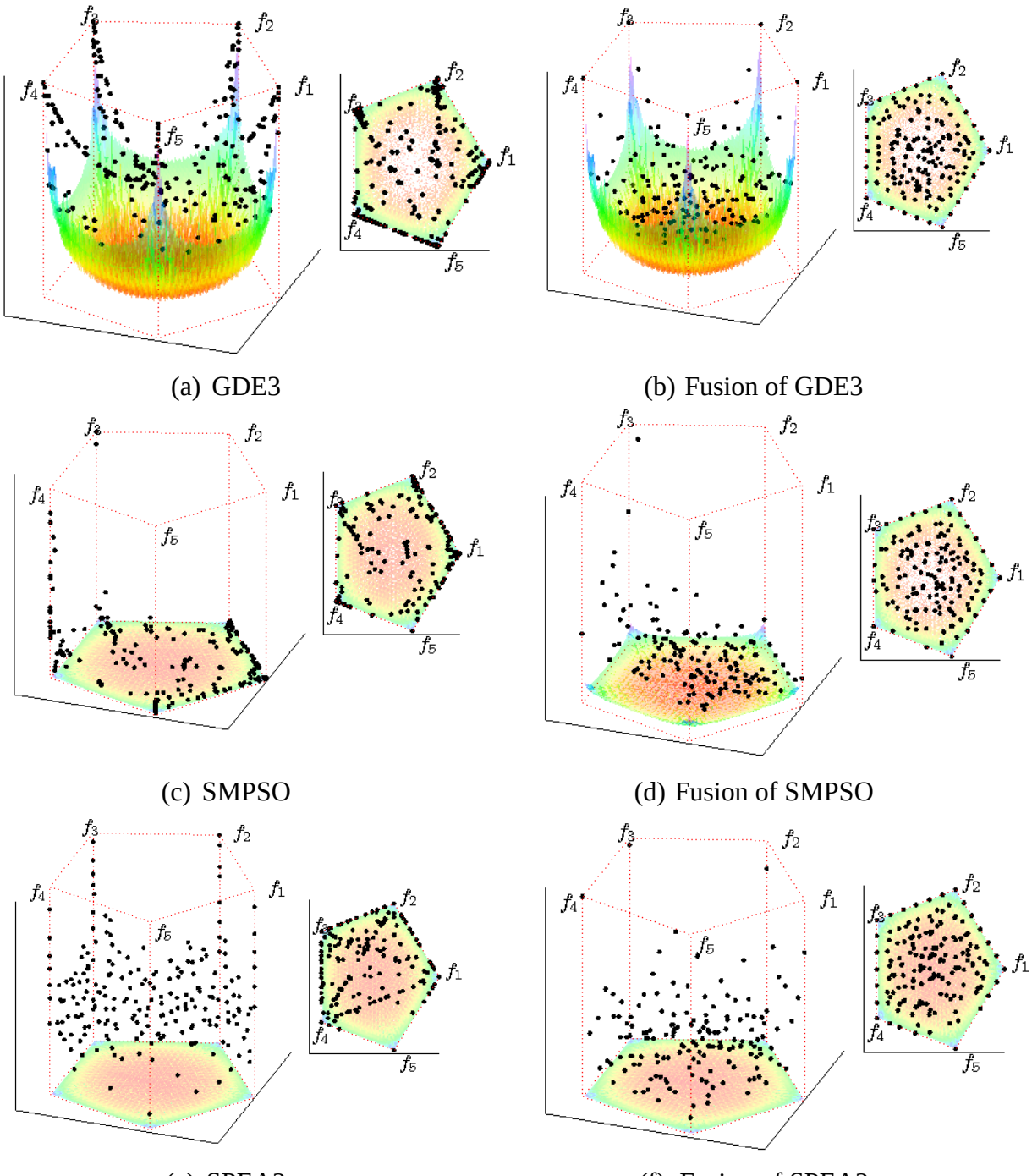

FIGURE 5-4 3D-RadVis plots of obtained solutions by GDE3, SMPSO and SPEA2 algorithms for five-objective convex DTLZ2 test problem. The surface for all plots are constructed from numerically generated Pareto-optimal front. The black dots from the top plots of (a), (b), and the left plot of (c) indicate the best set of solutions obtained by each algorithm based on the IGD metric. The black dots from the bottom plots of (a), (b), and the right plot of (c) show well-distributed solutions extracted using the proposed FNFR method.

5.3.4.2 Numerical Analysis of Solutions Obtained by each Algorithm Compared to the FNFR Method

Here, we investigate the performance of GDE3, SMPSO, and SPEA2 on seven benchmark test problems with 3-, 5-, 8-, and 10-objectives. Table provides 5.1 the best, median, worst IGD values for GDE3, SMPSO, and SPEA2 on 3- and 5-objective DTLZ1, convex DTLZ2 and WFG1 test problems in 20 runs. In all instances the solution set obtained through the FNFR method from each algorithm have better IGD values than the best IGD values attained by a single run. Moreover, the IGD value of the solution set extracted by the FNFR method from a large set of solutions collected during each algorithm's run is also better than the three above mentioned IGD values. The grey shade in Table 5.1 indicates the IGD values of solutions extracted by the FNFR method. When it comes to higher dimensional test problems, the FNFR scheme further proved its efficacy when comparing the IGD values of solutions extracted by the FNFR method against the best IGD values obtained by each algorithm in a single run.

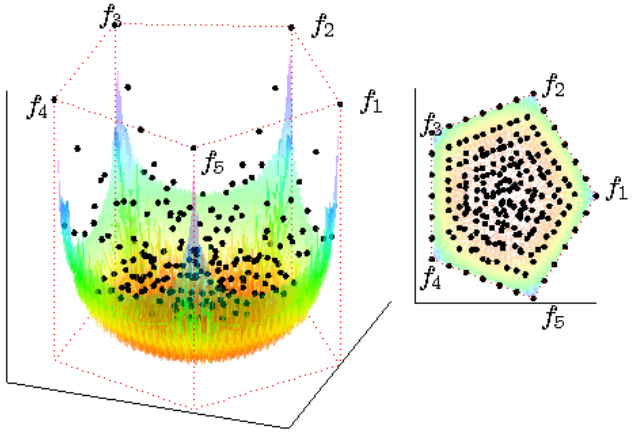

FIGURE 5-5 3D-RadVis plot of non-dominated solutions extracted using the proposed FNFR method. The black dots illustrate well-distributed solutions extracted using the proposed scheme from a large set of non-dominated solutions generated by the GDE3, SMPSO, and SPEA2 algorithms in 20 runs.

TABLE 5.1 Best, median, and worst IGD values for GDE3, SMPSO, and SPEA2 algorithms against the IGD value of solutions extracted by the FNFR method on 3- and 5-objective DTLZ1, convex DTLZ2, and WFG1 test problems.

	DTLZ1		Convex DTLZ2		WFG1	
M	3	5	3	5	3	5
Max Generation	400	600	400	600	400	600
GDE3 Best	7.43E-04	1.23E-03	7.09E-04	5.96E-04	1.23E-03	8.24E-04
GDE3 Median	8.10E-04	1.27E-03	7.70E-04	6.23E-04	1.40E-03	9.23E-04
GDE3 Worst	8.43E-03	1.31E-03	8.48E-04	7.09E-04	2.36E-03	1.26E-03
GDE3 FNFR	5.68E-04	9.27E-04	6.94E-04	4.96E-04	1.96E-04	7.49E-04
SMPSO Best	9.26E-04	2.21E-03	8.92E-04	1.29E-03	7.45E-03	6.04E-03
SMPSO Median	9.83E-04	2.48E-03	1.00E-03	1.83E-03	7.94E-03	6.44E-03
SMPSO Worst	1.05E-03	2.97E-03	1.15E-03	2.71E-03	8.11E-03	6.74E-03
SMPSO FNFR	6.99E-04	1.75E-03	8.27E-04	1.05E-03	6.41E-03	5.02E-03
SPEA2 Best	6.16E-04	2.23E-01	5.79E-04	2.19E-02	8.13E-04	7.48E-04
SPEA2 Median	6.35E-04	6.38E-01	6.03E-04	3.16E-02	1.04E-03	1.15E-03
SPEA2 Worst	6.90E-04	1.03E+00	6.39E-04	4.02E-02	3.56E-03	1.44E-03
SPEA2 FNFR	5.63E-04	2.23E-01	5.39E-04	2.48E-02	6.05E-04	8.21E-04
FNFR	4.54E-04	8.92E-04	7.00E-04	4.21E-04	1.42E-04	7.64E-04

TABLE 5.2 Best, median, and worst IGD values for GDE3, SMPSO, and SPEA2 algorithms against the IGD value of solutions extracted by the FNFR method on 8- and 10-objective DTLZ3, convex DTLZ4, and WFG2 test problems.

	DTLZ3		DTLZ4		WFG2	
M	**8**	**10**	**8**	**10**	**8**	**10**
GDE3 Best	1.26E-03	9.30E-04	2.83E-03	2.35E-03	2.23E-03	1.84E-03
GDE3 Median	2.95E-03	1.24E-03	2.97E-03	2.43E-03	2.64E-03	2.02E-03
GDE3 Worst	7.59E-03	1.42E-03	3.04E-03	2.53E-03	3.26E-03	2.24E-03
GDE3 Fusion	1.08E-03	7.10E-04	3.02E-03	2.40E-03	2.05E-03	1.71E-03
SMPSO Best	3.90E-03	1.11E-03	2.85E-03	2.59E-03	2.73E-03	1.97E-03
SMPSO Median	8.88E-03	2.05E-03	3.95E-03	2.85E-03	3.12E-03	2.18E-03
SMPSO Worst	8.77E-03	1.98E-03	3.67E-03	3.28E-03	2.42E-03	1.93E-03
SMPSO Fusion	3.77E-03	1.83E-03	3.01E-03	2.32E-03	2.55E-03	1.80E-03
Overall Fusion	3.34E-03	1.07E-03	1.99E-03	2.25E-03	2.09E-03	1.51E-03

Table 5.2 shows the best, median, and worst IGD values for GDE3 and SMPSO algorithms against the IGD value of a set solutions extracted by the FNFR method on 8- and 10-objective DTLZ3, convex DTLZ4, and WFG2 test problems.

5.3.4.3 Visual Analysis of Preferred Solutions Found by the FNFR Method

Here we investigate the effectiveness of the proposed FNFR method when dealing with extracting solutions close to preferred regions. In a practical multi- of many-objective optimization problems decision makers may be interested in visualizing (when possible) the entire Pareto-optimal front before selecting the one or more solutions for further investigation. In such a scenario, the FNFR scheme is an effective tool to construct the entire Pareto-optimal front and select Pareto-optimal points that are close to the supplied reference points. Figure 5-6 show preferred solutions extracted using the proposed FNFR method. The grey dotted background indicates non-dominated solutions obtained by the GDE3, SMPSO, and SPEA2 algorithms in 20 runs and the black dots illustrate preferred solutions extracted from these solutions using the proposed scheme.

5.4 Concluding Remarks

This chapter presented a novel hybridization of population-based metaheuristic algorithms called fusion of non-dominated fronts using reference points (FNFR) to gain combined benefit of several algorithms. The hybridization step in FNFR occurs after the completion of optimization process of multiple runs of several algorithms. In every run, FNFR assembles and constructs the entire Pareto-optimal from a large set of non-dominated solutions found using multiple algorithms. This step is crucial because no single algorithm is capable of producing well-distributed solutions for all types of problems all the time. Thereafter, FNFR uses predefined structured reference points or user selected reference points to extract preferred solutions from this set.

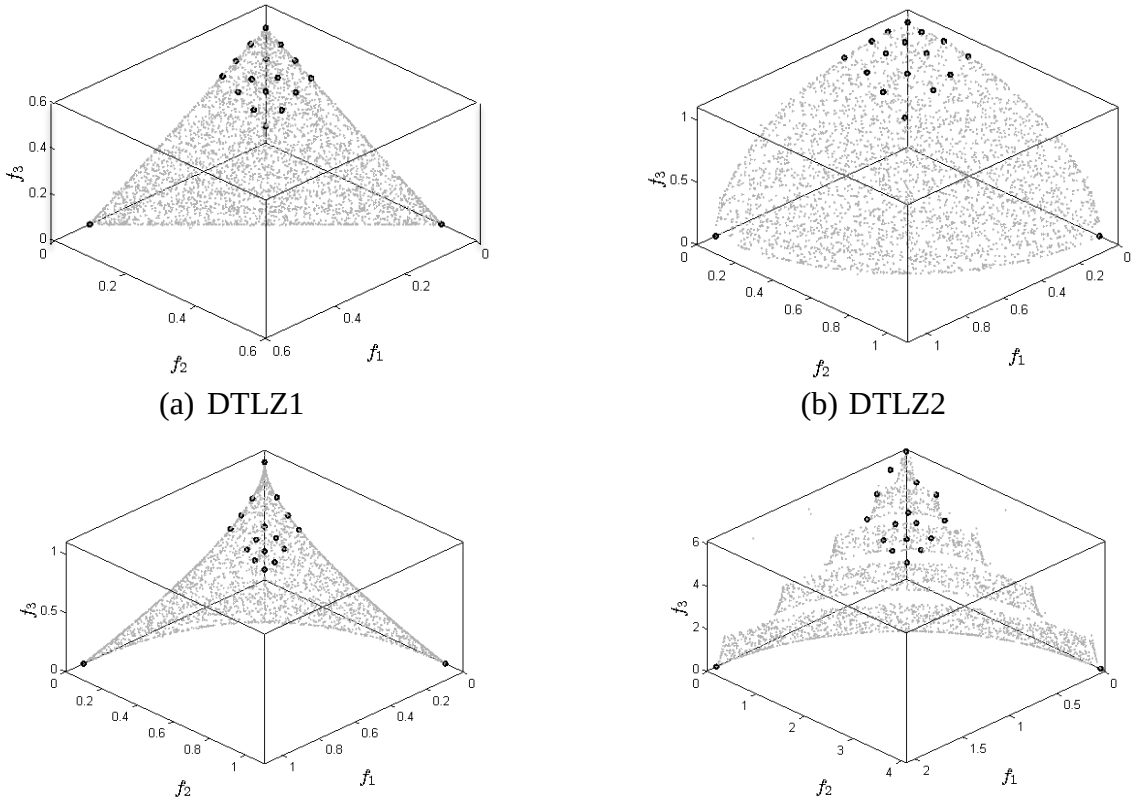

FIGURE 5-6 Preferred solutions extracted using the proposed FNFR method. The grey dotted background indicates non-dominated solutions obtained by the GDE3, SMPSO, and SPEA2 algorithms in 20 runs and the black dots illustrate preferred solutions extracted from these solutions using the proposed approach.

Experimental results showed the effectiveness of the proposed FNFR scheme with numerical experiments by considering three widely used optimization algorithms, GDE3, SMPSO, and SPEA2. The FNFR method is able to extract well-distributed solutions in a specific region of interest among thousands of non-dominated solutions collected after every run of multiple algorithms. Therefore, the FNFR scheme can effectively be used by decision makers to select and examine preferred solutions among a large set of solutions, which can be astronomically difficult to manage. In future, we would like to extend this study further by applying the FNFR scheme during the optimization process so that

preferred solutions can be extracted and inserted back to the current population to boost the search process.

Chapter 6

FUSION-BASED HYBRID MANY-OBJECTIVE OPTIMIZATION ALGORITHM

In the last three decades, there have been a number of efficient multi-objective optimization algorithms capable of solving real-world problems. However, due to the complexity of most real-world problems (high-dimensionality of problems, computational expense, and unknown function properties) researchers and decision makers are increasingly facing the challenge of selecting an optimization algorithm capable of solving their hard problems. This chapter proposes a simple yet efficient hybridization of multi- and many-objective optimization algorithms framework called hybrid many-objective optimization algorithm using the fusion of solutions obtained by several many-objective algorithms (Fusion) to gain the combined benefits of several algorithms and reducing the challenge of choosing one optimization algorithm to solve complex problems. During the optimization process, the Fusion framework (1) executes all optimization algorithms in parallel, (2) it combines solutions of these algorithms and extracts well-distributed solutions using predefined structured reference points or user-defined reference points, and (3) adaptively selects best-performing algorithm to tackle the problem at different stages of the search process. A case study of the Fusion framework by considering GDE3, SMPSO, and SPEA2 as multi-objective optimization algorithms is presented. Experimental results on five unconstrained and four constrained benchmark test problems with three to ten objectives show that the Fusion framework significantly outperforms all algorithms involved in the hybridization process as well as the NSGA-III algorithm in terms of diversity and convergence of obtained solutions. Furthermore, the proposed framework is consistently able to find accurate solutions for all test problems which can be interpreted as its high robustness characteristic.

6.1 Introduction

There have been numerous multi-objective algorithms that attempt to solve complex problems in the past thirty years. Nonetheless, researchers and decision makers are increasingly faced with the difficulty of choosing an appropriate algorithm capable of solving their problem in an effective manner due to a well-established "No-Free-Lunch" theorem [31]. This theorem stipulates that an algorithm that may have proven to give good performance on a particular class of problems may not provide the same level of performance on other classes of problems. Consequently, researchers shifted their focus instead to developing powerful algorithms that are more problem-specific or instance-specific. This task can be accomplished via the hybridization of optimization algorithms where new algorithms are developed by combining two optimization algorithms. Another way to accomplish this is by combining mathematical methods with an evolutionary optimization algorithm. Yet, another method incorporates evolutionary operators (selection, mutation, and crossover) into non-evolutionary optimization algorithms [92]. The expectation here is that hybridization combines the desirable properties of different approaches such that the hybrid algorithm exhibits improved exploration and exploitation capabilities.

For instance, a hybrid multi-objective evolutionary algorithm called HMOEA was proposed by Tan et a1. [101]. They utilized specialized genetic operators along with variable-length representation and a local search heuristic to find the Pareto-optimal routing solutions for the truck and trailer vehicle routing problem (TTVRP). Results from experiments showed that the HMOEA is effective in solving multi-objective and multi-modal combinatorial optimization problems. Xia and Wu [102] similarly proposed a hybrid

multi-objective algorithm by combining the PSO algorithm for its explorative power, and simulated annealing (SA) for its exploitations to solve the flexible job-shop scheduling problem (FJSP). A hybrid multi-objective algorithm based on the features of a biological immune system (IS) and bacterial optimization (BO) to find Pareto-optimal solutions for flow shop scheduling problem was proposed by Tavakkoli-Moghaddam et al. [103]. This particular algorithm uses the clonal selection principle in IS with highest affinity antibodies and criterion distinguishing between antigens and antibodies in BO for the Pareto dominance relationship among solutions. Also, Karthikeyan et al. [104] proposed a hybrid discrete firefly algorithm (HDFA) to solve the multi-objective FJSP problem. In this proposal, the discrete firefly algorithm and a local search (LS) method were combined to enhance the searching accuracy and information sharing among fireflies.

Another work by Wang et al. [96] proposed a hybrid evolutionary algorithm that is based on different crossover and mutation strategies along with an adaptive constrained-handling technique to deal with numerical and engineering constrained optimization problems. A hybrid and adaptive co-evolutionary optimization method that can efficiently solve a wide range of multi-objective optimization problems was proposed by Zăvoianu et al. [97]. This particular approach combines Pareto-based selection for survival, differential evolution's crossover and mutation operators, and decomposition-based strategies. An ensemble strategy was recently proposed to benefit from both the availability of diverse approaches and to overcome difficulties associated with fine tuning associated parameters. Such work includes ensemble of the ε parameter values and an ensemble of external archives in a multi-objective PSO algorithm [98], constraint handling methods to tackle constrained multi-objective optimization problems [98], and the various neighborhood

sizes in multi-objective evolutionary algorithm based on decomposition (MOEA/D) with online self-adaptation [100]. Other notable hybridization of selection mechanisms include selection hyper-heuristics (mixing selection, mutation operators and accepting strategies) [110] and bi-criterion evolution (hybridization of Pareto-based and non-Pareto-based selection criterions) [110].

A hybrid population-based algorithm, called PSOGSA, was proposed by Mirjalili and Hashim [93] by combining Particle Swarm Optimization (PSO) and the Gravitational Search Algorithm (GSA). The aim of the algorithm was the integration of the exploitation ability of PSO with the exploration ability of GSA to synthesize the strengths of both algorithms. Also, El-hossini et al. [94] proposed three hybrid algorithms that are based on the strength Pareto evolutionary algorithm 2 (SPEA2) and the PSO to solve multi-objective optimization problems. These algorithms use strength Pareto fitness assignment to maintain an external archive. The three algorithms are developed by alternating the evolutionary and PSO processes in a different order. Results showed that the proposed hybrid PSO algorithms have a comparable performance to SPEA2. Furthermore, Tang and Wang [95] proposed a novel hybrid multi-objective evolutionary algorithm (HMOEA) for real-valued multi-objective problems via incorporating the concepts of personal best and global best in PSO and evolutionary operators (i.e., multiple crossovers) to improve the robustness of evolutionary algorithms to solve different kinds of optimization problems.

In an effort to develop a powerful general-purpose hybridization framework, this chapter presents a novel hybridization of population-based multi- or many-objective optimization algorithms called hybrid many-objective algorithm using Fusion of solutions from multiple algorithms to gain the combined benefits of several multi-objective

optimization algorithms (MOOAs). Unlike other hybridization methods discussed above [93-104, 111], the main features of the proposed framework are as follows:

1) The Fusion framework allows users to select and include multiple optimization algorithms in the search process with highest flexibility
2) The parallel execution of multiple algorithms using the same population to determine best performing algorithms at every stage of the search process.
3) Since reference-point-based selection mechanism is utilized, Fusion maintains the diversity of solutions.
4) In the serial execution stage of the Fusion framework, best performing algorithms are given the chance to run independently and continue generating improved candidate solutions.
5) In the Fusion framework, several algorithms can be used without the need of extra parameter tuning so several optimization algorithms can be hybridized with minimal effort.

6.2 Proposed Fusion Framework

In this section, we present a novel hybridization technique called hybridization of multi- and many-objective optimization algorithms framework (called Hybrid Many-Objective Algorithm Using Fusion of Solutions from Several Many-Objective Algorithms) to gain the combined benefits of several algorithms and reducing the challenge of choosing one optimization algorithm to solve complex problems. The Fusion framework contains four modules and Figure 6-1 shows an overall flowchart of the framework.

6.2.1 Module 1: Initialization and Parameter Settings

In this module, multi-objective algorithms (Alg_1, Alg_2,…,Alg_n) with distinctive characteristics, which are suitable for solving the problem, are selected. For example, one can select an algorithm known for its diversity-preserving mechanism, and another known for its convergence ability, and another which is capable of maintaining good spread. Next, all parameters' settings required by each algorithm are set. Finally, the initial N random individuals for population (P_0) are created and objective functions, constraint functions and overall constraint violation for each solution are evaluated.

6.2.2 Module 2: Parallel Execution of all Algorithms

In this module, each algorithm involved in the Fusion framework is provided with the current population (P_0) and in turn generates a new population $\left(P_{Alg_i}\right)$, where $i = 1 \ldots n$, according to Alg_i procedures. Thereafter, each algorithm combines P_0 and P_{Alg_i} and selects the best N candidate solutions according to their selection mechanism. If any algorithm involved in this framework employs an external archive, then the archive is consolidated based on the new candidate solutions generated by the algorithm. Moreover, if the total number of function calls exceed the maximum number of function calls during parallel execution of algorithms, the process terminates and P_0 is reported. It is worth mentioning here that since all algorithms are supplied with the same population to generate and select a new population based on their mechanism, promising algorithms can adaptively be selected and used to generate improved candidate solutions in subsequent stages of the search process. In Module 3, we describe the steps used in identifying the best performing algorithms in each stage.

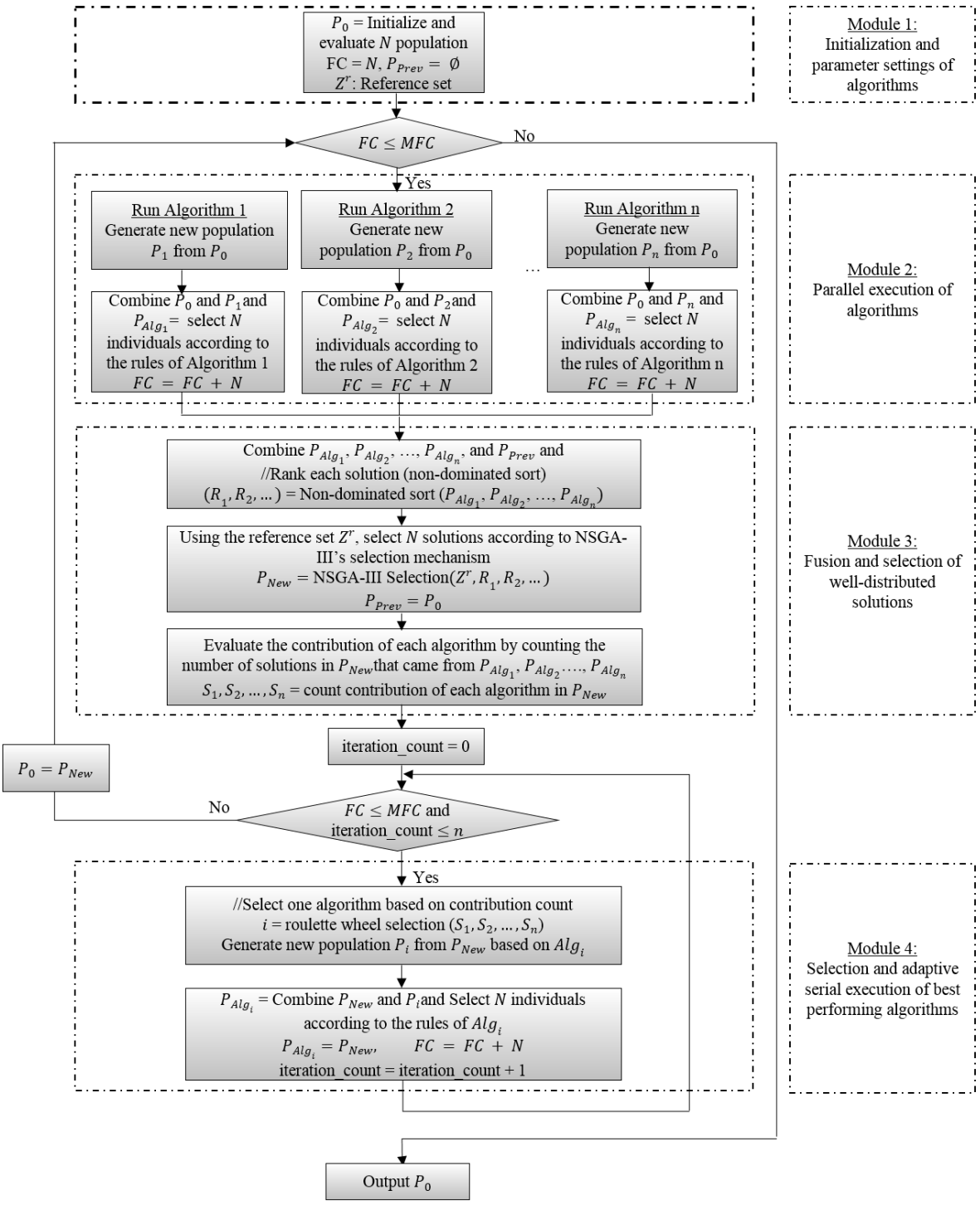

FIGURE 6-1 Flowchart illustrating hybridization of MOEAs using the fusion of solutions of several MOEAs, where FC is the number of function calls and MFC is the maximum number of function calls .

6.2.3 Module 3: Fusion and Selection of Best Solutions

In this module, first solutions obtained by Alg_1 to Alg_n are combined ($P_{Alg_i} \cup P_{Alg_i} \ldots P_{Alg_n}$) and sorted according to different non-domination levels (R_1, R_2,..). Second, all the solutions from each domination level are accepted one-by-one to construct elite population (P_{New}) until the size is equal to N. If the number of candidate solutions in the last domination level to be entered is greater than N, then the remaining solutions are selected based on NSGA-III's selection mechanism [112, 113]; which is a reference-point-based non-dominated sorting selection mechanism. Once the new population P_{New} reaches N, then, the contribution of each algorithm is evaluated by counting the number of solutions in P_{New} which came from each algorithm. By this way, the most suitable algorithm at the current search stage is identified. As a result: 1) well-distributed set of solutions at the current stage of the search process are selected, and 2) the contribution of each algorithm at the current stage are determined.

6.2.4 Module 4: Adaptive Serial Executions

After determining the contribution of each algorithm, we need to select the best performing algorithm to run for the next n iterations, where n is the number of algorithms involved in the Fusion framework. This way, algorithms performing well in the current stage have a higher chance to continue the search process independently so that they generate promising candidate solutions during subsequent generations. In this module, we utilize a roulette wheel-based selection mechanism according to each algorithm's contribution count. Then, the selected algorithm is given the chance to generate current population P_{Alg_i} from the population P_{New}. This current population is in turn combined with P_{New}, N candidate

solutions are then selected based on the algorithm's procedures and rules. This process is repeated n times so that highly performing algorithms have greater chance to be selected and to generate improved candidate solutions. Once this step is done, Modules 2 to 4 are repeated until the termination criteria is met.

6.2.5 Fusion for Bi-objective Problems

Many of the reference-based algorithms such as NSGA-III and MOEA/D primarily designed to solve many-objective (three or more) problems. This is because structured reference points can maintain the diversity of solutions through association of solutions to each reference point. Since reference-based algorithms are not proven two work well for bi-objective problems, we discuss how the proposed Fusion algorithm can be modified to solve problems composed of two objectives. Before we present the modified Fusion section mechanism, first we show the weakness of NSGA-III's selection mechanism when the problem is bi-objective.

Consider a solution set obtained by $Alg_1$to Alg_n $(P_{Alg_i} \cup P_{Alg_i} \dots P_{Alg_n})$ depicted in Figure 6-2 (a). Let us assume we need ten solutions to be selected and move to the next round. If the selection mechanism is NSGA-III's, then we first construct ten reference points in a normalized plane (see Figure 6-2 (b)). Thereafter, each solution is associated with a reference point that has the shortest perpendicular distance to the line constructed by joining the reference points to the origin. Finally, niching is applied to select ten solutions that are associated with the least represented reference points. As it can be seen from Figure 6-2 (a) due to the shape of the PF, the ten selected solutions using NSGA-III's

selection mechanism are widely dispersed leaving the two end regions of the PF unrepresented.

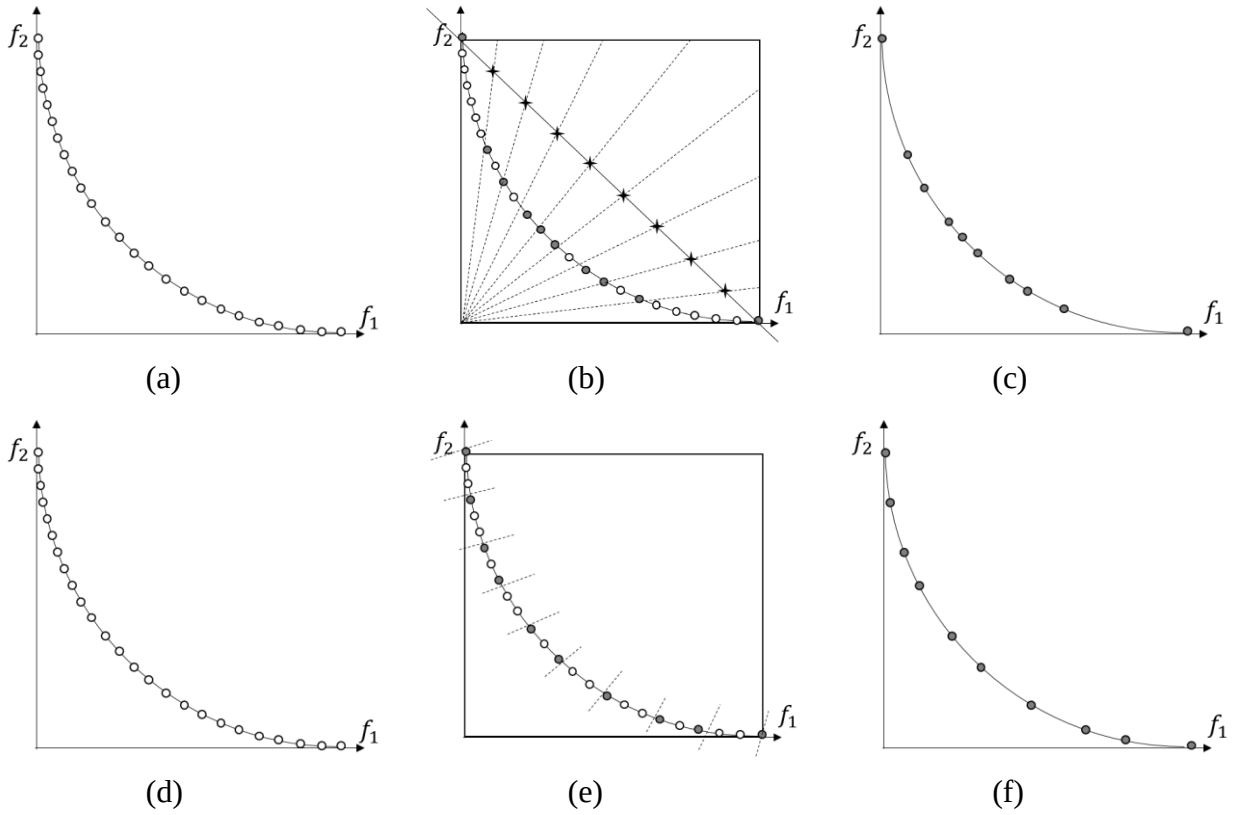

FIGURE 6-2 Selection procedure in NSGA-III and Fusion. (a) and (e) Bi-objective problem with 25 non-dominated solutions. (b) Ten structured reference points in a normalized reference line. (c) Ten solutions selected by NSGA-III's selection procedure. (e) Ten sturctured reference points on Pareto curve. (f) Ten solutions selected by the Fusion selection procedure.

Now, we present a novel selection mechanism for Fusion when the problem is bi-objective. In the Fusion algorithm, the niching strategy remains the same (i.e. NSGA-III's niching strategy), however the reference line creation and solution association is modified. Consider a set of solutions obtained by $Alg_1$to Alg_n ($F_t = P_{Alg_i} \cup P_{Alg_i} \dots P_{Alg_n}$) and we would like to select $popSize$ solutions (F_{t+1}) from F_t. First, F_t is sorted according to different non-domination levels ($R_1, R_2 \dots$). If the number of solutions in the first rank is

less than or equal to the required number of solutions ($popSize$), then NSGA-II's section is utilized to select $popSize$ solutions. However, if the number solutions in R_1 is greater than the $popSize$, then the solutions in R_1 are first sorted by their objective value. Thereafter, the geodesic distance between consecutive solutions are computed (E_d). These distances are then used to compute the cumulative distances starting from the first solution in the sorted list (cum_d). The cumulative distance for the first solution is set to zero and the remaining cumulative distances computed based on previously computed cumulative distance distances (e.g. the i^{th} cumulative distance is computed as the sum of cum_d ($i^{th} - 1$) and geodesic distance between the ($i - 1$) solution and the i^{th} solution. Note that the last cumulative distance will be the sum of geodesic distances starting from the first solution to the last solution. Next, the cumulative distances are normalized so that they have values in the range 0 to 1. One dimensional reference points (Z^r) are then constructed based on the required number of solutions in the range 0 and 1. For example, if we need $popSize$ number of solutions then we create reference points every $\frac{1}{popSize\ -1}$ starting from 0 ending at 1 $\left(Z^r = \{0, \frac{1}{popSize-1}, \frac{2}{popSize-1}, \dots, 1\}\right)$. Finally, $popSize$ solutions are selected using NSGA-III's niching strategy where solution associations are determined by the closest normalized cumulative value to the reference point. Figure 6-2 (d) – (f) illustrates the proposed selection mechanism where reasonably well-distributed solutions are selected despite the convexity of the PF. Algorithm 6.1 details the selection mechanism used in the Fusion algorithm when the problem is bi-objective. Chapters 8 and 9 investigate the efficacy of the proposed method when solving real-world bi-objective optimization problems.

Algorithm 6.1 Population Selection Procedure

Input: F_t: $N \times M$ (current population), popSize: Number of solutions to be selected

Output: F_{t+1} :popSize$\times M$ (Next population)

1: $(R_1, R_2 \ldots)$ = Non_Dminated_Sort(F_t)
2: **If** size(R_1) <= popSize **Then**
3: F_{t+1} = NSGAII_Selection(F_t)
4: **Else**
5: S = Sort(R_1)
// Compute distances between consecutive two points
6: $E\_d_1 = 0$
7: **For** $i = 2$ to size(S)
8: E_d_i = Euclidian_Distance(S_{i-1} ,S_i)
9: **End for**
10: **End if**
//Compute cumulative distances
11: $cum\_d_1 = 0$
12: **For** $i = 2$ to size(S)
13: $cum\_d_i = cum\_d_{i-1} + E\_d_i$
14: **End for**
//Normalize cumulative distances
15: $d_{Total} = cum\_d_{Last}$
16: **For** $i = 1$ to size(S)
17: $cum\_d_i = cum\_d_{i-1} + d_i$
18: **End for**
//Create reference points
19: $div = popSize - 1$
20: Z^r: $0, \frac{1}{div}, \frac{2}{div}, \frac{3}{div}, \ldots, 1$
//Associate cum_d to Z^r
21: **For** $i = 1$ to size(cum_d)
22: **For** $j = 1$ to size(Z^r)
23: $d_r(i,j) = abs(cum\_d_i - Z_i^r)$
24: **End for**
25: $[loc, dist] = min(d_r(i,:))$
26: Associate $\pi(loc).add(S_i)$
27: Assign $d(loc).add(dist)$
28: **End for**
29: F_{t+1} = NSGAIII_Niching(π, d, S, popSize)

6.3 Experimental Setup and Results

This section presents the algorithms used in the Fusion hybridization framework, parameter settings, and simulation results on 3- to 10- objective benchmark test problems.

6.3.1 Utilized Algorithms

In order to assess the search capability of the proposed Fusion framework, we have utilized three MOOAs that have considerable differences in their fitness assignment and diversity mechanism to gain the combined benefits of these algorithms during the search process. These MOOAs are the Generalized Differential Evolution Generation 3 (GDE3) [106], Speed-constrained Multi-objective Particle Swarm Optimization (SMPSO) [107], and the Strength Pareto Evolutionary Algorithm 2 (SPEA2) [39]. GDE3 uses a growing population and non-dominated sorting with pruning of non-dominated solutions to decrease the population size at the end of each generation. This mechanism improves the diversity of obtained solutions. On the other hand, since SMPSO mimics the social behaviour of birds flocking to find food, particles move in the search space in a cooperative manner where movements are performed by the velocity operator. The velocity operator is guided by a local and a social behaviour of swarm. SPEA2 maintains an external archive according to each individual's strength by counting the number of individuals that dominate it as well as the number of individuals by which it is dominated. Moreover, SPEA2 uses a nearest neighbor density estimation method to guide the search process efficiently and it preserves boundary solutions. All these three algorithms are well-known and commonly used ones.

Since our method uses structured reference points similar to the NSGA-III algorithm to maintain the distribution of solutions during the search process, we compare our proposed method with the NSGA-III algorithm.

TABLE 6.1 Benchmark test problems

Problem	Characteristics
DTLZ1	Unconstrained, linear
DTLZ2	Unconstrained, concave
Convex DTLZ2	Unconstrained, convex
DTLZ3	Unconstrained, concave, multimodal
DTLZ4	Unconstrained, concave, biased
C1-DTLZ1	Constrained, linear, has barrier created by constraints
C1-DTLZ3	Constrained, concave, multimodal, has large barrier created by constraints
C3-DTLZ1	Constrained, linear, the Pareto-optimal front moved to the added constraint surface
C3-DTLZ4	Constrained, concave, biased, the Pareto-optimal front moved to the added constraint surface

6.3.2 Test Problems

In order to test the quality of the proposed algorithm, we have used five unconstrained and four constrained many-objective benchmark test problems. The first sets of these test problems are the DTLZ (DTLZ1 – DTLZ4, Convex DTLZ2) family of test problems. The number of variables for these test problems are $(M + k - 1)$, where M is the number of objectives and $k = 5$ for DTLZ1, while $k = 10$ for DTLZ2, DTLZ3, DTLZ4, and Convex DTLZ2. The corresponding Pareto-optimal fronts lie in $f_i \in [0, 0.5]$ for the DTLZ1 problem and in $f_i \in [0, 1]$ for other DTLZ problems. The summary of the DTLZ problem characteristics is shown in Table 6.1.

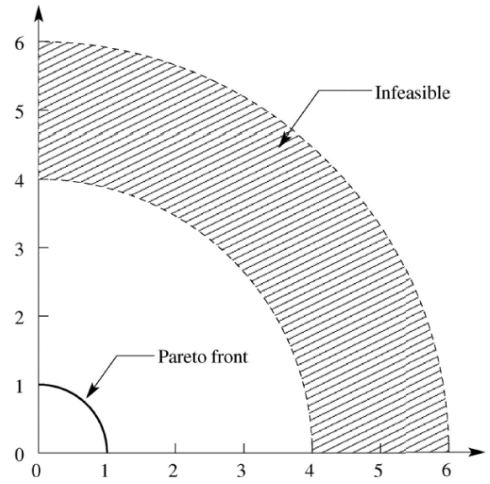

FIGURE 6-3 Two-objective version of the C1-DTLZ3 problem [112].

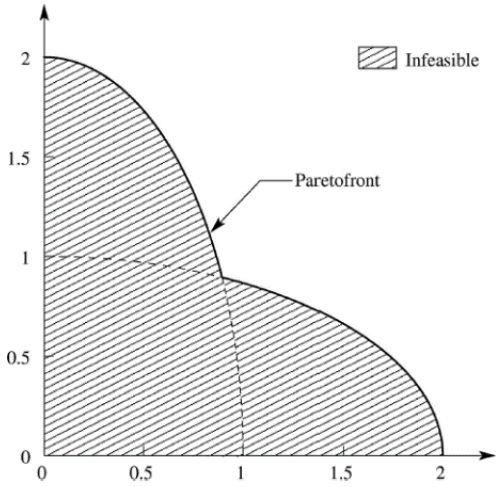

FIGURE 6-4 Two-objective version of the C3-DTLZ4 problem [112].

The second set of test problems utilized in this study are the four constrained versions of the DTLZ family test problems: Type-1 and Type-3. The Type-1 (C1-DTLZ1 and C2-DTLZ3) constrained problems contain the original DTLZ1 and DTLZ3 test problems. However, two constraints are added to create a barrier in approaching the original Pareto-optimal front. The C1-DTLZ1 test problem has a narrow feasible region surrounded by the infeasible region and this introduces a minor difficulty for optimizers to converge to the true Pareto-optimal front. The C1-DTLZ3 introduces a band of infeasible

region adjacent to the Pareto-optimal front. This creates the highest level of difficulty for optimizers to converge to the true Pareto-optimal front as they need to penetrate the band of the infeasible region when they travel from feasible to infeasible then to feasible region. The summary of the Type-1 problem characteristics is shown in Table 6.1. Figure 6-3 illustrates the feasible and the Pareto-optimal front of two-objective C1-DTLZ3 problems.

The Type-3 (C3-DTLZ1 and C3-DTLZ4) constrained problems contain the original DTZL1 and DTLZ4 test problems. However, M constraints are added to original problems so that the original Pareto-optimal front is no longer optimal. Instead, the new Pareto-optimal front is created by portions of constraint surfaces. These problems are deigned to assess the optimizers' ability to stay on the newly created Pareto-optimal surface. The summary of the Type-3 problem characteristics is shown in Table 6.1. Figure 6-4 illustrates the feasible and the Pareto-optimal front of two-objective C3-DTLZ4 problems.

6.3.3 Parameter and Experimental Settings

The GDE3 algorithm has two control parameters: mutation amplification factor (F) and crossover rate (CR). The SMPSO algorithm has three parameters: archive size, polynomial mutation (p_m), and mutation distribution index (η_m). The NSGA-III algorithm has four control parameters: SBX probability, polynomial mutation, crossover distribution index, and mutation distribution index. In addition to the NSGA-III control parameters, SPEA2 has archive size parameter. In order to maintain a consistent and fair comparison, the parameter settings for all algorithms including the Fusion framework are kept the same as the original studies of each algorithm.

Table 6.2 presents parameter settings used by GDE3, SMPSO, SPEA2, and NSGA-III algorithms. Furthermore, since the Fusion framework as well as the NSGA-III algorithm requires predetermined reference points to maintain the diversity of solutions, we have used the same setting reported in the original NSGA-III studies [112]. Table 6.3 shows the number of reference points (H), the population size (N), and the number of inner and outer divisions used for different dimensions of test problems.

TABLE 6.2 GDE3, SMPSO, SPEA2, and NSGA-III parameter settings. n is the number of variables and $|P|$ is the population size.

GDE3	
Mutation probability (F)	0.1
Crossover probability (CR)	0.5
SMPSO	
Archive size	$\|P\|$
Polynomial mutation (p_m)	$1/n$
Mutation Distribution Index (η_m)	20
SPEA2	
Archive size	$\|P\|$
SBX probability (p_c)	0.9
Polynomial mutation (p_m)	$1/n$
Crossover Distribution Index (η_c)	20
Mutation Distribution Index (η_m)	20
NSGA-III	
SBX probability (p_c)	1.0
Polynomial mutation (p_m)	$1/n$
Crossover Distribution Index (η_c)	30
Mutation Distribution Index (η_m)	20

TABLE 6.3 Number of reference points and population sizes used in NSGA-III and EliteNSGA-III algorithms.

Number of Objectives (M)	Divisions		Reference Points (H)	Population Size (N)
	Outer	Inner		
3	12	0	91	92
5	6	0	210	212
8	3	2	156	156
10	3	2	275	276

To evaluate the performance of the proposed algorithm, we have used the inverse generational distance (IGD) metric, which is capable of measuring the convergence and the diversity of the obtained Pareto-optimal solutions at the same time. The IGD measure has been predominantly used to evaluate the performance of evolutionary many-objective problems [107, 112]. The IGD metric measures the distances between each solution composing the Pareto-optimal front and the obtained solution. In this study, the reference PF is constructed by joining all results of all the executions and then selecting the non-dominated solutions. Furthermore, all algorithms were executed 20 times independently and the best, the worst, the median, and the average results of each algorithm is recorded. Additionally, the Wilcoxon's signed rank statistical test is conducted at a 5% significance level in order to evaluate the statistical significance of obtained results.

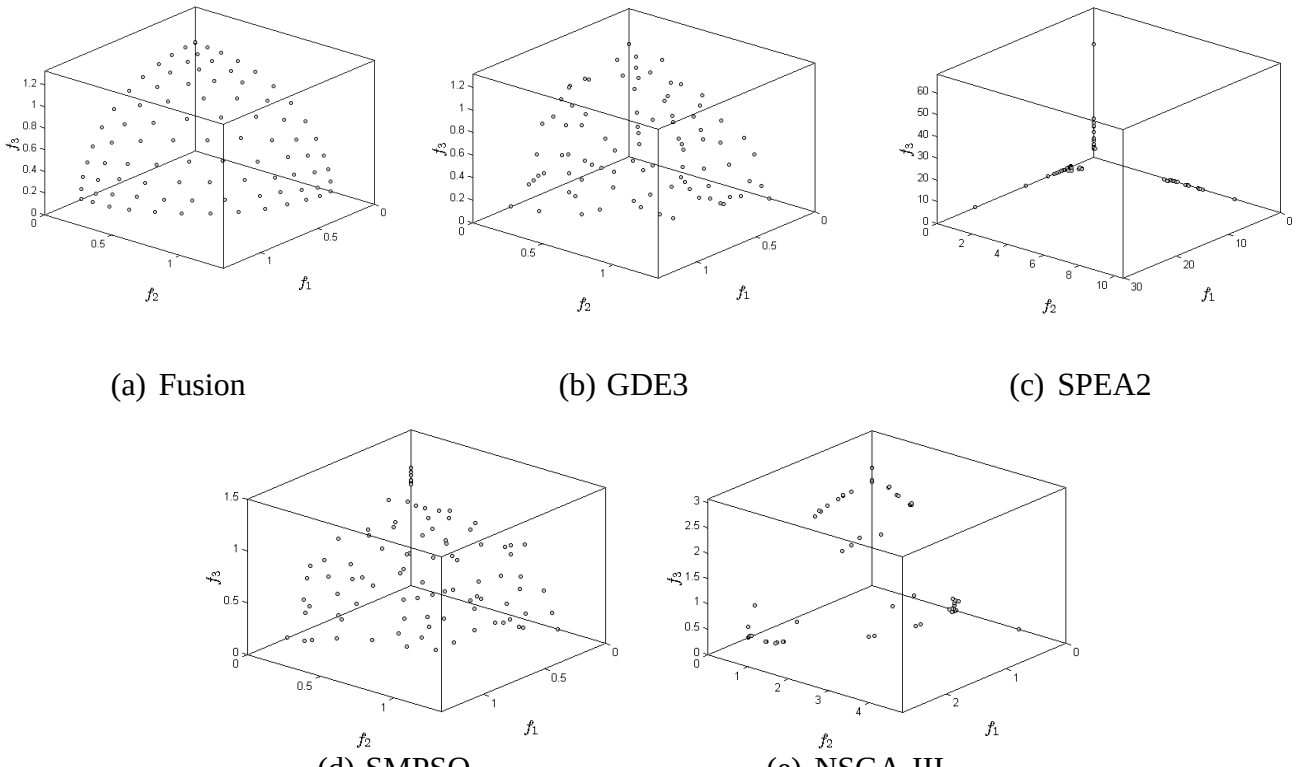

FIGURE 6-5 The trade-off plots of obtained solutions by Fusion, GDE3, SPEA2, SMPSO and NSGA-III algorithms for three-objective DTLZ3 test problem.

6.3.4 Experimental Results and Discussion

To evaluate the performance of the proposed algorithm, we have conducted two sets of experiments on constrained and unconstrained DTLZ family test problems containing three- to ten objectives. The first experiment investigates the performance of the proposed Fusion framework on unconstrained test problems with varying Pareto-optimal front shapes. The second experiment investigates how the proposed framework copes with constrained problems containing barriers in approaching the Pareto-optimal front and its ability tackle problems with their Pareto-optimal surface is created by portions of added constrained surface.

6.3.4.1 Unconstrained Problems

The first experiment investigates the performance of Fusion on problems with linear or concave Pareto- optimal fronts for three- to ten- objectives DTLZ1, DTLZ3 and DTLZ4 problems. Figure 6-5 shows the obtained PFs by Fusion, GDE3, SPEA2, SMPSO, and NSGA-III for the three-objective DTLZ3 test problem after 250 generations (250×92 function calls). It is evident from these diagrams that Fusion is able to find well-distributed solutions on the Pareto-optimal front. Table 6.4 provides the best, median, worst, and average IGD values of all algorithms for the above-mentioned test problems. From this, we can see that the performance of Fusion is significantly better than not only the algorithms involved in the hybridization process but also NSGA-III for almost all experiments conducted in this section.

TABLE 6.4 Best, median, worst, and average IGD values for Fusion, GDE3, SPEA2, SMPSO and NSGA-III on M-objective DTLZ1, DTLZ3, and DTLZ4 problems. Best performed algorithm is shown in dark gray and second best is shown light gray. * indicates a significance level of 0.05 between the top two algorithms.

Problem	M	MFC	Fusion	GDE3	SPEA2	SMPSO	NSGA-III
DTLZ1	3	250 x 92	4.99E-04	8.01E-04	7.14E-04	9.08E-04	5.14E-04
			5.02E-04	8.31E-04	8.80E-04	9.89E-04	6.82E-04
			5.13E-04	8.64E-03	2.18E-03	1.10E-03	8.64E-03
			5.03E-04*	1.62E-03	1.02E-03	9.91E-04	1.17E-03
	5	450 x 212	6.36E-04	1.14E-03	1.67E-01	2.08E-03	6.39E-04
			6.42E-04	1.16E-03	4.23E-01	2.26E-03	6.89E-04
			6.55E-04	1.22E-03	5.84E-01	2.70E-03	1.25E-03
			6.43E-04*	1.17E-03	4.00E-01	2.32E-03	7.71E-04
	8	700 x 156	1.32E-03	5.72E-03	1.76E+00	5.56E-03	1.23E-03
			1.36E-03	6.72E-03	4.06E+00	8.55E-03	1.56E-03
			1.52E-03	9.49E-03	5.99E+00	2.04E-01	2.46E-03
			1.37E-03*	6.81E-03	4.07E+00	2.24E-02	1.69E-03
	10	1000 x 276	9.71E-04	5.24E-03	2.20E+00	4.66E-03	8.21E-04
			1.05E-03	5.90E-03	3.53E+00	9.75E-03	9.68E-04
			1.23E-03	7.57E-03	4.36E+00	1.70E-01	1.81E-03
			1.06E-03	6.00E-03	3.40E+00	2.81E-02	1.11E-03
DTLZ3	3	250 x 92	3.47E-04	1.71E-03	5.03E-02	1.03E-03	7.95E-03
			5.18E-04	1.77E-03	1.91E-01	1.45E-03	5.09E-02
			6.83E-04	3.47E-02	3.06E-01	7.75E-03	1.55E-01
			4.95E-04*	7.05E-03	1.19E-01	3.13E-03	5.14E-02
	5	450 x 212	8.25E-04	9.13E-04	1.11E-02	2.36E-03	8.39E-04
			8.34E-04	9.72E-04	3.07E-02	3.29E-03	1.08E-03
			8.49E-04	1.02E-03	5.42E-02	4.18E-03	1.61E-03
			8.34E-04*	9.69E-04	3.06E-02	3.31E-03	1.10E-03
	8	700 x 156	1.19E-03	4.94E-03	2.47E-02	7.26E-03	1.81E-03
			1.54E-03	7.01E-03	4.02E-02	9.28E-03	1.88E-03
			1.80E-03	8.81E-03	2.86E-01	9.38E-03	4.04E-03
			1.55E-03*	7.11E-03	7.18E-02	9.09E-03	2.10E-03
	10	1000 x 276	1.10E-03	4.39E-03	1.54E-02	3.87E-03	1.68E-03
			1.63E-03	5.40E-03	2.69E-02	5.65E-03	1.71E-03
			2.14E-03	5.53E-03	2.20E-01	5.69E-03	1.74E-03
			1.61E-03	5.23E-03	4.10E-02	5.46E-03	1.71E-03
DTLZ4	3	400 x 92	5.58E-04	8.90E-04	7.32E-04	9.91E-04	5.57E-04
			5.60E-04	9.80E-04	7.59E-04	1.04E-03	5.61E-04
			5.63E-04	8.42E-03	8.42E-03	1.54E-03	1.27E-02
			5.60E-04*	1.35E-03	3.36E-03	1.08E-03	1.17E-03
	5	700 x 212	9.15E-04	1.42E-03	1.79E-03	1.77E-03	9.12E-04
			9.19E-04	1.46E-03	2.00E-03	2.29E-03	9.15E-04
			1.10E-03	1.50E-03	3.43E-03	2.67E-03	9.23E-04
			9.28E-04	1.46E-03	2.08E-03	2.30E-03	9.16E-04
	8	1100 x 156	1.89E-03	2.65E-03	8.97E-03	3.39E-03	1.86E-03
			1.91E-03	2.80E-03	9.19E-03	3.67E-03	1.89E-03
			1.94E-03	2.95E-03	9.38E-03	4.11E-03	2.02E-03
			1.91E-03	2.81E-03	9.18E-03	3.69E-03	1.90E-03
	10	1500 x 276	1.72E-03	2.09E-03	6.24E-03	2.30E-03	1.82E-03
			1.83E-03	2.23E-03	6.33E-03	2.54E-03	1.83E-03
			1.85E-03	2.36E-03	6.42E-03	2.85E-03	1.89E-03
			1.81E-03*	2.24E-03	6.33E-03	2.58E-03	1.84E-03
Number of statistically significant wins			8	0	0	0	0

TABLE 6.5 Best, median, worst, and average IGD values for Fusion, GDE3, SPEA2, SMPSO and NSGA-III on M-objective DTLZ2 and Convex DTLZ2 problems. Best performed algorithm is shown in dark gray and second best is shown light gray. * indicates a significance level of 0.05 between the top two algorithms.

Problem	M	MFC	Fusion	GDE3	SPEA2	SMPSO	NSGA-III
DTLZ2	3	250 x 92	6.31E-04	9.23E-04	7.07E-04	1.07E-03	6.28E-04
			6.36E-04	9.85E-04	7.98E-04	1.13E-03	6.34E-04
			6.43E-04	1.05E-03	8.27E-04	1.24E-03	6.56E-04
			6.36E-04	9.87E-04	8.00E-04	1.13E-03	6.36E-04
	5	450 x 212	9.90E-04	1.41E-03	1.64E-03	2.43E-03	9.83E-04
			9.93E-04	1.44E-03	1.78E-03	2.71E-03	9.86E-04
			1.00E-03	1.51E-03	1.92E-03	2.91E-03	1.02E-03
			9.94E-04	1.45E-03	1.79E-03	2.68E-03	9.89E-04*
	8	700 x 156	1.76E-03	3.92E-03	1.09E-02	5.30E-03	1.80E-03
			1.91E-03	4.23E-03	1.11E-02	5.81E-03	1.85E-03
			1.98E-03	4.86E-03	1.14E-02	6.57E-03	2.01E-03
			1.90E-03	4.25E-03	1.11E-02	5.80E-03	1.86E-03
	10	1000 x 276	1.44E-03	4.49E-03	8.27E-03	4.92E-03	1.49E-03
			1.55E-03	4.71E-03	8.40E-03	5.69E-03	1.52E-03
			1.70E-03	4.88E-03	8.64E-03	6.22E-03	1.70E-03
			1.55E-03	4.69E-03	8.41E-03	5.63E-03	1.55E-03
Convex DTLZ2	3	300 x 92	4.77E-04	6.18E-04	4.81E-04	7.93E-04	4.94E-04
			4.98E-04	6.78E-04	5.00E-04	8.46E-04	5.55E-04
			5.11E-04	7.65E-04	5.34E-04	9.64E-04	6.07E-04
			4.96E-04*	6.89E-04	5.05E-04	8.64E-04	5.55E-04
	5	500 x 212	4.11E-04	5.23E-04	8.00E-03	1.27E-03	4.49E-04
			4.33E-04	5.49E-04	1.88E-02	1.61E-03	5.13E-04
			4.96E-04	5.67E-04	2.34E-02	2.13E-03	7.45E-04
			4.36E-04*	5.50E-04	1.78E-02	1.59E-03	5.35E-04
	8	800 x 156	8.14E-04	1.10E-03	3.28E-03	1.54E-03	1.49E-03
			1.34E-03	1.16E-03	3.72E-03	2.19E-03	1.50E-03
			1.47E-03	1.28E-03	3.90E-03	3.02E-03	1.52E-03
			1.31E-03	1.16E-03*	3.69E-03	2.27E-03	1.50E-03
	10	1000 x 276	1.26E-03	5.68E-04	1.59E-03	7.75E-04	1.96E-03
			1.71E-03	6.41E-04	1.85E-03	1.18E-03	1.97E-03
			1.96E-03	7.83E-04	2.02E-03	1.55E-03	2.00E-03
			1.69E-03	6.53E-04*	1.85E-03	1.16E-03	1.97E-03
Number of statistically significant wins			2	2	0	0	1

The second experiment investigates the performance of Fusion on DTLZ2 and Convex DTLZ2 for three- to ten-objectives problems. From Table 6.5 we see that even though Fusion's IGD values are not statistically more significant than NSGA-III, they are

significantly better than algorithms involved in the hybridization process for almost all instances of the test problems. From the above two experiments, we see that none of the algorithms involved in Fusion experiment are not able to find well-distributed and well-converged solutions consistently. However, since Fusion uses predefined structured reference points to guide

and preserve the diversity of obtained solutions and adaptively select best performing algorithms in every stage of the search process, it consistently able to find well-distributed solutions that may not be possible using one optimization algorithm.

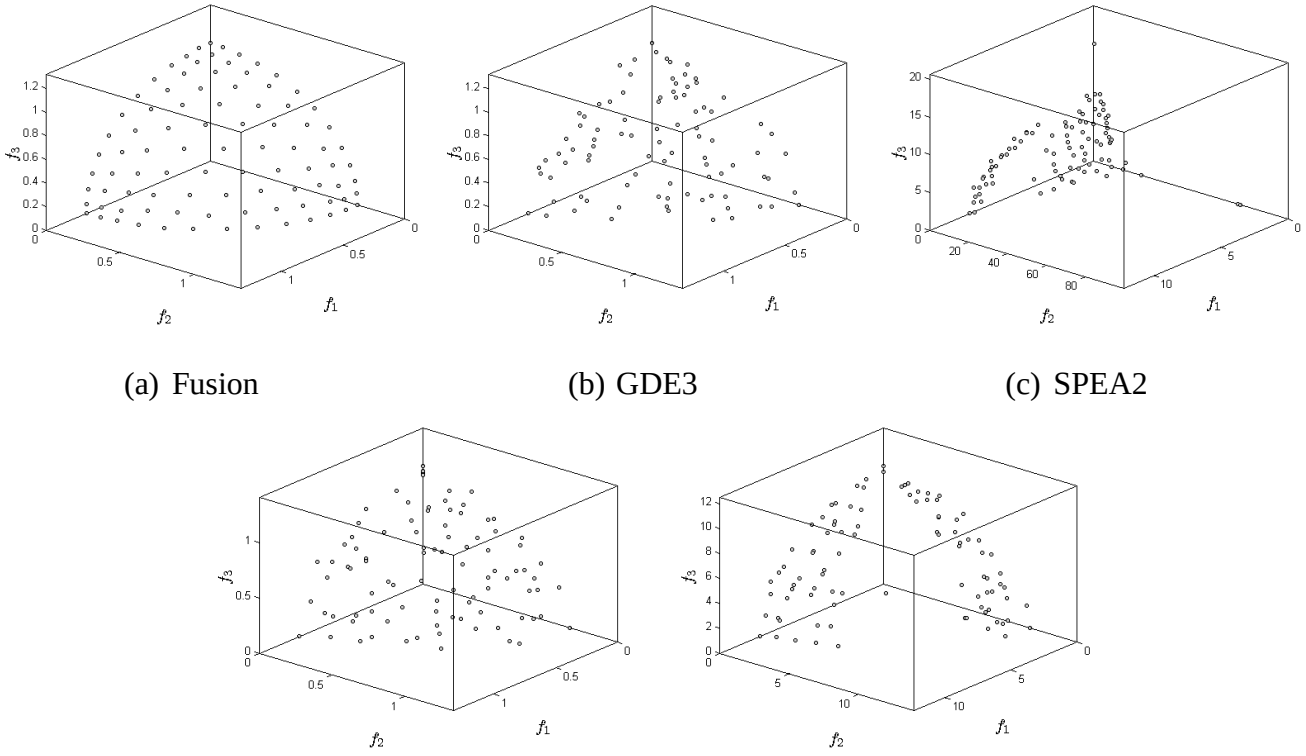

FIGURE 6-6 The trade-off plots of obtained solutions by Fusion, GDE3, SPEA2, SMPSO and NSGA-III algorithms for three-objective C1-DTLZ3 test problem.

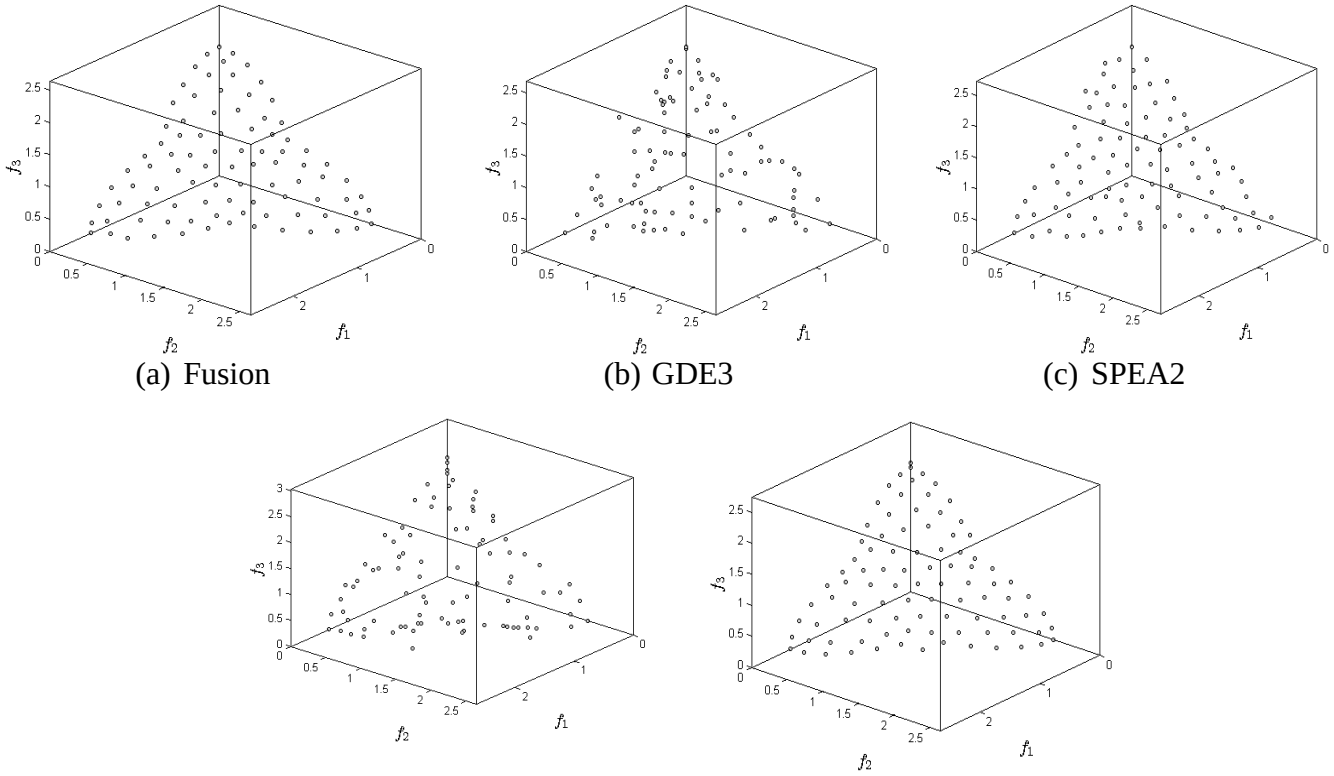

FIGURE 6-7 The trade-off plots of obtained solutions by Fusion, GDE3, SPEA2, SMPSO and NSGA-III algorithms for three-objective C3-DTLZ4 test problem.

6.3.4.2 Constrained Problems

The Type-1 constrained test problems challenge optimizers' ability to penetrate the barrier created by the constraints in order to reach the global Pareto-optimal front. Figure 12. shows obtained solutions by the Fusion, GDE3, SPEA2, SMPSO, and NSGA-III three-objective C1-DTLZ3 test problem after 300 generations (300 × 92 function calls). From this diagram, we can see that only the Fusion method is able to obtain well-distributed and converged solutions on the Pareto-optimal surface. However, when we look at Figure 6-6 (b), (c), and (d), none of the algorithms involved in the hybridization process individually are able to obtain well-distributed and converged solutions with the number of function

calls. Furthermore, from Figure 6-6 (c) and (e) we observe that the SPEA2 and NSGA-III algorithms are not only unable to penetrate the barrier created by the constraints of the test problem but also failed to find well-distributed on the newly created barrier surface. Table 6.6 shows that the proposed framework significantly outperformed the three algorithms in the hybridization process while showing comparable results with NSGA-III on C1-DTLZ1 and significantly better results on the C1-DTLZ3 problem with three- to ten- objectives.

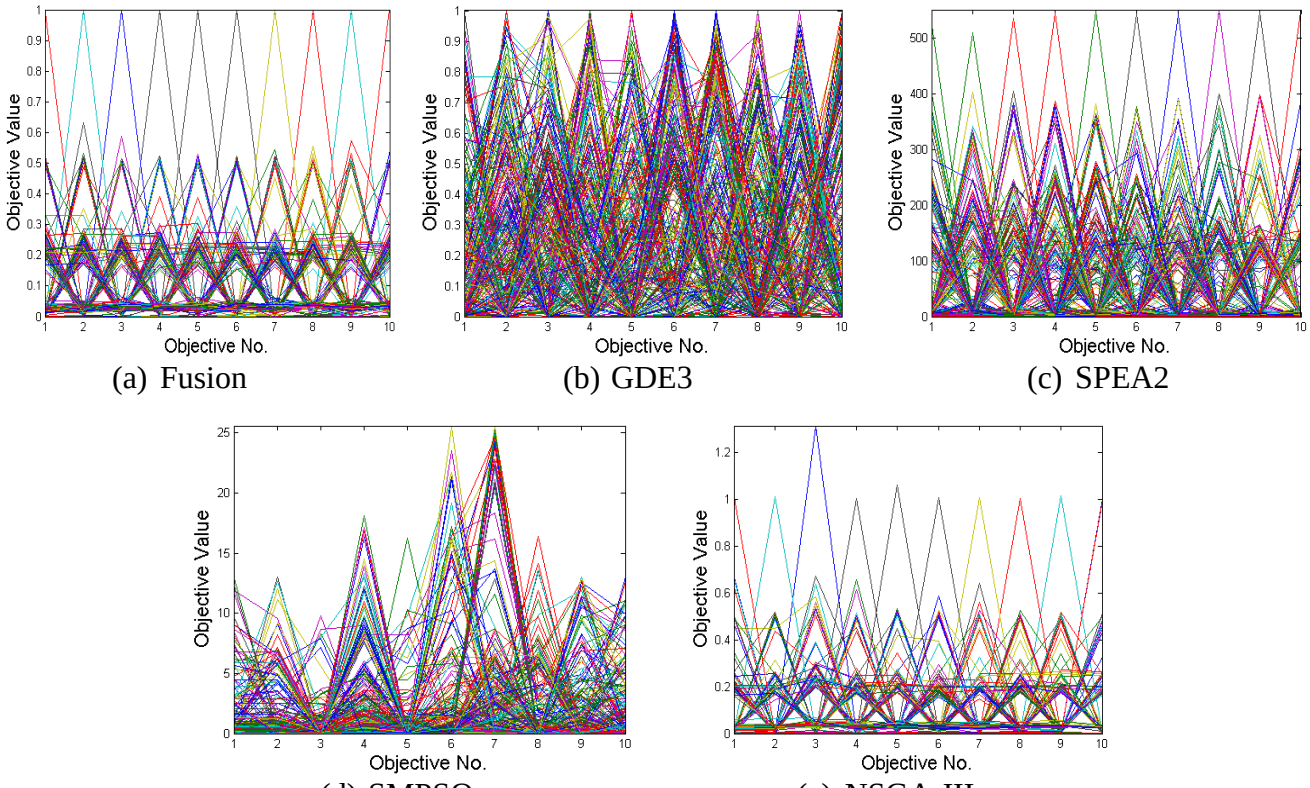

(a) Fusion (b) GDE3 (c) SPEA2

(d) SMPSO (e) NSGA-III

FIGURE 6-8 Value path comparison of obtained solutions by Fusion, GDE3, SPEA2, SMPSO and NSGA-III algorithms for ten-objective C3-DTLZ1 test problem.

TABLE 6.6 Best, median, worst, and average IGD values for Fusion, GDE3, SPEA2, SMPSO and NSGA-III on M-objective Convex C1-DTLZ1, C1-DTLZ3, C3-DTLZ1, and C3-DTLZ4 problems. Best performed algorithm is shown in dark gray and second best is shown light gray. * indicates a significance level of 0.05 between the top two algorithms.

Problem	M	NFC	Fusion	GDE3	SPEA2	SMPSO	NSGA-III
C1-DTLZ1	3	250 x 92	4.15E-04	6.22E-04	4.93E-04	6.80E-04	4.16E-04
			4.17E-04	6.71E-04	5.80E-04	7.52E-04	6.30E-04
			4.24E-04	1.07E-02	8.48E-04	2.53E-03	1.03E-02
			4.17E-04*	4.47E-03	6.07E-04	8.54E-04	2.29E-03
	5	450 x 212	5.23E-04	8.19E-04	6.27E-04	9.98E-04	5.10E-04
			5.26E-04	8.52E-04	6.56E-04	1.10E-03	5.17E-04
			5.29E-04	6.85E-03	7.58E-04	1.34E-03	5.24E-04
			5.26E-04	2.35E-03	6.68E-04	1.11E-03	5.17E-04*
	8	700 x 156	1.09E-03	1.74E-03	1.39E-03	2.17E-03	1.06E-03
			1.10E-03	1.78E-03	1.44E-03	2.41E-03	1.07E-03
			1.10E-03	1.70E-02	1.53E-03	2.59E-03	1.09E-03
			1.10E-03	4.15E-03	1.44E-03	2.40E-03	1.07E-03*
	10	1000 x 276	8.20E-04	1.36E-03	1.08E-03	1.64E-03	8.11E-04
			8.23E-04	1.37E-03	1.11E-03	1.84E-03	8.15E-04
			8.27E-04	1.27E-02	1.15E-03	2.10E-03	8.20E-04
			8.23E-04	2.44E-03	1.11E-03	1.85E-03	8.15E-04*
C1-DTLZ3	3	300 x 92	7.56E-04	1.43E-03	1.48E-01	1.46E-03	1.48E-01
			7.62E-04	4.84E-02	1.50E-01	1.76E-03	1.48E-01
			7.67E-04	1.48E-01	2.01E-01	9.25E-03	1.55E-01
			7.62E-04*	6.97E-02	1.53E-01	3.43E-03	1.49E-01
	5	500 x 212	9.06E-04	1.85E-03	4.37E-01	3.85E-03	5.13E-02
			9.16E-04	5.17E-02	8.94E-01	5.12E-03	5.18E-02
			9.28E-04	5.19E-02	1.56E+00	1.56E-01	5.35E-02
			9.16E-04*	3.49E-02	8.78E-01	1.30E-02	5.19E-02
	8	800 x 156	1.58E-03	6.58E-03	1.53E-02	9.29E-03	4.62E-03
			2.32E-03	8.94E-03	6.91E-02	1.06E-02	6.26E-03
			2.90E-03	1.03E-02	8.37E-01	1.08E-02	7.14E-03
			2.23E-03*	8.78E-03	1.27E-01	1.05E-02	6.17E-03
	10	1000 x 276	2.89E-03	4.42E-03	2.66E-02	4.66E-03	6.48E-03
			4.10E-03	5.49E-03	3.68E-02	5.20E-03	7.06E-03
			5.85E-03	5.89E-03	1.96E-01	5.39E-03	7.18E-03
			4.13E-03*	5.39E-03	5.69E-02	5.16E-03	6.97E-03
C3-DTLZ1	3	400 x 92	5.84E-03	3.20E-03	2.65E-01	5.38E-03	6.84E-03
			7.23E-03	3.61E-03	7.99E-01	1.17E-02	8.22E-03
			8.03E-03	5.33E-03	1.31E+00	1.35E-01	9.26E-03
			6.98E-03	3.70E-03*	8.01E-01	2.19E-02	8.26E-03
	5	700 x 212	8.92E-04	1.94E-03	2.23E-01	2.61E-03	1.00E-03
			9.14E-04	2.29E-03	3.52E-01	3.21E-03	1.25E-03
			1.13E-03	2.44E-03	4.97E-01	4.35E-03	1.54E-03
			9.23E-04*	2.25E-03	3.63E-01	3.25E-03	1.25E-03
	8	1100 x 156	1.49E-03	5.89E-03	1.32E+00	5.65E-03	1.76E-03
			1.64E-03	7.95E-03	2.33E+00	3.31E-02	2.15E-03
			1.83E-03	9.37E-03	3.09E+00	1.84E-01	3.82E-03
			1.64E-03*	7.79E-03	2.25E+00	5.30E-02	2.24E-03
	10	1500 x 276	1.21E-03	4.28E-03	1.17E+00	4.47E-03	1.19E-03
			1.31E-03	6.49E-03	1.79E+00	6.23E-02	1.53E-03
			1.40E-03	7.86E-03	2.22E+00	1.39E-01	2.77E-03
			1.30E-03*	6.54E-03	1.78E+00	6.18E-02	1.66E-03

C3-DTLZ4	3	400 x 92	5.74E-04	9.28E-04	7.34E-04	1.05E-03	5.78E-04
			5.89E-04	9.57E-04	7.97E-04	1.17E-03	5.99E-04
			6.23E-04	1.03E-03	7.65E-03	1.99E-03	6.67E-04
			5.90E-04*	9.66E-04	2.15E-03	1.31E-03	6.09E-04
	5	700 x 212	7.71E-04	1.48E-03	1.74E-03	1.82E-03	7.68E-04
			7.80E-04	1.56E-03	1.87E-03	2.05E-03	7.87E-04
			8.03E-04	1.67E-03	2.08E-03	2.18E-03	8.41E-04
			7.82E-04	1.56E-03	1.87E-03	2.03E-03	7.90E-04
	8	1100 x 156	1.83E-03	3.19E-03	7.67E-03	3.42E-03	1.80E-03
			1.85E-03	3.34E-03	7.96E-03	3.58E-03	1.83E-03
			1.88E-03	3.56E-03	8.16E-03	3.96E-03	1.87E-03
			1.85E-03	3.34E-03	7.91E-03	3.59E-03	1.83E-03*
	10	1500 x 276	1.50E-03	2.76E-03	5.89E-03	2.69E-03	1.50E-03
			1.55E-03	2.96E-03	5.98E-03	2.87E-03	1.53E-03
			1.56E-03	3.08E-03	6.13E-03	3.12E-03	1.58E-03
			1.55E-03	2.95E-03	5.99E-03	2.87E-03	1.54E-03
Number of statistically significant wins			9	1	0	0	4

On the other hand, Type-3 constrained problems are designed to test the ability of an optimizer to stay on the Pareto-optimal front created by portions of constraint surface. Figure 6-7 depicts obtained solutions by the Fusion, GDE3, SPEA2, SMPSO, and NSGA-III three-objective C3-DTLZ4 test problem after 400 generations (400×92 function calls). From this figure, we can see that Fusion, SPEA2 and NSGA-III are able to obtain comparable distribution of solutions on the Pareto-optimal front. However, from Figure 6-7 (b) and (d) we see that GDE3 and SMPSO failed to find well-distributed solutions over $f_i \in [0, 2]$. In Table 6.6 we see that Fusion outperformed every algorithm in almost all instances of C3-DTLZ1 and C3-DTLZ4 problems in terms of IGD metric, followed by NSGA-III. Also, from Figure 6-8 we see that Fusion is able to obtain well-distributed solutions for C3-DTLZ1 over $f_i \in [0, 1]$ for all ten objectives and trade-offs among them. However, Figure 6-8 (c) and (d) illustrate that SPEA2 and SMPSO individually are not able to converge their solutions on $f_i \in [0, 1]$.

6.4 Concluding Remarks

This chapter presented a novel hybridization of multi-and many-objective optimization algorithms framework called fusion-based hybrid many-objective optimization algorithm, which utilizes several many-objective algorithms to gain the combined benefits of several algorithms and reduce the challenge of choosing one optimization algorithm to solve complex problems. In the Fusion framework, several algorithms can be used without the need of extra parameter tuning so that several optimization algorithms can be hybridized with minimal effort. Furthermore, since Fusion uses predefined structured reference points to guide and preserve the diversity of obtained solutions and adaptively select best performing algorithms in every stage of the search process, it can consistently find a well-distributed solutions that may not be possible to find using only one optimization algorithm.

The efficacy of the proposed Fusion framework was investigated using three widely used optimization algorithms GDE3, SMPSO, and SPEA2. Experimental results on five unconstrained and four constrained benchmark test problems with three to ten objectives showed that the Fusion framework significantly outperformed all algorithms involved in the hybridization process as well as the NSGA-III algorithm in terms of diversity and convergence of obtained solutions. Furthermore, the numerical results also show that the proposed Fusion framework is able to consistently show good performance. In the future, we would like to investigate the performance of Fusion in practical many-objective problems.

Chapter 7

ELITENSGA-III: AN IMPROVED EVOLUTIONARY MANY-OBJECTIVE OPTIMIZATION ALGORITHM

Evolutionary algorithms are the most studied and successful population-based algorithms for solving single- and multi-objective unconstrained and constrained optimization problems. However, many studies have shown that these algorithms fail to perform well when handling many-objective (more than three objectives) problems due to the loss of selection pressure to pull the population towards the PF. As a result, there has been a number of efforts towards developing evolutionary algorithms that can successfully handle many-objective unconstrained and constrained optimization problems without deteriorating the effect of evolutionary operators. A reference-point based NSGA-II (NSGA-III) is one such algorithm designed to deal with many-objective problems, where the diversity of the solution set is guided by a number of well-spread reference points. However, NSGA-III still has difficulty preserving elite population as new solutions are generated. In this chapter, we propose an improved NSGA-III algorithm, called EliteNSGA-III to improve the diversity and accuracy of the NSGA-III algorithm. EliteNSGA-III algorithm maintains an elite population archive to preserve previously generated elite solutions that would probably be eliminated by NSGA-III's selection procedure. The proposed EliteNSGA-III algorithm is applied to 11 unconstrained many-objective test problems with three to 50 objectives and six constrained objective test problems with three to 15 objectives. Experimental results show that the proposed EliteNSGA-III algorithm outperforms the NSGA-III algorithm in terms of diversity and accuracy of the obtained solutions, especially for unconstrained test problems with higher objectives (greater than 15 objectives).

7.1 Introduction

Due to an ever increasing complexities inherently present in real-world problems (i.e. high number of objectives, high number of decision variables, unstable parameters, data/variable representation, discontinuities, etc…), we increasingly require optimization algorithms capable of addressing these complexities and arrive at "acceptable" solution in a "reasonable" time [114-116].

Evolutionary multi-objective (EMO) algorithms such as NSGA-II, SPEA2, GDE3, MOEA/D, and others [21, 39, 82, 106], have shown outstanding achievements in solving numerous economics, engineering and real-world scientific applications mainly involving 2 to 5 objectives. However, when solving problems involving higher number of objectives (usually more than 3 objectives, also known as many-objective optimization), a number of the evolutionary algorithms fail to find well-converged and well-diversified non-dominated solutions due to the loss of selection pressure in fitness evaluation [6]. In high-dimensional space the proportion of non-dominated individuals in a randomly generated initial population is often higher than 90% [8, 9, 117] and this will diminish the selection pressure considerably during the evolutionary process. Moreover, when the distance between nearly converged parent solutions is high, they will likely produce offspring solutions that are far from the true PF [10, 11, 118, 119].

Since the Pareto-dominance schemes used in evolutionary many-objective algorithms failed to provide adequate selection pressure to guide the population towards the Pareto-optimal front, the focus has been shifted to improving the diversity-preserving schemes used in EMOs [120]. One such approach is to use a predefined multiple search directions [82] or predefined reference points [112, 121-124] spanning the entire Pareto-

optimal front to aid solutions towards targeted locations. NSGA-III [112] is one of the recent effective reference-point-based many-objective optimization algorithm whose population are guided by multiple predefined structured reference points to preserve the diversity of offspring solutions. Due to its power in guiding solutions to any predefined direction, NSGA-III has been gaining more acceptance in solving real-world many-objective optimization problems [125-127].

Since the introduction of NSGA-III, there have been a number of research studies toward improving the convergence and the overall performance of this algorithm. Yuan et al. [128] conducted an experimental investigation of variation operators in a NSGA-III. Their investigation concluded that NSGA-III performs better when selecting one of the three different variation operators, i.e., SBX, DE operator, and polynomial mutation randomly to produce an offspring solution.

Yuan et al. [129] proposed an improved NSGA-III procedure, called θ-NSGA-III which aims to improve the convergence of NSGA-III in many-objective optimization. The θ-NSGA-III algorithm replaces the non-dominated sorting scheme utilized in NSGA-III by a θ-dominance scheme to rank solutions in the environmental selection phase to improve the convergence of NSGA-III. Although experimental results of θ-NSGA-III seem promising, it needs to incorporate a diversity enhancement strategy to improve the convergence and the diversity of obtained solutions.

Seada and Deb [130] proposed a unified evolutionary optimization algorithm, U-NSGA-III, for solving single-, multi- and many-objective problems. The proposed algorithm degenerates to an equivalent and efficient population-based optimization procedure just from the description of the number of specified objectives of a problem.

Yuan et al. [125] introduced an extension to NSGA-III where dominance relationship is determined based only on constraint violation. In case of constraint violation, infeasible solutions are repaired by modifying the decision variables in feasible zone according to the violation amount.

This chapter presents a novel elite population archive-based NSGA-III (EliteNSGA-III) to mitigate the above-mentioned problems associated with many-objective optimization algorithms through the introduction of elite population archive to preserve previously generated elite solutions that would probably be eliminated by NSGA-III's selection procedure.

7.2 Introduction to NSGA-III

NSGA-III [105, 112] is an extension of NSGA-II [21] designed for solving many-objective optimization problems. The fundamental components of NSGA-III are similar to NSGA-II algorithm, however, it has significant changes in its selection mechanism. In the original NSGA-II, the new population $P_{t+1}$is constructed from the combined population $R_t = P_t \cup Q_t$, in the order of their rankings. Let S_t be the population selected so far (including the last non-dominated front F_l). If the size of S_t is greater than the population size N, then the best members in F_l with the largest crowding distance values are selected. However, in NSGA-III the best members from the last non-dominated front $F_l$are selected based on the supplied reference points. In the original NSGA-III study, they have used Das and Dennis' [91] procedure to create these structured reference points.

First, each objective's values are adaptively normalized based on members of S_t. Then, reference lines corresponding to each reference point on the hyper-plane are constructed by joining the reference point with the origin. Thereafter, all population

members of S_t and F_l are associated with a reference point whose reference line is closest to a population member in the normalized objective space. Then, the number of population members from $P_{t+1} = S_t$ that are associated with each reference point are counted. If there is a reference point with no member associated with it and one or more members of F_l associated with the reference point, then the one having the shortest perpendicular distance from the reference line is added to P_{t+1}. However if all reference points are associated with at least one population member, then a randomly chosen member from F_l is added to P_{t+1}. This procedure is repeated until the desired population size is achieved. Algorithm 7.1 describes the NSGA-III algorithm.

The constrained handling mechanism used in NSGA-III [112, 131] is similar to the constraint-domination approaches proposed in [76, 132] and [61]. In the constraint-domination mechanism, preference is given to feasible and less constraint-violated population members. Before defining the constraint-domination, let's first define dominance in MOO.

Definition 1: A solution $\mathbf{u} = (u_1, \ldots, u_n)$ is said to $dominate$ $\mathbf{v} = (v_1, \ldots, v_n)$ (denoted by $\mathbf{u} \prec \mathbf{v}$) if and only if no component of v is smaller than the corresponding component of u and at least one component of u is strictly smaller, assuming that all objectives are minimization problem; that is,

$$\forall\, i \in \{1, \ldots, n\}, u_i \leq v_i \wedge \exists\, i \in \{1, \ldots, n\} : u_i < v_i. \tag{7.1}$$

Constraint-dominance in the NSGA-III is defined as follows:

Definition 2: A candidate solution **x** is said to constraint-dominate another candidate solution **v**, if any of the following conditions are true:

1) if **u** is feasible and **v** is infeasible;

2) if **u** and **v** are infeasible and **x** has a smaller constraint violation value; or,

3) if **u** and **v** are feasible and **u** dominates **v** (based on Definition 1).

Constraint violation is calculated as follow:

$$CV(\mathbf{x}) = \sum_{j=1}^{m} \bar{g}_j(\mathbf{x}) + \sum_{k=1}^{n} \left|\bar{h}_k(\mathbf{x})\right|, \tag{7.2}$$

where $\bar{g}_j(\mathbf{x})$ and $\bar{h}_k(\mathbf{x})$ are normalized inequality and equality constraints. If $g_i(\mathbf{x})$ is negative, then $\bar{g}_j(\mathbf{x})$ is equal to the negative normalized value of $g_i(\mathbf{x})$, and 0 otherwise.

Algorithm 7.1 Generation t of NSGA-III Procedure

Input: H structured reference points Zs or supplied aspiration points Za, parent population P_t,

Output: P_{t+1}

$S_t = \emptyset, i = 1$
Q_t = `Recombination + Mutation`(P_t)
$R_t = P_t \cup Q_t$
$(F1, F2, \ldots)$ = `Non-dominated-sort`(R_t)
repeat
    $S_t = S_t \cup Fi$ and $i = i + 1$
until $|S_t| \geq N$
//Last front to be included: $F_l = F_i$
if $|S_t| = N$ **then**
    $P_{t+1} = S_t$, break
else
    $P_{t+1} = \cup_{j=1}^{l-1} F_j$
    //Points to be chosen from F_l:
    $K = N - |P_{t+1}|$
    //Normalize objectives and create reference set Z^r:
    `Normalize`$(f^n, S_t, Z^r, Z^s, Z^a)$
    //Associate each member $\boldsymbol{s}$ of S_t with a reference point:
    $[\pi(\boldsymbol{s}), d(\boldsymbol{s})]$ = `Associate`(S_t, Z^r) // $\pi(\boldsymbol{s})$: closest reference point, *d:* distance between **s** and π(**s**)
    //Compute niche count of reference point $j \in \rho_j = Z^r$: $\sum_{\boldsymbol{s} \in S_t/F_l} (\pi(\boldsymbol{s}) = j \; ? \; 1 : 0)$
    //Choose *K* members one at a time from F_l to construct P_{t+1}:
    `Niching`$(K, \rho_j, \pi, d, Z^r, F_l, P_{t+1})$
end if

In NSGA-III, the above constraint-dominance definition is utilized to sort $2N$ population members to different domination levels. First, feasible solutions are sorted according to their non-domination levels. Then, infeasible solutions are sorted according to constraint violation (CV) values. A solution with the lowest CV value is given the next rank after the last feasible solution's rank and the next infeasible solution with smallest CV is assigned to the next rank. Note that if all solutions are infeasible, then we will have 2N levels unless there are solutions with the same CV value. In the original NSGA-III, parents are randomly selected for P_t to create offspring population Q_t. However, when there are infeasible solutions in the parent population, binary tournament selection is applied according to the following modified tournament selection procedure.

Definition 3: Given parents p_1 and p_2, p_1 is selected if any of the following conditions is true:

1) if p_1 is feasible and p_2 is infeasible;
2) if p_1 and p_2 are infeasible then and p_1 has a smaller constraint violation value; or,
3) if both p_1 and p_2 are feasible and p_1 is randomly selected.

7.3 Proposed EliteNSGA-III Approach

The framework of the proposed EliteNSGA-III algorithm is similar to NSGA-III; however, EliteNSGA-III introduces three mechanisms to improve the performance of NSGA-III. First, we introduce an elite archive to preserve elite members of the population which may have otherwise been eliminated by the NSGA-III selection procedure. Second, we introduce new parent selection mechanism to improve the diversity of parent population. Third, we introduce alternate constraint handling mechanism to deal with individuals in

elite archive and regular population. Algorithm 7.2 summarizes the proposed EliteNSGA-III algorithm. The following subsections explain the newly added segments of the proposed algorithm.

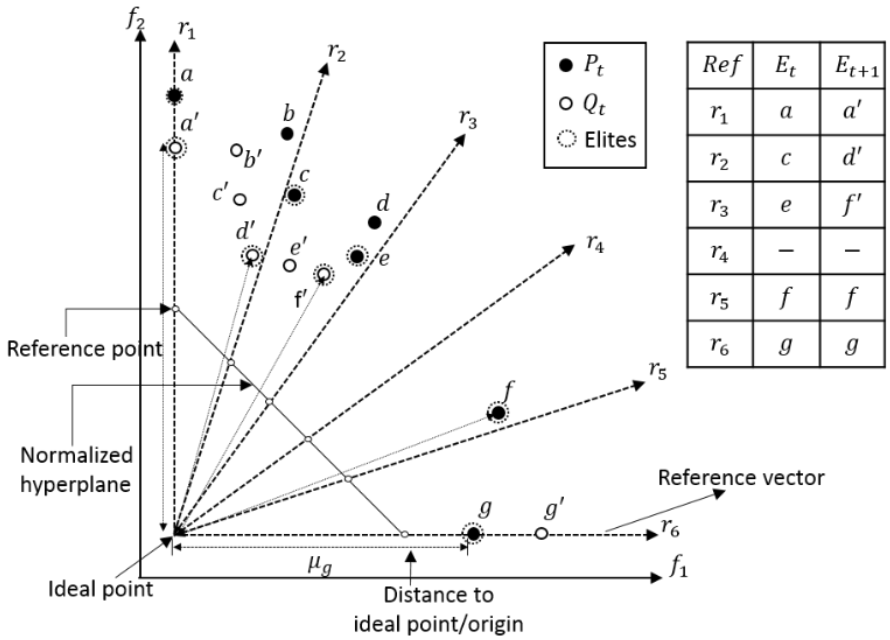

Ref	E_t	E_{t+1}
r_1	a	a'
r_2	c	d'
r_3	e	f'
r_4	–	–
r_5	f	f
r_6	g	g

FIGURE 7-1 Illustration of an elite population mechanism used in EliteNSGA-III

7.3.1 Elite Population Archive

The use of external archive to preserve obtained solutions in each generation is not new - in the past, elite-preserving external archives in NSGA [133] and NSGA-II [134] have shown respectable results compared to parent algorithms. The shaded areas of Algorithm 7.2 show the contribution of the current work. This subsection details the updateElite procedure (explanation as per Figure 7-1). Assume P_t is the current population which is depicted by the bold dots on Figure 6-1. Let $E_t(i)$ be the elite member associated with reference point r_i. Also, let π_i be a set of current solutions as well as previously archived elite member solutions associated with r_i. At every generation, $E_{t+1}(i)$ is updated according to the following:

$$E_{t+1}(i) = min_{j=1}^{|\pi_i|} d(\pi_{i,j}), \tag{7.3}$$

where $d(\pi_{i,j})$ is the Euclidean distance between the j^{th} member solution and the origin. Note that when no new solution is associated with r_i, the previously archived elite solution is retained. For further explanation refer to Algorithm 7.3.

Algorithm 7.2 EliteNSGA-III Procedure

1: $P_0 =$ InitializePopulation() %uniform random
2: $Z^r =$ GenerateReferencePoints()
3: $E_0 = \emptyset$ % $|E_0| = |Z^r|$
4: $\mu_0 = \infty$ % $|\mu_0| = |E_0|$
5: $[E_{t+1}, \mu_{t+1}]$ = `updateElite`(Z^r, P_0, E_0, μ_0)
6: **while** termination criteria is not met **do**
7: $S_t = \emptyset, i = 1$
8: Q_t = `Recombination + Mutation`(P_t, E_t)
9: $R_t = P_t \cup Q_t$
10: $(F1, F2, \ldots)$ = `Non-dominated-sort`(R_t)
11: **repeat**
12: $S_t = S_t \cup Fi$ and $i = i + 1$
13: **until** $|S_t| \geq N$
14: Last front to be included: $F_l = F_i$
15: **if** $|S_t| = N$ **then**
16: $P_{t+1} = S_t$, break
17: **else**
18: $P_{t+1} = \cup_{j=1}^{l-1} F_j$
19: Points to be chosen from F_l: $K = N - |P_{t+1}|$
20: Normalize objectives `Normalize`$(f^n, S_t, Z^r, Z^s, Z^a)$
21: Associate each member $\boldsymbol{s}$ of S_t with a reference point: $[\pi(\boldsymbol{s}), d(\boldsymbol{s})]$ = `Associate`(S_t, Z^r) $//\pi(\boldsymbol{s})$: closest reference point, *d:* distance between **s** and π(**s**)
22: Compute niche count of reference point $j \in \rho_j = Z^r$: $\sum_{\boldsymbol{s} \in S_t/F_l}((\pi(\boldsymbol{s}) = j \,?\, 1 : 0)$
23: Choose *K* members one at a time from F_l to construct P_{t+1}: `Niching`$(K, \rho_j, \pi, d, Z^r, F_l, P_{t+1})$
24: **end if**
25: Update elite archive and their distance to ideal point $[E_{t+1}, \mu_{t+1}]$ = `updateElite`$(Z^r, P_{t+1}, E_t, \mu_t)$
26: **end while**

The main advantage of this elite archive is the preservation of elite members of the population which may have otherwise been eliminated by the NSGA-III selection procedure. As a result, the diversity of an offspring population is improved. In Figure 7-1, the black dots represent P_t while the white dots represent Q_t, the offspring population. In this example, the population size is six. Since solutions a, c, e, f, and g have the lowest distance in their respective reference point location; they will be archived in E_t. According to NSGA-III, since solution f is not in rank 1 and rank 1 contains more than six solutions, solution f will be eliminated and consequently won't be part of P_{t+1}. This renders the solution set in P_{t+1} less diverse than that of P_t. However, since solution member f was preserved in E_t and no better solution exists in its respective reference point location, solution member f will also be part of E_{t+1}. Note that other elite members will get replaced with a better solution (if any exists) which results in the preservation of solutions that are well-spread and has better convergence.

7.3.2 Parent Selection Procedure

The other contribution of EliteNSGA-III is in parent diversity improvement. In NSGA-III, early generations of the population are associated with few of the supplied reference points. Subsequently, when selecting parent population, there is a likelihood of selecting parents associated with the same reference point. This might lead to the generation of offspring solutions that are close to their parents resulting in a reduction of diversity.

In EliteNSGA-III, and as explained by Algorithm 7.4, parent populations are selected with equal probability from both the current population and the elite archive. Also, since there is at most one elite member representing a reference point, the likelihood of

selecting parents associated with the same reference point is minimized - hence improving diversity.

Algorithm 7.3 UpdateElite (Z^r, P_t, E_t, μ_t) Procedure

Input: References points on normalized hyper-plane Z^r: each $\boldsymbol{z} \in Z^r$ identified by its location 1…$|Z^r|$, Parent population P_t, elite population E_t, elite population distance to ideal point μ_t

Output: E_{t+1}, μ_{t_+1}

1: Associate each member $\boldsymbol{p}$ of P_t with a reference point: $[\pi(\boldsymbol{p}), d(\boldsymbol{p})]$ = `Associate`(P_t, Z^r)
   // $\pi(\boldsymbol{p})$: closest reference point, *d:* distance between $\boldsymbol{p}$ and $\pi(\boldsymbol{p})$
2: **for** $i = \boldsymbol{p} \in P_t$
3: Find the location of the reference point associated with $\boldsymbol{p}$: loc = location ($\pi(\boldsymbol{p})$)
4: Calculate the Euclidian distance between $\boldsymbol{p}$ and the ideal point: $\mu'_t(loc) = dist(\boldsymbol{p}, z^{min})$
5: **if** $\mu'_t(loc) < \mu_t(loc)$ **then**
6: $\mu_{t+1}(loc) = \mu'_t(loc)$
7: $E_{t+1}(loc) = \boldsymbol{p}$
8: **else**
9: $\mu_{t+1}(loc) = \mu_t(loc)$
10: $E_{t+1}(loc) = E_t(loc)$
11: **end if**
12: **end for**

Algorithm 7.4 Recombination + Mutation (P_t, E_t) Procedure

Input: Parent population P_t, elite population E_t

Output: Q_t

1: $Q_t = \emptyset$
2: s_P = size (P_t)
3: s_E = size (E_t)
4: **for** $i = 1$ *to* $s_P/2$
5: $r_1 = rand(1, s_P)$
6: $r_2 = rand(1, s_P),\ r_1 \neq r_2$
7: $p_P^1 = P_t(r_1),\ p_P^2 = P_t(r_2)$
8: $r_3 = rand(1, s_E),\ E_t(r_3) \neq null$
9: $r_4 = rand(1, s_E),\ E_t(r_4) \neq null$ and $r_3 \neq r_4$
10: $p_E^1 = E_t(r_3),\ p_E^2 = E_t(r_4)$
11: $p_1 = rand < 0.5\ ?\ P_t(r_1) : E_t(r_3)$
12: $p_2 = rand < 0.5\ ?\ P_t(r_2) : E_t(r_4)$
13: $[o_1, o_2]$ = crossover + mutation (p_1, p_2)
14: $Q_t = Q_t \cup [o_1, o_2]$
15: **end for**

7.4 Experimental Setup and Results for Unconstrained Test Problems

In this section, we describe the test problems used, parameter settings, and simulation results of EliteNSGA-III on 3- to 50-objective optimization problems.

7.4.1 Test Problems

In order to test the quality of the proposed algorithm, we used 11 many-objective benchmark test problems. The first sets of these test problems are the DTLZ (DTLZ1 – DTLZ4) family of test problems introduced by Deb et al. [61]. The number of variables are $(M + k - 1)$, where M is the number of objectives and $k = 5$ for DTLZ1, while $k = 10$ for DTLZ2, DTLZ3, and DTLZ4. The corresponding Pareto-optimal fronts lie in $f_i \in [0, 0.5]$ for the DTLZ1 problem and in $f_i \in [0, 1]$ for other DTLZ problems. The DTLZ1 problem has a linear Pareto-optimal front and DTLZ2 to DTLZ4 problems have concave Pareto-optimal fronts.

TABLE 7.1 Test problems

Problem	Characteristics
DTLZ1	Linear, Multimodal
DTLZ2	Concave
Convex DTLZ2	Convex
DTLZ3	Concave, Multimodal
DTLZ4	Concave, Biased
WFG1	Convex, Mixed, Biased
WFG2	Convex, Disconnected, Multimodal
WFG4	Concave, Multimodal
WFG5	Concave
WFG6	Concave
WFG7	Concave, Biased

TABLE 7.2 NSGA-III and EliteNSGA-III Parameter Settings. n is the Number of Variables.

Parameters	NSGA-III	EliteNSGA-III
SBX probability (p_c)	0.9	0.9
Polynomial mutation (p_m)	$1/n$	$1/n$
Crossover Distribution Index (η_c)	30	30
Mutation Distribution Index (η_m)	20	20

TABLE 7.3 Number of Reference Points and Population Sizes Used in NSGA-III and EliteNSGA-III Algorithms.

Number of Objectives (M)	Divisions		Reference Points(H)	Population Size (N)
	Outer	Inner		
3	12	0	91	92
5	6	0	210	212
8	3	2	156	156
10	3	2	275	276
15	2	1	135	136

The second sets of test problems utilized in this study are the WFG (WFG1, WFG2, and WFG4 – WFG7) family of test problems introduced by Huband et al. [135]. The number of position parameters is set to $k = M$, where M is the number of objectives and the number of distance parameters is set to $l = 3$ for all dimensions. The WFG1 has a mixed Pareto-optimal front, WFG2 problem has a convex Pareto-optimal front and WFG4 to WFG7 problems have concave Pareto-optimal fronts. The Pareto-optimal fronts for WFG test problems used in this work in $f_i \in [0, 2i]$. Table 7.1 presents detailed characteristics of the test problems used in this study.

The last test problem used in this study is a convex DTLZ2 problem. The construction of the convex DTLZ2 is similar to DTLZ2, however the convex DTLZ2 test problem powers the objective values of DTLZ2 $(1 \ldots (M-1))$ by 4 and squares the M^{th} objective value. The corresponding Pareto-optimal fronts for convex DTZ2 in $f_i \in [0, 1]$.

7.4.2 Parameter and Experimental Settings

The NSGA-III algorithm has four control parameters: SBX probability(p_c), Polynomial mutation(p_m), Crossover Distribution Index (η_c), and Mutation Distribution Index (η_m) which need to be tuned by the user. Similar to NSGA-III, EliteNSGA-III does not require any new parameter other than the above-mentioned genetic algorithm related parameters used in NSGA-III. In order to maintain a consistent and fair comparison, the parameter settings of NSGA-III and EliteNSGA-III are kept the same for all experiments. However, EliteNSGA-III requires a dependent variable (archive size) to maintain the elite population throughout the generations. The archive size is set to H; where H is the number of reference points used and it is directly related to the desired number of trade-off points. In all experiments the archive size is kept the same as the number of reference points used for each test problems. Table 7.2 presents parameter settings used by NSGA-III and EliteNSGA-III algorithms.

Table 7.3 shows the number of reference points (H), the population size (N), and the number of inner and outer divisions used for different dimensions of test problems. These values are similar to the values used in the original NSAG-III study which included test problems with up to 50 objectives.

To evaluate the performance of the proposed algorithm, we have used the inverse generational distance (IGD) metric, which is capable of measuring the convergence and the diversity of the obtained Pareto-optimal solutions. The IGD measure has been predominantly used to evaluate the performance of evolutionary many-objective problems [136], [117], [137], [112], [113]. The IGD metric measures the distances between each solution composing the Pareto-optimal front and the obtained solution. In this study, the

reference PF is constructed by joining all results of all the executions and then selecting the non-dominated solutions (Note: the jMetal framework is used for all experimentation conducted in this study [138]). Furthermore, all algorithms were executed 20 times independently and the best, the worst, the median, and the average results of each algorithm are recorded. Additionally, the Wilcoxon's signed rank statistical test [139] is conducted at a 5% significance level in order to evaluate the statistical significance of the obtained results.

7.4.3 Experimental Results and Discussion

Three sets of experiments have been conducted to evaluate the performance of the proposed algorithm. The first set of experiments are designed to investigate the performance of the proposed algorithm for 3- to 15-objective DTLZ (DTLZ1, DTLZ2, DTLZ3, DTLZ4, and convex DTLZ2) and WFG (WFG1 to WFG7, except WFG3) test problems. The second set of experiments investigate the influence of elite archive for the proposed algorithm by examining the distribution of obtained solutions throughout the generation. The last set of experiments investigate how the proposed algorithm cope with problems containing higher number of objectives (25- and 50-objectives).

7.4.3.1 Lower Dimension Test Problems (3- to 15-objectives)

The first experiment investigates the performance of EliteNSGA-III on problems having linear or concave Pareto-optimal fronts for 3- to 15-objectives DTLZ (DTLZ1 to DTLZ4) problems. Table 7.4 provides the best, median, worst, average IGD values of EliteNSGA-III and NSGA-III algorithms for DTLZ test problems. From this we can see that the performance of EliteNSGA-III is significantly better that NSGA-III for most of the test

problems. Figure 7-2 show the obtained PFs by NSGA-III and EliteNSGA-III algorithms for the three-objective DTLZ4 test problem. These diagrams are associated with the median value of IGD performance after 250 generations. It is clear that both algorithms are able to find uniformly distributed solutions for these test problems. However, as the dimension of the test problem increases, EliteNSGA-III is able to perform significantly better in terms of the IGD metric. From Figure 7-3 we can clearly see that NSGA-III is not able to find uniformly distributed sets of solution for the 15-objective DTLZ1 problem.

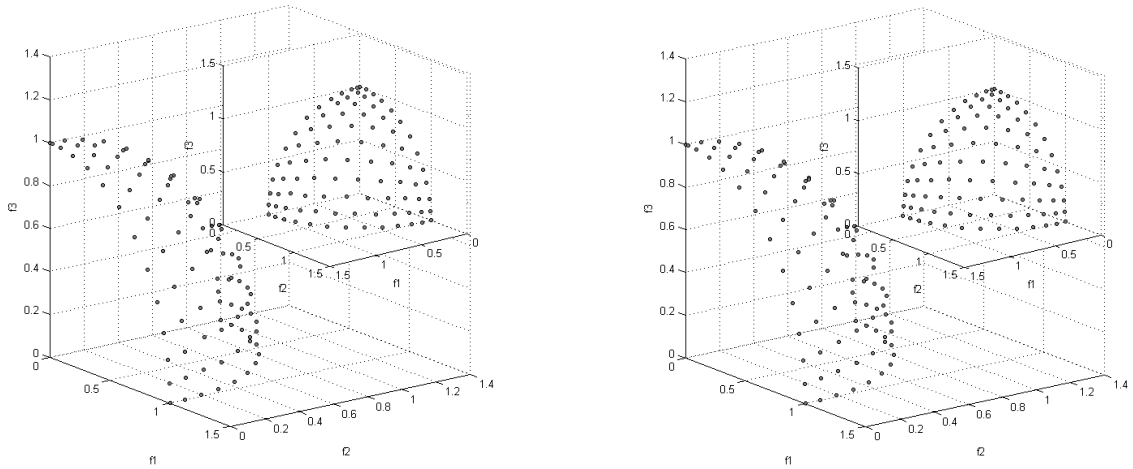

(a) NSGA-III (b) EliteNSGA-III

FIGURE 7-2 Obtained solutions by NSGA-III and EliteNSGA-III for DTLZ4 test problem.

The second experiment investigates the performance of EliteNSGA-III on problems having linear or concave Pareto-optimal fronts for 3- to 15-objectives WFG (WFG4 to WFG7) problems. Table 7.5 shows the IGD metric values for EliteNSGA-III are significantly better than the NSGA-III algorithm, especially when the dimension of the test problems approaches 15 objectives. Figure 7-4 shows the obtained PFs by NSGA-III and EliteNSGA-III algorithms for three-objective WFG7 test problem. These diagrams are associated with the median value of IGD performance after 400 generations. From this

figures we can see that the EliteNSGA-III algorithm is able to find well-distributed solutions along the Pareto-optimal front.

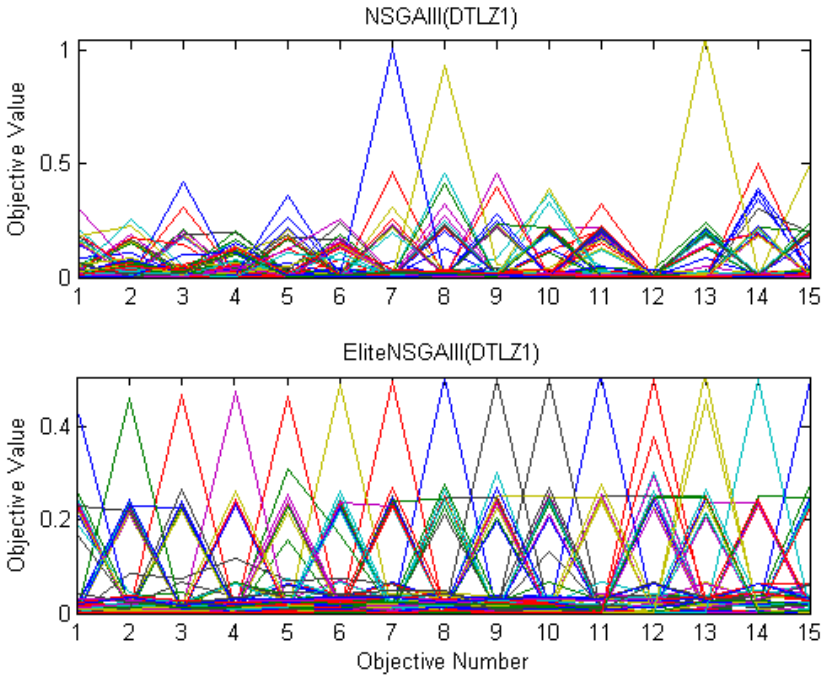

FIGURE 7-3 Value path plot comparison of the obtained solutions by NSGA-III and EliteNSGA-III for 15-objective DTLZ1 test problem.

The third experiment investigates the performance of the EliteNSGA-III algorithm on problems having convex or mixed Pareto-optimal fronts for 3- to 15-objectives DTLZ (convex DTLZ2) and WFG (WFG1 and WFG2) problems. Similar to the above results, EliteNSGA-III is able to significantly outperform NSGA-III in almost all instances except for the 3-objective WFG1 test problem. Table 7.3 provides IGD metric values of each compared algorithm for convex DTLZ1, WFG1 and WFG2 problems having 3 to 15 objectives. Figure 7-5 illustrates the distribution of the obtained solutions for NSGA-III and EliteNSGA-III algorithms for three-objective convex DTLZ2 test problem.

TABLE 7.4 Best, median, worst, and average IGD values for EliteNSGA-III and NSGA-III on M-objective DTLZ test problems. Best performing algorithm is shown in bold. Gray shade indicates a significance level of 0.05.

Problem	M	Max Gen	EliteNSGA-III	NSGA-III	Problem	M	Max Gen	EliteNSGA-III	NSGA-III
DTLZ1	3	400	6.80E-04	**6.75E-04**	DTLZ3	3	250	**1.04E-03**	1.05E-03
			7.26E-04	1.06E-03				**1.05E-03**	1.87E-03
			8.23E-04	5.24E-03				**1.16E-03**	7.81E-03
			7.31E-04	1.26E-03				**1.06E-03**	2.51E-03
	5	1000	7.57E-04	**7.50E-04**		5	500	**9.59E-04**	9.84E-04
			9.81E-04	1.20E-03				**9.71E-04**	4.35E-03
			3.92E-03	9.16E-03				**7.83E-03**	8.57E-03
			1.61E-03	2.51E-03				**1.31E-03**	4.36E-03
	8	1500	1.84E-03	**1.83E-03**		8	750	**1.32E-03**	2.42E-03
			3.36E-03	9.94E-03				**2.22E-03**	5.12E-03
			5.82E-03	1.11E-02				1.31E-02	**7.61E-03**
			3.14E-03	8.01E-03				**3.43E-03**	4.75E-03
	10	2000	1.55E-03	**1.55E-03**		10	1000	**1.45E-03**	2.51E-03
			2.89E-03	6.73E-03				**3.04E-03**	5.39E-03
			4.21E-03	8.63E-03				**6.21E-03**	1.23E-02
			2.75E-03	5.20E-03				**3.30E-03**	5.36E-03
	15	2500	**2.13E-03**	2.72E-03		15	1250	**2.57E-03**	2.94E-03
			3.50E-03	1.00E-02				3.99E-03	**3.64E-03**
			7.90E-03	1.14E-02				**4.20E-03**	1.08E-01
			3.58E-03	8.63E-03				**3.66E-03**	9.72E-03
DTLZ2	3	250	**3.05E-04**	3.07E-04	DTLZ4	3	250	**6.88E-04**	6.93E-04
			3.09E-04	3.33E-04				**1.13E-03**	1.26E-03
			3.16E-04	1.50E-03				**4.93E-03**	1.75E-02
			3.10E-04	4.02E-04				**2.13E-03**	5.55E-03
	5	500	**2.72E-04**	2.78E-04		5	500	**8.97E-04**	9.07E-04
			2.76E-04	2.96E-04				**1.01E-03**	1.49E-03
			4.26E-03	**3.80E-04**				8.56E-03	**6.01E-03**
			4.76E-04	**3.01E-04**				2.00E-03	**1.68E-03**
	8	750	**2.32E-03**	2.36E-03		8	750	**1.41E-03**	1.53E-03
			2.33E-03	8.08E-03				**1.42E-03**	4.29E-03
			1.01E-02	1.06E-02				1.29E-02	**1.06E-02**
			4.25E-03	6.59E-03				**2.73E-03**	4.30E-03
	10	1000	1.70E-03	**1.70E-03**		10	1000	**8.45E-04**	8.87E-04
			1.71E-03	6.64E-03				**8.47E-04**	1.28E-03
			1.01E-02	**8.67E-03**				1.01E-02	**1.01E-02**
			3.71E-03	5.42E-03				2.51E-03	**2.37E-03**
	15	1250	**3.58E-03**	8.04E-03		15	1250	**2.25E-03**	3.50E-03
			9.98E-03	**8.13E-03**				9.85E-03	**6.09E-03**
			1.52E-02	**9.04E-03**				1.63E-02	**9.38E-03**
			9.26E-03	**8.44E-03**				9.30E-03	**6.21E-03**

TABLE 7.5 Best, median, worst, and average IGD values for NSGA-III and EliteNSGA-III on M-objective WFG test problems. Best performing algorithm is shown in bold. Gray shade indicates a significance level of 0.05.

Problem	M	Max Gen	EliteNSGA-III	NSGA-III	Problem	M	Max Gen	EliteNSGA-III	NSGA-III
WFG4	3	400	**1.16E-03**	1.25E-03	WFG6	3	400	**1.65E-03**	1.73E-03
			1.21E-03	1.33E-03				**1.69E-03**	1.82E-03
			2.37E-03	**1.41E-03**				2.43E-03	**2.07E-03**
			1.29E-03	1.33E-03				**1.75E-03**	1.85E-03
	5	750	**1.67E-03**	1.68E-03		5	750	1.97E-03	**1.96E-03**
			1.70E-03	1.75E-03				2.04E-03	**2.03E-03**
			6.72E-03	**1.83E-03**				4.18E-03	**2.12E-03**
			2.24E-03	**1.75E-03**				2.44E-03	**2.03E-03**
	8	1500	**4.20E-03**	5.23E-03		8	1500	**4.56E-03**	6.12E-03
			4.36E-03	7.57E-03				**4.74E-03**	9.75E-03
			8.75E-03	1.25E-02				**1.20E-02**	1.25E-02
			5.72E-03	7.71E-03				**6.70E-03**	9.53E-03
	10	2000	**3.34E-03**	4.19E-03		10	2000	**3.92E-03**	4.85E-03
			3.56E-03	5.43E-03				**4.11E-03**	7.57E-03
			6.57E-03	7.67E-03				1.14E-02	**1.01E-02**
			4.27E-03	5.62E-03				**5.44E-03**	7.36E-03
	15	3000	**5.52E-03**	9.35E-03		15	3000	**8.47E-03**	1.09E-02
			9.75E-03	1.26E-02				**1.49E-02**	1.21E-02
			1.18E-02	1.57E-02				**1.64E-02**	2.02E-02
			8.67E-03	1.26E-02				**1.38E-02**	1.28E-02
WFG5	3	400	**8.85E-04**	1.04E-03	WFG7	3	400	**1.23E-03**	1.36E-03
			9.02E-04	1.09E-03				**1.28E-03**	1.44E-03
			1.02E-03	1.23E-03				**1.31E-03**	1.52E-03
			9.11E-04	1.10E-03				**1.27E-03**	1.43E-03
	5	750	**1.44E-03**	1.56E-03		5	750	**1.72E-03**	1.73E-03
			1.48E-03	1.60E-03				**1.77E-03**	1.78E-03
			2.08E-03	5.37E-03				6.02E-03	**1.87E-03**
			1.59E-03	1.79E-03				2.61E-03	**1.79E-03**
	8	1500	**3.18E-03**	3.63E-03		8	1500	**3.73E-03**	5.73E-03
			3.28E-03	6.04E-03				**4.38E-03**	7.95E-03
			9.50E-03	1.30E-02				**7.57E-03**	1.64E-02
			3.84E-03	6.84E-03				**5.04E-03**	8.45E-03
	10	2000	**2.79E-03**	2.84E-03		10	2000	**3.23E-03**	3.76E-03
			3.07E-03	4.34E-03				**4.71E-03**	5.97E-03
			6.73E-03	7.03E-03				**6.00E-03**	7.51E-03
			3.90E-03	4.52E-03				**4.69E-03**	5.79E-03
	15	3000	**3.84E-03**	8.28E-03		15	3000	**4.48E-03**	6.27E-03
			7.85E-03	1.16E-02				**7.62E-03**	1.07E-02
			1.08E-02	1.32E-02				**9.07E-03**	1.50E-02
			7.14E-03	1.15E-02				**7.42E-03**	1.08E-02

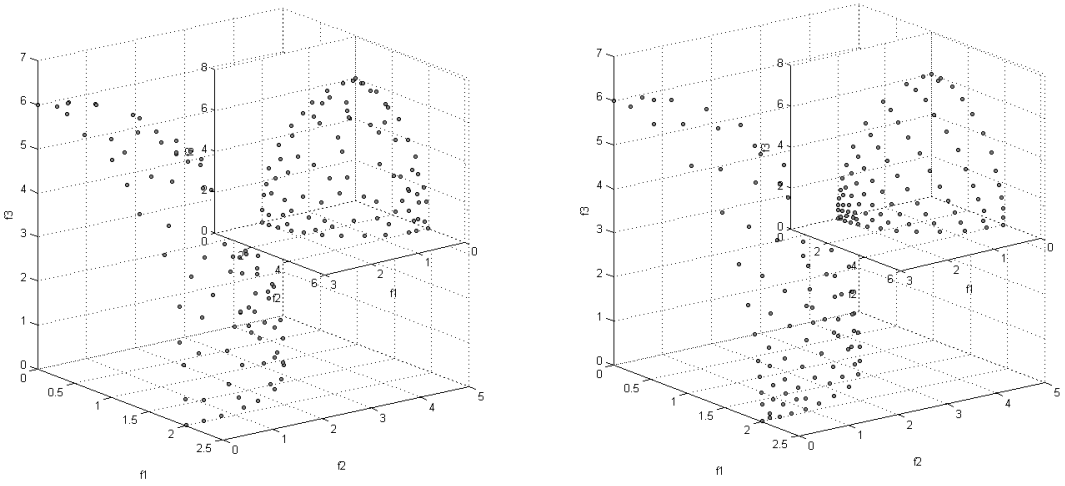

(a) NSGA-III (b) EliteNSGA-III

FIGURE 7-4 Obtained solutions by NSGA-III and EliteNSGA-III for WFG7 test problem.

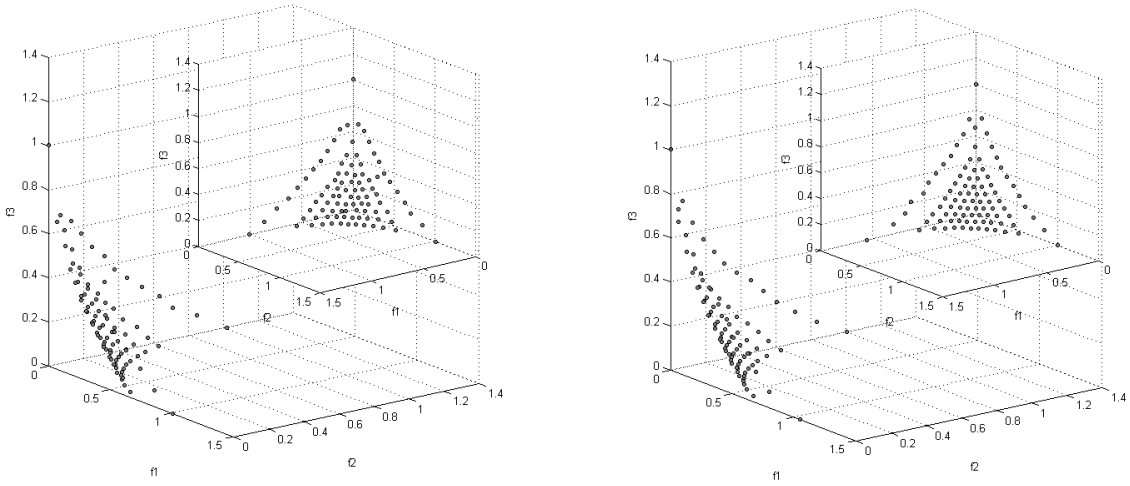

(a) NSGA-III (b) EliteNSGA-III

FIGURE 7-5 Obtained solutions by NSGA-III and EliteNSGA-III for convex DTLZ2 test problem.

7.4.3.2 Influence of EliteNSGA-III Archive

The main goal of the NSGA-III algorithm is to generate well-converged and well-distributed sets of solutions over multiple runs. However, as the number of objectives increase, NSGA-III loses its power to achieve this goal. In this section, we investigate the influence of an elite population archive on the distribution of obtained solutions throughout

the generation. Since NSGA-III continuously try to find one population member corresponding to each supplied reference point close to the Pareto-optimal front, we investigate the number of reference points associated with at least one solution member in every generation. Since the number of reference points are equivalent to the population size, a well-distributed solution set should have one member associated with one reference point.

Tables 7.7 to 7.9 present how many times (in terms of percentage) the target algorithm reached its goal for the 3- to 15-objective test problems listed in Table 7.1 over 20 runs. The goal is to associate 90% (for 3- to 8-objective test problems) and 80% (for 10- and 15-objective test problems) of the supplied reference points with at least one population member before the maximum generation is reached. The overall results show that as the number of objectives increase, the NSGA-III algorithm has difficulty maintaining well-distributed solutions throughout the generations.

However, from Table 7.7 we see that EliteNSGA-III is able to reach its goal 95% of the time as the dimension of DTLZ4 test problem reached 15 objectives. Moreover, for the WFG, with concave Pareto-optimal from test problems (WFG4 to WFG7), EliteNSGA-III is able to reach its goal 100% of the time as the WFG6 test problem dimension reached 15 objectives. Figure 7-6 and Figure 7-7 show the correlation between the number of reference points associated with at least one population member at each generation and the quality of the obtained Pareto-optimal solution set by the target algorithm.

When the number of reference points associated to at least one population member is high, it leads to achieving well-distributed Pareto-optimal front. From Figure 7-6 we see that both algorithms were able to diversify the population members and hence they are able to find well-distributed solutions for the 10-objective DTLZ4 problem. From Figure 7-7

TABLE 7.6 Best, median, worst, and average IGD values for NSGA-III and EliteNSGA-III on M-objective Convex DTLZ2, WFG1, and WFG2 test problems. Best performing algorithm is shown in bold. Gray shade indicates a significance level of 0.05.

Problem	M	Max Gen	EliteNSGA-III	NSGA-III	Problem	M	Max Gen	EliteNSGA-III	NSGA-III
DTLZ2Cvx	3	250	**5.48E-04**	**5.72E-04**	WFG2	3	250	**9.77E-04**	1.02E-03
			5.62E-04	**7.83E-04**				**1.06E-03**	1.13E-03
			5.96E-04	**2.04E-03**				**1.25E-03**	1.35E-03
			5.64E-04	**9.22E-04**				**1.06E-03**	1.15E-03
	5	750	**4.91E-04**	6.68E-04		5	500	**9.17E-04**	1.12E-03
			5.03E-04	7.66E-04				**9.67E-04**	1.81E-03
			1.33E-03	1.38E-03				**2.29E-03**	2.56E-03
			5.44E-04	8.44E-04				**1.03E-03**	1.86E-03
	8	2000	**1.42E-03**	2.08E-03		8	750	**1.67E-03**	1.92E-03
			1.69E-03	3.39E-03				**1.81E-03**	2.47E-03
			3.48E-03	5.39E-03				**3.20E-03**	4.21E-03
			2.06E-03	3.19E-03				**1.97E-03**	2.68E-03
	10	4000	**1.24E-03**	2.12E-03		10	1000	**1.08E-03**	1.35E-03
			2.14E-03	2.38E-03				**1.25E-03**	1.61E-03
			2.78E-03	3.90E-03				**1.86E-03**	2.32E-03
			2.11E-03	2.69E-03				**1.34E-03**	1.69E-03
	15	4500	1.76E-03	**1.75E-03**		15	1250	**1.93E-03**	2.44E-03
			2.54E-03	**2.24E-03**				**2.60E-03**	2.86E-03
			3.84E-03	**3.73E-03**				**3.53E-03**	4.84E-03
			2.56E-03	**2.33E-03**				**2.55E-03**	3.07E-03
WFG1	3	250	4.32E-03	**1.56E-03**					
			9.03E-03	**3.85E-03**					
			1.21E-02	**6.99E-03**					
			9.09E-03	**4.02E-03**					
	5	500	1.93E-03	**1.88E-03**					
			3.77E-03	**3.44E-03**					
			6.77E-03	7.15E-03					
			3.61E-03	4.00E-03					
	8	750	**2.04E-03**	2.53E-03					
			2.28E-03	3.15E-03					
			1.51E-02	**7.29E-03**					
			2.92E-03	3.27E-03					
	10	1000	**1.22E-03**	1.65E-03					
			1.38E-03	1.90E-03					
			1.56E-03	2.34E-03					
			1.38E-03	1.93E-03					
	15	1250	**3.05E-03**	3.33E-03					
			3.21E-03	3.55E-03					
			3.88E-03	3.92E-03					
			3.26E-03	3.55E-03					

we see that NSGA-III is not able to generate well-distributed solutions throughout the generations and resulting poorly dispersed sets of solutions for the 10-objective WFG6 problem. However, EliteNSGA-III is able to find well-distributed solutions over $f_i \in [0, 2i]$ for all ten objectives and a trade-off among them can be seen from the value path plots in Figure 7-7.

TABLE 7.7 The percentage of runs for which the target algorithm is able to associate 90% (for 3- to 8-objective) and 80% (for 10- and 15-objective DTLZ1 to DTLZ4 Test Problems) of the supplied reference points with at least one population member before the maximum generation is reached.

Problem	M	Max Gen	EliteNSGA-III	NSGA-III
DTLZ1	3	1000	100%	55%
	5	1500	90%	30%
	8	2000	40%	20%
	10	3000	30%	35%
	15	5000	15%	0%
DTLZ2	3	1000	100%	100%
	5	1500	90%	100%
	8	2000	45%	60%
	10	3000	70%	15%
	15	5000	80%	0%
DTLZ3	3	1000	100%	65%
	5	1500	100%	40%
	8	2000	45%	0%
	10	3000	30%	5%
	15	5000	40%	0%
DTLZ4	3	1000	95%	50%
	5	1500	100%	50%
	8	2000	80%	45%
	10	3000	95%	85%
	15	5000	95%	45%

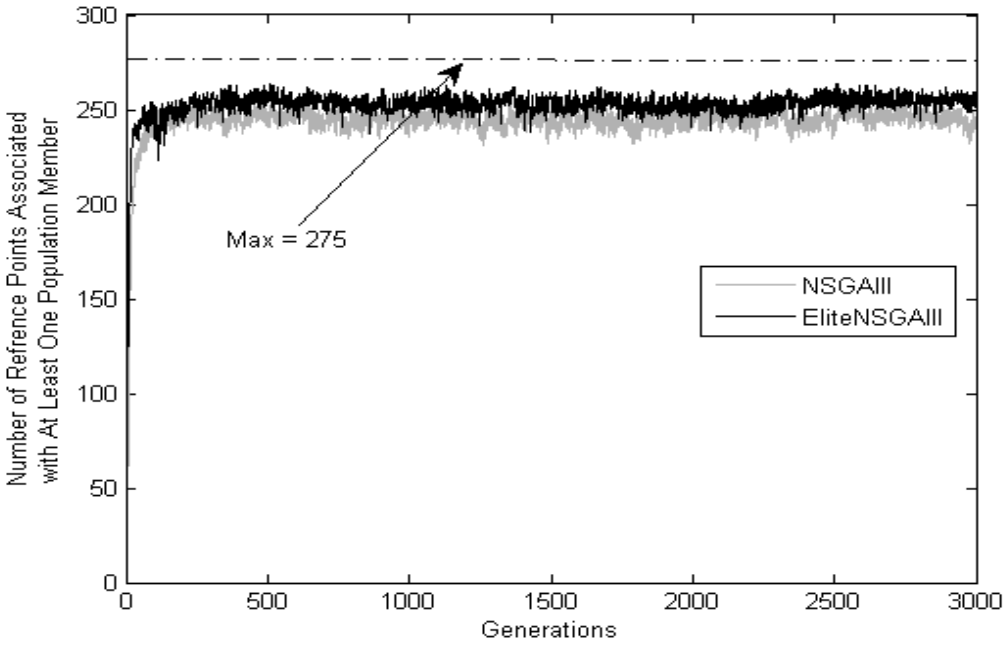

(a) DTLZ4 (10 Objectives)

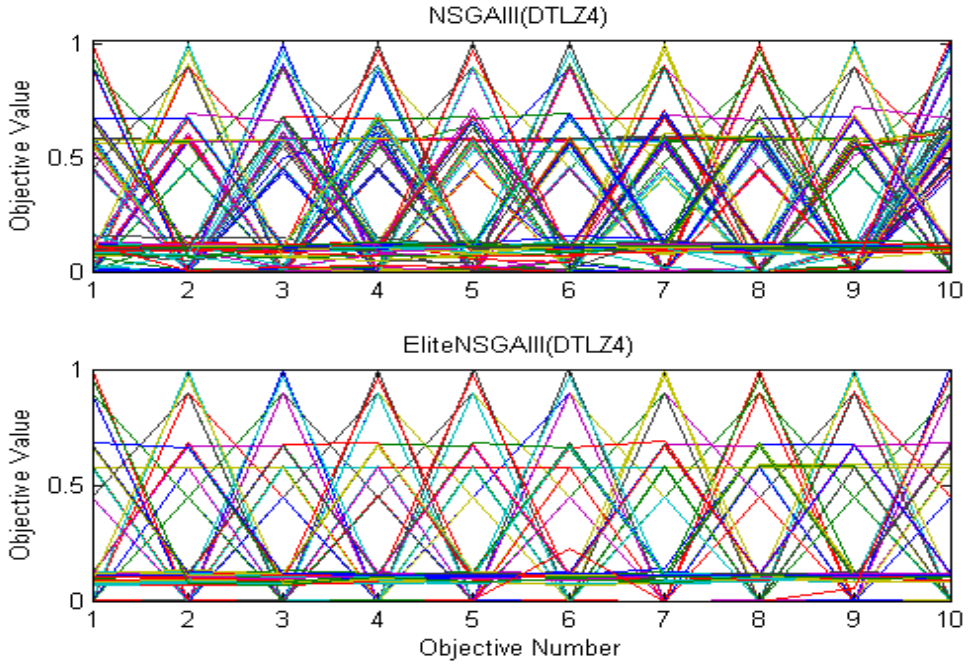

(b) DTLZ4 (10 Objectives)

FIGURE 7-6 Comparison of the number of reference points associated with at least one population member after each generation and value path plot for the obtained solutions by NSGA-III and EliteNSGA-III for DTLZ4 test problems with 10 objectives. Figure (a) shows the average value of 20 independent runs.

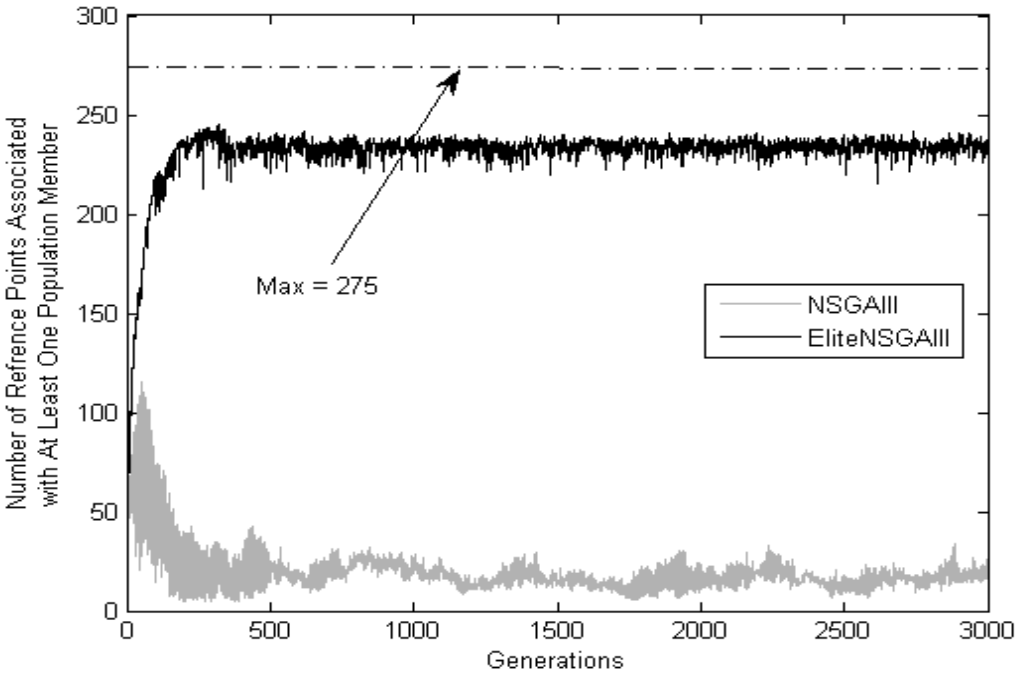

(a) WFG6 (10 Objectives)

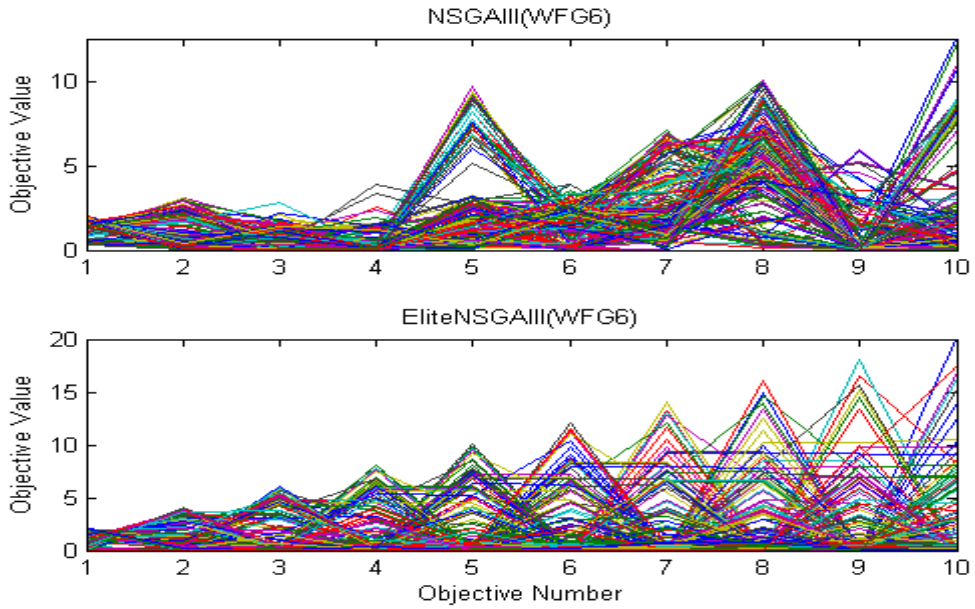

(b) WFG6 (10 Objectives)

FIGURE 7-7 Comparison of the number of reference points associated with at least one population member after each generation and value path plot for the obtained solutions by NSGA-III and EliteNSGA-III for WFG6 test problems with 10 objectives. Figure (a) show the average value of 20 independent runs.

TABLE 7.8 The Percentage of Runs for which the Target Algorithm is Able to Associate 90% for 3 to 8 objectives) and 80% (for 10- and 15-objective Convex DTLZ2, WFG1, and WFG2 Test Problems) of the Supplied Reference Points with at Least One Population Member before the Maximum Generation is Reached.

Problem	M	Max Gen	EliteNSGA-III	NSGA-III
DTLZ2Cvx	3	1000	100%	100%
	5	1500	100%	40%
	8	2000	65%	40%
	10	3000	40%	5%
	15	5000	40%	0%
WFG1	3	1000	10%	30%
	5	1500	0%	0%
	8	2000	0%	0%
	10	3000	0%	0%
	15	5000	0%	0%
WFG2	3	1000	100%	90%
	5	1500	100%	5%
	8	2000	90%	0%
	10	3000	90%	0%
	15	5000	70%	0%

TABLE 7.9 The Percentage of Runs for which the Target Algorithm is Able to Associate 90% (for 3 to 8 objectives) and 80% (for 10- and 15-objective WFG4 to WFG7 Test Problems) of the Supplied Reference Points with at Least One Population Member before the Maximum Generation is Reached.

Problem	M	Max Gen	EliteNSGA-III	NSGA-III
WFG4	3	1000	100%	100%
	5	1500	85%	40%
	8	2000	70%	0%
	10	3000	90%	0%
	15	5000	95%	0%
WFG5	3	1000	100%	100%
	5	1500	100%	25%
	8	2000	95%	0%
	10	3000	100%	25%
	15	5000	95%	10%
WFG6	3	1000	100%	100%
	5	1500	95%	0%
	8	2000	75%	0%
	10	3000	85%	5%
	15	5000	100%	0%
WFG7	3	1000	100%	100%
	5	1500	90%	0%
	8	2000	50%	0%
	10	3000	45%	0%
	15	5000	75%	0%

7.4.3.3 High Dimension Test Problems (25- and 50-objectives)

The third sets of experiment comprise of 25- and 50-objective test problems to investigate how NSGA-III cope with higher dimensional problems. Tables 7.10, 7.11, and 7.12, summarize the IGD metric values for linear and concave DTLZ problems (DTLZ1 to DTLZ4), convex DTLZ2 and WFG (WFG1 and WFG2) and concave WFG (WFG4 to WFG7) test problems, respectively. Figure 7-8 show the distribution of the obtained points for DTLZ1 problems for 10-, 15-, and 50-objectives. From these value path diagrams, it's clear that NSGA-III is not able to find well-distributed solutions as the problems' dimension increases to 50-objectives. Similarly, Figure 7-9 shows value path diagrams of the obtained solutions by NSGA-III and EliteNSGA-III as the problem dimension increases from 10- to 25- then 50-objectives for the WFG7 test problem. This figure indicates that NSGA-III is not able to find well-distributed solutions for 25- and 50-objectives.

Figure 7-9 (b) and (c) show that NSGA-III is not able to find solutions with larger $f1$ to $f6$ objective values for 25-objective as well as larger $f1$ to $f33$ objective values for 50-objective WFG7 test problem. On the other hand, EliteNSGA-III is able to find well-distributed solutions over $f_i \in [0,2i]$ for all 25 objectives and the trade-offs among them are evident from the value path plot in Figure 7-9 (b). Similarly, for the 50-objective WFG7 problem depicted in Figure 7-9 (c), Elite NSGA-III was able to find a well-distributed solutions for objectives $f15$ to $f50$.

7.5 Proposed Constraint-EliteNSGA-III Algorithm

Similar to constrained NSGA-III, constrained EliteNSGA-III needs to modify its population selection, parent selection, and elite archive update mechanisms. The

population selection mechanism for constrained EliteNSGA-III remains the same as constrained NSGA-III described in Section 6.2. In the next two subsections, we propose an extension to EliteNSGA-III in order to handle many-objective optimization problems with equality and inequality constraints.

TABLE 7.10 Best, median, worst, and average IGD values for NSGA-III and EliteNSGA-III on M-objective DTLZ test problems. Best performance algorithm is shown in bold. Gray shade indicates a significance level of 0.05.

Problem	M	Max Gen	EliteNSGA-III	NSGA-III
DTLZ1	25	5000	**1.36E-03**	1.48E-03
			2.50E-03	6.93E-03
			3.14E-03	8.28E-03
			2.45E-03	6.05E-03
	50	10000	**4.67E-03**	7.03E-03
			6.33E-03	1.58E-02
			1.01E-02	1.75E-02
			6.48E-03	1.42E-02
DTLZ2	25	2500	**3.15E-03**	5.71E-03
			4.91E-03	5.99E-03
			8.90E-03	**6.55E-03**
			5.26E-03	5.95E-03
	50	5000	**5.86E-03**	9.82E-03
			6.43E-03	1.25E-02
			7.90E-03	1.74E-02
			6.60E-03	1.29E-02
DTLZ3	25	5000	**1.85E-03**	2.17E-03
			2.72E-03	3.62E-03
			4.02E-03	1.59E+00
			2.83E-03	8.76E-02
	50	10000	**4.53E-03**	1.34E-02
			5.31E-03	1.47E-02
			6.71E-03	1.49E-02
			5.32E-03	1.46E-02
DTLZ4	25	6000	**1.29E-03**	1.34E-03
			8.72E-03	**2.63E-03**
			9.90E-03	**3.97E-03**
			7.39E-03	**2.49E-03**
	50	12000	1.12E-02	**9.54E-03**
			1.37E-02	**1.11E-02**
			1.43E-02	**1.24E-02**
			1.35E-02	**1.12E-02**

Algorithm 7.5 Constrained Recombination + Mutation (P_t, E_t) Procedure

Input: Parent population P_t, elite population E_t

Output: Q_t

1: $Q_t = \emptyset$
2: s_P = size (P_t)
3: s_E = size (E_t)
4: **for** $i = 1\ to\ s_P/2$
    //select the first parent from P_t based on Definition 3
5: $r_1 = rand(1, s_P)$
6: $r_2 = rand(1, s_P)$, $r_1 \neq r_2$
7: p_P^1 = `binaryTournament`$(P_t(r_1), P_t(r_2))$
    //select the second parent from P_t
8: $r_1 = rand(1, s_P)$, $P_t(r_1) \neq p_P^1$
9: $r_2 = rand(1, s_P)$, $r_1 \neq r_2$ and $P_t(r_2) \neq p_P^1$
10: p_P^2 = `binaryTournament`$(P_t(r_1), P_t(r_2))$
    //select the first parent from E_t
11: $r_1 = rand(1, s_E)$, $E(r_1) \neq null$
12: $r_2 = rand(1, s_E)$, $r_1 \neq r_2$ and $E(r_2) \neq null$
13: p_E^1 = `binaryTournament`$(E_t(r_1), E_t(r_2))$
    //select the second parent from E_t
14: $r_1 = rand(1, s_E)$, $E(r_1) \neq null$ and $E_t(r_1) \neq p_E^1$
15: $r_2 = rand(1, s_E)$, $r_1 \neq r_2$ and $E(r_2) \neq null$ and $E_t(r_2) \neq p_E^1$
16: p_E^2 = `binaryTournament`$(E_t(r_1), E_t(r_2))$
17: $p_1 = rand < 0.5\ ?\ p_P^1 : p_E^1$
18: $p_2 = rand < 0.5\ ?\ p_P^2 : p_E^2$
19: $[o_1, o_2]$ = `crossover + mutation` (p_1, p_2)
20: $Q_t = Q_t \cup [o_1, o_2]$
21: **end for**

7.5.1 Modification in Creation of Offspring

Recall that in the EliteNSGA-III, first, we randomly select two parents from the elite archive (p_E^1 and p_E^2) and two parents from the current population (p_P^1 and p_P^2). Then, we select two parents from p_E^1, p_E^2, p_P^1, and p_P^2 with equal probability to create offspring population. However, when we are dealing with constrained problems, the selection mechanism needs to be updated to discriminate feasible solutions over infeasible solutions.

Therefore, we introduce constrained-domination binary tournament (see Definition 3) to select parents from the elite archive and current population. Algorithm 7.5 describes the overall procedure of offspring creation mechanism utilized in constrained EliteNSGA-III algorithm.

TABLE 7.11 Best, median, worst, and average IGD values for NSGA-III and EliteNSGA-III on M-objective DTLZ test problems. Best performance algorithm is shown in bold. Gray shade indicates a significance level of 0.05.

Problem	M	Max Gen	EliteNSGA-III	NSGA-III
WFG4	25	5000	**4.47E-03**	6.47E-03
			6.26E-03	8.01E-03
			7.59E-03	1.08E-02
			6.08E-03	8.12E-03
	50	10000	**1.38E-02**	1.73E-02
			1.64E-02	1.80E-02
			2.03E-02	2.16E-02
			1.62E-02	1.84E-02
WFG5	25	5000	**3.03E-03**	4.38E-03
			4.79E-03	8.55E-03
			6.54E-03	1.18E-02
			4.81E-03	8.05E-03
	50	10000	**6.24E-03**	1.44E-02
			1.16E-02	1.55E-02
			1.38E-02	1.73E-02
			1.12E-02	1.56E-02
WFG6	25	5000	7.48E-03	**7.16E-03**
			9.44E-03	**8.68E-03**
			1.05E-02	1.21E-02
			9.32E-03	**9.05E-03**
	50	10000	**2.45E-02**	2.47E-02
			2.74E-02	2.78E-02
			2.85E-02	3.03E-02
			2.71E-02	2.75E-02
WFG7	25	5000	**3.84E-03**	5.34E-03
			5.19E-03	6.44E-03
			7.67E-03	**6.99E-03**
			5.42E-03	6.31E-03
	50	10000	**8.57E-03**	1.73E-02
			1.14E-02	1.79E-02
			1.55E-02	2.01E-02
			1.15E-02	1.79E-02

TABLE 7.12 Best, median, worst, and average IGD values for NSGA-III and EliteNSGA-III on M-objective Convex DTLZ2, WFG1, and WFG2 test problems. Best performance algorithm is shown in bold. Gray shade indicates a significance level of 0.05.

Problem	M	Max Gen	EliteNSGA-III	NSGA-III
DTLZ2Cvx	25	8000	**1.21E-03**	1.58E-03
			1.58E-03	1.92E-03
			2.01E-03	2.99E-03
			1.57E-03	1.97E-03
	50	14000	**4.66E-03**	4.92E-03
			5.73E-03	**5.44E-03**
			7.06E-03	8.46E-03
			5.76E-03	**5.71E-03**
WFG1	25	5000	**1.45E-03**	1.84E-03
			1.68E-03	1.94E-03
			1.89E-03	2.28E-03
			1.68E-03	1.99E-03
	50	10000	**8.24E-03**	9.01E-03
			8.99E-03	9.80E-03
			9.61E-03	1.11E-02
			8.94E-03	9.89E-03
WFG2	25	5000	**1.06E-03**	1.35E-03
			1.28E-03	1.48E-03
			1.84E-03	2.30E-03
			1.32E-03	1.52E-03
	50	10000	**5.65E-03**	5.89E-03
			7.38E-03	**6.42E-03**
			9.85E-03	1.82E-02
			7.32E-03	8.43E-03

7.5.2 Modification in Constrained Elite Archive Update

In EliteNSGA-III, the elite archive is updated in every generation so that the archive contains only one best candidate solution per reference point. An elite member in location i is replaced by a new candidate solution if and only if there is a candidate solution associated with reference i that has shorter Euclidian distance to the origin than the current elite member. However, in the presence of candidate solutions, the elite archive is updated based the following procedure.

Algorithm 7.6 Constrained UpdateElite (Z^r, P_t, E_t) Procedure

Input: References points on normalized hyper-plane Z^r: each $\boldsymbol{z} \in Z^r$ identified by its location 1…$|Z^r|$, Parent population P_t, elite population E_t,

Output: E_{t+1}

1: Associate each member $\boldsymbol{p}$ of P_t with a reference point:
$[\pi(\boldsymbol{p}), d(\boldsymbol{p})]$ = `Associate`(P_t, Z^r) // $\pi(\boldsymbol{p})$: closest reference point, *d:* perpendicular distance from $\boldsymbol{p}$ to $\pi(\boldsymbol{p})$
2: **for** $i = \boldsymbol{p} \in P_t$
3: //Find the location of the reference point associated with $\boldsymbol{p}$:
4: loc = location ($\pi(\boldsymbol{p})$)
//update elite archive based on definition 2 and Euclidian distance of solution to the ideal point
5: **if** $\boldsymbol{p}$ is feasible and $E_t(loc)$ is infeasible **then**
6: $E_{t+1}(loc) = \boldsymbol{p}$
7: **else if** $\boldsymbol{p}$ is feasible and $E_t(loc)$ is feasible **then**
//Calculate the Euclidian distance between $\boldsymbol{p}$ and the //ideal point as well as $E_t(loc)$ and the ideal point:
8: $d_1 = dist(\boldsymbol{p}, z^{min})$
9: $d_2 = dist(E_t(loc), z^{min})$
10: **if** $d_1 < d_2$ **then**
11: $E_{t+1}(loc) = \boldsymbol{p}$
12: **end if**
13: **else if** $\boldsymbol{p}$ and $E_t(loc)$ are infeasible **then**
//compare $\boldsymbol{p}$ and $E_t(loc)$ based on constraint //violation value
14: **if** $CV(\boldsymbol{p}) < CV(E_t(loc))$ **then**
15: $E_{t+1}(loc) = \boldsymbol{p}$
16: **end if**
17: **end if**
18: **end for**

Definition 4: An elite member candidate solution located at i (e_i) is replaced by a candidate solution associated to reference point i (p_i),

1) if p_i is feasible and e_i is infeasible;
2) if p_i and e_i are infeasible and p_i has a smaller constraint violation value; or,
3) if p_i and e_i are feasible and $dist(p_i)$ is smaller than $dist(e_i)$, where $dist$ is the Euclidian distance from the solution to the origin. Algorithm 5 describes the overall

procedure of updating elite archive in the presence of infeasible candidate solutions in the population.

Algorithm 7.6 presents constrained EliteNSGA-III's elite population archive update in every generation.

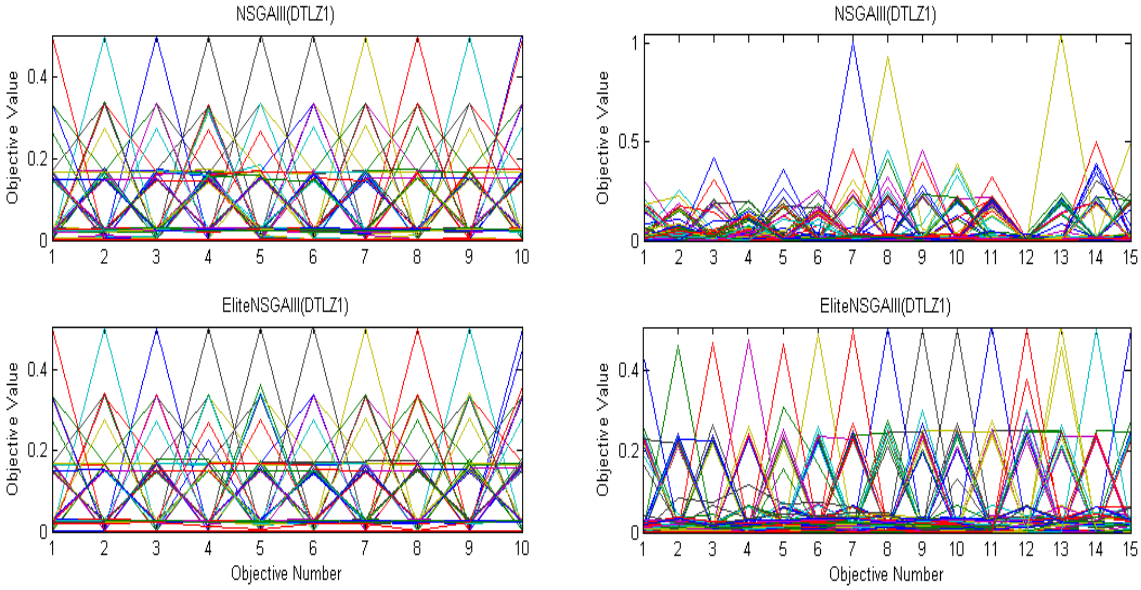

(a) DTLZ1 (10 objectives) (b) DTLZ1 (15 objectives)

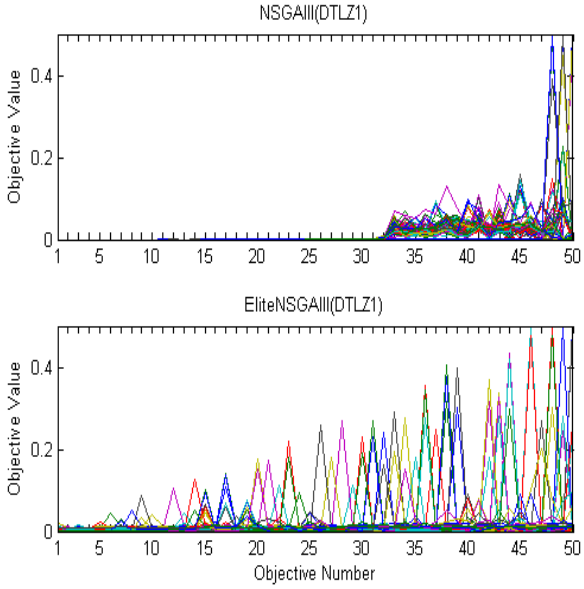

(c) DTLZ1 (50 objectives)

FIGURE 7-8 Value path plot comparison of the obtained solutions by NSGA-III and EliteNSGA-III for DTLZ1 test problem as the dimension increases from 10- to 15-, then to 50-objectives.

7.6 Experimental Setup and Results for Constraint-EliteNSGA-III

In this section, we present the results of the proposed constraint-EliteNSGA-III and constraint-NSGA-III algorithms.

7.6.1 Test Problems

In order to test performance of the proposed algorithm, we have used three types of constrained many-objective test problems introduced in [112] [113] (six problems in total).

Type-1 (C1-DTLZ1 and C2-DTLZ3) constrained problems contain the original DTLZ1 and DTLZ3 test problems. However, two constraints are added to create a barrier in approaching the original Pareto-optimal front. The C1-DTLZ1 test problem has a narrow feasible region surrounded by the infeasible region and this introduces a minor difficulty for optimizers to converge to the true Pareto-optimal front. The C1-DTLZ3 introduces a band of infeasible region adjacent to the Pareto-optimal front. Therefore, this creates the highest level of difficulty for optimizers to converge to the true Pareto-optimal front as they need to penetrate the band of the infeasible region as they travel from feasible to infeasible then to feasible region. Table 7.13 describes the constraints added to the original DTLZ1 and DTLZ3 problems and illustrates the feasible and the Pareto-optimal front of two-objective C1-DTLZ1 and C1-DTLZ3 problems.

Type-2 (C2-DTLZ2 and Convex C2-DTLZ2) constrained problems comprise of the original DTZL2 and Convex DTLZ2 test problems. However, two constraints are added to introduce patch of feasible and infeasible regions to the original Pareto-optimal front. These problems are designed to assess the optimizers' ability in dealing with discontinuities in the Pareto-optimal fronts. Table 7.13 describes the constraints added to

the original DTLZ2 and Convex DTLZ2 problems and illustrates the feasible and the Pareto-optimal front of two-objective C2-DTLZ2 and Convex C2-DTLZ2 problems.

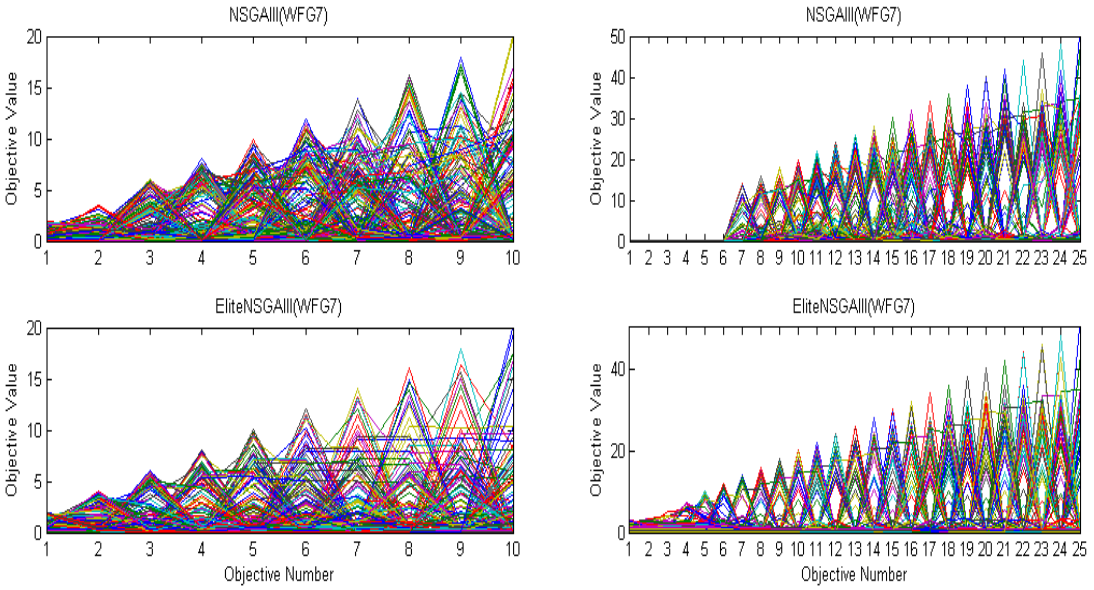

(a) WFG7 (10 objectives) (b) WFG7 (25 objectives)

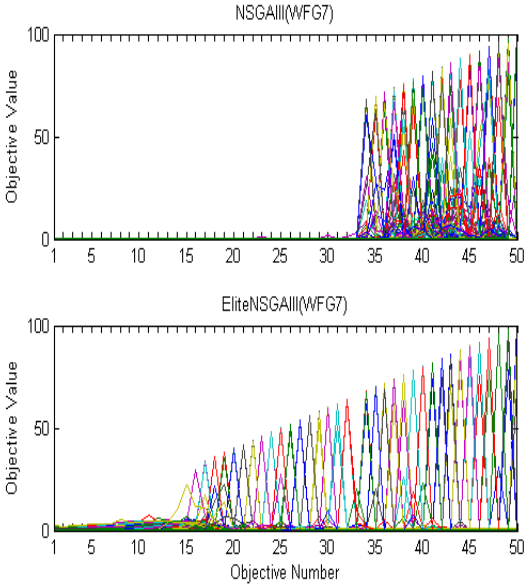

(c) DTLZ1 (50 objectives)

FIGURE 7-9 Value path plot comparison of the obtained solutions by NSGA-III and EliteNSGA-III for WFG7 test problem as the dimension increases from 10- to 25-, then to 50-objectives.

Type-3 (C3-DTLZ1 and C3-DTLZ4) constrained problems contain the original DTZL1 and DTLZ4 test problems. However, M constraints are added to original problems so that the original Pareto-optimal front is no longer optimal. Instead, the new Pareto-optimal front is created by portions of constraint surfaces. These problems are deigned to assess the optimizers' ability to stay on the newly created Pareto-optimal surface. Table 7.13 describes the constraints added to the original DTLZ1 and DTLZ4 problems and illustrates the feasible and the Pareto-optimal front of two-objective C3-DTLZ1 and Convex C3-DTLZ4 problems.

7.6.2 Parameter and Experimental Settings

To maintain the consistency and fair comparison of NSGA-III and EliteNSGA-III algorithms, parameter and experimental setting were kept similar to the original NSGA-III [112] [113] study. Table 7.2 presents the parameters used by the NSGA-III and EliteNSGA-III algorithms. Also, a portion of Table 7.3 (for M = {3, 5, 8, 10 15}) shows the number of reference points (H), the population size (N), and the number of inner and outer divisions used for different dimensions of test problems.

All algorithms were executed 20 times independently and the best, the worst, the median, and the average results of each algorithm are reported. Furthermore, the Wilcoxon's signed rank statistical test is conducted at a 5% significance level in order to evaluate the statistical significance of obtained results. To evaluate the performance of the proposed algorithm, we have used the IGD measure with reference PF constructed from the combination of results obtained in all executions and then selecting non-dominated solutions. In addition, for all experiments the closest (maximum of one point) Pareto-optimal point to the reference point is considered.

TABLE 7.13 Constrained test problems [112] [113]

Type	Problem	Constraints	Shape
Type-1	C1-DTLZ1	$c(\mathbf{x}) = \frac{f_M(\mathbf{x})}{0.6} - \sum_{i=1}^{M-1} \frac{f_i(\mathbf{x})}{0.5} \geq 0$	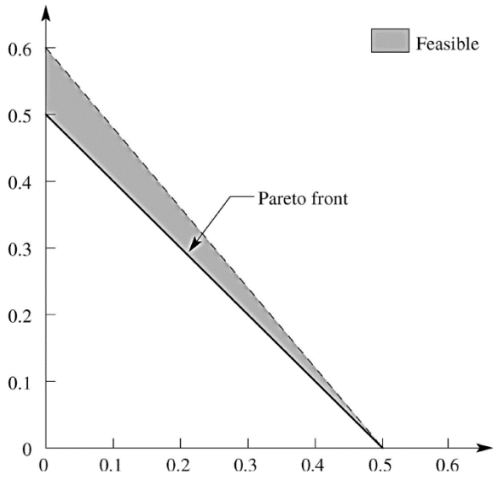
	C1-DTLZ3	$c(\mathbf{x}) = \left(\sum_{i=1}^{M} f_i(\mathbf{x})^2 - 16\right) - (\sum_{i=1}^{M} f_i(\mathbf{x})^2 - r^2) \geq 0$ $r = \{9, 12.5, 12.5, 15, 15\}$ for $M = \{3, 5, 8, 10, 15\}$	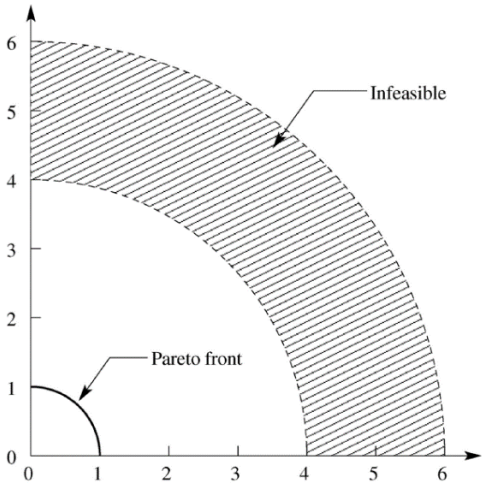
Type-2	C2-DTLZ2	$c(\mathbf{x}) = -\min\left\{\min_{i=1}^{M}\left[(f_i(\mathbf{x}) - 1)^2 + \sum_{i=1, j\neq i}^{M} f_j(\mathbf{x})^2 - r^2\right], \left[\sum_{i=1}^{M}\left(f_i(\mathbf{x}) - \frac{1}{\sqrt{M}}\right)^2 - r^2\right]\right\} \geq 0$ $r = 0.4$ for $M = 3$ and $r = 0.4$ $M > 3$.	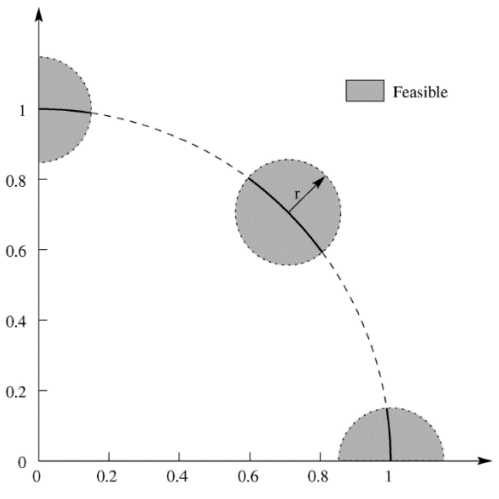

Type	Problem	Constraints	Shape
	Convex C2-DTLZ2	$c(\mathbf{x}) = \sum_{i=1}^{M} (f_i(\mathbf{x}) - \lambda)^2 - r^2 \geq 0$ $\lambda = \frac{1}{M} \sum_{i=1}^{M} f_i(\mathbf{x})^2$ r = {0.225, 0.225, 0.26, 0.26, 0.27} for M = {3, 5, 8, 10, 15}	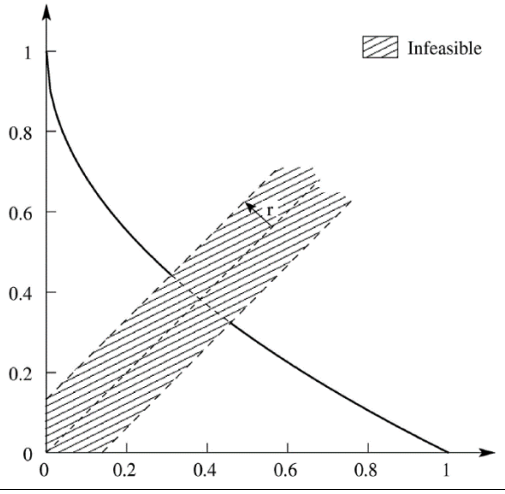
Type-3	C3-DTLZ1	$c_j(\mathbf{x}) = f_j(\mathbf{x}) + \sum_{i=1, j \neq i}^{M} \frac{f_i(\mathbf{x})}{0.5} - 1 \geq 0 \quad \forall j = 1, 2, \ldots, M$	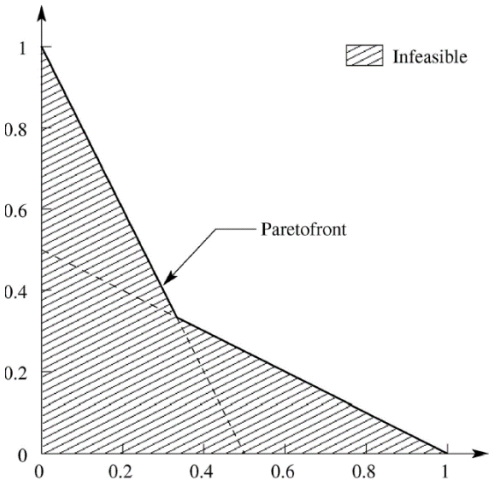
	C3-DTLZ4	$c_j(\mathbf{x}) = \frac{f_j(\mathbf{x})}{4} + \sum_{i=1, j \neq i}^{M} f_i(\mathbf{x})^2 - 1 \geq 0 \quad \forall j = 1, 2, \ldots, M$	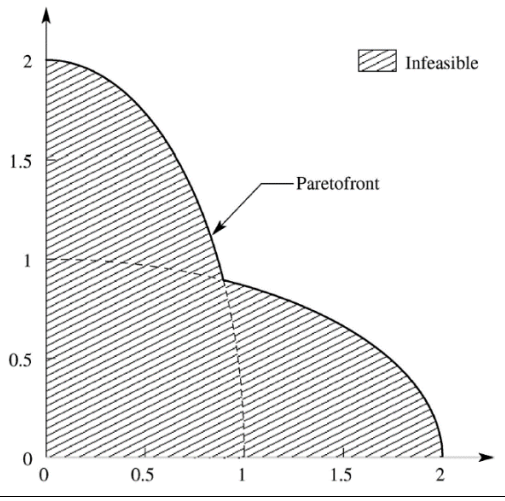

TABLE 7.14 Best, median, worst, and average IGD values for EliteNSGA-III and NSGA-III on M-objective Type-1 constrained test problems. Best performance algorithm is shown in bold. Gray shade indicates a significance level of 0.05.

Problem	M	Max Gen	EliteNSGA-III	NSGA-III
C1-DTLZ1	3	500	7.00E-04	**6.75E-04**
			1.12E-03	1.06E-03
			5.64E-03	5.24E-03
			1.57E-03	1.26E-03
	5	1000	5.83E-04	**5.81E-04**
			1.45E-03	**5.95E-04**
			5.42E-03	6.85E-03
			1.97E-03	**9.09E-04**
	8	1500	**1.63E-03**	1.64E-03
			3.57E-03	4.21E-03
			6.41E-03	8.72E-03
			3.80E-03	4.58E-03
	10	2000	**1.61E-03**	1.62E-03
			4.70E-03	7.11E-03
			6.19E-03	7.24E-03
			4.12E-03	5.67E-03
	15	3000	**4.33E-03**	6.01E-03
			7.26E-03	1.29E-02
			1.21E-02	2.45E-02
			7.72E-03	1.29E-02
C1-DTLZ3	3	1000	**7.82E-04**	1.21E-03
			8.25E-04	2.51E-03
			9.89E-04	1.47E-02
			8.39E-04	3.71E-03
	5	1500	**4.11E-03**	4.33E-03
			4.46E-03	6.36E-03
			1.04E-02	1.16E-02
			5.08E-03	7.06E-03
	8	2500	**2.14E-03**	8.34E-03
			4.71E-03	1.28E-02
			1.59E-02	**1.58E-02**
			6.53E-03	1.20E-02
	10	3500	**2.13E-03**	4.76E-03
			6.40E-03	6.60E-03
			1.08E-02	**9.33E-03**
			5.95E-03	6.84E-03
	15	5000	**5.67E-03**	1.08E-02
			1.04E-02	1.49E-02
			2.63E-02	3.12E-02
			1.08E-02	1.56E-02

TABLE 7.15 Best, median, worst, and average IGD values for EliteNSGA-III and NSGA-III on M-objective Type-2 constrained test problems. Best performance algorithm is shown in bold.

Problem	M	Max Gen	EliteNSGA-III	NSGA-III
C2-DTLZ2	3	250	**3.78E-04**	5.86E-04
			4.61E-04	7.15E-04
			7.10E-04	1.80E-02
			4.83E-04	2.24E-03
	5	500	**4.92E-04**	6.02E-04
			5.36E-04	7.76E-04
			1.29E-02	**1.18E-02**
			2.76E-03	**1.73E-03**
	8	750	**3.12E-03**	3.24E-03
			2.15E-02	**2.01E-02**
			2.72E-02	2.77E-02
			1.99E-02	**1.60E-02**
	10	1000	2.53E-03	**2.38E-03**
			1.45E-02	**1.34E-02**
			2.15E-02	**1.47E-02**
			1.37E-02	**1.05E-02**
	15	1250	**6.05E-03**	1.86E-02
			1.56E-02	2.33E-02
			3.03E-02	3.07E-02
			1.66E-02	2.44E-02
C2-DTLZ2Cvx	3	250	**7.72E-04**	1.01E-03
			8.07E-04	1.32E-03
			1.13E-03	1.90E-03
			8.27E-04	1.35E-03
	5	750	**6.71E-04**	1.03E-03
			7.23E-04	1.43E-03
			7.73E-04	1.80E-03
			7.25E-04	1.42E-03
	8	1500	**2.16E-03**	2.76E-03
			6.15E-03	**5.08E-03**
			8.28E-03	**7.86E-03**
			5.21E-03	**5.09E-03**
	10	2500	**1.57E-03**	2.55E-03
			4.93E-03	**4.41E-03**
			6.78E-03	7.91E-03
			4.17E-03	4.87E-03
	15	3500	**3.53E-03**	8.00E-03
			9.87E-03	**9.20E-03**
			2.14E-02	**1.30E-02**
			9.65E-03	**9.37E-03**

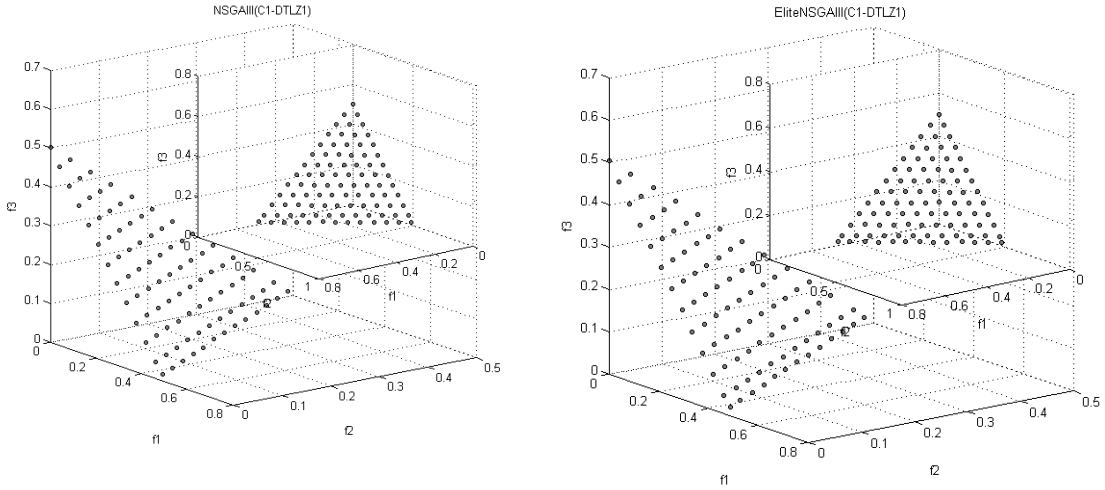

(a) NSGA-III (b) EliteNSGA-III

FIGURE 7-10 Obtained solutions by NSGA-III and EliteNSGA-III for 3-objective C1-DTLZ1 test problem.

7.6.3 Experimental Results and Discussion

To evaluate the performance of the proposed algorithm, we have conducted three sets of experiments with constrained test problems containing 3- to 15 objectives. The first experiment series investigates how the proposed algorithm copes with problems containing barriers in approaching the Pareto-optimal front. The second experiment series examines the capability of EliteNSGA-III in tackling discontinuities created by constraints in the Pareto-optimal front. The last experiment series investigates the ability of the proposed algorithm when the Pareto-optimal surface is created by portions of added constrained surface.

7.6.3.1 Type-1 Constrained Problems

The Type-1 constrained problems challenges the ability of optimizers to penetrate the barrier created by the constraints in order to reach the global Pareto-optimal front. Figure

7-10 show obtained solutions by the NSGA-III and EliteNSGA-III for 15-objective C1-DTLZ1 test problem. From this diagram, we can see that both algorithms are able to find fairly distributed solutions. However, Table 7.14 shows that EliteNSGA-III outperforms NSGA-III as the number of objectives grow to 15 objectives. When it comes to C3-DTLZ3 test problem, both algorithms are not able to reach the global Pareto-optimal front within the allotted amount of generations in any of the 20 runs. This challenge is caused by the large band of barrier present in the test problem. Recall that the combined population, R_t, in both algorithms, is sorted according to constraint-domination mechanism. As a result, the only way this barrier can be penetrated when either the majority of the combined population are infeasible or the combined population contains at least one solution in the feasible region close to the Pareto-optimal front (this is mainly achieved through the mutation operator). Figure 7-11 depicts obtained solutions by the NSGA-III and EliteNSGA-III for the 3-objectie C1-DTLZ3 test problem. Even though both algorithms are not able to reach the global Pareto-optimal front, Table 7.14 shows that EliteNSGA-III outperforms NSGA-III in all instances of this problem.

7.6.3.2 Type-2 Constrained Problems

These benchmark problems test the optimizers' ability in dealing with discontinuities created by constraints on the Pareto-optimal front surface. Figure Figure 7-12 illustrates obtained solutions by the NSGA-III and EliteNSGA-III for 3-objective C2-DTLZ2 problem. It can be observed that both algorithms are able to find well-distributed disconnected Pareto-optimal fronts for the 3-objective C2-DTLZ2 problem. Also, the value path plot comparison in the Figure 7-13 shows similar distribution obtained by NSGA-III and EliteNSGA-III for the 8-objective C2-DTLZ2 test problem. However, from Figure

7-14 it can be seen that EliteNSGA-III is able to find well-distributed Pareto-optimal solutions for 3-objective Convex C2-DTLZ2 problem than NSGA-III. In overall, from Table 7.15, we observe that either of the algorithms did not exhibit statistical significance performance for the majority of the instances, however, EliteNSGA-III was able to significantly outperform NSGA-III on 15-objective C2-DTLZ2 and 3- and 5-objective Convex C2-DTLZ2 test problems.

7.6.3.3 Type-3 Constrained Problems

Type-3 constrained problems are designed to test the ability of an optimizer to stay on the Pareto-optimal front created by portions of constraint surface. Figure 7-15 and Figure 7-16 show the obtained solutions by the NSGA-III and EliteNSGA-III for 3-objective C3-DTLZ1 and C3-DTLZ4 problems. It can be seen that EliteNSGA-III is able to find well-distributed solutions over the entire PF. Table 7.16 shows that EliteNSGA-III significantly outperformed NSGA-III on all instances of the C3-DTLZ1 problem. On the other hand, the value path diagram, shown in Figure 7-17, illustrates that both algorithms are able to generate well-distributed solutions over $f_i \in [0, 2i]$ for all ten objectives and a trade-off among them. However, from Figure 7-18 and Table 7.16 (for 10- and 15-objective C3-DTLZ problems) we can see that part of the final population (individuals located in infeasible region) of EliteNSGA-III were eliminated due constraint-domination sorting mechanism utilized in both algorithms.

TABLE 7.16 Best, median, worst, and average IGD values for EliteNSGA-III and NSGA-III on M-objective Type-3 constrained test problems. Best performance algorithm is shown in bold. Gray shade indicates a significance level of 0.05.

Problem	M	Max Gen	EliteNSGA-III	NSGA-III
C3-DTLZ1	3	750	**7.62E-04**	1.24E-03
			8.79E-04	1.57E-03
			1.04E-03	3.85E-03
			8.94E-04	1.83E-03
	5	1500	**8.20E-04**	9.22E-04
			9.09E-04	1.91E-03
			3.00E-03	1.51E-02
			1.11E-03	3.73E-03
	8	2000	**2.05E-03**	2.85E-03
			5.19E-03	1.50E-02
			8.50E-03	1.91E-02
			4.77E-03	1.37E-02
	10	3000	3.38E-03	**2.16E-03**
			5.01E-03	1.61E-02
			9.01E-03	1.88E-02
			5.35E-03	1.36E-02
	15	4000	**4.24E-03**	8.22E-03
			7.96E-03	1.81E-02
			1.39E-02	2.48E-02
			7.70E-03	1.79E-02
C3-DTLZ4	3	750	**9.37E-04**	1.01E-03
			1.39E-03	1.54E-03
			8.31E-03	1.34E-02
			2.43E-03	2.70E-03
	5	1500	**7.10E-04**	7.47E-04
			8.14E-04	1.15E-03
			2.01E-03	2.06E-03
			1.00E-03	1.21E-03
	8	2000	**1.48E-03**	1.66E-03
			1.61E-03	1.94E-03
			7.12E-03	7.29E-03
			2.56E-03	2.59E-03
	10	3000	**1.13E-03**	1.17E-03
			1.19E-03	1.30E-03
			4.66E-03	**3.16E-03**
			2.30E-03	**1.58E-03**
	15	4000	8.91E-03	**6.71E-03**
			1.23E-02	**8.92E-03**
			1.30E-02	**1.08E-02**
			1.19E-02	**8.74E-03**

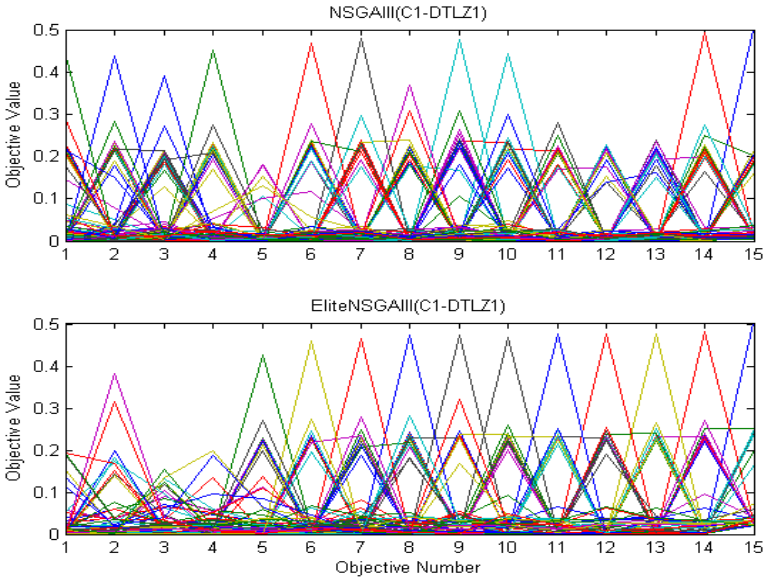

FIGURE 7-11 Value path plot comparison of the obtained solutions by NSGA-III and EliteNSGA-III for 15-objective C1-DTLZ1 test problem.

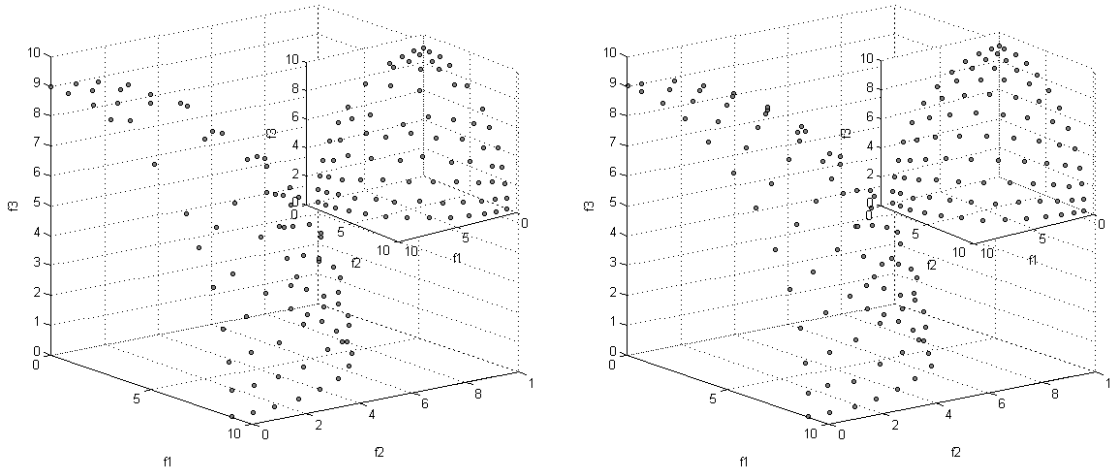

(a) NSGA-III (b) EliteNSGA-III

FIGURE 7-12 Obtained solutions by NSGA-III and EliteNSGA-III for 3-objective C1-DTLZ3 test problem.

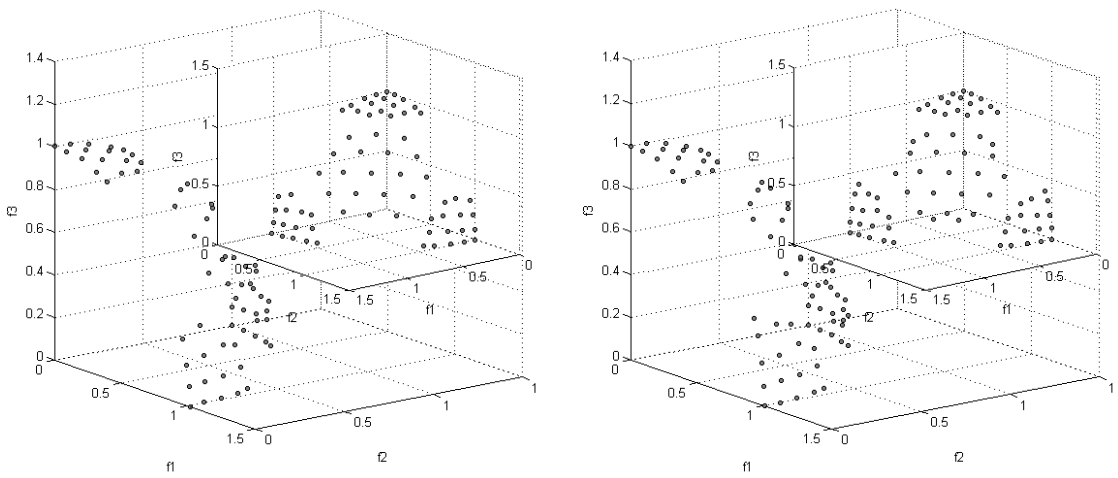

(a) NSGA-III (b) EliteNSGA-III

FIGURE 7-13 Obtained solutions by NSGA-III and EliteNSGA-III for 3-objective C2-DTLZ2 test problem.

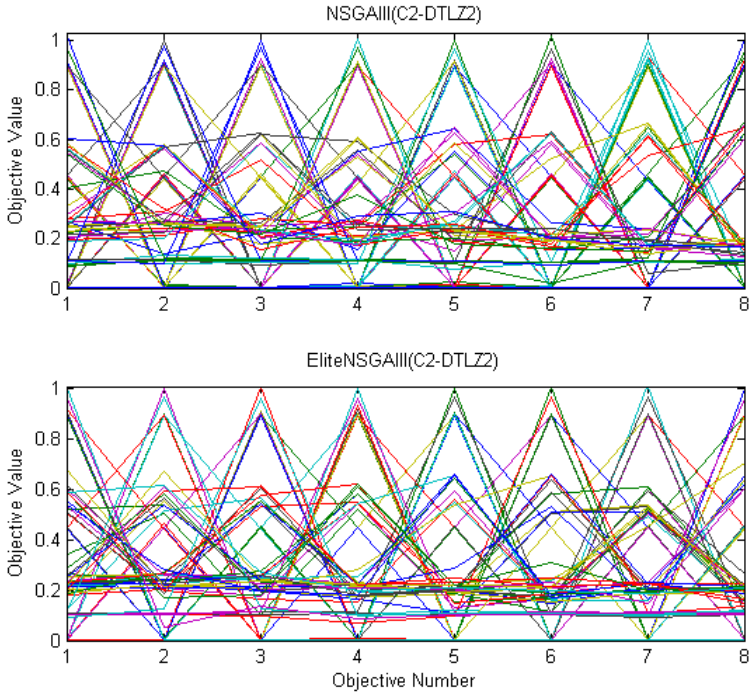

FIGURE 7-14 Value path plot comparison of the obtained solutions by NSGA-III and EliteNSGA-III for 8-objective C2-DTLZ2 test problem.

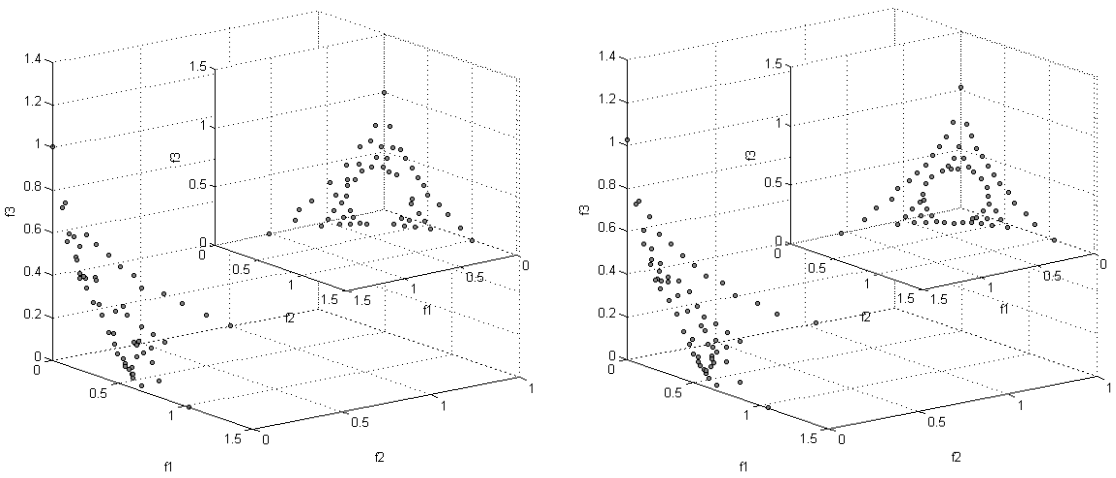

(a) NSGA-III (b) EliteNSGA-III

FIGURE 7-15 Obtained solutions by NSGA-III and EliteNSGA-III for 3-objective Convex C2-DTLZ2 test problem.

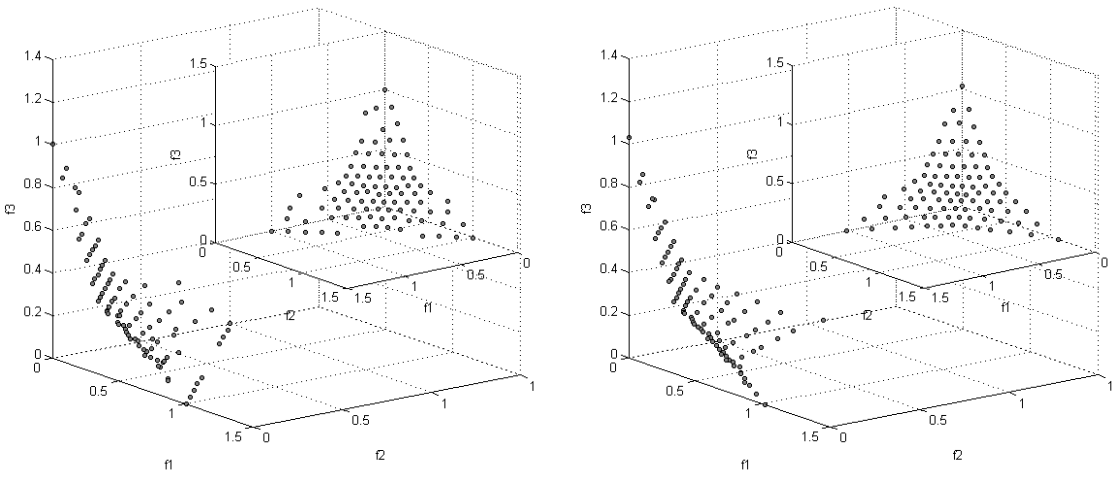

(a) NSGA-III (b) EliteNSGA-III

FIGURE 7-16 Obtained solutions by NSGA-III and EliteNSGA-III for 3-objective C3-DTLZ1 test problem.

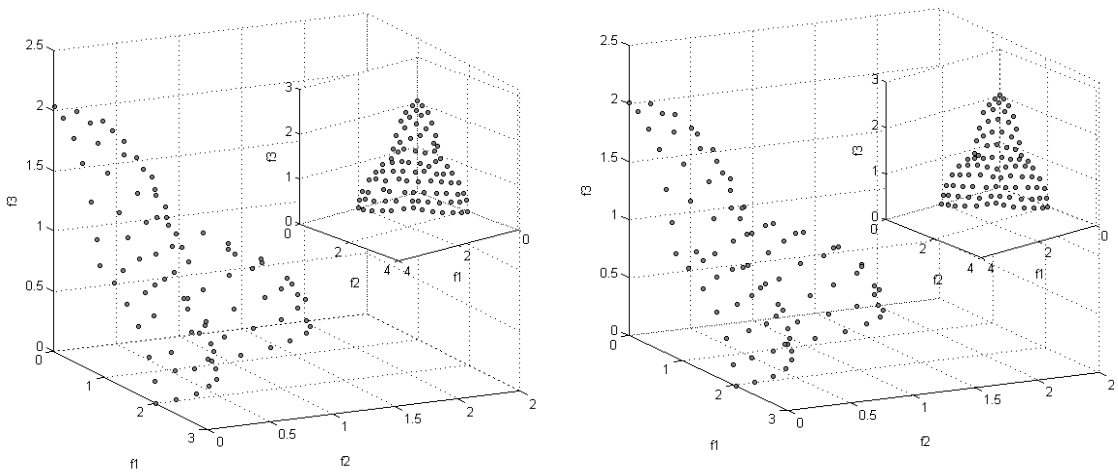

(a) NSGA-III (b) EliteNSGA-III

FIGURE 7-17 Obtained solutions by NSGA-III and EliteNSGA-III for 3-objective C3-DTLZ4 test problem.

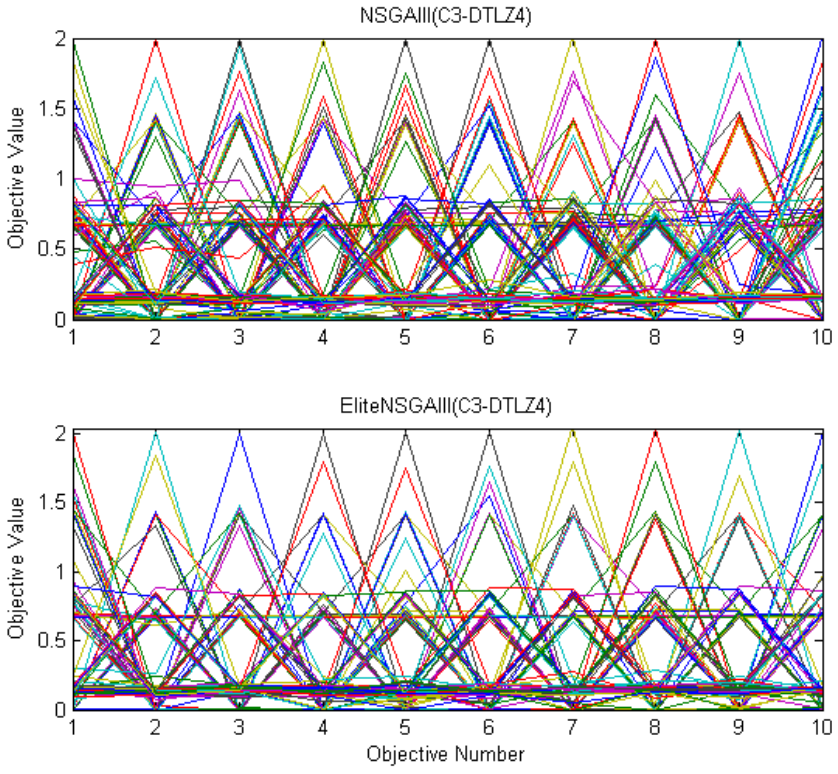

FIGURE 7-18 Value path plot comparison of the obtained solutions by NSGA-III and EliteNSGA-III for 10-objective C3-DTLZ4 test problem.

7.7 Conclusion

This chapter presented a novel elite archive-based NSGA-III, called EliteNSGA-III. EliteNSGA-III uses an elite population to store previously generated individuals that can probably be eliminated by NSGA-III's pruning mechanism. EliteNSGA-III also modifies the parent selection mechanism employed by NSGA-III to diversify the parent selection pool by giving equal chance to the elite population archive and the current population. The performance of EliteNSGA-III was compared with NSGA-III on 11 widely used many-objective test problems with dimension ranging from 3 to 15 objectives. Experimental results on these test problems showed that the performance of the traditional NSGA-III algorithm can significantly be improved through the introduction of an elite population archive.

Almost in all test problems, the proposed algorithm outperformed the parent algorithm in terms of convergence and accuracy of the obtained solutions. As the number of objectives increased, the performance of the corresponding EliteNSGA-III algorithm significantly outperformed NSGA-III in almost all instances. Moreover, our study on the influence of elite population archive proved the capability of the proposed algorithm in preserving diverse sets of elite population members and hence improving the diversity of an offspring population.

In the future, first, we would like to extend this study to investigate the impact of an elite population archive when alternate recombination operators are used (e.g. differential evolution (DE) instead of SBX and polynomial mutation operators). Second, we would like to investigate the impact of an elite population archive when only neighbouring elite solutions are used to create offspring population. And last, we would

like a penalty mechanism to avoid the generated solutions being attracted to few reference points.

Chapter 8

MULTI-OBJECTIVE OPTIMIZATION DESIGN OF A PHOTOVOLTAIC FARM

Recently, several parts of the world suffer from electrical black-outs due to high electrical demands during peak hours. Stationary photovoltaic (PV) collector arrays produce clean and sustainable energy especially during peak hours, which are generally daytime. In addition, PVs do not emit any waste or emissions, and are silent in operation. The incident energy collected by PVs is mainly dependent on the number of collector rows, distance between collector rows, dimension of collectors, collectors inclination angle and collectors azimuth. The objective is to achieve optimal design of a PV farm yielding two conflicting objectives namely maximum field incident energy and minimum of the deployment cost. This chapter investigates how the proposed Fusion algorithm compares against four state-of-the-art MOEAs, how the proposed ECM plot help us visualize and identify relationships among decision and objective variables, how the proposed performance measure (ObjIGD) complement existing performance measures by quantifying convergence and distribution of solutions along each objective, and finally how the proposed FNFR method benefit decision makers to select preferred solutions among thousands of possible solutions.

8.1 Introduction

Solar energy is one of the most widely used renewable energies; because it is emission free and it is easily deployable. Several sun-based energy generation methods exist, such as, photovoltaic farms (PV), concentrated solar power plants, and solar thermal electricity plants. These systems can be used for meeting the global energy crisis due to rising world-wide demands and insufficient supply of electricity throughout the world by deploying the appropriate systems in the required areas. For example, PV are inefficient in very hot areas, such as desert, but are more efficient in mild to cold areas. In this chapter, PV panels are selected because of mild-cold weather conditions in Canada. Although Canada produces

enough electricity to fulfill the national demand, nevertheless solar energy is of special interest due to PV non-polluting properties.

Concentrated solar systems like the parabolic trough heat transfer fluid/steam systems can typically generate full rated electrical output for 10-12 hours a day [140]. Other solar power generation systems include large solar updraft towers which can produce large amounts of electricity via utilizing air flow created by heated air which drives pressure staged turbines [141]. In spite of these available large-scale technologies, photovoltaic panels are the most popular method of harvesting solar energy, because they directly convert the Sun's rays into electrical power. In addition, photovoltaic panels can be deployed anywhere and can provide a relatively stable electrical output. However, there are several drawbacks; they are subject to changing output efficiencies based on external factors such as shade, cloudy weather, covered by sands, and others.

Photovoltaic systems consist in converting solar radiation (sunlight) directly to electricity. There are two types of solar radiations on the Earth: *direct* and *diffuse* radiations. The direct radiation is the light received directly from the Sun without having been dispersed by the atmosphere due to clouds, water vapor, and other molecules. Whereas the diffuse radiation is the sunlight that has been scattered by molecules and particles in the atmosphere but that has still made it down to the surface of the earth. As a result, the total energy absorbed by the PV panels are the sum of the amount of light received from direct and diffuse radiations.

In this chapter, we use of the proposed Fusion algorithm along four state-of-the-art MOEAs, namely, SMPSO, GDE3, SPEA2, and NSGA-III to optimize the deployment of solar PV farms. Furthermore, we utilize the proposed ECM plot to visually investigate the

relationship between the decision variables and objective functions, the ObjIGD measure to quantitatively asses the convergence and distribution of solutions along each objective, and the FNFR method extract preferred solutions among numerous solutions. The objectives consisted in maximizing the total incident solar energy and minimizing the cost of PV panel deployment in a specific field. As in Refs. [139] and [2], the cost was limited to initial investment because the paper focused only on the PV configuration setup. However, a real PV farm requires overhead costs such as maintenance costs, residual fees, energy storage component fee and others. Six decision variables composed the optimization problem, namely, the number of collector rows, the distance among collector rows, the dimension of collectors, the collector's inclination angle, and the collectors' azimuth angle.

8.2 Related Work

In the last few decades, there has been a large number of studies on single-objective and multi-objective real-life applications [2]. However, most real-life problems are multi-objective problems by nature because they involve variant conflicting objectives. The development of efficient multi-objective metaheuristics such as evolutionary multi-objective algorithms played an integral role in the design of complex energy systems. This section presents the most recent optimization works applied to design solar energy systems.

A genetic algorithm for the maximization of thermal performance of flat plate solar air heaters to optimize operating parameters and various systems was implemented by Varun [142]. Basic values like the number of glass covers, plate tilt angle, emissivity of plate, Irradiance and Reynold number are optimized for maximizing thermal performance.

Thiaux et al. [143] used NSGA-II algorithm to optimize the impact of load profile on stand-alone photovoltaic system gross energy requirement. A hybrid optimized solar-wind system was developed by Yang et al. [144] where the components' capacity sizes of hybrid solar-wind power generation systems, which employs a battery bank, was optimized. Chang [145] tried maximizing the electrical energy output of photovoltaic modules using a hybrid heuristic method. In that case, PSO was combined with nonlinear time-varying evolution to determine the optimal tilt angle of the modules.

Deb et al. [146] have recently attempted to solve a four-objective optimization model of a solar thermal power plant operation system. These objectives were: pollution, profit, total investment costs, and internal rate of return. Clustered NSGA-II algorithm was used first to find a set of trade-off solutions over the entire Pareto-optimal front. Next, a reference point was used based on Multiple Criterion Decision Making (MCDM) approach along with the clustered NSGA-II to find preferred solutions on some parts of the Pareto-optimal front. It was shown that multi-objective optimization procedure with user decision-making interaction can be used to find a single preferred solution.

Mellit et al. [147] describes the effect of utilizing various models and artificial intelligence based design methods to increase the efficiency of solar-wind hybrid plants. The proposed system was especially efficient for rural and isolated areas, which suffer from lack of meteorological data due the limited weather station, a simulation method is used for completing the missing data.

The shading among solar panels was modeled in a related study and a simulation-based algorithm was developed in order to predict the loss of energy due to shade in three individual locations in Arizona [148]. Myers et al. [149] proposed and then simulated a

theoretical solar cell by using modified genetic optimization algorithm for shaping solar cells. This resulted in a 3D shape which fits within the area and volume of a conventional solar cell but one that is drastically more efficient than the regular rectangular shapes.

O. Ekren and Y. Ekren [150] used Simulated Annealing (SA), which are simulation and single-solution based metaheuristic algorithm, to optimize the size of a PV-wind integrated hybrid energy system with battery storage. In this case, the objective function was the minimization of the hybrid energy system's total cost. The optimum result obtained by the SA algorithm showed a 10.13% improvement on the objective function as compared to their simulation model.

Appelbaum and Weinstock [151] studied electrical output maximization for photovoltaic farms by focusing on shading and spacing issues. In that study, Sequential Quadratic Programming was used for optimization. In a more recent work, the azimuth angle of a solar panel was added as a new variable to the problem [152]; however, this variable is manipulated in a manual fashion while the system itself is optimized automatically. A 12% in efficiency enhancement was reached for a small scale photovoltaic array by reducing the amount of shading. The maximum annual incident energy captured by the solar collectors was compared by Bourennani et al. [153] where Differential Evolution (DE), along with simulation-based optimization methods, were used. The comparison found that the captured energy was similar between the simulation approach and DE.

This study is inspired from [153], [151, 152] works; however, the problem was transformed into a multi-objective problem. Rarely multi-objective optimization methods were used in PV field. Ref. [143] used MOO but they focused on the optimization of the

entire solar farm assuming a certain static setup whereas this study focuses on the setup of PV panels which is composed of six decision variables namely, the number of collector rows (a discrete variable), distance among the collector rows, the inclination of the PV panels, the height of a PV panel, collector's azimuth due south, and collector's clearance above ground.

8.3 Photovoltaic Solar Farm Model

The objective of the problem is to find the optimal deployment of stationary photovoltaic (PV) panels that maximize the incident energy collected by the PVs while minimizing material cost. PV collectors are fixed in the field as shown in Figure 8-1 where it can be seen that the collectors are inclined at an angle β facing roughly the south. Here, the dimension of the collectors are referred to as length L and as height H. L is equal to the length of the field whereas the width is W. A minimum clearance of E (above the ground) should exist to minimize the collectors of dust, debris, or snow.

Collector maintenance requires the height of the solar cells above the ground to be limited. Furthermore, the minimum distance, D between two rows is limited to allow easy access between PV panels. The height H of the solar cells is itself limited by the manufacturer [151]. Thus,

$$H' + E \leq A_{max} \,, \tag{8.1}$$

$$H \leq H_{max} \,, \tag{8.2}$$

where $H' = Hsin\beta$.

The configuration factors for un-shaded and shaded are given by as follow, respectively:

$$F_d = cos^2\left(\frac{\beta}{2}\right), \tag{8.3}$$

$$F_d^{sh} = F_d - \left[(d^2+1)^{\frac{1}{2}} - d\right] sin\beta, \tag{8.4}$$

where d is the normalized distance between two rows given by $d = D/H'$.

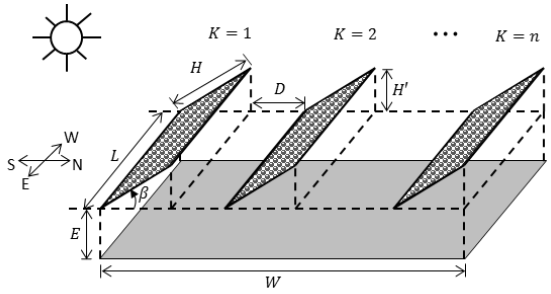

FIGURE 8-1 Collectors arrangement in a stationary solar field, K indicates row number, L indicates length of PV, W indicates the width of the solar field, D indicates the distance between collector rows, β indicates PVs' inclination angle, and H′ indicates the perpendicular distance created by the PVs.

The incidence angle θ is the angle between a normal to the collector face and the incoming solar beam and it depends on the sun angles (altitude and azimuth) and collector angles (see Figure 8-2).

$$cos\,\theta = cos\beta sin\alpha + sin\beta cos\alpha cos\gamma, \tag{8.5}$$

where α is the sun elevation angle; β is the collector inclination angle and $\gamma = \gamma_S - \gamma_C$ is the difference between the sun and collector azimuth with respect to south.

The relative shaded area is calculated by:

$$a_s = \frac{l_s}{L} \times \frac{h_s}{H}, \tag{8.6}$$

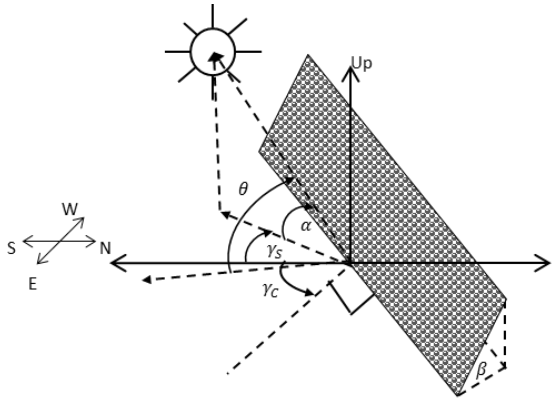

FIGURE 8-2 Incidence angle θ (angle between a normal to the collector face and the incoming solar beam).

where,

$$l_s = 1 - \frac{d\sin\beta+\cos\beta}{l} \times \frac{|\sin\gamma|}{\cos\beta\tan\alpha+\sin\beta\cos\gamma}\,, \tag{8.7}$$

and

$$h_s = 1 - \frac{dsin\beta+cos\beta}{cos\beta+\frac{sin\beta cos\gamma}{tan\alpha}}\,, \tag{8.8}$$

where $l = L/H'$ is the normalized collector length.

The yearly direct (q_b) and diffuse (q_d) beam irradiation per unit area of an un-shaded collector (first row) are calculated by:

$$q_b = \sum_{n=1}^{n=365} \sum_{T_R}^{T_S} G_b \cos\theta \ \Delta\,\mathrm{T}, \tag{8.9}$$

and

$$q_d = F_d \sum_{n=1}^{n=365} \sum_{T_R}^{T_S} G_{dh}\,\Delta\,\mathrm{T}, \tag{8.10}$$

The average yearly direct (q_b^{sh}) and diffuse (q_d^{sh}) beam irradiation per unit area of an un-shaded collector $((K-1)$ row) are given by:

$$q_b^{sh} = \sum_{n=1}^{n=365} \sum_{T_R}^{T_S} G_b \cos\theta \ (1 - \ a_s)\Delta T, \tag{8.11}$$

and

$$q_d^{sh} = F_d^{sh} \sum_{n=1}^{n=365} \sum_{T_{SR}}^{T_{SS}} G_{dh} \, \Delta \, T, \tag{8.12}$$

where ΔT is the summation time interval from sun rise T_R to sunset T_S on the collector for the beam irradiance, and from sun rise T_{SR} to sun set T_{SS} for the diffuse irradiance. The outer summation represents one year term from January 1st ($n = 1$) to December 31st ($n = 365$). Figure 8-3 shows the sixth decision variable (γ_C); collectors azimuth with respect south and limited to $[-45^o, 45^o]$.

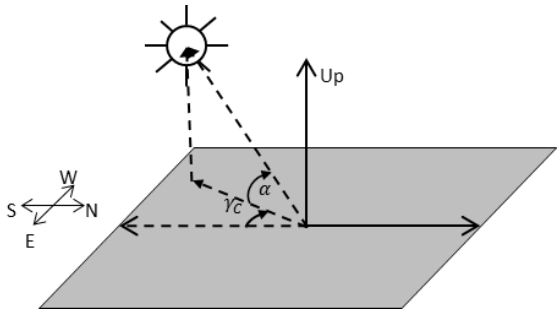

FIGURE 8-3 Collector azimuth with respect to south (γ_C).

The optimization problem is composed of two objectives, six variables, and two constraints. A final optimal solution is composed of the following variables: the number of collector rows, distance between collector rows, dimension of collectors, collectors' inclination angle, and collectors' azimuth angle. The objectives, constraints, and variable domains are described below in Equations (8.13) to (8.22).

The two objectives are the maximization of incident energy and minimization of the installation and material cost.

Incident energy: the yearly absorbed incident energy should be maximized in order to generate the maximum possible electricity.

Cost: the cost of PV array collector's installation should be as low as possible.

The mathematical formulation of the optimization problem is defined as follows:

$$\max \mathrm{Q} = K \times L \times \left[q_b + q_d + (K-1)\left(q_b^{sh} + q_d^{sh}\right)\right] \tag{8.13}$$

$$\min C = K \times L \times H \times P \tag{8.14}$$

$$s.t. K \times H \times cos\beta + (K-1) \times D \leq W \tag{8.15}$$

$$H + E \leq A_{max} \tag{8.16}$$

Variable bounds:

$$2 \leq K \leq 10 \tag{8.17}$$

$$0.2 \leq H \leq 2 \tag{8.18}$$

$$0^o \leq \beta \leq 90^o \tag{8.19}$$

$$0.8 \leq D \leq 2.5 \tag{8.20}$$

$$-45^o \leq \gamma_C \leq 45^o \tag{8.21}$$

$$0.5 \leq E \leq 2 \tag{8.22}$$

where $K \in Z^+$and $\$H, \beta, D, \gamma, E \in$ R.

- P is the price of PV panel per square meter.
- q_b is the yearly beam irradiation per unit area of an un-shaded collector (first row).

- q_d is the yearly diffuse irradiation per unit area of an un-shaded collector (first row).
- q_b^{sh} is the average yearly beam irradiation per unit area of shaded collectors $(n-1\ rows)$.
- q_d^{sh} is the average yearly diffuse irradiation per unit area of shaded collectors $(n-1\ rows)$.

8.4 Problem Complexities

The multi-objective optimization PV farm design is composed of several complexities that make it hard to solve. It is composed of mixed-type integer and real variables. The first objective is multimodal because it encompasses trigonometric functions which are hard to solve. The PF geometry is two disconnected linear shapes. The second portion of the linear component is shorter and difficult for an optimizer to get to this region.

Some variables take widely different ranges of values, thereby making it difficult for the solvers to provide adequate emphasis to correct variable combinations. Despite the existence of only six variables (6D), this problem exhibits a wide and non-uniform range of variable values. In addition, the non-dominated solutions' variables are composed of other complexities which are a) non-extremal and b) non-medial having a c) dissimilar parameter domains and d) many-to-one mappings which make the problem more complicated to solve [60]. Dissimilar parameter domains consist of variables with completely dissimilar parameter domains. For example, the height and inclination angle are defined as follows $0.2 \leq H \leq 2$ and $0^o \leq \beta \leq 90^o$. Many-to-one mappings imply that different combination of parameters can generate exactly the same solutions (same fitness

values). For example, in Figure 8-4 you can see that two adjacent solutions, where one solution has five rows of PV panels with small dimensions and the next one has only two rows with very large panel dimensions. Both cases result roughly in the same cost and the energy generation.

8.5 Experimental Setup and Results

8.5.1 Climate Information

The selected location for the photovoltaic system optimization experiments is the city of Toronto, Ontario, Canada (Latitude 43.45^{o}/ Longitude -79.25^{o}). Appendix A, Table A.1 and Table A.2 show the 30 years of monthly average hourly direct normal beam irradiance in addition to horizontal diffuse irradiance in KWh/m^2 (employed in Equations (8.9) to (8.12)) [154]. These datasets were created by joining 12 typical meteorological months that were extracted from a database of 30 years of Canadian Weather Energy and Engineering Datasets (CWEEDS) data. Appendix A, Table A.3 and Table A.4 show the 22 years monthly average hourly solar angles relative to the horizon and solar azimuth angles due south in degrees (employed in Equations (8.5) and (8.7)). These solar datasets were selected from the NASA GEOS-4 [155].

8.5.2 PV Panel Specifications

There are various types of PV panels on the market today. The price of PV panels are based on their electrical characteristics such as: Rated power, Voltage, Current, Module efficiency, Short-circuit current, Open-circuit voltage, Maximum series fuse rating, and Maximum system voltage. The price is also based on the mechanical characteristics such

as: Dimensions, Weight, Frame, number of Solar Cells. In our experiment Ameresco Solar BP 90 Watt, 12Vsolar panel priced at \$616.59/m^2 was used [156]. Keep in mind that despite the use of a specific solar panel for the experiments, the solution would not necessarily be affected if other panels are used. Overall, the current PV panels' average price in Ontario is \$4.50 per KWh (including all installation fees and required material).

TABLE 8.1 Parameters' settings used in the solar PV farm design. n is the number of variables in the problem.

For All	
Population size (P)	100
Number generations	1000
GDE3	
Mutation probability (F)	0.1
Crossover probability (CR)	0.5
SMPSO	
Archive size	$\|P\|$
Polynomial mutation (p_m)	$1/n$
Mutation Distribution Index (η_m)	20
SPEA2	
Archive size	$\|P\|$
SBX probability (p_c)	0.9
Polynomial mutation (p_m)	$1/n$
Crossover Distribution Index (η_c)	20
Mutation Distribution Index (η_m)	20
NSGA-III	
SBX probability (p_c)	1.0
Polynomial mutation (p_m)	$1/n$
Crossover Distribution Index (η_c)	30
Mutation Distribution Index (η_m)	20
Fusion	
Number of Reference Points	100

8.5.3 Parameter Settings

In this case study, the Fusion framework, SMPSO, GDE3, SPEA2, and NSGA-III are utilized to investigate the optimal design of a PV farm yielding two conflicting objectives, namely maximum field incident energy and minimum of the deployment cost. Due to the stochastic nature of heuristic algorithms, the proposed algorithms were executed 25 times and the stopping criterion was set to 10^5 function evaluations. In addition, the hypervolume (HV) [15], the inverted generational distance (IGD), the Spread, and objective-wise IGD (ObjIGD) measures were used to compare the performance of each algorithm. The HV and IGD indicators measure the distribution and the convergence of the approximation set to the optimal PF. The spread indicator measures the distribution and the level of spread achieved among the approximate solutions. The ObjIGD parameter measures the distribution and range of approximate solutions along each objective. Among all measures, the HV metric is the only indicator that exhibits strict Pareto compliance, which is a highly desirable feature. In other words, if A strictly dominates B, then the HV value of A is higher than the HV value of B. Furthermore, the FNFR method is used to extract well-distributed solutions from the non-dominated ones collected during the 25 runs of each algorithm. The FNFR method is designed to help decision makers extract a subset of well-distributed solutions on the entire Pareto-optimal surface or within a preferred region. Table 8.10 shows the parameter settings used in this case study.

8.5.4 Numerical Results and Analysis

The proposed five multi-objective optimization methods found a variety of optimal PV farm design solutions, which would not have been found using single objective

optimization. For instance, some intermediate solutions could be of interest with regards to other non-expressed objectives or secondary objectives such as space between solar panels or other technical aspects. Table 8.2 shows the two extreme (end) solutions obtained through the proposed algorithms. These solutions indicate the maximum and minimum possible energy and cost that can be achieved through the current design. The HV, IGD, Spread, and ObjIGD results (see Table 32.3) indicate that the SMPSO algorithm slightly outperforms the Fusion algorithm. Appendix B, Tables B.1 to B.5 show the best (based on IGD measure) set of non-dominated solutions the corresponding decision variables found by the Fusion, SMPSO, GDE3, SPEA2, and NSGA-III algorithms.

There were notable differences among the best solutions found by these five algorithms. The most important difference is that the GDE3, SPEA2, and NSGA-III failed to find a complete spectrum of solutions on the Pareto-optimal front. For most of the runs, the GDE3, SPEA2, and NSGA-III algorithms failed to converge to the second portion of the Pareto-optimal front and hence their performance suffered.

TABLE 8.2 The maximum and minimum power and cost obtained for the photovoltaic energy system case study.

Algorithm	Max. Energy (MWh/year)	Min. Energy (MWh/year)	Max. Cost (USD)	Min. Cost (USD)
Fusion	109.41	4.19	$55,492.93	$1849.76
SMPSO	109.05	4.19	$55,492.93	$1849.76
GDE3	100.62	4.19	$46,244.11	$1849.76
SPEA2	100.58	4.19	$46,244.03	$1849.76
NSGA-III	107.63	4.19	$54,150.55	$1849.76

As can be seen in Figure 8-4 (a), the Fusion algorithm was able to get well-distributed solutions on the Pareto-optimal front and was able to get the two extreme solutions. In Figure 8-4 (b), the solutions were observed to be diverse with respect to the

number of collector rows (K). This is an attractive feature to decision makers because it gives more options.

TABLE 8.3 Min, max, mean, and standard deviation of IGD, HV, Spread, and ObjIGD measures for the PV farm optimization problem.

Metric	Fusion	SMPSO	GDE3	SPEA2	NSGAIII
IGD	6.18E-05	5.94E-05	2.02E-04	2.02E-04	6.65E-05
	2.00E-04	6.29E-05	2.42E-04	2.05E-04	2.05E-04
	2.01E-04	2.03E-04	9.41E-04	9.42E-04	9.54E-04
	1.72E-04	8.06E-05	2.73E-04	2.68E-04	3.20E-04
HV	5.47E-01	5.46E-01	5.43E-01	5.42E-01	5.47E-01
	5.43E-01	5.45E-01	5.39E-01	5.41E-01	5.42E-01
	5.43E-01	5.42E-01	4.99E-01	4.99E-01	4.98E-01
	5.44E-01	5.45E-01	5.38E-01	5.38E-01	5.35E-01
Spread	1.13E-01	1.04E-01	2.45E-01	2.37E-01	1.56E-01
	1.84E-01	1.55E-01	2.81E-01	2.79E-01	1.76E-01
	2.33E-01	2.02E-01	4.07E-01	4.19E-01	4.53E-01
	1.78E-01	1.56E-01	2.85E-01	2.88E-01	2.26E-01
ObjIGD	4.33E-05	3.96E-05	1.34E-04	1.34E-04	4.67E-05
	1.33E-04	4.17E-05	1.64E-04	1.37E-04	1.37E-04
	1.34E-04	1.36E-04	6.65E-04	6.65E-04	6.74E-04
	1.15E-04	5.40E-05	1.86E-04	1.82E-04	2.20E-04

Figure 8-5 shows the ECM plot of the fusion algorithms. As the figure shows, as K increases, the energy absorbed (Q) increases as well (the second half of the figure shows particularly high correlation). Of interest is that the fact that between the regions (4.19 MWh, \$1,849) and (100 MWh, \$46,244) the optimal gamma equals -2.4^o. Similarly, between the regions (100.5 MWh, \$46,250) and (109MWh, \$55,492) the optimal gamma equals -16^o. A high correlation was observed between the Height of the collector (H), the PV Cost (C) and Q (as H increases, C and Q increase). For lower values of K (2 and 3), the distance between the rows (D), did not matter (can be set to 2.5 meters). However, as K increases, the value of D decreases to accommodate the space required to put more panels.

The distance of the collector above ground (E) was observed to be random and fluctuated between 0.5 and 1.3 meters.

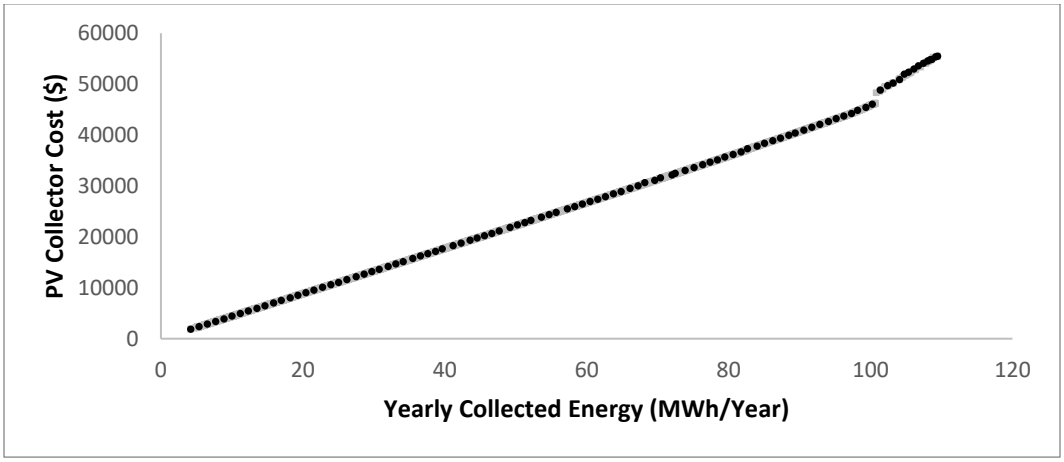

(a)

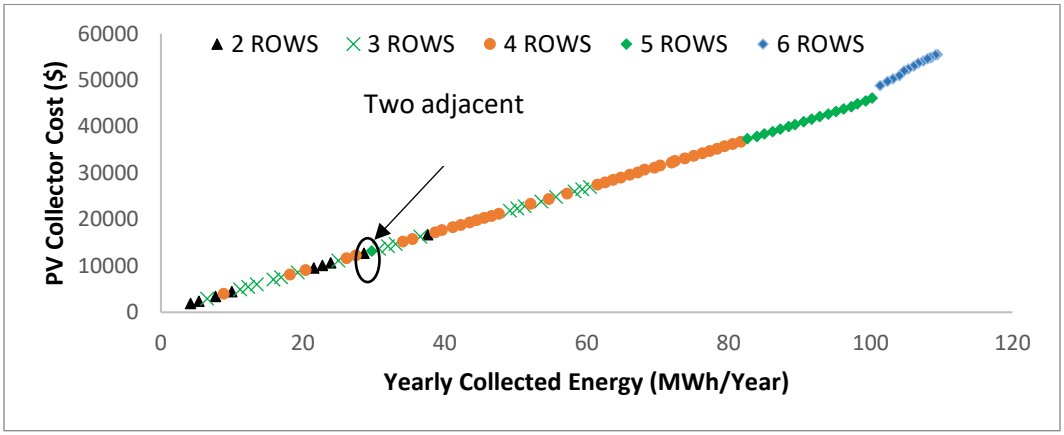

(b)

FIGURE 8-4 The best set of non-dominated solution set (Based on IGD measure) found by Fusion. (a) The grey dotted background indicated the non-dominated solutions assembled during 25 runs of all algorithms and the black dots indicate the best solution set obtained by Fusion.

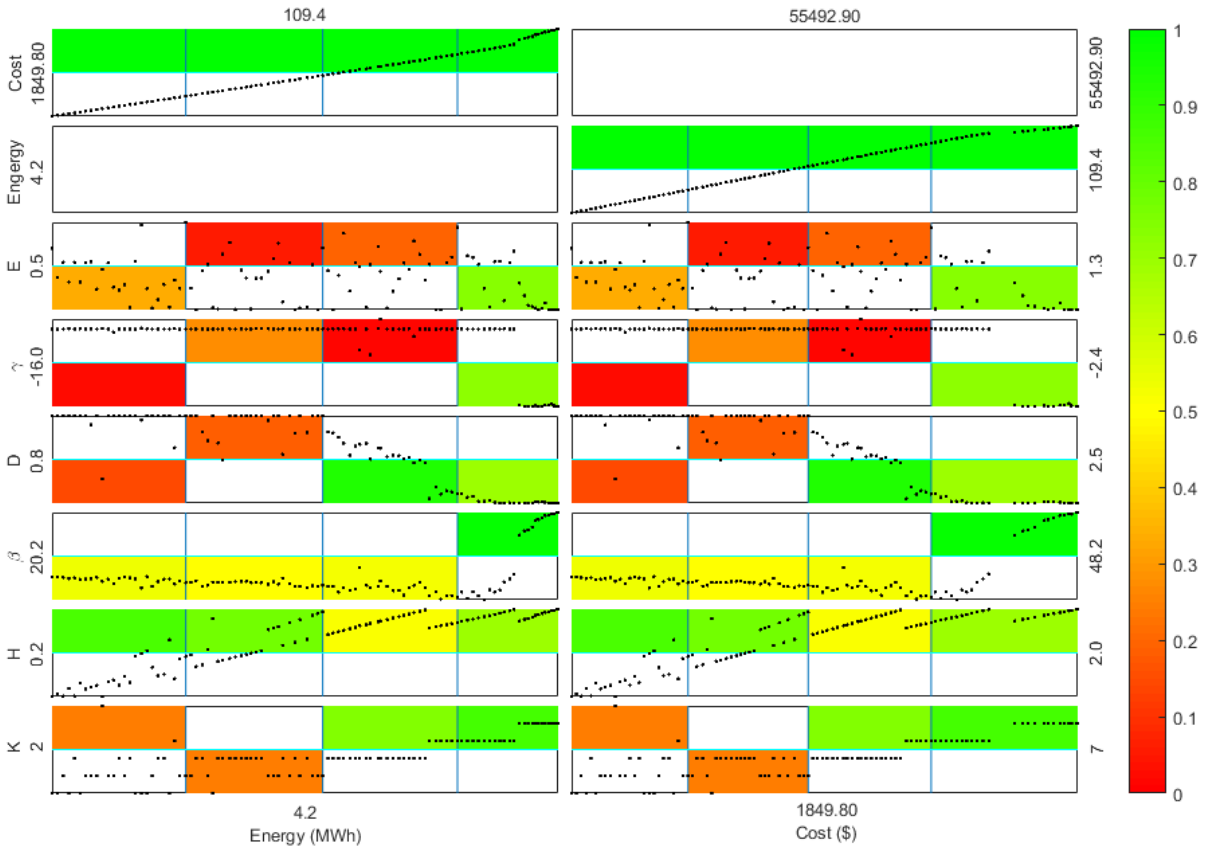

FIGURE 8-5 ECM plot of the best set of non-dominated solution set (Based on IGD measure) found by the Fusion algorithm.

Figure 8-6 (a), which represents SMPSO, shows good diverse solutions between the two extreme solutions. However, Figure 8-6 (b) illustrates poor diversity with respect to K ($K = 5$ being the dominant solution). This is undesirable result because it will limit the options available to the decision-maker.

Similar to the fusion algorithms, Figure 8-7 shows high correlation between the Q and C with respect to H and D. As H and K increase, the energy absorbed and associated costs increase. However, as K increases, the distance between the panels decreases. Interestingly, and unlike other algorithms, there appears to be a correlation between the height of the panel (E) above ground and the absorbed energy (Q) and cost (C).

Specifically, as E decreases from 1.9 to 0.5 meters, Q increases (from 4.2 to 108 MWh) and increases (from \$1,850 to \$54,930).

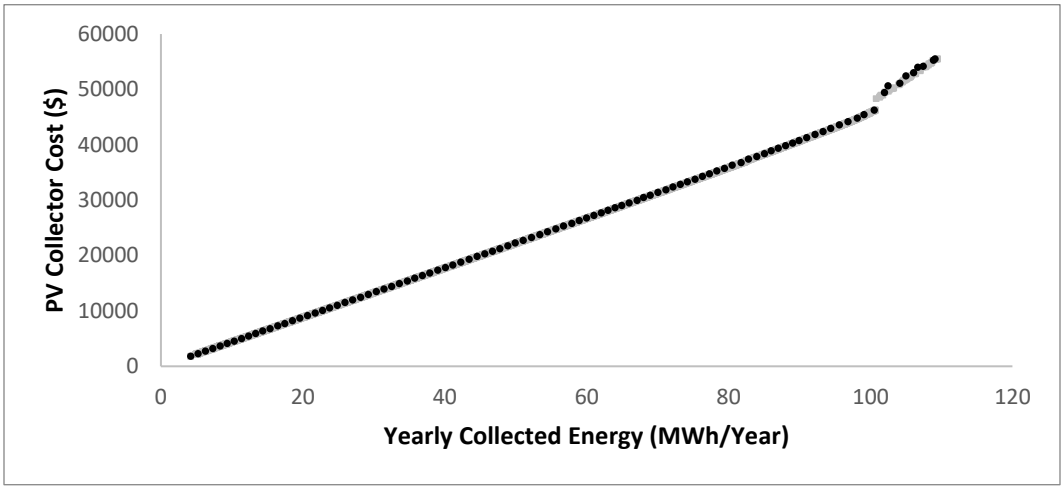

(a)

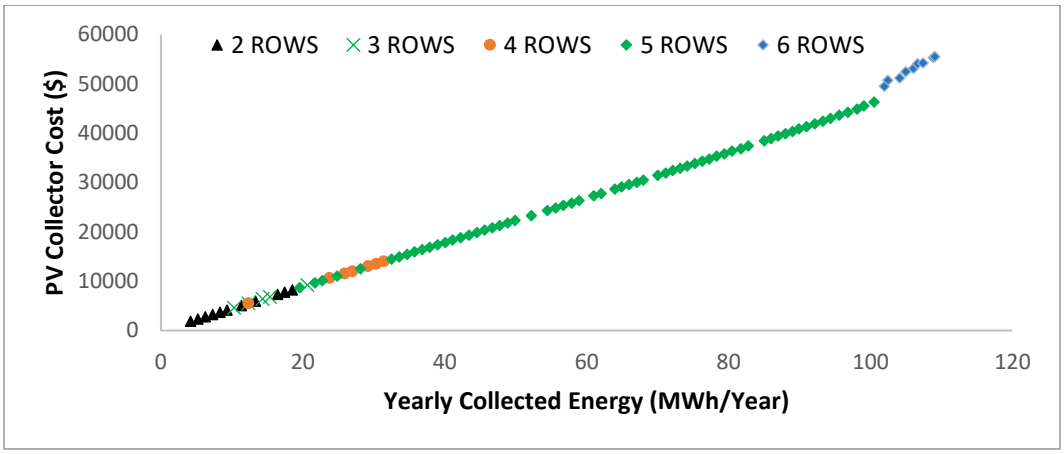

(b)

FIGURE 8-6 The best set of non-dominated solution set (Based on IGD measure) found by SMPSO. (a) The grey dotted background indicated the non-dominated solutions assembled during 25 runs of all algorithms and the black dots indicate the best solution set obtained by SMPSO based on the IGD measure. (b) Best solution set found by the SMPSO algorithm with respect to the number of collector rows associated with each solution.

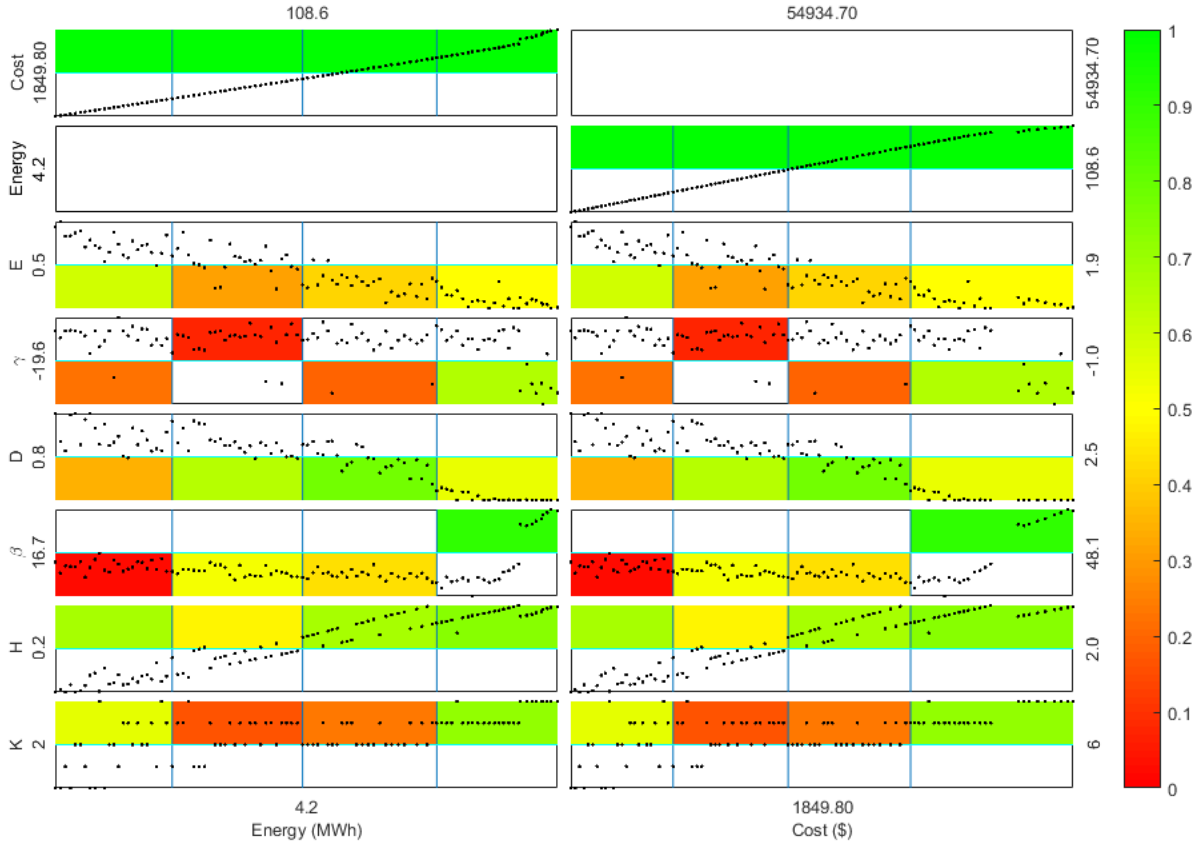

FIGURE 8-7 ECM plot of the best set of non-dominated solution set (Based on IGD measure) found by the SMPSO algorithm

Figure 8-8 (a), which shows solutions found by GDE3 algorithm, shows well-distributed solutions. However, it failed to find the extreme solutions beyond 100MWh. In Figure 8-8 (b), a diverse set of solutions with respect K was found (for K between 2 and 5 rows). However, only one solution was obtained for $K = 6$ and the associated energy was approximately 18 MWh. Furthermore, for $K = 7$, the associated energy was approximately 70 MWh. In Figure 8-9, a unique observation was made; specifically, the value of gamma was -4^{o} throughout. Again, the value of E was observed to be random ranging between 0.5 and 1.4 meters. K and H had a high positive correlation.

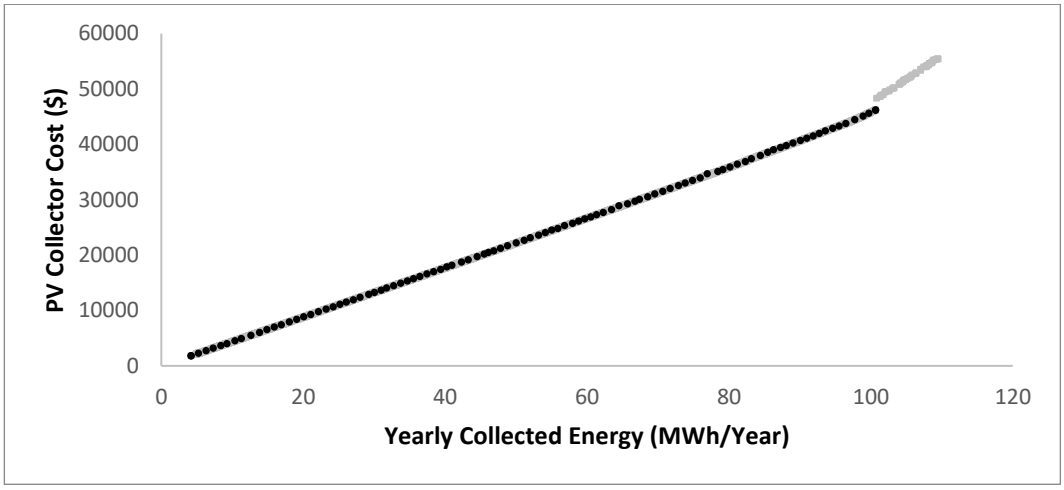

(a)

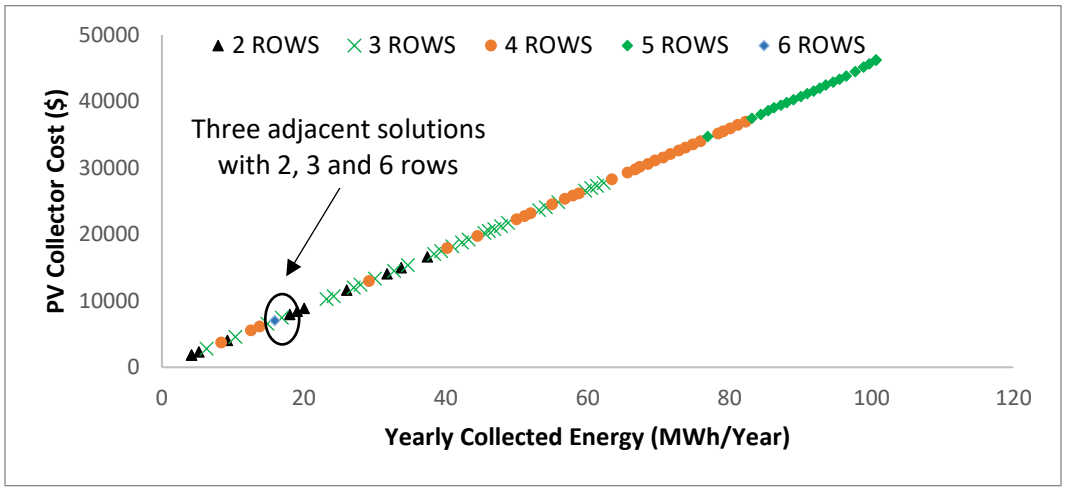

(b)

FIGURE 8-8 The best set of non-dominated solution set (Based on IGD measure) found by GDE3. (a) The grey dotted background indicated the non-dominated solutions assembled during 25 runs of all algorithms and the black dots indicate the best solution set obtained by GDE3 based on the IGD measure. (b) Best solution set found by the GDE3 algorithm with respect to the number of collector rows associated with each solution

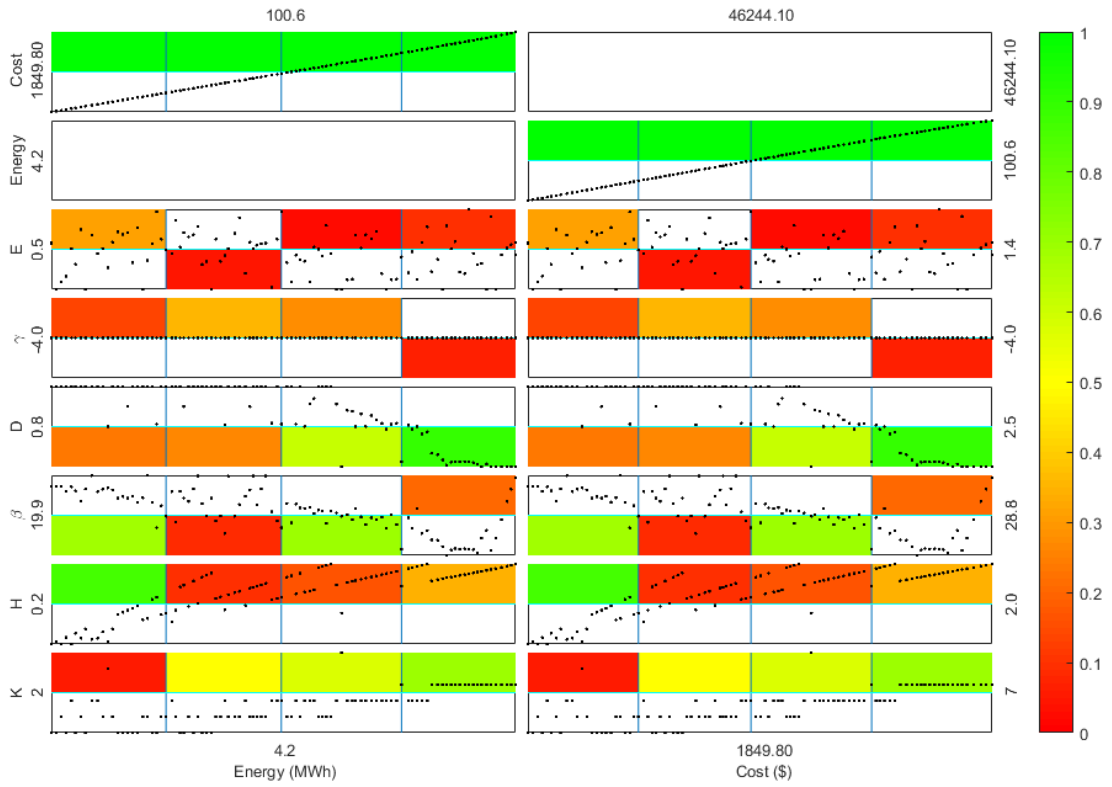

FIGURE 8-9 ECM plot of the best set of non-dominated solution set (Based on IGD measure) found by the GDE3 algorithm

In Figure Figure 8-10 (a), where SPEA2 is illustrated, a well-distributed solution was obtained – however, no extreme solutions beyond 100 MWh was obtained. Figure Figure 8-10 (b) has a good diverse solutions with respect to K; however, no solutions were obtained for $K > 5$. Figure Figure 8-11 illustrates a random distribution of E (between 0.5 and 1.3 meters) and gamma was -3.1^{o} throughout (except for few solutions where gamma reached -16^{o}). Interestingly, when $K = 5$, and between the regions (76 MWh, \$34,172) and (101 MWh, \$46,244), H and D exhibited very high linear negative correlation.

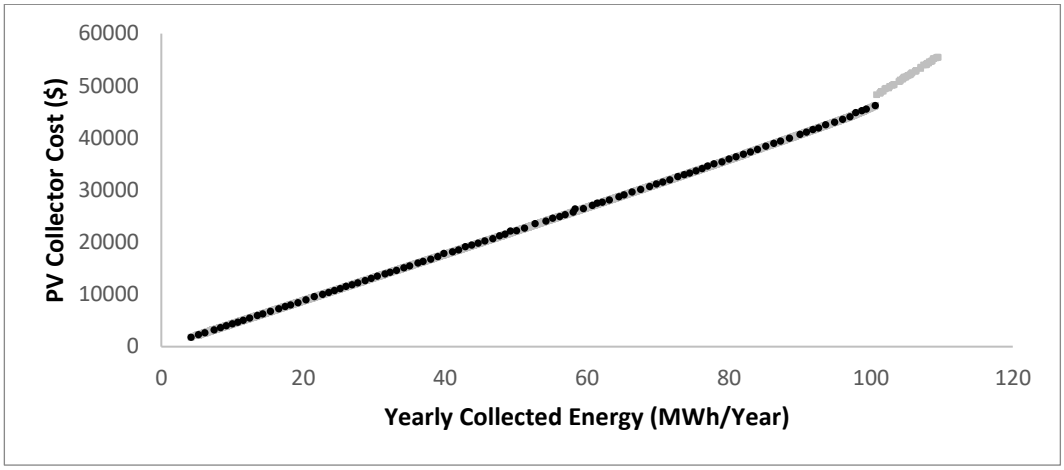

(a)

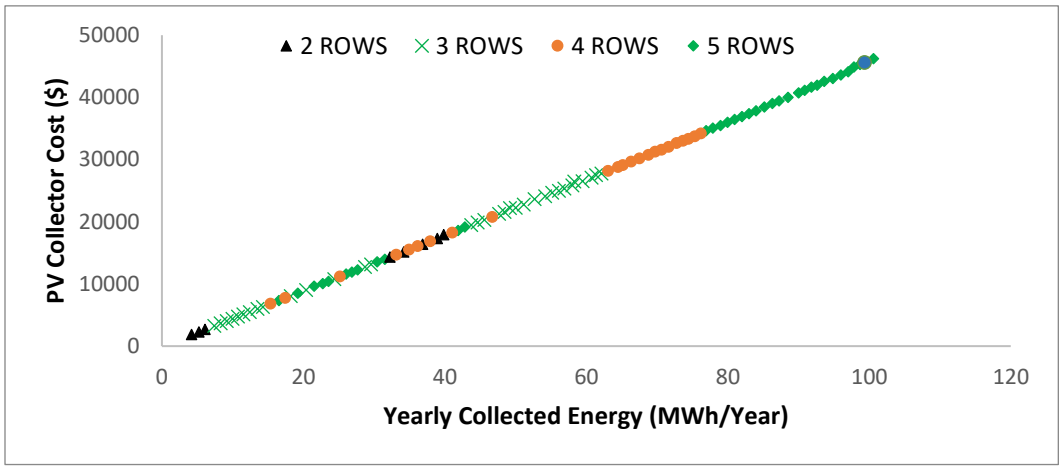

(b)

FIGURE 8-10 The best set of non-dominated solution set (Based on IGD measure) found by SPEA2. (a) The grey dotted background indicated the non-dominated solutions assembled during 25 runs of all algorithms and the black dots indicate the best solution set obtained by SPEA2 based on the IGD measure. (b) Best solution set found by the SPEA2 algorithm with respect to the number of collector rows associated with each solution.

NSGA-III, which is shown in Figure 8-12, shows a good distribution and the ability to obtain some extreme solutions - as can be shown in Figure 8-12 (a). Figure 8-12 (b) shows that solutions associated K ranging between 2 and 6 are well represented. Figure 8-13, E was observed to be random (from 0.5 to 1.2 meters) and gamma remained constant (at -4^{o}) except around the extreme solutions were it equaled -16^{o}. As K ranged from 4 to 6,

a high correlation was observed between Q and C. For K equals 2 or 3, D was constant at 2.5 meters but goes down to 0.8 meters as K increases to 6.

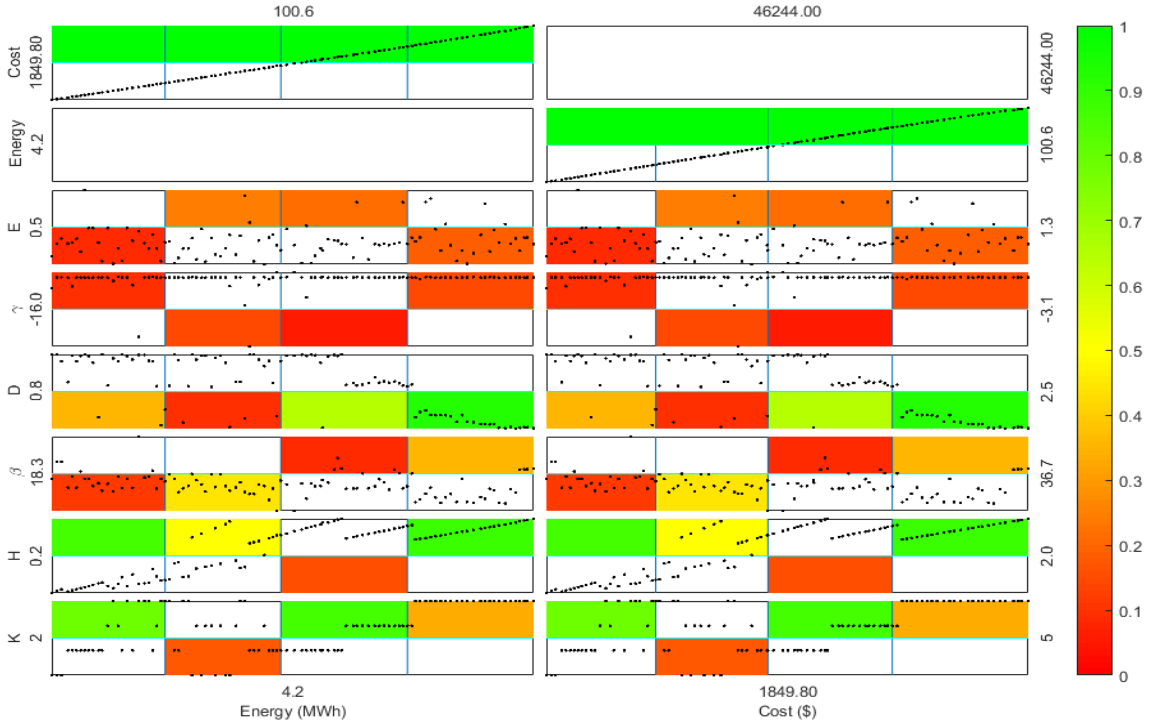

FIGURE 8-11 ECM plot of the best set of non-dominated solution set (Based on IGD measure) found by the SPEA2 algorithm

The overall findings can be summarized as follows:

- As K increases, Q and C increase
- In all the algorithms, H and K are highly correlated. By keeping K constant, increasing H leads to high values of Q and C.
- The optimal β ranged between 27° and 33° for energy absorbed up to 100 MWh and equaled 48° for anything above 100 MWh.
- The optimal distance between collectors was 2.5 for energy absorbed up to 100 MWh and equaled 0.8 for anything above 100 MWh.
- The optimal gamma throughout ranged between -2 and -4 degrees for energy.

- The value of the height above ground (E) appeared to be random and ranged between 0.5 and 1.5 meters.
- In general, Fusion and SMPSO yielded the best overall results with respect to finding extreme solutions and well-distributed solutions.

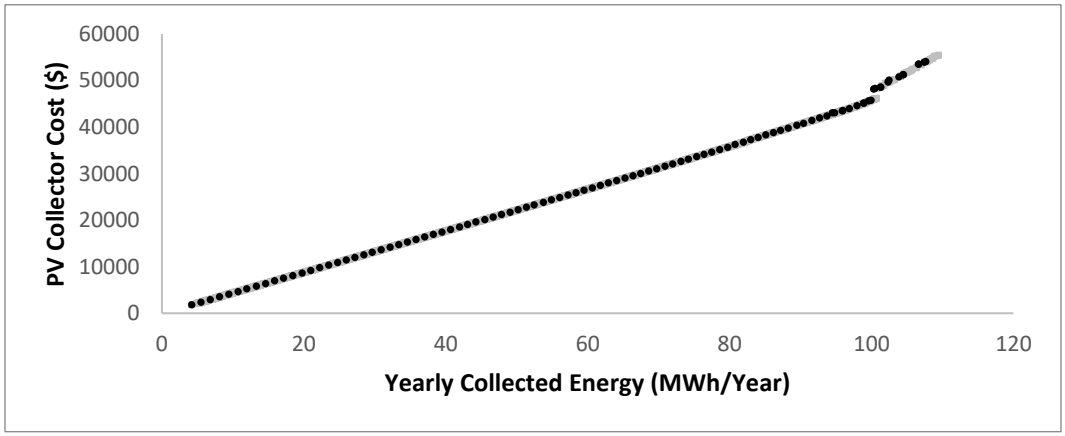

(a)

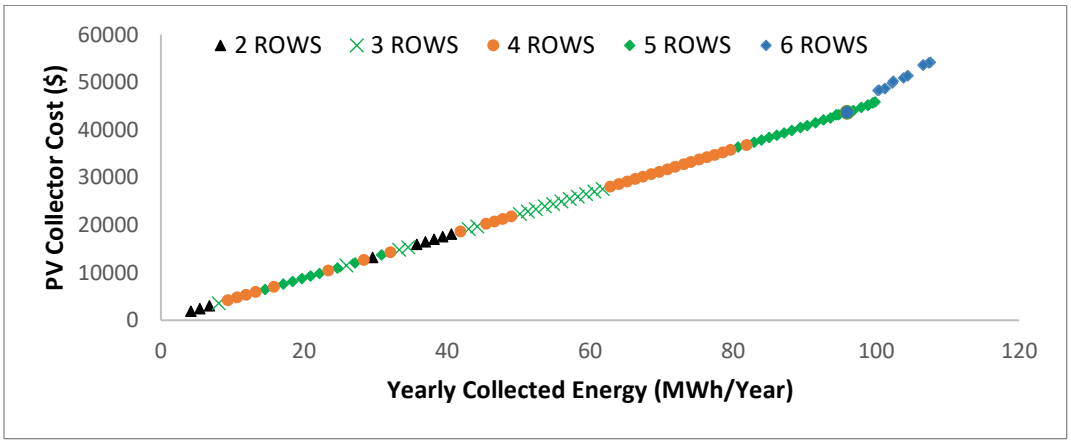

(b)

FIGURE 8-12 The best set of non-dominated solution set (Based on IGD measure) found by NSGA-III. (a) The grey dotted background indicated the non-dominated solutions assembled during 25 runs of all algorithms and the black dots indicate the best solution set obtained by NSGA-III based on the IGD measure. (b) Best solution set found by the NSGA-III algorithm with respect to the number of collector rows associated with each solution.

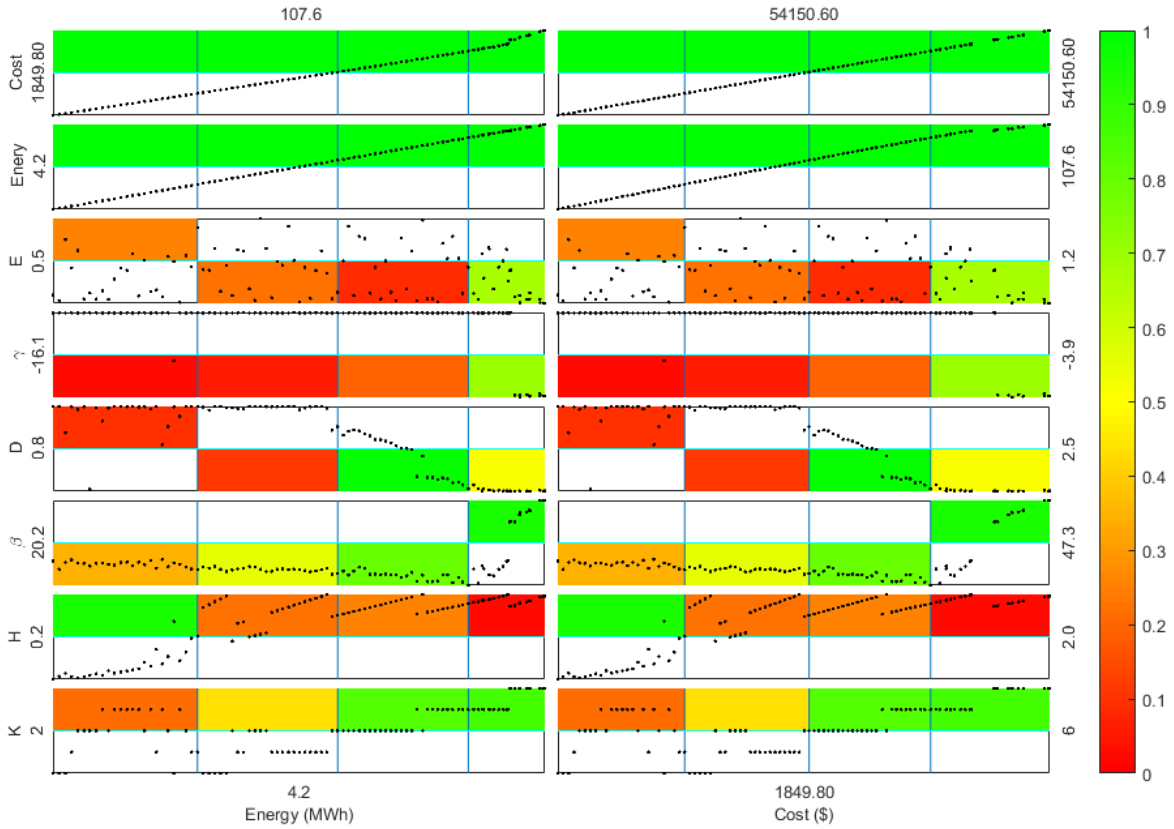

FIGURE 8-13 ECM plot of the best set of non-dominated solution set (Based on IGD measure) found by the NSGA-III algorithm

8.5.5 Solution Extraction using the FNFR Method

Often times we evolutionary optimizers require large population size (normally 100 for bi-objective problems) to be able to sufficiently explore the landscape and cover the PF surface. Moreover, when a number of runs required to assess the quality of solutions the number of non-dominated solutions collected from the many runs can reach to thousands. In this section we discuss how the proposed FNFR method is able to extract well-distributed subset of solutions in a preferred region among thousands of potential solutions. Consequently, a decision maker can easily assess limited number of solutions and arrive at one optimal solution.

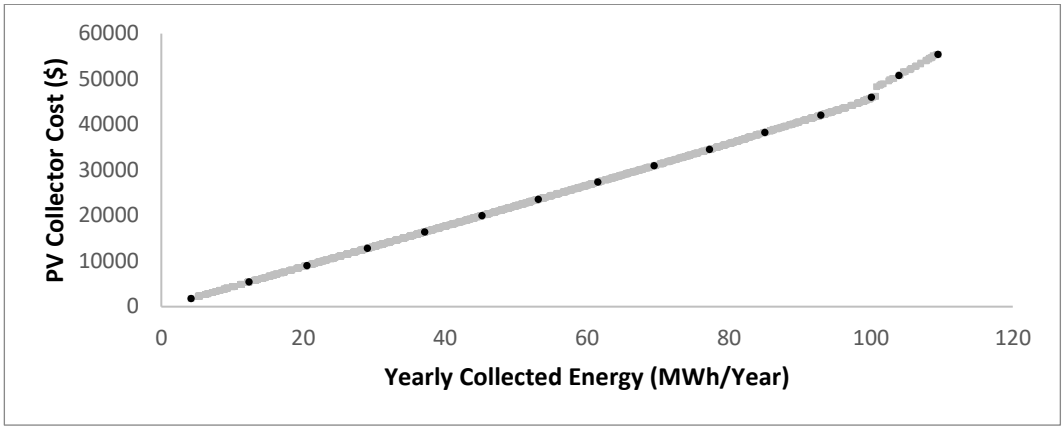

FIGURE 8-14 Well-distributed solutions extracted by the FNFR scheme. The black dots illustrate 15 uniformly distributed solutions extracted from non-dominated solutions (grey dotted background) assembled during 25 runs of the Fusion algorithm.

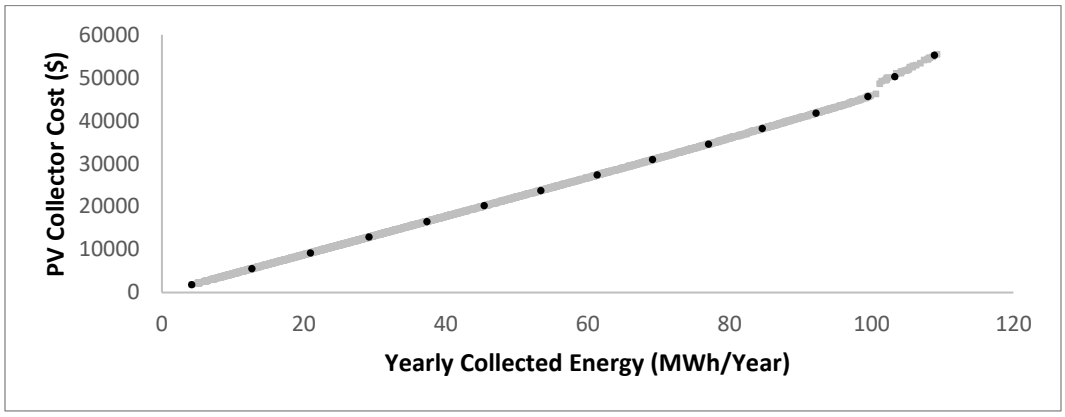

FIGURE 8-15 Well-distributed solutions extracted by the FNFR scheme. The black dots illustrate 15 uniformly distributed solutions extracted from non-dominated solutions (grey dotted background) assembled during 25 runs of the SMPSO algorithm.

Figure 8-14 to Figure 8-18 show well-distributed solutions extracted using the FNFR method. The black dots illustrate 15 uniformly distributed solutions extracted from non-dominated solutions (grey dotted background) assembled during 25 runs of the Fusion, SMPSO, GDE3, SPEA2, and NSGA-III algorithms. The Fusion, SMPSO and NSGA-III algorithms were able to cover the entire Pareto-optimal front in 25 runs and as a result the FNFR method was able to select a subset of well-distributed solutions spanning the entire front. On the other hand the obtained solutions by the GDE3 and SPEA2 algorithms failed

to cover the entire Pareto-optimal front and hence the FNFR method was able to select the 15 well-distributed solutions with the two extreme solutions found by these algorithms.

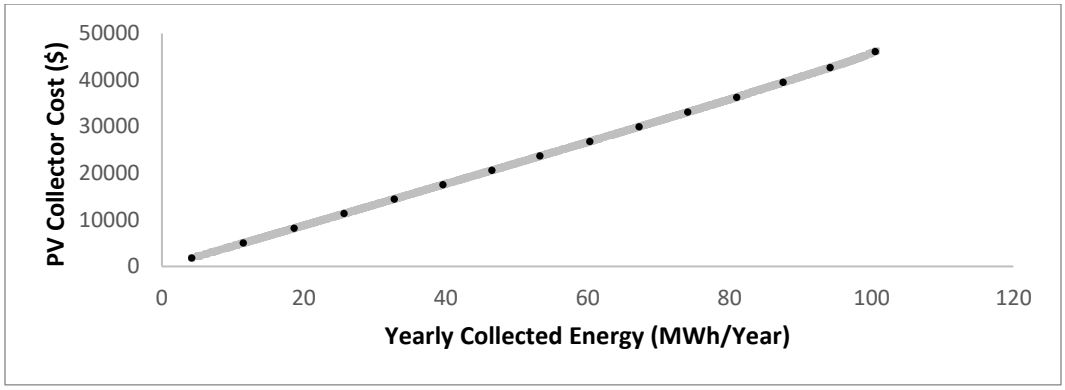

FIGURE 8-16 Well-distributed solutions extracted by the FNFR scheme. The black dots illustrate 15 uniformly distributed solutions extracted from non-dominated solutions (grey dotted background) assembled during 25 runs of the GDE3 algorithm.

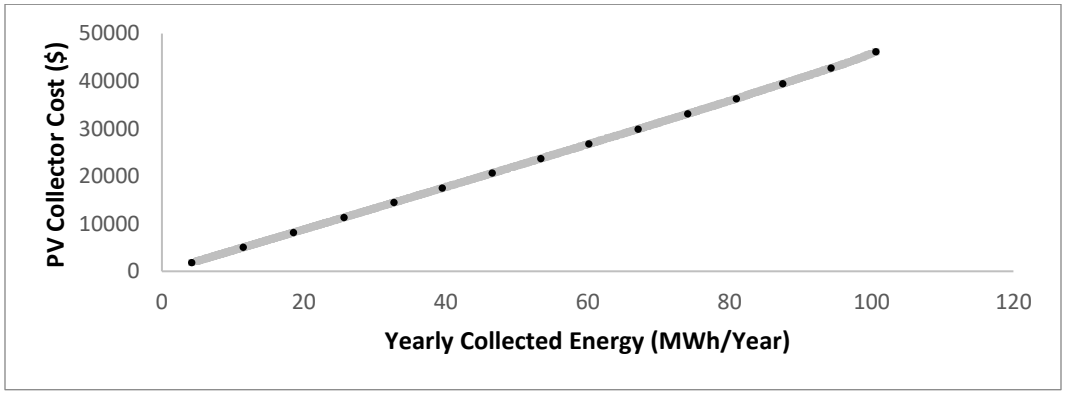

FIGURE 8-17 Well-distributed solutions extracted by the FNFR scheme. The black dots illustrate 15 uniformly distributed solutions extracted from non-dominated solutions (grey dotted background) assembled during 25 runs of the SPEA2 algorithm.

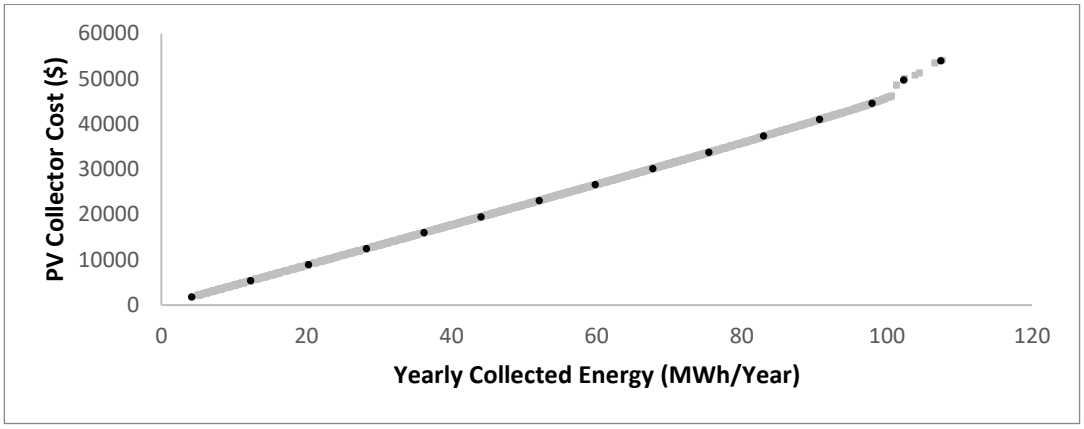

FIGURE 8-18 Well-distributed solutions extracted by the FNFR scheme. The black dots illustrate 15 uniformly distributed solutions extracted from non-dominated solutions (grey dotted background) assembled during 25 runs of the NSGA-III algorithm.

Figure 8-19 show 15 well-distributed solutions extracted from thousands of solutions obtained by all algorithms collectively during 25 runs. Figure 8-20 show the capability of the FNFR method to extract well-distributed solutions in multiple regions of the Pareto-optimal front. The black dots illustrate three clusters of 15 uniformly distributed solutions extracted from non-dominated solutions (grey dotted background) assembled during 25 runs of the Fusion, SMPSO, GDE3, SPEA2, and NSGA-III algorithms.

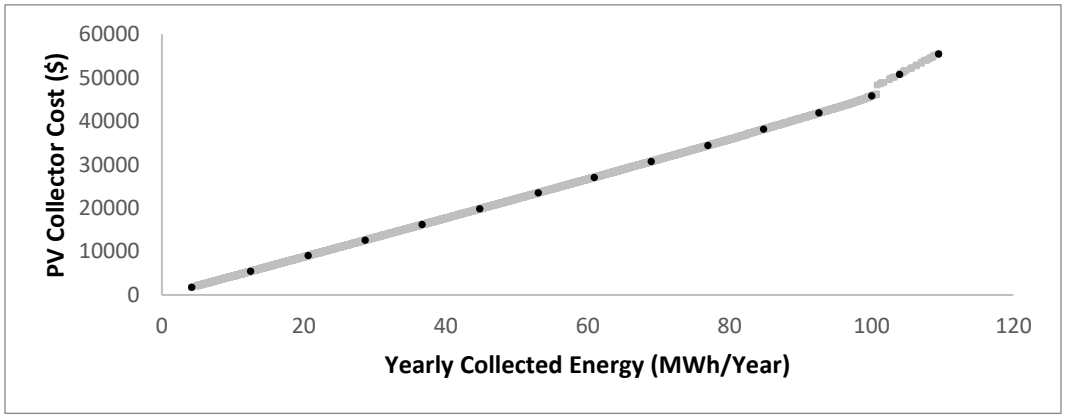

FIGURE 8-19 Well-distributed solutions extracted by the FNFR scheme. The black dots illustrate 15 uniformly distributed solutions extracted from non-dominated solutions (grey dotted background) assembled during 25 runs of the Fusion, SMPSO, GDE3, SPEA2, and NSGA-III algorithms.

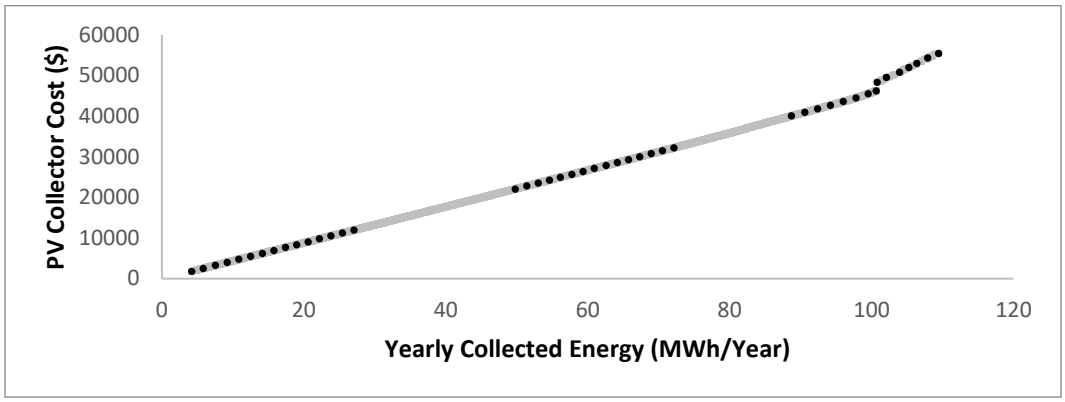

FIGURE 8-20 Preferred solutions extracted by the FNFR scheme. The black dots illustrate three clusters of 15 uniformly distributed solutions extracted from non-dominated solutions (grey dotted background) assembled during 25 runs of the Fusion, SMPSO, GDE3, SPEA2, and NSGA-III algorithms.

8.6 Conclusion

In this chapter, four state-of-the art MOEAs, namely SMPSO, GDE3, SPEA2 and NSGA-III, and the proposed Fusion algorithm were used for optimal deigning of solar farm. The objectives were the maximization of the total incident solar energy and the minimization of the cost of deployment for a specific field. The decision variables consisted in number of collector rows, distance between collector rows, dimension of collectors, collectors inclination angle and collectors azimuth.

The optimization methods used in this study were able to find a variety of optimal PV farm design solutions which would not possible using single objective solutions. For example, some intermediate solutions could be of interest with regards to other non-expressed objectives or secondary objectives such as space between solar panels or other technical aspects. Based on the result, the Fusion algorithm able to find the maximum energy $Q = 109.41$ MWh/year when the number of rows $K = 6$, the PV panel height

$H = 1.97$ meters, the PV inclination angle $\beta = 47.76°$, the distance between subsequent panels D = 80 cm, and the PV clearance above the ground E=50 cm. From the ECM plots, it was found that the optimal inclination angle of the PV was between 27 and 33 degrees for energy absorbed up to 100 MWh and 48^o when the energy absorbed was above 100 MWh. Furthermore, the optimal distance between collectors was 2.5 meters for energy absorbed up to 100 MWh and 0.8 meters beyond 100 MWh. The optimal gamma throughout ranged between -2 and -4^o for the optimal energy absorbed.

Experimental results showed that overall the Fusion and SMPSO algorithms significantly outperformed the GDE3, SPEA2, and NSGA-III algorithms. Their performance suffered mainly due to that fact that they failed find solutions beyond the 100.63 MWh/year. When comparing the SMPSO and the Fusion algorithms, the Fusion algorithm was able to find broad spectrum of solutions (with regard to the number of rows of the PV panels) despite the marginally better IGD value of obtained by the SMPSO algorithm.

For future work, we would like to use solar farms with tracking capability as supposed to stationary solar farms that were discussed in this chapter. Additionally, we would like to investigate gradual linear land inclination between rows in order to minimize the shadow on subsequent rows. Finally, we would like look into using ray focusing mirrors to direct the radiation in cases where the sun's ray is not in the direction of the solar panels.

Chapter 9

MULTI-OBJECTIVE THERMAL ANALYSIS OF A THERMOELECTRIC DEVICE: INFLUENCE OF GEOMETRIC FEATURES ON DEVICE CHARACTERISTICS

Proper assessment of geometric features of a thermoelectric generator is important to design devices with improved performance features such as high efficiency and output power. This chapter presents multi-objective optimization of the geometric features of a thermoelectric generator for improved efficiency and output power while incorporating different operating conditions. The parameters assessing geometric features of the device include shape factor and pin length size while operating parameters include temperature ratio and external load parameter. Thermal analysis incorporating geometric features and operating parameters of the device is introduced prior to the optimization study. Continuing from Chapter 8, this chapter further investigates how the proposed algorithm (Fusion), visualization scheme (ECM), performance measure (ObjIGD), and solution(s) selection mechanism (FNFR) can help the optimization process of multi-objective geometric design of the thermoelectric generator and assist decision maker to arrive at an optimal solution.

9.1 Introduction

Increasing demand for electrical energy consumption led to the development of efficient energy conversion devices, which use clean energy resources. Sustainable development of energy efficient devices requires extensive research into design and operation of the electrical energy generation devices through integration of renewable energy technologies. Thermoelectric power generator is one of these devices, which involves efficient electrical energy generation from waste heat. Although efficiency of traditional thermal to electric generators is several times higher than the efficiency of a thermoelectric system for large electrical power generation applications, the traditional systems are expensive, due to large-scale energy requirements, and they operate at high temperatures. On the other hand, for applications requiring less than 100 Watts, thermoelectric generators become less costly

and have several advantages over the traditional thermal to electric generators [157]. The recent developments in thermoelectric materials extend the thermodynamics analysis to cover high temperature ranges. This is vital since the efficiency of a thermoelectric converter depends heavily on the temperature differences. In addition, efficiency of thermoelectric devices can also be enhanced through modifying device geometric configurations [158-160]. Therefore, it is essential to carefully investigate the influence of geometric configuration of thermoelectric device performance such as efficiency and power.

Considerable research studies have been carried out to examine thermoelectric device performance for various applications. Exergy analysis and performance assessment of thermoelectric generator were carried out by Wang et al. [161]. Their findings revealed that both the maximum energy efficiency and exergy efficiency increased with increasing hot-reservoir temperature for the case where the Seebeck coefficient and thermal conductivity was temperature-dependent. Performance of a solar heat pipe thermoelectric generator unit was carried out by He et al. [162]. They presented the influence of basic parameters on device performance. These parameters included solar irradiation, cooling water temperature, thermo-element length and cross-section area, and a number of thermo-elements. Efficiency improvement of thermoelectric generators was investigated by Patyk [163]. He demonstrated that, under various operating conditions, thermoelectric generators in power units could save waste energy and reduce the environmental burden due to their eco-efficient characteristics. Parametric and exergetic analysis of waste heat recovery system based on thermoelectric generator was carried out by Shu et al. [164]. They suggested that combined thermoelectric and an organic cycle system was suitable for waste

heat recovery from engines. In this case, thermoelectric generation could extend the temperature range of a heat source and thereby improve the fuel economy of engines.

Thermoelectric energy conversion incorporating linear and nonlinear temperature dependence of material properties was examined by Wee et al. [165]. They indicated that inclusion of the Thomson effect was essential to assess the qualitative behaviour of thermoelectric energy conversion system. Influences of effective temperature differences and electrical parameters on performance of thermoelectric generators were studied by Kim [166]. He showed that approximately 25% of the maximum output power was lost because of the parasitic thermal resistance of the thermoelectric module. Efficiency analysis of thermoelectric combined energy systems was carried out by Chen et al. [167]. They indicated that the overall conversion efficiency of the thermal system could be improved significantly through integration of thermoelectric devices.

With regard to multi-objective optimization, a few notable recent studies have been carried out to investigate the performance of thermoelectric devices under various operating conditions and device configurations. Rao and Patel [168] successfully utilized a modified Teaching-Learning based multi-objective optimization (TLBO) algorithm to maximize the cooling capacity and the coefficient of performance of thermoelectric cooler (TEC). In this study, they have considered two different configurations of TECs, electrically separated and electrically connected in series as well as the contact and spreading resistance of the TEC. On the other hand, Belanger and Gosselin [169] developed a simulation model of a heat exchanger with thermoelectric generators in its walls to optimize the total volume, total number of thermoelectric modules, output power, and pumping power. Their results showed that the number of sub-channels in the heat

exchanger has a more significant impact on the overall performance than the fin geometry. Moreover, the net output power is largely dependent on the number of thermoelectric modules but not on the heat exchanger volume. NSGA-II was widely used in optimization of thermal systems for improved performances [170-179]. Optimization of thermodynamic system incorporating an ammonia-water power cycle was carried out by Wang et al. [170]. They demonstrated that the optimization provided the useful information to maximize the exergy efficiency and minimize the total heat transfer capability and turbine size parameter under the given waste heat conditions. The Pareto-optimal solutions for an Organic Rankine Cycle for diesel engine waste heat recovery system were introduced by Hajabdollahi et al. [171] using the NSGA-II algorithm. They indicated that the algorithm used maximized the thermal efficiency and minimized the total annual cost simultaneously. Design and optimization of a tubular recuperative heat exchanger used in a regenerative gas turbine cycle were carried out by Sayyaadi et al. [172]. They showed that the multi-objective optimization scenario incorporating the NSGA-II algorithm could be considered as a generalized optimization approach in which balances between economical viewpoints of both heat exchanger manufacturer and end user of recuperater could be achieved. Systematic analysis of the heat exchanger arrangement problem using multi-objective genetic optimization was presented by Daroczy et al. [173]. In the analysis, they considered the conditions, which were particularly suited for low-power applications, as found in a growing number of practical systems in an effort toward increasing energy efficiency.

Ibrahim et al. [174] used the NSGA-II and GDE3 algorithms to investigate the optimal photovoltaic (PV) farm design yielding the maximum field incident energy collected while minimizing the deployment cost of PVs in the Toronto area, Canada. They

were able to find a diverse set of optimal PV farm design solutions which would not be possible to achieve using single objective algorithms.

With regard to energy planning, Silva et al. [180] have utilized three recent Particle Swarm Optimization (PSO) based multi-objective optimizers, MOPSO-CDR, MOPSO-DFR, and SMPSO to investigate the optimal operational planning involving hydrothermal systems composed of eight Brazilian hydroelectric plants. The optimization problem involved minimizing the total cost of thermal power while maximizing the total stored energy in all reservoirs. They have shown that it is possible to approach the planning of hydrothermal systems as a multi-objective problem.

The performance characteristics of thermoelectric devices, mainly, depend on the design parameters and operating conditions. The design configuration can be improved through the enhancement of the average Figure of Merit ($ZT_{average}$) and re-sizing of the thermoelectric active elements such as thermoelectric pins [158]. Enhancement of the averaged Figure of Merit requires improvement in the pin materials, such as Bi_2Te_3 and Skutterudites [181]. Since the improvement of the device, active material involves material science research, this is not considered in the present study. However, the influence of geometric configurations on thermal performance of thermoelectric devices was investigated previously [159, 160, 181], where the main focus was the assessment of device performance as a result of a single parametric variation. Therefore, the geometric parameters maximizing device performance are considered in the present study in line with the previous findings [158-160]. However, optimization study for device performance considering all geometric configurations under various operating conditions was not thoroughly investigated. Moreover, the two objectives, namely, the maximization of power

and efficiency are conflicting objectives. To fill out this gap, the present study uses the Fusion algorithm along four state-of-the-art MOEAs, namely, SMPSO, GDE3, SPEA2, and NSGA-III to optimize the efficiency and the output power of a thermoelectric device. The optimization of thermoelectric device performance due to different device geometric configurations and operating conditions are presented, yielding an analysis of optimum device geometric configurations for high thermal efficiency and output power. Furthermore, the proposed ECM plot, ObjIGD measure, and FNFR method are used to visually and quantitatively investigate the optimization decision making process.

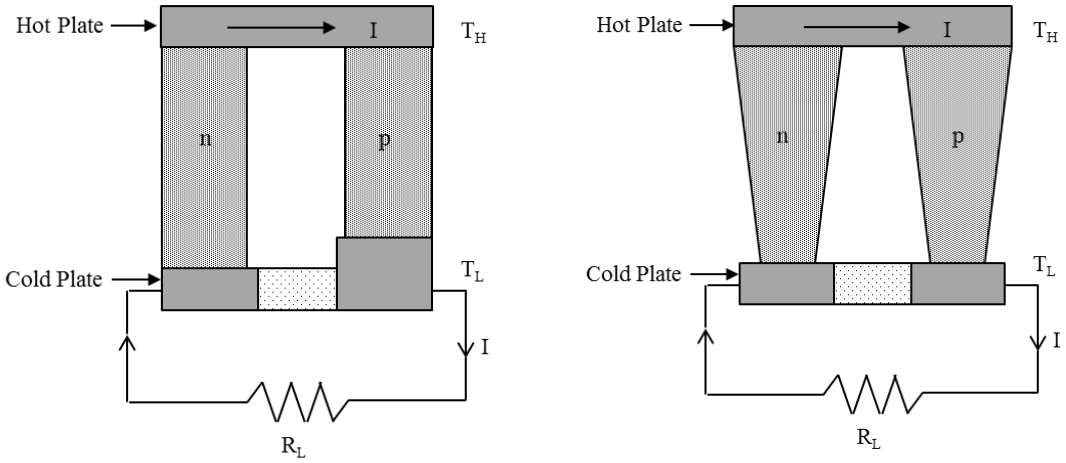

FIGURE 9-1 A schematic view of thermoelectric generator for different geometric configurations: (a) size of pin legs is different and (b) shape factor is different.

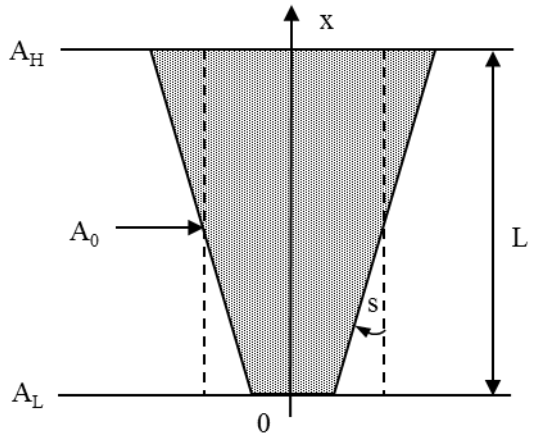

FIGURE 9-2 Schematic view of geometric configuration of thermoelectric pin.

9.2 Analysis of Thermoelectric Device

The objective of the problem is to optimize the geometric features of a thermoelectric generator that can improve the efficiency and output power of the thermoelectric device while incorporating different operating conditions. The parameters assessing geometric features of the device include shape factor and pin length size while operating parameters include temperature ratio and external load parameter.

Thermal efficiency of the thermoelectric generator due to pin geometric configurations, as shown in Figure 9-1, can be written as [159]:

$$\eta = \frac{I^2 R_L}{\alpha I T_1 + K(T_1 - T_2) - \frac{1}{2} I^2 R}, \tag{9.1}$$

where K is the thermal conductance and R is the electrical resistivity of the thermoelectric generator.

The current I is a function of the net Seebeck coefficient $\alpha = \alpha_p - \alpha_n$ (the difference between the Seebeck coefficients of *p* and *n* junctions), the upper and lower junction temperatures (T_1 and T_2), the electrical resistance R and the external load resistance R_L as:

$$I = \frac{\alpha(T_1 - T_2)}{R_L + R}. \tag{9.2}$$

Substituting Equation (9.2) in Equation (9.1) the efficiency becomes

$$\eta = \frac{\alpha^2 (T_1 - T_2) R_L}{K(R_L + R)^2 + \alpha^2 T_1 (R_L + R) - \frac{1}{2}\alpha^2 (T_1 - T_2) R}. \tag{9.3}$$

The cross-sectional area of the pin (leg) of the thermoelectric generator, as shown in Figure 9-2, can be written as [159]:

$$A(x) = A_0 + S\left(x - \frac{L}{2}\right)\delta, \tag{9.4}$$

where A_0 is the average (mid-height) cross-sectional area, L is the height of the pin, δ is the thickness of the pin, and S is the shape factor of the pin, i.e.,

$$S = \frac{1}{\delta}\frac{dA}{dx}. \tag{9.5}$$

After assuming a steady heating situation and isolated leg surfaces, the rate of heat transfer along the x-axis in the pin can be written as [159]:

$$\dot{Q} = \frac{kS\delta}{\ln\left(\frac{A_0 + S\delta\frac{L}{2}}{A_0 - S\delta\frac{L}{2}}\right)}(T_1 - T_2), \tag{9.6}$$

The overall thermal conductance of the pin in Equation (9.6) is:

$$K_{leg} = \frac{kS\delta}{\ln\left(\frac{A_0 + S\delta\frac{L}{2}}{A_0 - S\delta\frac{L}{2}}\right)}. \tag{9.7}$$

Total thermal conductance of the thermoelectric generator due to two pins can be written as:

$$K = \frac{(k_p + k_n)S\delta}{\ln\left(\frac{A_0 + S\delta\frac{L}{2}}{A_0 - S\delta\frac{L}{2}}\right)}, \tag{9.8}$$

where k_p and k_n are the thermal conductivities of the p-type and n-type pins, respectively. The overall electrical resistance of the pin ($R_{leg} = \int_0^L \frac{dx}{kA(x)}$) can be obtained by substituting $A(x)$ from Equation (9.5) and performing the integration; therefore, the overall electrical resistance becomes:

$$R_{leg} = \frac{1}{k_e m\delta}\ln\left(\frac{A_0 + S\delta\frac{L}{2}}{A_0 - S\delta\frac{L}{2}}\right). \tag{9.9}$$

Thus, the total electrical resistance of the thermoelectric generator due to two pins is given by:

$$R = \left(\frac{1}{k_{e,p}} + \frac{1}{k_{e,n}}\right)\frac{1}{S\delta}\ln\left(\frac{A_0 + S\delta\frac{L}{2}}{A_0 - S\delta\frac{L}{2}}\right) = \frac{k_{e,p} + k_{e,n}}{k_{e,p}k_{e,n}S\delta}\ln\left(\frac{A_0 + S\delta\frac{L}{2}}{A_0 - S\delta\frac{L}{2}}\right), \tag{9.10}$$

where k_{ep} and k_{en} are the electrical conductivities of the p-type and n-type pins, respectively. Substituting Equations (9.8) and (9.10) in Equation (9.3), efficiency of the thermoelectric generator can be written in dimensionless form as [159]:

$$\eta = (1-\theta)\frac{2ZT_{ave}\left(1+\sqrt{\frac{r_k}{r_{ke}}}\right)^2\left(\frac{R_L}{R_0}\right)}{(1+\theta)\left(\frac{K}{K_0}\right)\left(\frac{R_L}{R_0}+\frac{R}{R_0}\right)^2+2ZT_{ave}\left(1+\sqrt{\frac{r_k}{r_{ke}}}\right)^2\left[\frac{R_L}{R_0}+\frac{1}{2}\frac{R}{R_0}(1+\theta)\right]}, \quad (9.11)$$

where $\theta = \frac{T_2}{T_1}$ is the temperature ratio; $r_k = \frac{k_p}{k_n}$ is the thermal conductivity ratio; $r_{ke} = \frac{k_{e,p}}{k_{e,n}}$ is the electrical conductivity ratio; $ZT_{ave} = \frac{\alpha^2\left(\frac{k_{e,n}}{k_n}\right)T_1}{\left(1+\sqrt{\frac{r_k}{r_{ke}}}\right)^2}\left(\frac{1+\theta}{2}\right)$ is the figure of merit based on the average temperature; $K_0 = \frac{A_0 k_n}{L}$ is the reference thermal conductance; and $R_0 = \frac{L}{A_0 k_{e,n}}$ is the reference electrical resistivity of the thermoelectric device.

Hence, the overall thermal conductance and overall electrical resistivity can be written in dimensionless form as:

$$\frac{K}{K_0} = \frac{\mu(r_k+1)}{\ln\left(\frac{1+\mu/2}{1-\mu/2}\right)}, \quad (9.12)$$

and

$$\frac{R}{R_0} = \left(\frac{1+r_{ke}}{r_{ke}}\right)\frac{\ln\left(\frac{1+\mu/2}{1-\mu/2}\right)}{\mu}, \quad (9.13)$$

where μ is the dimensionless slope parameter and is defined as $\mu = \frac{S\delta L}{A_0}$.

The power generation from the thermoelectric power generator is $\dot{W} = I^2 R_L$, which yields:

$$\dot{W} = \frac{\alpha^2 (T_1 - T_2)^2}{(R_L + R)^2} R_L \,, \tag{9.14}$$

and thus the dimensionless power generation can be written as [159]:

$$\frac{\dot{W}}{K_0 T_2} = 2\frac{(1-\theta)^2}{\theta(1+\theta)} \frac{ZT_{ave}\left(1+\sqrt{\frac{r_k}{r_{ke}}}\right)^2 \left(\frac{R_L}{R_0}\right)}{\left(\frac{R_L}{R_0}+\frac{R}{R_0}\right)^2}. \tag{9.15}$$

The optimization problem is composed of two problems: the optimization of the output power and efficiency of a thermoelectric device without considering the shape factor (see Figure 9-1 (a)) and the optimization of the output power and efficiency of a thermoelectric device when considering the shape factor (see Figure 9-1 (b) and Figure 9-2). The optimization problem without the shape factor comprises of two objectives and seven variables; while the optimization problem with the shape factor contains two objectives and six variables. These two objectives in both problems are the maximization of thermal efficiency (η) and output power (Ẇ) based on Equations (9.1) and (9.14), respectively. The seven variables used in the first problem are the upper and lower temperatures (T_1 and T_2), the external load resistance (R_L), the cross-sectional area of the pins ($A_n$and A_p), and the height of the pins (L_n and L_p). The six variables used in optimization with shape factor are the same as the above-mentioned variables except A_n and A_p are replaced by the average (mid-height) cross-sectional area of the pin (A_o), L_n and L_p replaced by the average pin height (L) and additional variable, the shape factor (S). The mathematical formulation of the optimization problem is defined as follows:

Maximize (For both optimization problems) based on Equations (9.1) and (9.14):

$$\eta = \frac{I^2 R_L}{\alpha I T_1 + K(T_1 - T_2) - \frac{1}{2} I^2 R}$$

$$\dot{W} = \frac{\alpha^2 (T_1 - T_2)^2}{(R_L + R)^2} R_L$$

Variable Bounds (Optimization without Shape Factor):

The upper and lower junction temperatures range between 273K (0℃) and 600K (327℃).

$$300 \leq T_1 \leq 600 \quad (9.16)$$

$$273 \leq T_2 \leq 400 \quad (9.17)$$

The external load resistance is kept at a maximum of 100 Ω.

$$0.1 \leq R_L \leq 100 \quad (9.18)$$

The cross-sectional area of the pins and the height the pins capped to:

$$10^{-6} \leq A_n \leq 5.0 \times 10^{-4} \, (m^2) \quad (9.19)$$

$$10^{-6} \leq A_p \leq 5.0 \times 10^{-4} \, (m^2) \quad (9.20)$$

$$10^{-3} \leq L_n \leq 4.0 \times 10^{-3} (m) \quad (9.21)$$

$$10^{-3} \leq L_p \leq 4.0 \times 10^{-3} (m) \quad (9.22)$$

Variable bounds (Optimization with shape factor):

$$300 \leq T_1 \leq 600 \quad (9.23)$$

$$273 \leq T_2 \leq 400 \quad (9.24)$$

$$0.1 \leq R_L \leq 100 \quad (9.25)$$

$$10^{-6} \leq A_o \leq 5.0 \times 10^{-4} \, (m^2) \quad (9.26)$$

$$10^{-3} \leq L \leq 4.0 \times 10^{-3} (m) \quad (9.27)$$

The shape factor is limited between 0 and 1. The zero shape factors correspond to vertically parallel pins while 1 corresponds to a horizontal pin (this is an extreme case implying the contact area of the lower junction is 0). The shape factor 0.5 corresponds to pin vertical slope of $45°$.

$$0 \leq S < 1 \tag{9.28}$$

where:

$$T_1, T_2, R_L, A_n, A_p, A_0, L_n, L_p, L \in \mathbb{R}.$$

TABLE 9.1 Parameters' settings used in the Thermal experiments. n is the number of variables in the problem.

For All	
Population size (P)	100
Number generations	250
GDE3	
Mutation probability (F)	0.1
Crossover probability (CR)	0.5
SMPSO	
Archive size	$\|P\|$
Polynomial mutation (p_m)	$1/n$
Mutation Distribution Index (η_m)	20
SPEA2	
Archive size	$\|P\|$
SBX probability (p_c)	0.9
Polynomial mutation (p_m)	$1/n$
Crossover Distribution Index (η_c)	20
Mutation Distribution Index (η_m)	20
NSGA-III	
SBX probability (p_c)	1.0
Polynomial mutation (p_m)	$1/n$
Crossover Distribution Index (η_c)	30
Mutation Distribution Index (η_m)	20
Fusion	
Number of Reference Points	99

9.3 Experimental Setup and Results

Optimization study of thermoelectric power generator for improved thermal efficiency and output power is considered, and the optimum device geometric configuration is identified. Thermal efficiency and output power are formulated in terms of device geometric configurations. The findings are validated against the results of previous studies in [159] and [160]. The parameters incorporated in the two optimization problems include shape factor, length of the pins, external load parameter, and operating temperature ratio. It should be noted that shape factor and pin length size define the geometric features of the device while external load parameter and operating temperature ratio are related to the operating conditions of the device.

9.3.1 Parameter Settings

In this case study, the proposed Fusion, SMPSO, GDE3, SPEA2, and NSGA-III are utilized to investigate the optimal geometric features of a thermoelectric generator for improved efficiency and output power while incorporating different operating conditions. Due to the stochastic nature of heuristic algorithms, the proposed algorithms were executed 25 times and the stopping criterion was set to 2.5×10^4 function evaluations. In addition, the HV, IGD, Spread, and ObjIGD measures are used to compare the performance of each result. Table 9.1 show the parameter settings used in this case study.

TABLE 9.2 The maximum power and efficiency obtained for the optimal thermal design problems.

Algorithm	Max. Power (Watts)	Max. Efficiency (%)
Fusion	0.3395	18.438
SMPSO	0.3395	18.438
GDE3	0.3397	18.438
SPEA2	0.3403	18.438
NSGA-III	0.3404	18.438

(a) Without the shape factor

Algorithm	Max. Power (Watts)	Max. Efficiency (%)
Fusion	0.3647	18.418
SMPSO	0.3649	18.418
GDE3	0.3659	18.418
SPEA2	0.3659	18.418
NSGA-III	0.3659	18.418

(b) With the shape factor.

9.3.2 Optimization without the Shape Factor

In order to validate the optimization results, the first optimization problem implemented to determine the influence of operating and device parameters of the thermoelectric device on the maximum efficiency and the maximum output power (see Figure 9-1 (a)). Figure 9-3 (a), Figure 9-5 (a), Figure 9-7 (a), Figure 9-9 (a), and Figure 9-11(a) present the distribution of Pareto-optimal solutions (based on the best IGD results) obtained by the proposed algorithms, Fusion, SMPSO, GDE3, SPEA2, and NSGA-III, respectively. Table 9.2 (a) shows the two extreme (end) solutions obtained through the proposed algorithms. These solutions indicate the maximum possible output power and efficiency that can be achieved through the current design (see Figure 9-1 (a)) and its variable bounds (see Equations (9.16) – (9.22)). The HV, IGD, Spread, and ObjIGD results (see Table 9.3 (a)) indicate that the quality of the solutions obtained through these algorithms are comparable.

However, the Fusion algorithm marginally outperformed the other four algorithms in terms of solutions' accuracy, spread, and distribution of solutions over the PF as well as along each objective (see to ObjIGD values in Table 9.3 (b)). Moreover, the Fusion algorithm was able to produce consistent results over many runs, regardless of the initial randomized population.

According to the results found in [160], at a fixed temperature, the thermoelectric power is a function of the external load resistance. The output power is maximized when $\frac{\partial \dot{W}}{\partial R_L} = 0$. Thus,

$$(R_L)_{opt} = R \tag{9.29}$$

$$\dot{W}_{max} = \frac{\alpha^2 (T_1 - T_2)}{4R} \tag{9.30}$$

Similarly, a fixed temperature, the thermoelectric efficiency is a function of the external load resistance. The efficiency is maximized when $\frac{\partial \eta}{\partial R_L} = 0$. Thus,

$$(R_L)_{opt} = R\sqrt{1 + ZT_{avg}}, \tag{9.31}$$

$$\eta_{max} = \left. \frac{\alpha^2 (T_1 - T_2) R_L}{K(R_L + R)^2 + \alpha^2 T_1 (R_L + R) - \frac{1}{2}\alpha^2 (T_1 - T_2) R} \right|_{R_L = R\sqrt{1+ZT_{avg}}}. \tag{9.32}$$

TABLE 9.3 Min, max, mean, and standard deviation of HV measures for the optimal thermal design problem.

Metric	Fusion	SMPSO	GDE3	SPEA2	NSGAIII
IGD	6.25E-05	6.16E-05	6.64E-05	6.95E-05	1.01E-04
	6.43E-05	6.36E-05	6.88E-05	8.67E-05	1.16E-04
	6.89E-05	6.48E-05	7.52E-05	3.41E-04	2.16E-04
	6.50E-05	6.34E-05	6.91E-05	1.04E-04	1.23E-04
HV	6.81E-01	6.82E-01	6.81E-01	6.81E-01	6.81E-01
	6.81E-01	6.82E-01	6.81E-01	6.80E-01	6.80E-01
	6.81E-01	6.81E-01	6.80E-01	6.79E-01	6.80E-01
	6.81E-01	6.82E-01	6.81E-01	6.80E-01	6.80E-01
Spread	1.03E-01	6.37E-02	1.34E-01	1.30E-01	3.26E-01
	1.25E-01	8.54E-02	1.59E-01	1.76E-01	3.59E-01
	1.82E-01	7.43E-01	1.84E-01	2.26E-01	7.67E-01
	1.31E-01	1.11E-01	1.60E-01	1.79E-01	3.79E-01
ObjIGD	4.09E-05	4.32E-05	4.54E-05	4.70E-05	6.97E-05
	4.16E-05	4.38E-05	4.63E-05	6.13E-05	7.68E-05
	4.54E-05	4.58E-05	4.78E-05	2.93E-04	1.43E-04
	4.18E-05	4.39E-05	4.66E-05	8.77E-05	8.61E-05

(a) Without the shape factor

Metric	Fusion	SMPSO	GDE3	SPEA2	NSGAIII
IGD	3.61E-05	3.87E-05	4.07E-05	4.20E-05	7.49E-05
	3.62E-05	4.05E-05	4.32E-05	4.32E-05	7.69E-05
	3.69E-05	4.26E-05	4.49E-05	4.51E-05	7.81E-05
	3.62E-05	4.06E-05	4.32E-05	4.33E-05	7.68E-05
HV	6.89E-01	6.89E-01	6.88E-01	6.88E-01	6.88E-01
	6.89E-01	6.89E-01	6.88E-01	6.88E-01	6.88E-01
	6.89E-01	6.89E-01	6.88E-01	6.88E-01	6.88E-01
	6.89E-01	6.89E-01	6.88E-01	6.88E-01	6.88E-01
Spread	1.12E-02	5.85E-02	1.59E-01	1.36E-01	3.39E-01
	2.28E-02	7.83E-02	1.77E-01	1.64E-01	3.54E-01
	6.09E-02	1.05E-01	1.96E-01	1.90E-01	3.75E-01
	2.28E-02	7.79E-02	1.77E-01	1.64E-01	3.54E-01
ObjIGD	2.63E-05	2.77E-05	2.97E-05	2.96E-05	4.97E-05
	2.63E-05	2.89E-05	3.08E-05	3.10E-05	5.08E-05
	2.64E-05	3.00E-05	3.18E-05	3.18E-05	5.15E-05
	2.63E-05	2.90E-05	3.08E-05	3.10E-05	5.08E-05

(b) With the shape factor.

TABLE 9.4 Fifteen uniformly distributed non-dominated solutions extracted from solutions assembled during 25 runs of the Fusion, SMPSO, GDE3, SPEA2, and NSGA-III algorithms using the FNFR scheme.

$\dot{W}$ $(Watts)$	$\eta(\%)$	$T_1(K)$	$T_2(K)$	$R_L(\Omega)$	$A_p(m^2)$	$A_n(m^2)$	$L_p(m)$	$L_n(m)$
0.14784	18.438	600	273	0.1	8.10E-05	1.19E-04	3.92E-03	2.43E-03
0.16903	18.289	600	273	0.1	1.47E-04	1.34E-04	3.64E-03	3.60E-03
0.18919	17.878	600	273	0.1	1.39E-04	1.34E-04	3.00E-03	2.83E-03
0.20791	17.258	600	273	0.1	8.42E-05	1.61E-04	3.00E-03	1.44E-03
0.22507	16.483	600	273	0.1	2.51E-04	2.43E-04	3.83E-03	3.60E-03
0.24071	15.593	600	273	0.1	2.21E-04	2.62E-04	3.51E-03	2.68E-03
0.25532	14.593	600	273	0.1	1.40E-04	1.80E-04	2.03E-03	1.44E-03
0.26880	13.519	600	273	0.1	4.66E-04	3.63E-04	3.52E-03	4.00E-03
0.28125	12.386	600	273	0.1	1.42E-04	2.42E-04	1.98E-03	1.03E-03
0.29290	11.195	600	273	0.1	4.06E-04	4.07E-04	2.76E-03	2.48E-03
0.30364	9.975	600	273	0.1	3.46E-04	3.77E-04	2.08E-03	1.79E-03
0.31367	8.718	600	273	0.1	4.70E-04	2.23E-04	1.00E-03	2.01E-03
0.32312	7.431	600	273	0.1	3.00E-04	4.60E-04	1.69E-03	1.01E-03
0.33210	6.097	600	273	0.1	4.65E-04	4.66E-04	1.32E-03	1.21E-03
0.34047	4.747	600	273	0.1	5.01E-04	5.00E-04	1.00E-03	1.00E-03

(a) Multi-objective optimization without shape factor

$\dot{W}$ $(Watts)$	$\eta(\%)$	$T_1(K)$	$T_2(K)$	S	$L(m)$	$R_L(\Omega)$	$A_0(m^2)$
0.14774	18.418	600	273	1.00E-08	1.00E-03	0.1	3.19E-05
0.17110	18.239	600	273	1.69E-01	2.60E-03	0.1	2.26E-04
0.19367	17.729	600	273	1.45E-01	3.01E-03	0.1	2.42E-04
0.21505	16.938	600	273	8.88E-02	2.84E-03	0.1	2.01E-04
0.23501	15.917	600	273	2.57E-01	2.06E-03	0.1	2.48E-04
0.25337	14.717	600	273	2.21E-01	2.56E-03	0.1	3.38E-04
0.27028	13.374	600	273	1.00E-08	3.35E-03	0.1	3.76E-04
0.28581	11.920	600	273	3.34E-01	1.07E-03	0.1	2.15E-04
0.30006	10.380	600	273	2.51E-01	2.47E-03	0.1	1.89E-04
0.31325	8.761	600	273	2.12E-01	3.90E-03	0.1	1.81E-04
0.32543	7.085	600	273	1.04E-01	2.60E-03	0.1	2.30E-05
0.33667	5.369	600	273	2.35E-01	2.17E-03	0.1	6.82E-05
0.34710	3.614	600	273	2.95E-01	3.20E-03	0.1	1.01E-04
0.35681	1.827	600	273	2.05E-01	2.73E-03	0.1	1.99E-05
0.36592	0.003	600	273	9.80E-01	3.98E-03	0.1	1.01E-06

(b) Multi-objective optimization with shape factor.

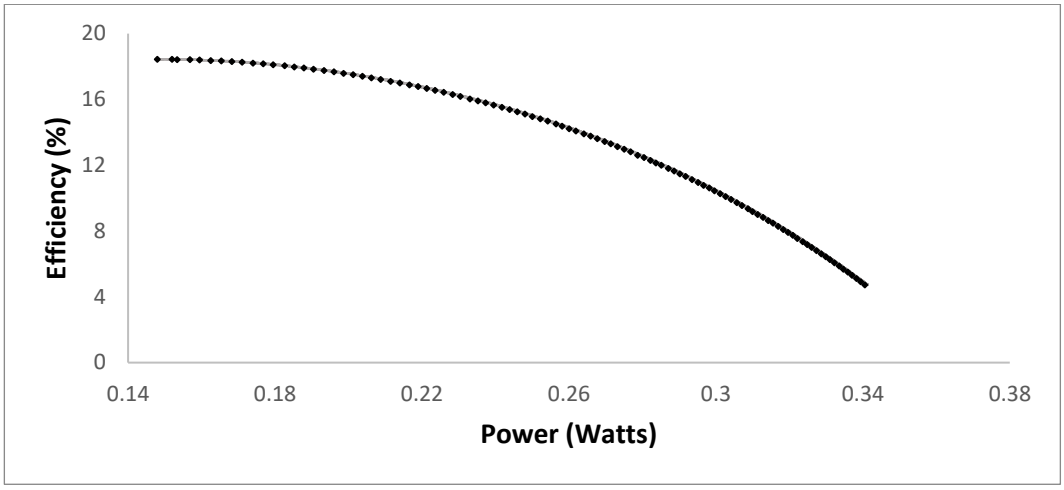

(a)

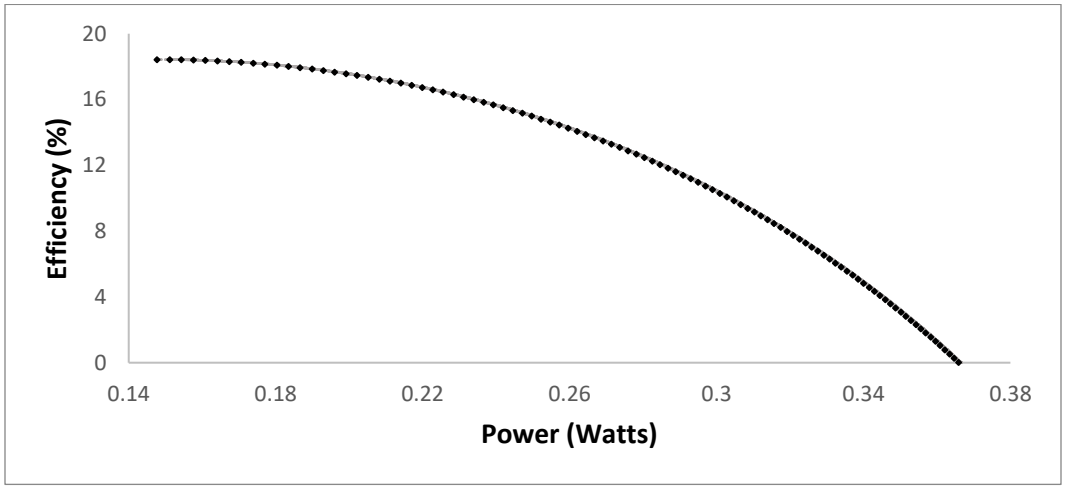

(b)

FIGURE 9-3 The best set of non-dominated solution set (Based on IGD measure) found by the Fusion algorithm. The grey dotted background indicates the non-dominated solutions assembled during 25 runs of all algorithms and the black dots indicate the best solution set obtained by the Fusion algorithm based on the IGD measure. (a) Optimization without shape factor. (b) Optimization with shape factor.

However, the study was only able to obtain the two extreme optimal solutions (i.e., the maximum power and efficiency). Meanwhile all proposed algorithms permitted to find a spectrum of optimal thermal operating conditions as well as device parameters, which would be difficult to find using the analytical analysis conducted in [160]. The maximum

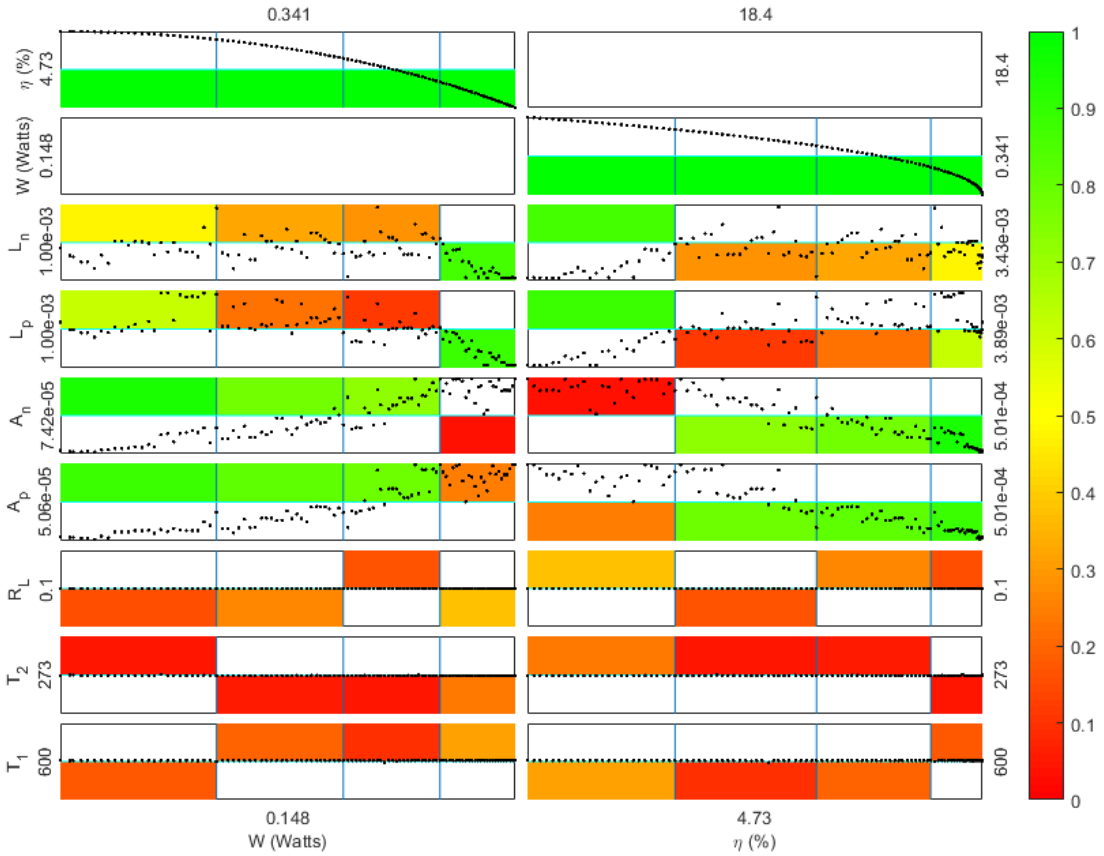

FIGURE 9-4 ECM plot of the best set of non-dominated solution set (Based on IGD measure) found by the Fusion algorithm for the optimization of the thermoelectric generator with shape factor.

power, based on the lower and upper limits of design and operational parameter settings (Equations (9.16) – (9.22)), is 0.34 Watts and the efficiency corresponding to the maximum power is 4.73%. Similarly, the maximum efficiency is 18.44% and the corresponding power to the maximum efficiency is 0.14 Watts. Equivalently, the proposed algorithms were able to find these extreme solutions with a margin of error equal to $\pm 0.1\%$.

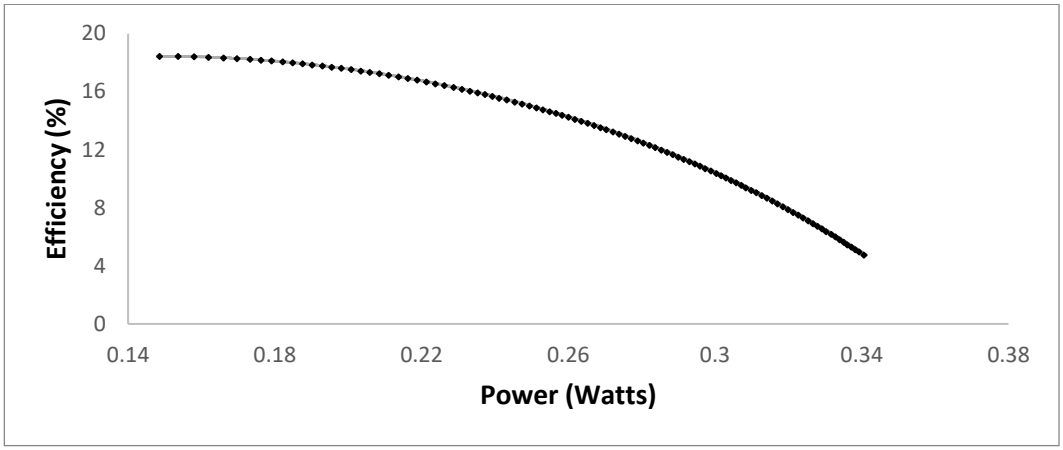

(a)

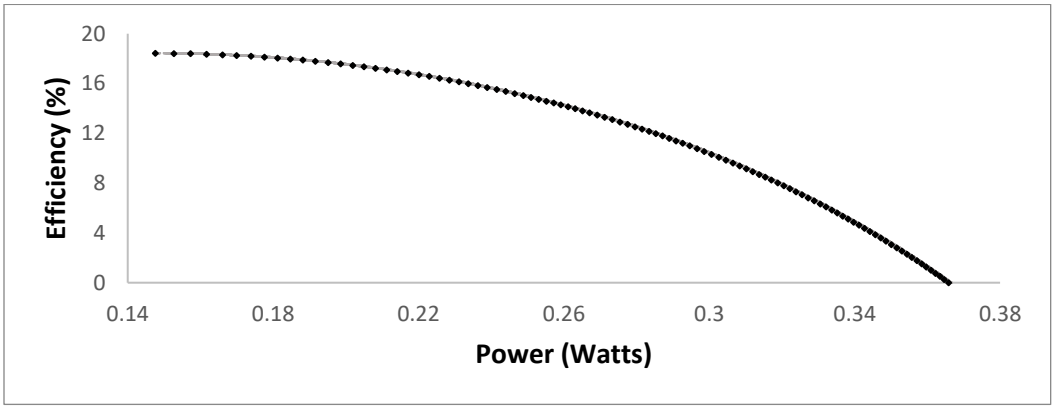

(b)

FIGURE 9-5 The best set of non-dominated solution set (Based on IGD measure) found by the SMPSO algorithm. The grey dotted background indicates the non-dominated solutions assembled during 25 runs of all algorithms and the black dots indicate the best solution set obtained by the SMPSO algorithm based on the IGD measure. (a) Optimization without shape factor. (b) Optimization with shape factor.

Moreover, since the obtained solution set through the proposed algorithms include a spectrum of optimal solutions, it is possible to select a compromising solution acceptable by the designer of the thermoelectric device. For example, one such compromising solution found by the NSGA-II algorithm is 0.19 Watts of power at 17.88% efficiency (3% drop of efficiency but 29% rise of power). Table 9.4 (a) lists 15 (out of thousands) well-distributed non-dominated extracted from solutions assembled during 25 runs of the Fusion, SMPSO,

GDE3, SPEA2, and NSGA-III algorithms using the FNFR scheme. This table includes each solutions' corresponding design and operation parameters. Appendix C1 to C5 (a) present fifteen uniformly distributed non-dominated solutions extracted from solutions assembled during 25 runs each algorithm using the FNFR scheme. An interesting observation was that the distribution of solutions obtained by the NSGA-III algorithm suffered due to linear structured reference points utilized the algorithm for concave PF (for further discussion see Section 5.2.5). Hence, NSGA-III's performance results were the worst among all algorithms.

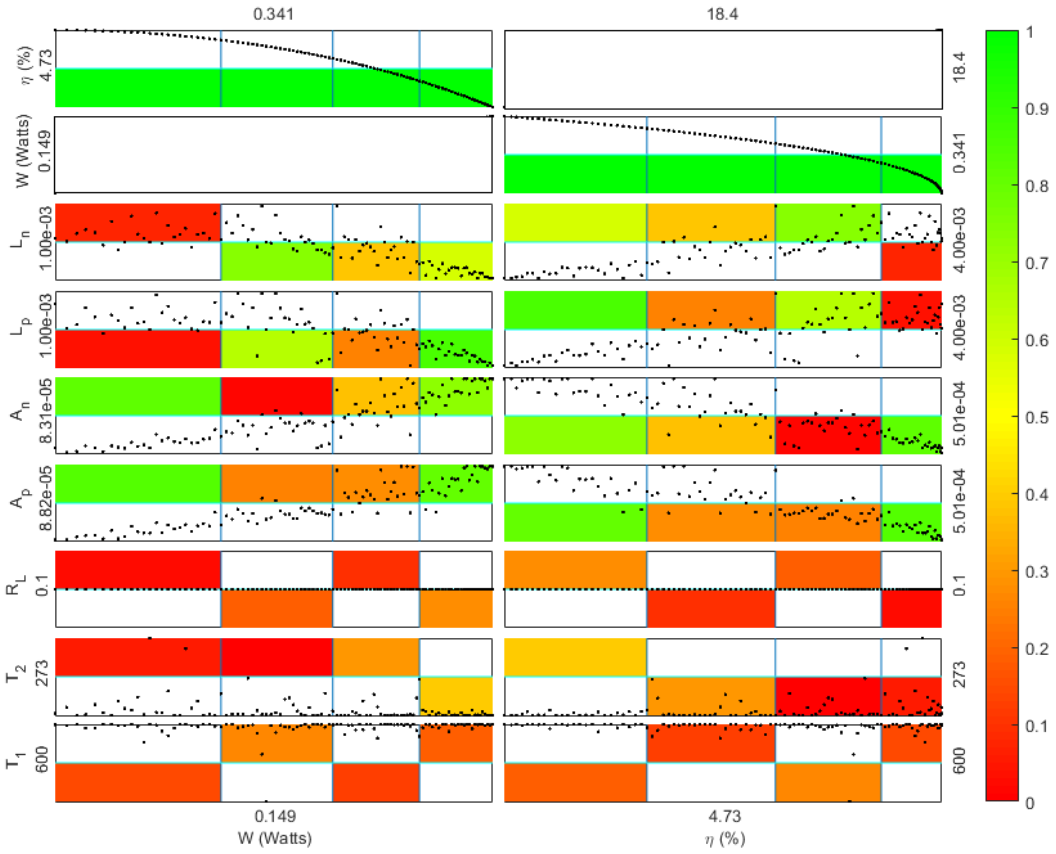

FIGURE 9-6 ECM plot of the best set of non-dominated solution set (Based on IGD measure) found by the SMPSO algorithm for the optimization of the thermoelectric generator with shape factor.

Figure 9-4, Figure 9-6, Figure 9-8, Figure 9-10, and Figure 9-12 show ECM plots the best (based on the best IGD results) solution set obtained by the proposed algorithms, Fusion, SMPSO, GDE3, SPEA2, and NSGA-III respectively. The overall observation from these plots can be summarized as follows:

- The correlation between the upper junction temperature (T_1) and power generated as well as the correlation between the upper junction temperature and efficiency of the thermoelectric device is close to zero. Hence, from the ECM plot we see that the upper junction temperature must be kept at 273K ($0℃$) to obtain solutions on the Pareto-optimal front.
- Similarly, the correlation between the lower junction temperature (T_2) and power generated as well as the correlation between the lower junction temperature and efficiency of the thermoelectric device is close to zero. Hence, from the ECM plot we see that the lower junction temperature must be kept at 600K ($327℃$) to obtain solutions on the Pareto-optimal front.
- The correlation between the external load resistance (R_L) and power generated as well as the correlation between the external load resistance and efficiency of the thermoelectric device is also close to zero. Again, from the ECM plot we conclude that the external load resistance must be kept at 0.1 ohms to obtain solutions on the Pareto-optimal front.
- The cross-sectional area of the pins (A_p and A_n) showed a strong correlation with the power generated and efficiency. From our observation as the value of A_p and A_n increase from 8.10×10^5 to $5.01 \times 10^4\ m^2$ for A_p and 1.19×10^4 to

$5.00 \times 10^4\ m^2$ for A_n, the power generated increase from 0.15 to 0.34 Watts and the efficiency decreases from 18.44% to 4.74%.

- The height of the pins (L_n and L_p) did not exhibit a strong correlation with the two objectives in the mid region of the Pareto-optimal front. Therefore further investigation is required.

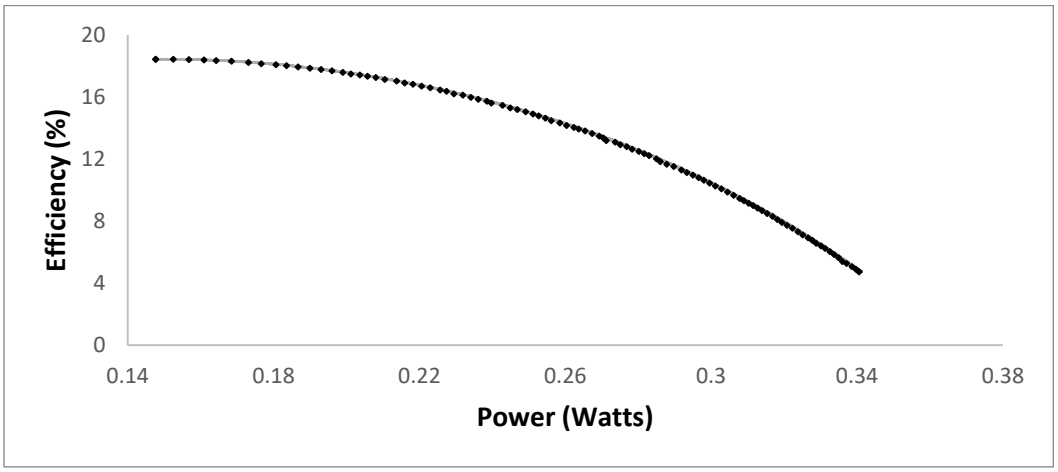

(a)

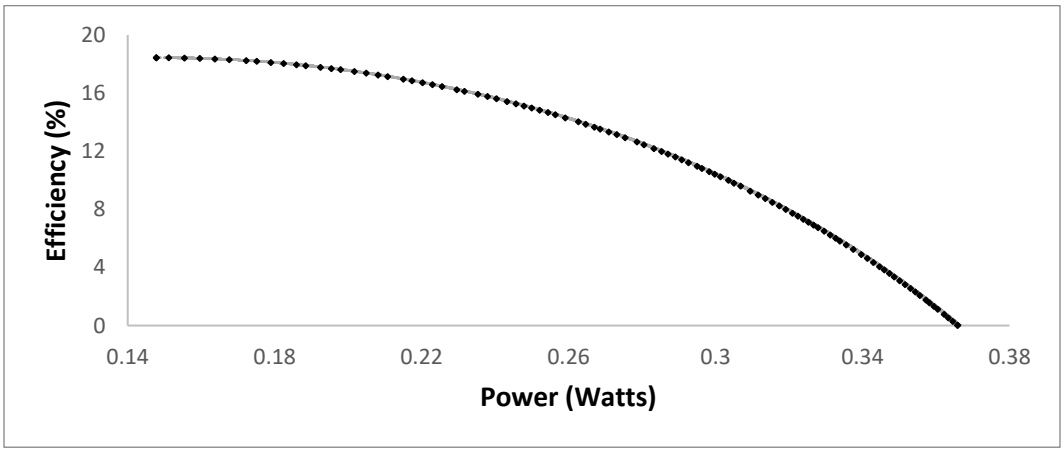

(b)

FIGURE 9-7 The best set of non-dominated solution set (Based on IGD measure) found by the GDE3 algorithm. The grey dotted background indicates the non-dominated solutions assembled during 25 runs of all algorithms and the black dots indicate the best solution set obtained by the GDE3 algorithm based on the IGD measure. (a) Optimization without shape factor. (b) Optimization with shape factor.

9.3.3 Optimization with the Shape Factor

To investigate the effect of pin geometry in the optimal thermoelectric device output power and efficiency, a new variable, shape factor, is introduced. When the shape factor is 0, the problem is similar to vertically parallel pin configuration as depicted in Figure 9-1 (b). Figure 9-3 (b), Figure 9-5 (b), Figure 9-7 (b), Figure 9-9 (b), and Figure 9-11 (b) present the distribution of Pareto-optimal solutions (based on the best IGD results) obtained by the proposed algorithms. Table 9.2 (b) shows the two extreme solutions obtained through the proposed algorithms. These solutions indicate the maximum possible

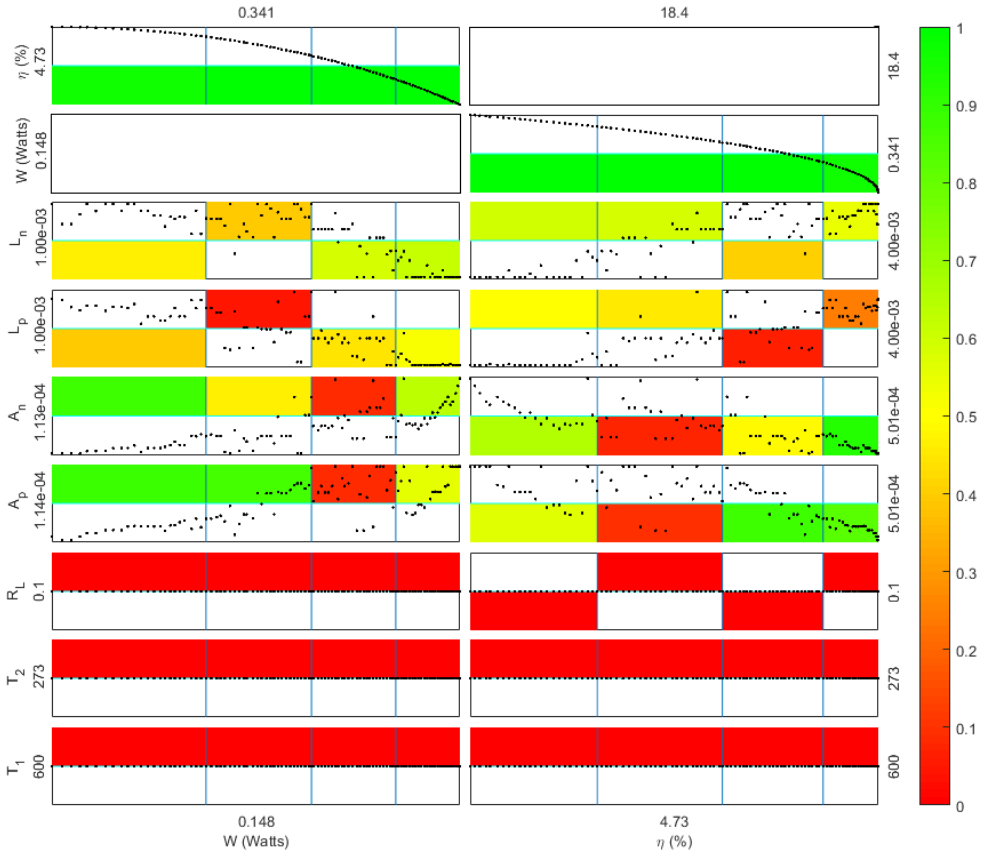

FIGURE 9-8 ECM plot of the best set of non-dominated solution set (Based on IGD measure) found by the GDE3 algorithm for the optimization of the thermoelectric generator with shape factor.

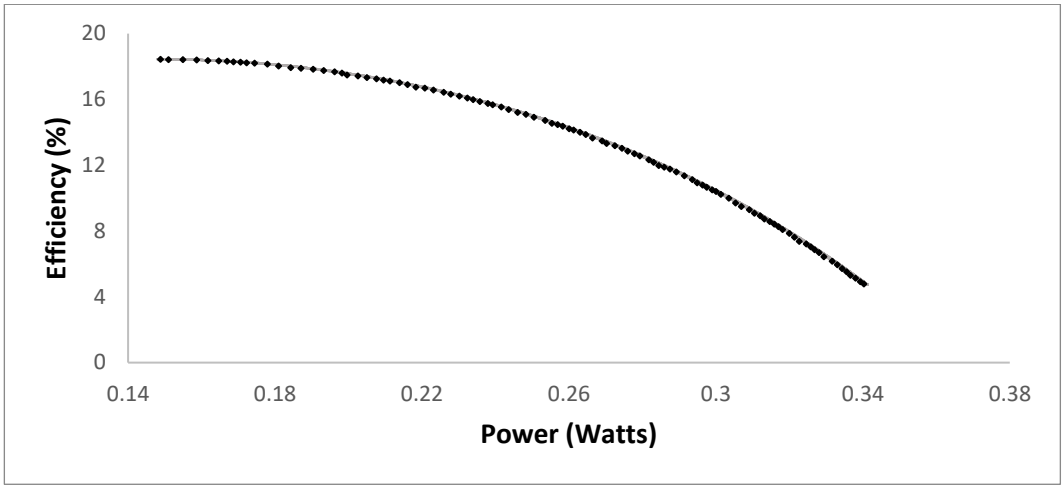

(a)

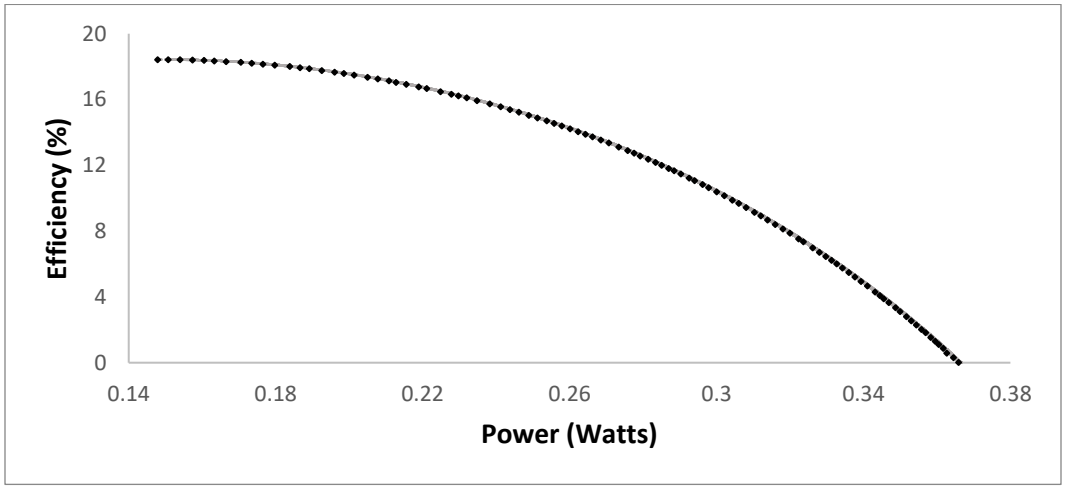

(b)

FIGURE 9-9 The best set of non-dominated solution set (Based on IGD measure) found by the SPEA2 algorithm. The grey dotted background indicates the non-dominated solutions assembled during 25 runs of all algorithms and the black dots indicate the best solution set obtained by the SPEA2 algorithm based on the IGD measure. (a) Optimization without shape factor. (b) Optimization with shape factor.

output power and efficiency that can be achieved through the second thermoelectric device design (see Figure 9-1 (b)) and its variable bounds (see Equations (9.23) – (9.27)). The maximum efficiency attained, under these constraints is ~18.42% and the corresponding power is ~0.147 Watts. Similarly, the maximum power is ~0.366 Watts and the corresponding efficiency is close to 0%. The corresponding shape factor at this maximum

power is $S \approx 1$ (pin with vertical slope of ~90^{o}). The HV results (see Table 9.3 (b)) indicate the quality (accuracy and spread) of the solutions obtained through these algorithms is comparable.

However, the Fusion algorithm consistently exhibited marginally results in almost all performance measures used in this study. Table 9.4 (b) lists 15 (out of thousands) well-distributed non-dominated extracted from solutions assembled during 25 runs of the Fusion, SMPSO, GDE3, SPEA2, and NSGA-III algorithms using the FNFR scheme. This table also includes each solutions' corresponding design and operation parameters. Appendix C1 to C5 (b) present fifteen uniformly distributed non-dominated solutions extracted from solutions assembled during 25 runs of each algorithm using the FNFR scheme.

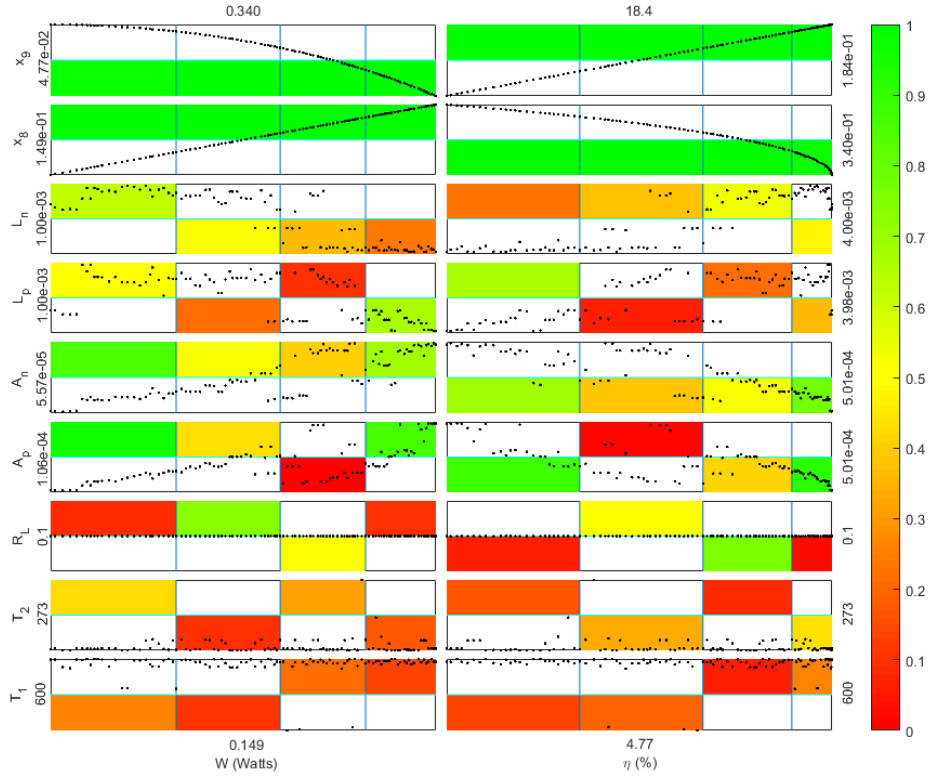

FIGURE 9-10 ECM plot of the best set of non-dominated solution set (Based on IGD measure) found by the SPEA2 algorithm for the optimization of the thermoelectric generator with shape factor.

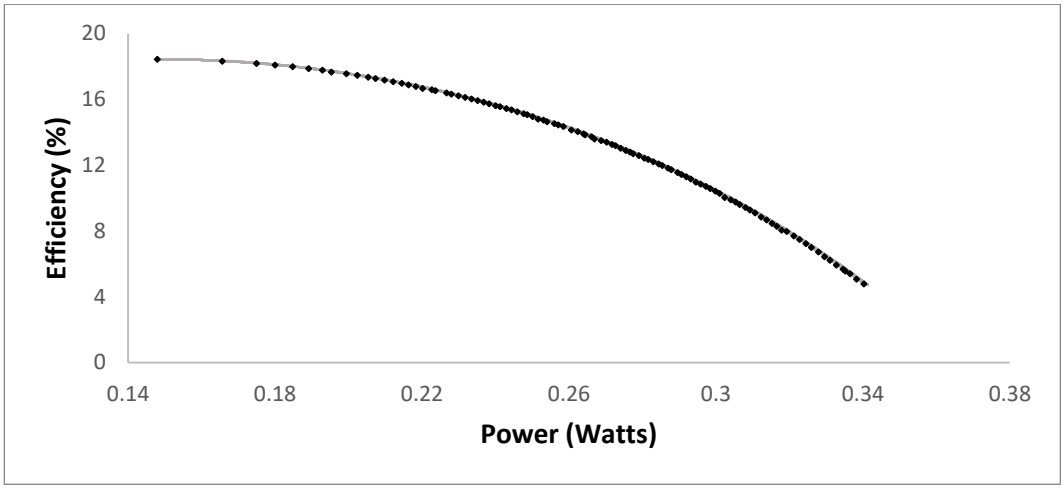

(a)

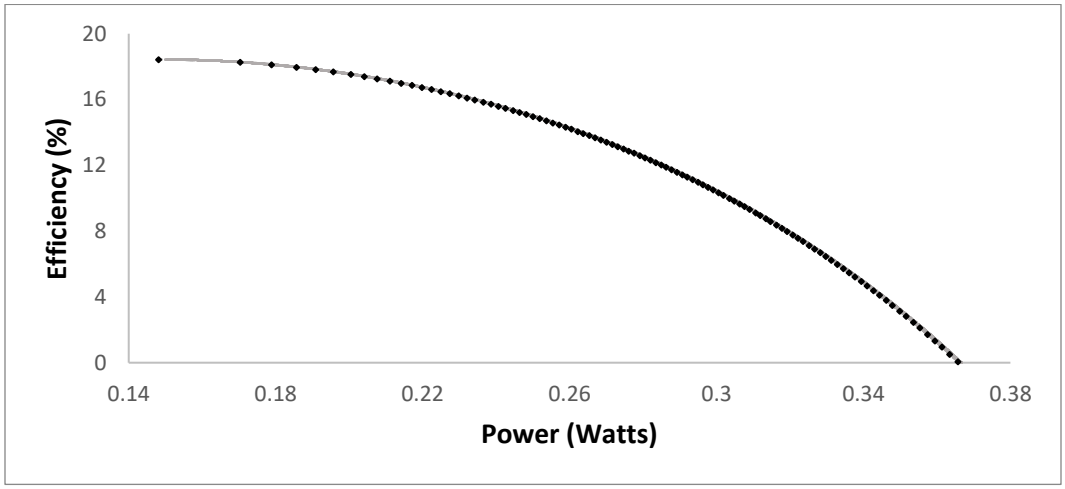

(b)

FIGURE 9-11 The best set of non-dominated solution set (Based on IGD measure) found by the NSGA-III algorithm. The grey dotted background indicates the non-dominated solutions assembled during 25 runs of all algorithms and the black dots indicate the best solution set obtained by the NSGA-III algorithm based on the IGD measure. (a) Optimization without shape factor. (b) Optimization with shape factor.

9.3.4 Solution Extraction using the FNFR Method

Figure 9-13 to Figure 9-17 show well-distributed solutions extracted by the FNFR scheme. The black dots illustrate 15 uniformly distributed solutions extracted from non-dominated solutions (grey dotted background) assembled during 25 runs of the Fusion, SMPSO, GDE3, SPEA2, and NSGA-III algorithms. All the algorithms except NSGA-III were able

to cover able to cover the entire Pareto-optimal front in 25 runs and as a result the FNFR method was able to extract a subset of well-distributed solutions spanning the entire front.

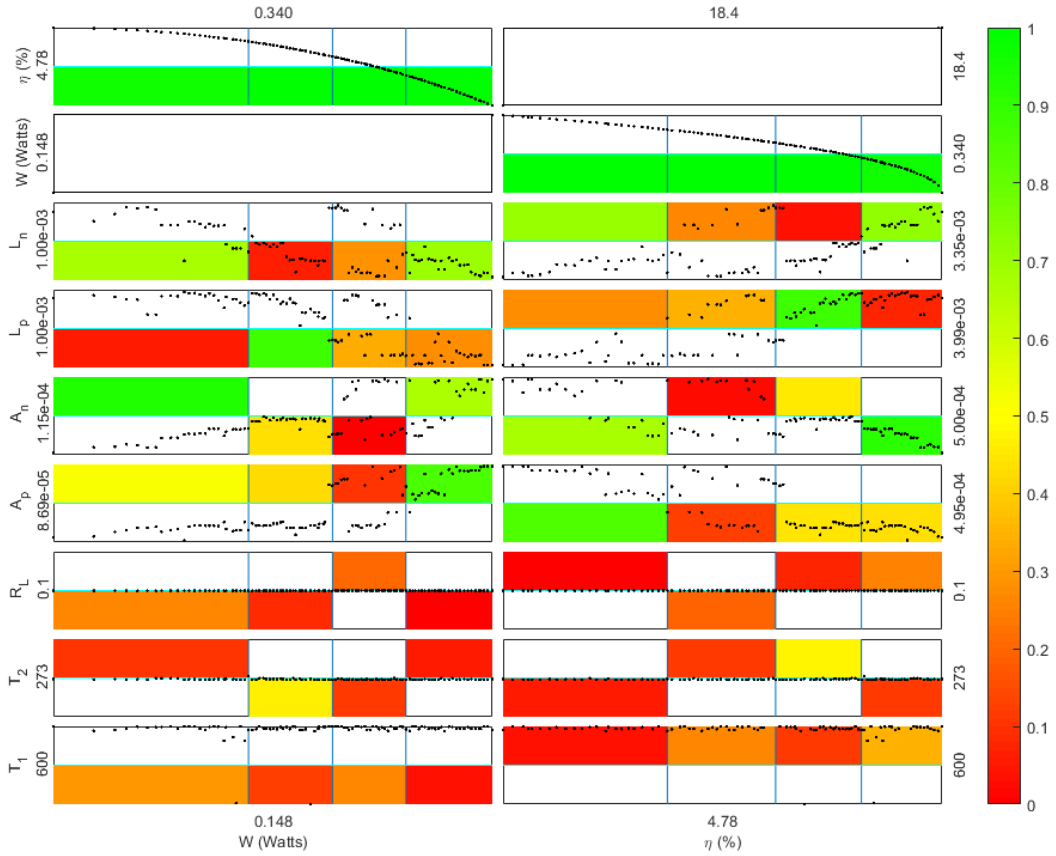

FIGURE 9-12 ECM plot of the best set of non-dominated solution set (Based on IGD measure) found by the NSGA-III algorithm for the optimization of the thermoelectric generator with shape factor.

Figure 9-18 illustrates 15 uniformly distributed solutions (black dots) extracted from non-dominated solutions (grey dotted background) assembled during 25 runs of the Fusion, SMPSO, GDE3, SPEA2, and NSGA-III algorithms. Figure 9-19 shows three clusters (on preferred regions) of well-distributed solution sets extracted from thousands of solutions collected during 25 runs of all utilized algorithms in this study. It can be seen that as the number of collected solutions increase and cover the entire Pareto-optimal front the easier for the FNFR scheme to find solutions very close to the preferred reference lines.

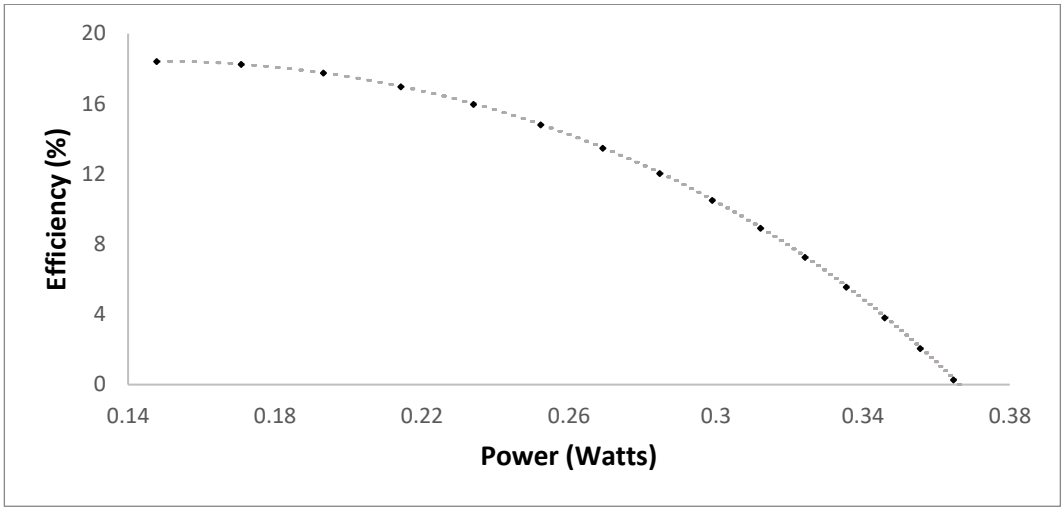

FIGURE 9-13 Well-distributed solutions extracted by the FNFR scheme. The black dots illustrate 15 uniformly distributed solutions extracted from non-dominated solutions (grey dotted background) assembled during 25 runs of the Fusion algorithm.

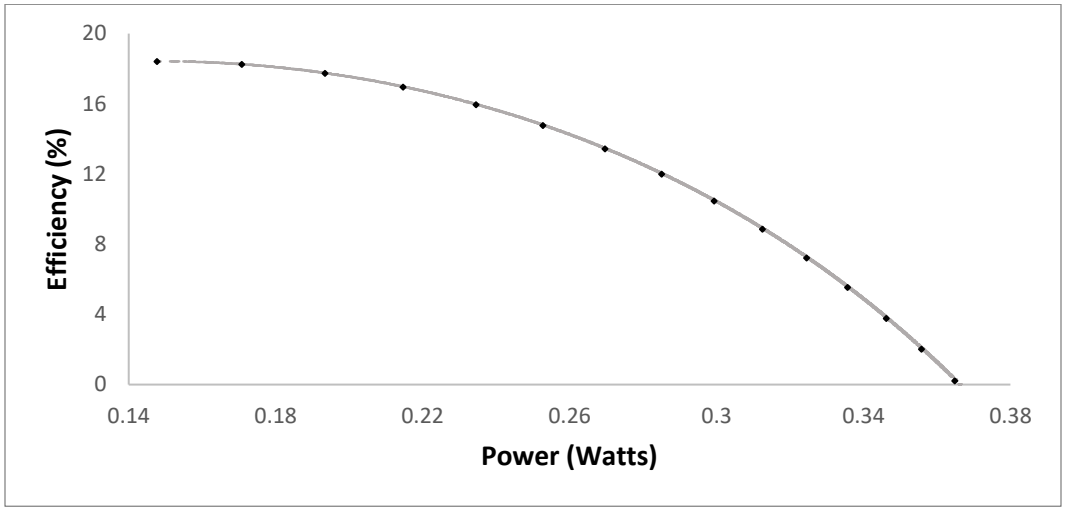

FIGURE 9-14 Well-distributed solutions extracted by the FNFR scheme. The black dots illustrate 15 uniformly distributed solutions extracted from non-dominated solutions (grey dotted background) assembled during 25 runs of the SMPSO algorithm.

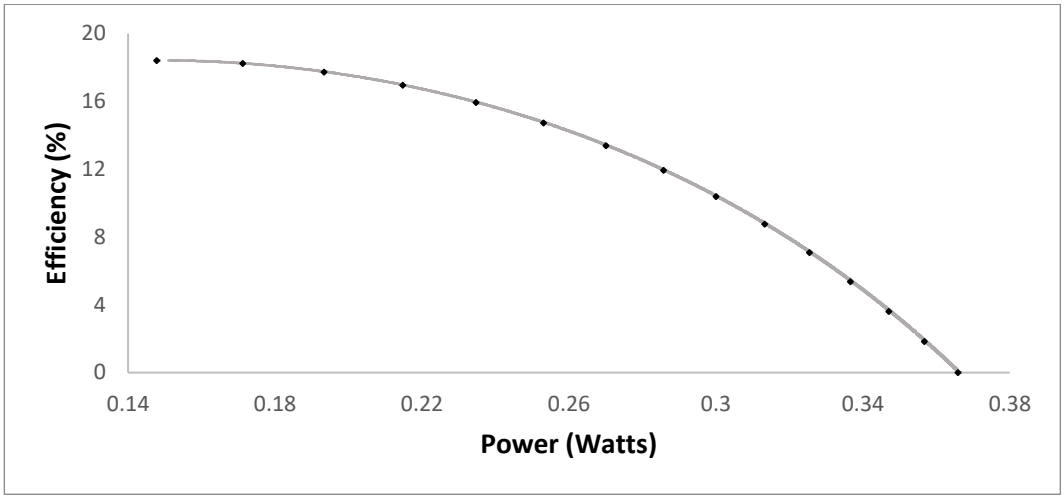

FIGURE 9-15 Well-distributed solutions extracted by the FNFR scheme. The black dots illustrate 15 uniformly distributed solutions extracted from non-dominated solutions (grey dotted background) assembled during 25 runs of the GDE3 algorithm.

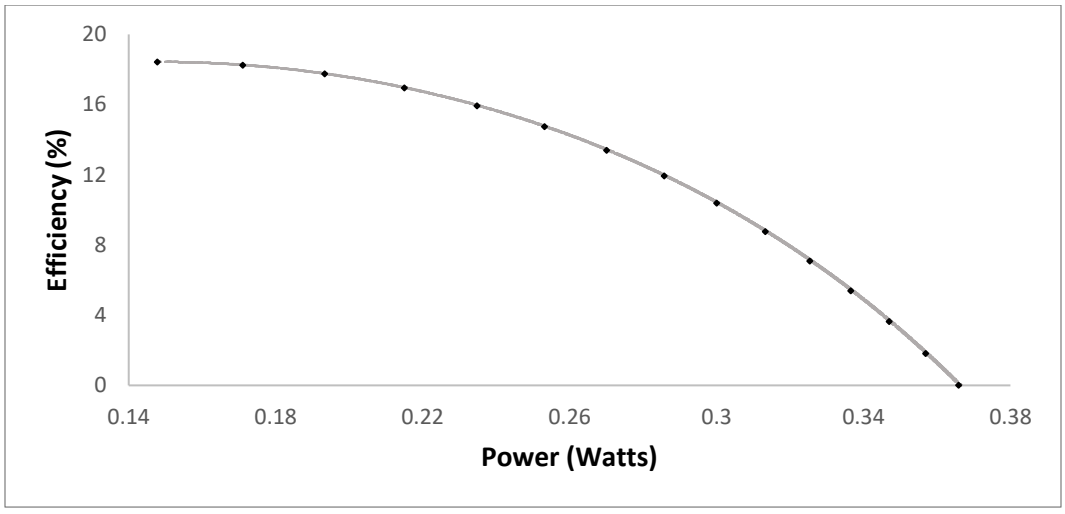

FIGURE 9-16 Well-distributed solutions extracted by the FNFR scheme. The black dots illustrate 15 uniformly distributed solutions extracted from non-dominated solutions (grey dotted background) assembled during 25 runs of the SPEA2 algorithm.

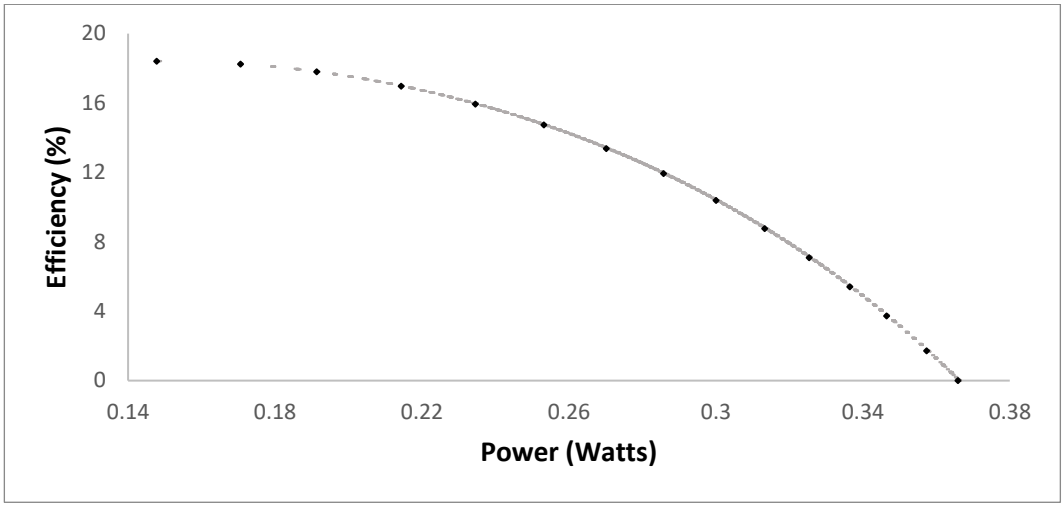

FIGURE 9-17 Well-distributed solutions extracted by the FNFR scheme. The black dots illustrate 15 uniformly distributed solutions extracted from non-dominated solutions (grey dotted background) assembled during 25 runs of the NSGA-III algorithm.

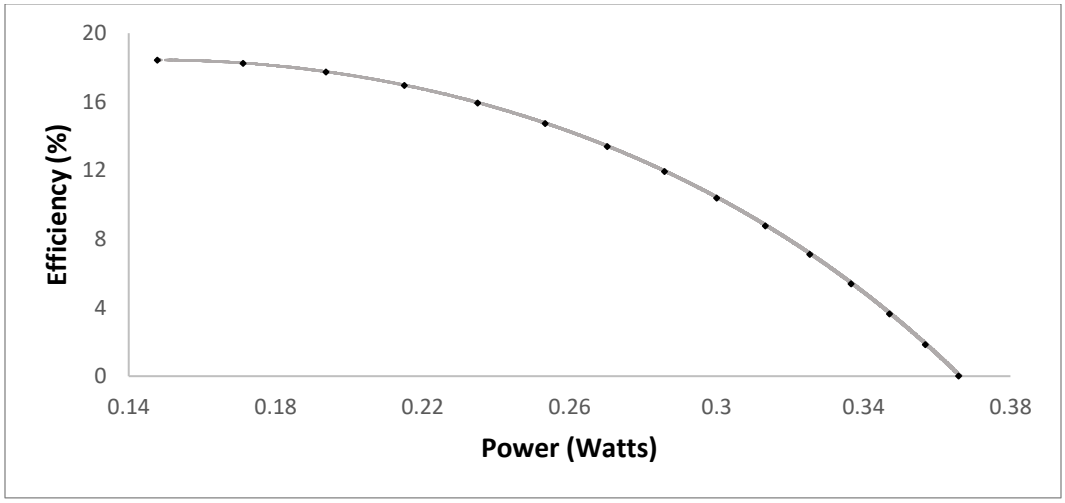

FIGURE 9-18 Well-distributed solutions extracted by the FNFR scheme. The black dots illustrate 15 uniformly distributed solutions extracted from non-dominated solutions (grey dotted background) assembled during 25 runs of the Fusion, SMPSO, GDE3, SPEA2, and NSGA-III algorithms.

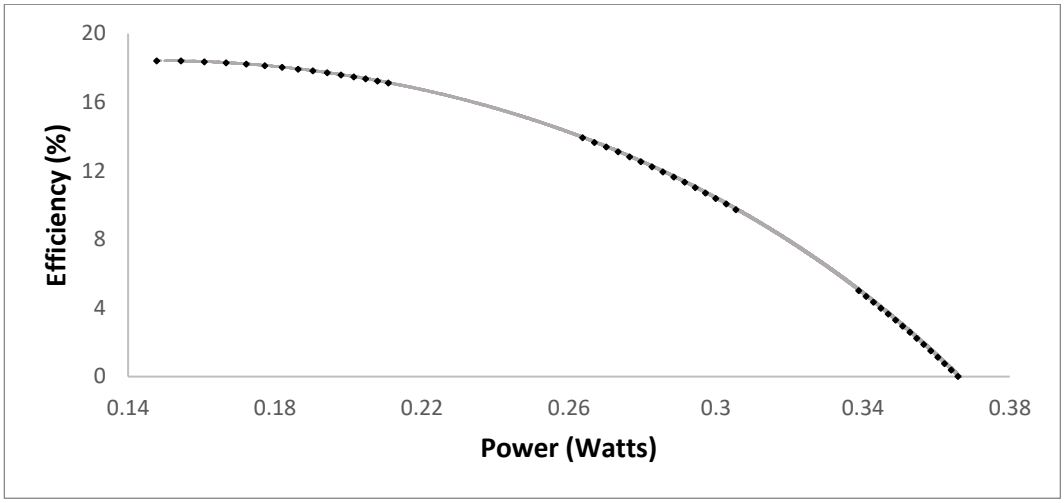

FIGURE 9-19 Preferred solutions extracted by the FNFR scheme. The black dots illustrate three clusters of 15 uniformly distributed solutions extracted from non-dominated solutions (grey dotted background) assembled during 25 runs of the Fusion, SMPSO, GDE3, SPEA2, and NSGA-III algorithms.

9.4 Conclusion

Thermal analysis of thermoelectric generator is considered and influence of geometric features on efficiency and output power of the device is examined. A multi-objective optimization study is carried out to maximize the efficiency and output power of a thermoelectric device including the geometric features of shape factor and pin length, as well as operational parameters such as temperature ratio and external load parameter. The utilized multi-objective algorithms (Fusion, SMPSO, GDE3, SPEA2, and NSGA-III) enabled to find a diverse set of optimal solutions which would be difficult to find using analytical methods. For example, some intermediate solutions could be of interest with regards to other non-expressed objectives or secondary objectives such as operating conditions, device dimension or other technical aspects. Overall, the performance of the five algorithms was comparable. However, the Fusion algorithm marginally outperformed

the other algorithms in terms of solution accuracy, distribution and spread of solutions over the PF as well as distribution of solutions along each objective.

It is found that small change in shape factor alters thermal efficiency and output power. In this case, efficiency, first, increases to reach its maximum and, later, reduces sharply with increasing shape factor. Output power also increases sharply and remains the same with increasing shape factor. The similar effect is also observed for the size of pin length. In any case, the geometric feature of the device corresponding to the maximum efficiency does not give rise to the maximum output power. This is associated with the complex effect of shape factor and pin length on the device efficiency. Thermal efficiency reduces significantly for large value of shape factor (S = 0.5), which corresponds to 45^o vertical slope of pins. In addition, output power remains almost the same for varying pin length size for S = 0.5. This indicates that output power of the thermoelectric device maintains high regardless of pin length size, provided that thermal efficiency reduces significantly. The locus of the intersection of efficiency and output power, due to different geometric configurations, can provide the optimum design configurations of the thermoelectric device; in which case, a unique geometric configuration is resulted for the fixed operating conditions. Increasing temperature ratio or external load parameter alters the geometric configuration corresponding to the optimum efficiency and output power of the device. Therefore, for a fixed operational condition, non-parallel pins are favorable because of achieving high efficiency and output power of the device. In addition, decreasing temperature ratio enhances device efficiency and output power when the optimum design conditions are satisfied.

Chapter 10

CONCLUSION AND FUTURE WORK

This thesis introduced several ideas to help improve the complex steps involved in optimization and decision making areas. First, it introduced three visualization techniques capable of showing the convergence and distribution of solutions on the Pareto-optimal front but also distribution of solutions along each objective for multi- and many-objective problem. In addition, it introduced the first visualization method in the optimization field capable of showing the relationship between decision variables and objective function values. Second, it introduced the first performance measure in the optimization field capable of assessing the distribution and spread of solutions along each objective. Third, it introduced reference based hybrid optimization framework that allows multiple optimization algorithms to work together and arrive at improved solutions. This hybrid framework is also capable of extracting a subset of well-distributed solutions from thousands of non-dominated solutions collected during the optimization process of several algorithms. Fourth, the proposed algorithms, visualization techniques, and performance measures were applied to multi-objective renewable energy systems to assess the efficacy when dealing with real-world problems. The conclusion and future work of this thesis is described in the next two sections.

10.1 Conclusions

In recent years real-world problems are increasingly becoming complex due to the number of objectives involved, the number of decision variables required to model the problem, and the complexities (e.g. multimodality, non-linearity, mixed-type decision variables, discontinuity, etc.) present in the model. Although there have been several advancements in the field of optimization, visualization, and decision-making techniques, there are still a number of challenges in the overall optimization and decision making process when the

number of objectives are greater than three. This thesis focused on the improvements of several areas of the optimization and decision making process. These areas include, the enhancement of currently existing state-of-the-art multi- and many-objective optimization algorithms, the innovation of powerful visualization tools for many-objective optimization problems, the extension of performance measures to complement currently existing performance metrics, and the establishment of algorithms to simplify the complexities involved in the decision making process. Below are the main contributions of this thesis.

1. It proposed three multi- and many-objective visualization methods namely, 3D-RadVis [67], 3D-RadVis Antenna [182], and Enhanced Correlation Matrix (ECM) plot for visualizing the distribution, convergence and relationship between decision variables and objective functions.
    - The 3D-RadVis and 3D-RadVis Antenna plots use a radial coordinate system to map M-dimensional objectives space to a 2-dimensional space (u_x, u_y) and a distance (d) to maintain the location of non-dominated solutions from a reference hyper-plane constructed using the extreme points. The radial coordinates, (u_x, u_y), show the distribution of the solutions and the combination of these radial coordinates with the distance metric d, show the shape and accuracy of the solution set.
    - The 3D-RadVis Antenna plot incorporates additional dimension to the 3D-RadVis plot to visualize the distribution of solutions as along each objective. From the experimental tests on widely used MaOO test problems, 3D-RadVis and 3D-RadVis Antenna plots are able to precisely show the shape,

distribution, and convergence of approximate solutions on the PF surface as well as distribution of these solutions along each objective.

- The Enhanced Correlation Matrix (ECM) plot provides visual correlation information between each decision variable and objective functions as well as objective-wise relationship for different regions of the Pareto-optimal front. Moreover, it is capable of providing visual distribution of solutions along each objective.
- From the experimental tests on widely used MaOO test problems, the three proposed visualization methods were able to precisely show the shape, distribution, and convergence of approximate solutions on the PF surface as well as distribution of these solutions along each objective. These visualization tools can effectively be used by researchers and decision makers to explore and understand the search behaviour of an algorithm at each generation whereby gaining useful information regarding an algorithm to improve their search ability and ultimately, we hope, the development of new optimization algorithms.

2. It also presented two multi- or many-objective performance measures; objective-wise inverse generational distance (ObjIGD) and line distribution (Δ_{Line}) to measure the convergence and distribution of solutions along each objective [182]. Experimental results have shown these two measures can be used as reliable complementary measures along with other widely used performance measures to compare many-objective solution sets.

3. Two multi- and many-objective optimization algorithms are also proposed in this thesis.
    - The first optimization algorithm involves a hybridization of multi-and many-objective optimization algorithms called Fusion [183]. The Fusion framework uses several multi- and many-objective algorithms to gain the combined benefits of several algorithms and reduce the challenges associated with choosing one optimization algorithm to solve complex problems. A case study of the Fusion framework using the GDE3, SMPSO, and SPEA2 to solve constrained and unconstrained benchmark test with three to ten objectives show that the Fusion framework significantly outperforms all algorithms involved in the hybridization process as well as the NSGA-III algorithm in terms of diversity and convergence of obtained solutions.
    - The second proposed many-objective algorithm is called EliteNSGA-III [184]. EliteNSGA-III is an extension of NSGA-III algorithm where it incorporates elite population archive to improve the diversity and accuracy of the NSGA-III algorithm. The elite population archive maintains previously generated elite solutions that would probably be eliminated by NSGA-III's selection procedure. The proposed EliteNSGA-III algorithm is applied to 11 unconstrained many-objective test problems with three to 50 objectives and six constrained objective test problems with three to 15 objectives. Experimental results show that the proposed EliteNSGA-III algorithm outperforms the NSGA-III algorithm in terms of diversity and accuracy of the obtained solutions.

4. Further, it presented a novel hybridization of population-based metaheuristic algorithms called fusion of non-dominated fronts using reference points (FNFR) framework to assist decision makers in extracting a subset of well-distributed solutions from a large set of non-dominated solutions using predefined structured reference points or user-defined reference points [111]. The hybridization step in FNFR occurs after the completion of optimization process of multiple runs of several algorithms. Experimental results showed that the FNFR method is able to extract well-distributed solutions in a specific region of interest among thousands of non-dominated solutions collected after every run of multiple algorithms. Therefore, the FNFR scheme can effectively be used by decision makers to select and examine preferred solutions among a large set of solutions which can be astronomically difficult to manage.
5. The efficacy of the proposed Fusion algorithm, ECM plot, ObjIGD performance measure, and the FNFR solution extraction methods are proved using two real-world renewable energy systems.
    - The first problem is the multi-objective design of a photovoltaic farm in the Toronto, Ontario region [174]. The optimization problem is composed of two objectives, six variables, and two constraints. The two objectives are the maximization of incident energy and minimization of the installation and material cost.
    - The second problem is multi-objective optimization of the geometric features of a thermoelectric generator for improved efficiency and output power while incorporating different operating conditions [185].

- Experimental results in both cases showed that the Fusion algorithm outperformed the other algorithms by generating broad spectrum of solutions. Furthermore, the ECM plots were able to effectively identify the relationship between the decision variables and objective functions and consequently classify the optimal design parameters.

10.2 Future Work

Although this thesis proposed several important tools towards the improvement of the steps involved in the optimization and decision making process, there still exist areas for continued development and improvement of optimization, visualization and decision making tools. Below are recommendations to further improve the efficacy of the proposed contributions of this thesis.

1. Improving 3D-RadVis and 3D-RadVis Antenna plots
    - The core complement of the proposed 3D-RadVis and 3D-RadVis Antenna plots is the RadVis mapping of M-dimensional solutions to a 2-dimensional xy plane. As the number of high-dimensional data points increases, the RadVis mapping fails to capture high-dimensional dataset in the lower dimension. On the other hand there an alternate mapping method called t-SNE where the mapping process proven to produce significantly better visualization the reduction of crowd from the center of the map hence preserving much of the significant structure of the high-dimensional data in the low-dimensional map [186]. Thus, we recommend investigating how the t-SNE method can be incorporated into the 3D-RadVis plot while preserving the shape and location of the PF data set.

- The integration of virtual reality (VR) technologies and 3D-RadVis visualization in order to bring more simplicity to complex data set.

2. Further investigation and possible extension of EliteNSGA-III
    - Extend the EliteNSGA-III study to investigate the impact of an elite population archive when alternate recombination operators are used (e.g. differential evolution (DE) instead of SBX and polynomial mutation operators).
    - Investigate the impact of an elite population archive when only neighbouring elite solutions are used to create offspring population.
    - Investigate the influence of using an additional elite-population archive to separate feasible and infeasible candidate solutions.
    - Apply penalty mechanism to avoid the generated solutions being attracted to few reference points.
3. Improving reference-based algorithms
    - Currently the main focus of reference-based algorithms is improving the distribution of obtained solutions around the entire front through the use of systematically generated reference points. However, these methods normally fail to obtain well-distributed solutions along each objective when the shape of the PF is concave or convex
    - Hence, careful investigation is required to generate well-balanced reference points that have good distribution on the hyper-plane as well as along each objective function.
4. Extension of multi-objective design of a photovoltaic (PV) farm

- Extend the PV farm study so that the PV panels can be deployed with tracking capability as supposed to stationary PV panels proposed in this thesis.
- Investigate gradual linear land inclination between rows to minimize the shadow casted on subsequent rows.
- Investigate the use of ray focusing mirrors to redirect the radiation of the sun when the sun's ray is not in the direction of the PV panels.

REFERENCES

[1] S. Binitha and S. S. Sathya, "A survey of bio inspired optimization algorithms," *International Journal of Soft Computing and Engineering,* vol. 2, no. 2, pp. 137-151, 2012.

[2] E.-G. Talbi, *Metaheuristics: from design to implementation*. John Wiley & Sons, 2009.

[3] M. Gendreau and J. Potvin, "Handbook of Metaheuristics. International Series in Operations Research & Management Science," ed: Springer, 2010.

[4] S. Kirkpatrick and M. Vecchi, "Optimization by simmulated annealing," *science,* vol. 220, no. 4598, pp. 671-680, 1983.

[5] F. Glover, "Tabu search-part I," *ORSA Journal on computing,* vol. 1, no. 3, pp. 190-206, 1989.

[6] Z. He and G. Yen, "Many-Objective Evolutionary Algorithm: Objective Space Reduction+ Diversity Improvement," 2012.

[7] Z. He, G. G. Yen, and J. Zhang, "Fuzzy-based Pareto optimality for many-objective evolutionary algorithms," *Evolutionary Computation, IEEE Transactions on,* vol. 18, no. 2, pp. 269-285, 2014.

[8] K. Deb, *Multi-objective optimization using evolutionary algorithms*. John Wiley & Sons Chichester, 2001.

[9] M. Garza-Fabre, G. T. Pulido, and C. A. C. Coello, "Ranking methods for many-objective optimization," in *Mexican International Conference on Artificial Intelligence*, 2009, pp. 633-645: Springer.

[10] H. Ishibuchi, Y. Tanigaki, H. Masuda, and Y. Nojima, "Distance-based analysis of crossover operators for many-objective knapsack problems," in *International Conference on Parallel Problem Solving from Nature*, 2014, pp. 600-610: Springer.

[11] H. Sato, H. Aguirre, and K. Tanaka, "Variable space diversity, crossover and mutation in MOEA solving many-objective knapsack problems," *Annals of Mathematics and Artificial Intelligence,* vol. 68, no. 4, pp. 197-224, 2013.

[12] D. J. Walker, R. Everson, and J. E. Fieldsend, "Visualizing mutually nondominating solution sets in many-objective optimization," *IEEE Transactions on Evolutionary Computation,* vol. 17, no. 2, pp. 165-184, 2013.

[13] K. Deb and D. Saxena, "Searching for Pareto-optimal solutions through dimensionality reduction for certain large-dimensional multi-objective optimization problems," in *Proceedings of the World Congress on Computational Intelligence (WCCI-2006),* 2006, pp. 3352-3360.

[14] H. Ishibuchi, N. Tsukamoto, and Y. Nojima, "Evolutionary many-objective optimization: A short review," in *Evolutionary Computation, 2008. CEC 2008.(IEEE World Congress on Computational Intelligence). IEEE Congress on*, 2008, pp. 2419-2426: IEEE.

[15] E. Zitzler and L. Thiele, "Multiobjective evolutionary algorithms: a comparative case study and the strength Pareto approach," *Evolutionary Computation, IEEE Transactions on,* vol. 3, no. 4, pp. 257-271, 1999.

[16] C. M. Fonseca, L. Paquete, and M. López-Ibánez, "An improved dimension-sweep algorithm for the hypervolume indicator," in *2006 IEEE International Conference on Evolutionary Computation*, 2006, pp. 1157-1163: IEEE.

[17] N. Beume, C. M. Fonseca, M. López-Ibáñez, L. Paquete, and J. Vahrenhold, "On the complexity of computing the hypervolume indicator," *IEEE Transactions on Evolutionary Computation*, vol. 13, no. 5, pp. 1075-1082, 2009.

[18] L. While, L. Bradstreet, and L. Barone, "A fast way of calculating exact hypervolumes," *IEEE Transactions on Evolutionary Computation*, vol. 16, no. 1, pp. 86-95, 2012.

[19] D. A. Van Veldhuizen and G. B. Lamont, "Multiobjective evolutionary algorithm test suites," in *Proceedings of the 1999 ACM symposium on Applied computing*, 1999, pp. 351-357: ACM.

[20] E. Zitzler, L. Thiele, M. Laumanns, C. M. Fonseca, and V. G. Da Fonseca, "Performance assessment of multiobjective optimizers: an analysis and review," *IEEE transactions on evolutionary computation*, vol. 7, no. 2, pp. 117-132, 2003.

[21] K. Deb, A. Pratap, S. Agarwal, and T. Meyarivan, "A fast and elitist multiobjective genetic algorithm: NSGA-II," *Evolutionary Computation, IEEE Transactions on*, vol. 6, no. 2, pp. 182-197, 2002.

[22] S. Jiang, Y.-S. Ong, J. Zhang, and L. Feng, "Consistencies and contradictions of performance metrics in multiobjective optimization," *IEEE transactions on cybernetics*, vol. 44, no. 12, pp. 2391-2404, 2014.

[23] R. R. Yager, "Multiple objective decision-making using fuzzy sets," *International Journal of Man-Machine Studies*, vol. 9, no. 4, pp. 375-382, 1977.

[24] W. Ho, X. Xu, and P. K. Dey, "Multi-criteria decision making approaches for supplier evaluation and selection: A literature review," *European Journal of operational research*, vol. 202, no. 1, pp. 16-24, 2010.

[25] V. Chankong and Y. Y. Haimes, *Multiobjective decision making: theory and methodology*. Courier Dover Publications, 2008.

[26] E. A. Demirtas and Ö. Üstün, "An integrated multiobjective decision making process for supplier selection and order allocation," *Omega*, vol. 36, no. 1, pp. 76-90, 2008.

[27] A. Inselberg, "The plane with parallel coordinates," *The Visual Computer*, vol. 1, no. 2, pp. 69-91, 1985.

[28] A. Pryke, S. Mostaghim, and A. Nazemi, "Heatmap visualization of population based multi objective algorithms," in *Evolutionary multi-criterion optimization*, 2007, pp. 361-375: Springer.

[29] T. Kohonen, "Self-organizing maps, vol. 30 of Springer Series in Information Sciences," ed: Springer Berlin, 2001.

[30] P. Hoffman, G. Grinstein, K. Marx, I. Grosse, and E. Stanley, "DNA visual and analytic data mining," in *Visualization'97., Proceedings*, 1997, pp. 437-441: IEEE.

[31] D. H. Wolpert and W. G. Macready, "No free lunch theorems for optimization," *IEEE transactions on evolutionary computation*, vol. 1, no. 1, pp. 67-82, 1997.

[32] B. Luo, J. Zheng, J. Xie, and J. Wu, "Dynamic crowding distance? A new diversity maintenance strategy for MOEAs," in *Natural Computation, 2008. ICNC'08. Fourth International Conference on*, 2008, vol. 1, pp. 580-585: IEEE.

[33] D. E. Goldberg and J. Richardson, "Genetic algorithms with sharing for multimodal function optimization," in *Genetic algorithms and their applications: Proceedings of the Second International Conference on Genetic Algorithms*, 1987, pp. 41-49: Hillsdale, NJ: Lawrence Erlbaum.

[34] K. Deb and D. E. Goldberg, "An investigation of niche and species formation in genetic function optimization," in *Proceedings of the 3rd International Conference on Genetic Algorithms*, 1989, pp. 42-50: Morgan Kaufmann Publishers Inc.

[35] P. Czyżak and A. Jaszkiewicz, "Pareto simulated annealing," in *Multiple Criteria Decision Making*: Springer, 1997, pp. 297-307.

[36] T. Murata, H. Ishibuchi, and M. Gen, "Specification of genetic search directions in cellular multi-objective genetic algorithms," in *Evolutionary Multi-Criterion Optimization*, 2001, pp. 82-95: Springer.

[37] T. Murata, H. Nozawa, Y. Tsujimura, M. Gen, and H. Ishibuchi, "Effect of local search on the performance of cellular multiobjective genetic algorithms for designing fuzzy rule-based classification systems," in *Computational Intelligence, Proceedings of the World on Congress on*, 2002, vol. 1, pp. 663-668: IEEE.

[38] H. Lu and G. G. Yen, "Rank-density-based multiobjective genetic algorithm and benchmark test function study," *Evolutionary Computation, IEEE Transactions on*, vol. 7, no. 4, pp. 325-343, 2003.

[39] E. Zitzler *et al.*, "SPEA2: Improving the strength Pareto evolutionary algorithm," ed: Eidgenössische Technische Hochschule Zürich (ETH), Institut für Technische Informatik und Kommunikationsnetze (TIK), 2001.

[40] M. Farina and P. Amato, "A fuzzy definition of" optimality" for many-criteria optimization problems," *Systems, Man and Cybernetics, Part A: Systems and Humans, IEEE Transactions on*, vol. 34, no. 3, pp. 315-326, 2004.

[41] H. Jin and M.-L. Wong, "Adaptive diversity maintenance and convergence guarantee in multiobjective evolutionary algorithms," in *Evolutionary*

Computation, 2003. CEC'03. The 2003 Congress on, 2003, vol. 4, pp. 2498-2505: IEEE.

[42] G. Rudolph, "Convergence analysis of canonical genetic algorithms," *Neural Networks, IEEE Transactions on,* vol. 5, no. 1, pp. 96-101, 1994.

[43] M. Laumanns, E. Zitzler, and L. Thiele, "On the effects of archiving, elitism, and density based selection in evolutionary multi-objective optimization," in *Evolutionary multi-criterion optimization*, 2001, pp. 181-196: Springer.

[44] D. A. Van Veldhuizen and G. B. Lamont, "Multiobjective evolutionary algorithm research: A history and analysis," Citeseer1998.

[45] J. Knowles, L. Thiele, and E. Zitzler, "A tutorial on the performance assessment of stochastic multiobjective optimizers," *Tik report,* vol. 214, pp. 327-332, 2006.

[46] A. Zhou, Y. Jin, Q. Zhang, B. Sendhoff, and E. Tsang, "Combining model-based and genetics-based offspring generation for multi-objective optimization using a convergence criterion," in *Evolutionary Computation, 2006. CEC 2006. IEEE Congress on*, 2006, pp. 892-899: IEEE.

[47] M. P. Hansen and A. Jaszkiewicz, *Evaluating the quality of approximations to the non-dominated set*. IMM, Department of Mathematical Modelling, Technical Universityof Denmark, 1998.

[48] D. Brockhoff, T. Wagner, and H. Trautmann, "On the Properties of the R2 Indicator," in *Proceedings of the fourteenth international conference on Genetic and evolutionary computation conference,* 2012, pp. 465-472: ACM.

[49] H. Li and Q. Zhang, "Multiobjective optimization problems with complicated Pareto sets, MOEA/D and NSGA-II," *Evolutionary Computation, IEEE Transactions on,* vol. 13, no. 2, pp. 284-302, 2009.

[50] J. J. Durillo, J. García-Nieto, A. J. Nebro, C. A. C. Coello, F. Luna, and E. Alba, "Multi-objective particle swarm optimizers: An experimental comparison," in *Evolutionary Multi-Criterion Optimization*, 2009, pp. 495-509: Springer.

[51] J. J. Durillo, A. J. Nebro, C. A. Coello Coello, F. Luna, and E. Alba, "A comparative study of the effect of parameter scalability in multi-objective metaheuristics," in *Evolutionary Computation, 2008. CEC 2008.(IEEE World Congress on Computational Intelligence). IEEE Congress on*, 2008, pp. 1893-1900: IEEE.

[52] A. J. Nebro, J. J. Durillo, F. Luna, B. Dorronsoro, and E. Alba, "Mocell: A cellular genetic algorithm for multiobjective optimization," *International Journal of Intelligent Systems,* vol. 24, no. 7, pp. 726-746, 2009.

[53] A. J. Nebro, F. Luna, E. Alba, B. Dorronsoro, J. J. Durillo, and A. Beham, "AbYSS: Adapting scatter search to multiobjective optimization," *Evolutionary Computation, IEEE Transactions on*, vol. 12, no. 4, pp. 439-457, 2008.

[54] T. Tušar and B. Filipič, "Differential evolution versus genetic algorithms in multiobjective optimization," in *Evolutionary Multi-Criterion Optimization*, 2007, pp. 257-271: Springer.

[55] L. Bradstreet, L. Barone, L. While, S. Huband, and P. Hingston, "Use of the WFG Toolkit and PISA for Comparison of MOEAs," in *Computational Intelligence in Multicriteria Decision Making, IEEE Symposium on*, 2007, pp. 382-389: IEEE.

[56] T. Robič and B. Filipič, "DEMO: Differential evolution for multiobjective optimization," in *Evolutionary Multi-Criterion Optimization*, 2005, pp. 520-533: Springer.

[57] J. D. Schaffer, "Some experiments in machine learning using vector evaluated genetic algorithms (artificial intelligence, optimization, adaptation, pattern recognition)," 1984.

[58] F. Kursawe, "A variant of evolution strategies for vector optimization," in *Parallel Problem Solving from Nature*: Springer, 1991, pp. 193-197.

[59] C. M. Fonseca and P. J. Fleming, "An overview of evolutionary algorithms in multiobjective optimization," *Evolutionary computation*, vol. 3, no. 1, pp. 1-16, 1995.

[60] S. Huband, P. Hingston, L. Barone, and L. While, "A review of multiobjective test problems and a scalable test problem toolkit," *Evolutionary Computation, IEEE Transactions on*, vol. 10, no. 5, pp. 477-506, 2006.

[61] K. Deb, L. Thiele, M. Laumanns, and E. Zitzler, "Scalable multi-objective optimization test problems," in *Proceedings of the Congress on Evolutionary Computation (CEC-2002),(Honolulu, USA)*, 2002, pp. 825-830: Proceedings of the Congress on Evolutionary Computation (CEC-2002),(Honolulu, USA).

[62] S. Huband, L. Barone, L. While, and P. Hingston, "A scalable multi-objective test problem toolkit," in *Evolutionary multi-criterion optimization*, 2005, pp. 280-295: Springer.

[63] A. Osyczka and S. Kundu, "A new method to solve generalized multicriteria optimization problems using the simple genetic algorithm," *Structural optimization*, vol. 10, no. 2, pp. 94-99, 1995.

[64] M. Tanaka, H. Watanabe, Y. Furukawa, and T. Tanino, "GA-based decision support system for multicriteria optimization," in *Systems, Man and Cybernetics, 1995. Intelligent Systems for the 21st Century., IEEE International Conference on*, 1995, vol. 2, pp. 1556-1561: IEEE.

[65] N. Srinivas and K. Deb, "Muiltiobjective optimization using nondominated sorting in genetic algorithms," *Evolutionary computation*, vol. 2, no. 3, pp. 221-248, 1994.

[66] A. López Jaimes and C. A. Coello Coello, "Some techniques to deal with many-objective problems," in *Proceedings of the 11th Annual Conference Companion on Genetic and Evolutionary Computation Conference: Late Breaking Papers*, 2009, pp. 2693-2696: ACM.

[67] A. Ibrahim, S. Rahnamayan, M. V. Martin, and K. Deb, "3D-RadVis: Visualization of Pareto front in many-objective optimization," in *Evolutionary Computation (CEC), 2016 IEEE Congress on*, 2016, pp. 736-745: IEEE.

[68] Z. He and G. G. Yen, "Visualization and performance metric in many-objective optimization," *IEEE Transactions on Evolutionary Computation*, vol. 20, no. 3, pp. 386-402, 2016.

[69] T. Tušar and B. Filipič, "Visualization of Pareto front approximations in evolutionary multiobjective optimization: A critical review and the prosection method," *IEEE Transactions on Evolutionary Computation*, vol. 19, no. 2, pp. 225-245, 2015.

[70] S. Manjrekar, S. Sandilya, D. Bhosale, S. Kanchi, A. Pitkar, and M. Gondhalekar, "CAVE: An Emerging Immersive Technology--A Review," in *Computer Modelling and Simulation (UKSim), 2014 UKSim-AMSS 16th International Conference on*, 2014, pp. 131-136: IEEE.

[71] S. D. Miyahira, R. A. Folen, M. Stetz, A. Rizzo, and M. M. Kawasaki, "Use of immersive virtual reality for treating anger," *Stud Health Technol Inform*, vol. 154, pp. 82-86, 2010.

[72] C. A. Kilmon, L. Brown, S. Ghosh, and A. Mikitiuk, "Immersive virtual reality simulations in nursing education," *Nursing education perspectives*, vol. 31, no. 5, pp. 314-317, 2010.

[73] M. Carrozzino and M. Bergamasco, "Beyond virtual museums: Experiencing immersive virtual reality in real museums," *Journal of Cultural Heritage*, vol. 11, no. 4, pp. 452-458, 2010.

[74] B. Bideau, R. Kulpa, N. Vignais, S. Brault, F. Multon, and C. Craig, "Using virtual reality to analyze sports performance," *IEEE Computer Graphics and Applications*, vol. 30, no. 2, pp. 14-21, 2010.

[75] A. Inselberg, *Parallel coordinates*. Springer, 2009.

[76] C. M. Fonseca and P. J. Fleming, "Multiobjective optimization and multiple constraint handling with evolutionary algorithms. II. Application example," *Systems, Man and Cybernetics, Part A: Systems and Humans, IEEE Transactions on*, vol. 28, no. 1, pp. 38-47, 1998.

[77] P. J. Fleming, R. C. Purshouse, and R. J. Lygoe, "Many-objective optimization: An engineering design perspective," in *Evolutionary multi-criterion optimization*, 2005, pp. 14-32: Springer.

[78] D. Carr and W. Nicholson, "Evaluation of graphical techniques for data in dimensions 3 to 5: scatter plot matrix, glyph and stereo examples," Pacific Northwest Labs., Richland, WA (USA)1985.

[79] M. Ashby, "Multi-objective optimization in material design and selection," *Acta materialia*, vol. 48, no. 1, pp. 359-369, 2000.

[80] S. Poles, P. Geremia, F. Campos, S. Weston, and M. Islam, "MOGA-II for an automotive cooling duct optimization on distributed resources," in *Evolutionary Multi-Criterion Optimization*, 2007, pp. 633-644: Springer.

[81] A. Ultsch, *U*-matrix: a tool to visualize clusters in high dimensional data*. Fachbereich Mathematik und Informatik Marburg, 2003.

[82] Q. Zhang and H. Li, "MOEA/D: A multiobjective evolutionary algorithm based on decomposition," *Evolutionary Computation, IEEE Transactions on*, vol. 11, no. 6, pp. 712-731, 2007.

[83] H. Scheffé, "Experiments with mixtures," *Journal of the Royal Statistical Society. Series B (Methodological)*, pp. 344-360, 1958.

[84] J. Siwei, C. Zhihua, Z. Jie, and O. Yew-Soon, "Multiobjective optimization by decomposition with Pareto-adaptive weight vectors," in *Natural Computation (ICNC), 2011 Seventh International Conference on*, 2011, vol. 3, pp. 1260-1264: IEEE.

[85] L. While, P. Hingston, L. Barone, and S. Huband, "A faster algorithm for calculating hypervolume," *IEEE transactions on evolutionary computation,* vol. 10, no. 1, pp. 29-38, 2006.

[86] E. Zitzler and L. Thiele, "Multiobjective optimization using evolutionary algorithms—a comparative case study," in *International Conference on Parallel Problem Solving from Nature,* 1998, pp. 292-301: Springer.

[87] D. A. Van Veldhuizen, "Multiobjective evolutionary algorithms: classifications, analyses, and new innovations," DTIC Document1999.

[88] J. Wu and S. Azarm, "Metrics for quality assessment of a multiobjective design optimization solution set," *Journal of Mechanical Design,* vol. 123, no. 1, pp. 18-25, 2001.

[89] S. Yang, M. Li, X. Liu, and J. Zheng, "A grid-based evolutionary algorithm for many-objective optimization," *Evolutionary Computation, IEEE Transactions on,* vol. 17, no. 5, pp. 721-736, 2013.

[90] M. Li, S. Yang, and X. Liu, "Shift-based density estimation for Pareto-based algorithms in many-objective optimization," *Evolutionary Computation, IEEE Transactions on,* vol. 18, no. 3, pp. 348-365, 2014.

[91] I. Das and J. E. Dennis, "Normal-boundary intersection: A new method for generating the Pareto surface in nonlinear multicriteria optimization problems," *SIAM Journal on Optimization,* vol. 8, no. 3, pp. 631-657, 1998.

[92] E. Nwankwor, A. K. Nagar, and D. Reid, "Hybrid differential evolution and particle swarm optimization for optimal well placement," *Computational Geosciences,* pp. 1-20, 2013.

[93] S. Mirjalili and S. Z. M. Hashim, "A new hybrid PSOGSA algorithm for function optimization," in *Computer and information application (ICCIA), 2010 international conference on*, 2010, pp. 374-377: IEEE.

[94] A. Elhossini, S. Areibi, and R. Dony, "Strength Pareto particle swarm optimization and hybrid EA-PSO for multi-objective optimization," *Evolutionary Computation,* vol. 18, no. 1, pp. 127-156, 2010.

[95] L. Tang and X. Wang, "A hybrid multiobjective evolutionary algorithm for multiobjective optimization problems," *IEEE Transactions on Evolutionary Computation,* vol. 17, no. 1, pp. 20-45, 2013.

[96] Y. Wang, Z. Cai, Y. Zhou, and Z. Fan, "Constrained optimization based on hybrid evolutionary algorithm and adaptive constraint-handling technique," *Structural and Multidisciplinary Optimization*, vol. 37, no. 4, pp. 395-413, 2009.

[97] A.-C. Zăvoianu, E. Lughofer, G. Bramerdorfer, W. Amrhein, and E. P. Klement, "DECMO2: a robust hybrid and adaptive multi-objective evolutionary algorithm," *Soft Computing*, vol. 19, no. 12, pp. 3551-3569, 2015.

[98] S.-Z. Zhao and P. N. Suganthan, "Multi-objective evolutionary algorithm with ensemble of external archives," *International Journal of Innovative Computing, Information and Control,* vol. 6, no. 1, pp. 1713-1726, 2010.

[99] B. Y. Qu and P. N. Suganthan, "Constrained multi-objective optimization algorithm with an ensemble of constraint handling methods," *Engineering Optimization,* vol. 43, no. 4, pp. 403-416, 2011.

[100] S.-Z. Zhao, P. N. Suganthan, and Q. Zhang, "Decomposition-based multiobjective evolutionary algorithm with an ensemble of neighborhood sizes," *IEEE Transactions on Evolutionary Computation,* vol. 16, no. 3, pp. 442-446, 2012.

[101] K. C. Tan, Y. Chew, and L. H. Lee, "A hybrid multi-objective evolutionary algorithm for solving truck and trailer vehicle routing problems," *European Journal of Operational Research,* vol. 172, no. 3, pp. 855-885, 2006.

[102] W. Xia and Z. Wu, "An effective hybrid optimization approach for multi-objective flexible job-shop scheduling problems," *Computers & Industrial Engineering,* vol. 48, no. 2, pp. 409-425, 2005.

[103] R. Tavakkoli-Moghaddam, A. Rahimi-Vahed, and A. H. Mirzaei, "A hybrid multi-objective immune algorithm for a flow shop scheduling problem with bi-objectives: weighted mean completion time and weighted mean tardiness," *Information Sciences,* vol. 177, no. 22, pp. 5072-5090, 2007.

[104] S. Karthikeyan, P. Asokan, S. Nickolas, and T. Page, "A hybrid discrete firefly algorithm for solving multi-objective flexible job shop scheduling problems," *International Journal of Bio-Inspired Computation,* vol. 7, no. 6, pp. 386-401, 2015.

[105] K. Deb and H. Jain, "An evolutionary many-objective optimization algorithm using reference-point-based nondominated sorting approach, part I: solving problems with box constraints," *Evolutionary Computation, IEEE Transactions on,* vol. 18, no. 4, pp. 577-601, 2014.

[106] S. Kukkonen and J. Lampinen, "GDE3: The third evolution step of generalized differential evolution," in *Evolutionary Computation, 2005. The 2005 IEEE Congress on*, 2005, vol. 1, pp. 443-450: IEEE.

[107] A. J. Nebro, J. Durillo, J. Garcia-Nieto, C. Coello Coello, F. Luna, and E. Alba, "Smpso: A new pso-based metaheuristic for multi-objective optimization," in *Computational intelligence in miulti-criteria decision-making, 2009. mcdm'09. ieee symposium on*, 2009, pp. 66-73: IEEE.

[108] A. J. Nebro, J. J. Durillo, J. Garcia-Nieto, C. C. Coello, F. Luna, and E. Alba, "Smpso: A new pso-based metaheuristic for multi-objective optimization," in *Computational intelligence in miulti-criteria decision-making, 2009. mcdm'09. ieee symposium on*, 2009, pp. 66-73: IEEE.

[109] A. Ibrahim, S. Rahnamayan, M. Vargas Martin, and K. Deb, "3D-RadVis: Visualization of Pareto Front in Many-Objective Optimization," in *IEEE World Congress on Computational Intelligence (IEEE WCCI)*, 2016, p. In presss.

[110] C. Qian, K. Tang, and Z.-H. Zhou, "Selection Hyper-heuristics Can Provably Be Helpful in Evolutionary Multi-objective Optimization," in *International Conference on Parallel Problem Solving from Nature*, 2016, pp. 835-846: Springer.

[111] A. Ibrahim, S. Rahnamayan, M. V. Martin, and K. Deb, "Fusion of Many-Objective Non-dominated Solutions Using Reference Points," in *International Conference on Evolutionary Multi-Criterion Optimization*, 2017, pp. 314-328: Springer.

[112] K. Deb and H. Jain, "An evolutionary many-objective optimization algorithm using reference-point-based nondominated sorting approach, part I: Solving problems

with box constraints," *IEEE Trans. Evolutionary Computation,* vol. 18, no. 4, pp. 577-601, 2014.

[113] H. Jain and K. Deb, "An Evolutionary Many-Objective Optimization Algorithm Using Reference-Point Based Nondominated Sorting Approach, Part II: Handling Constraints and Extending to an Adaptive Approach," *IEEE Trans. Evolutionary Computation,* vol. 18, no. 4, pp. 602-622, 2014.

[114] S. Greco, K. Klamroth, J. D. Knowles, and G. Rudolph, "Understanding complexity in multiobjective optimization (Dagstuhl Seminar 15031)," in *Dagstuhl Reports*, 2015, vol. 5, no. 1: Schloss Dagstuhl-Leibniz-Zentrum fuer Informatik.

[115] M. W. Mkaouer, M. Kessentini, S. Bechikh, K. Deb, and M. Ó Cinnéide, "High dimensional search-based software engineering: finding tradeoffs among 15 objectives for automating software refactoring using NSGA-III," in *Proceedings of the 2014 Annual Conference on Genetic and Evolutionary Computation*, 2014, pp. 1263-1270: ACM.

[116] J. G. Herrero, A. Berlanga, and J. M. M. Lopez, "Effective Evolutionary Algorithms for Many-Specifications Attainment: Application to Air Traffic Control Tracking Filters," *IEEE Trans. Evolutionary Computation,* vol. 13, no. 1, pp. 151-168, 2009.

[117] Z. He, G. G. Yen, and J. Zhang, "Fuzzy-based Pareto optimality for many-objective evolutionary algorithms," *IEEE Transactions on Evolutionary Computation,* vol. 18, no. 2, pp. 269-285, 2014.

[118] R. C. Purshouse and P. J. Fleming, "Evolutionary many-objective optimisation: An exploratory analysis," in *Evolutionary Computation, 2003. CEC'03. The 2003 Congress on*, 2003, vol. 3, pp. 2066-2073: IEEE.

[119] V. Khare, X. Yao, and K. Deb, "Performance scaling of multi-objective evolutionary algorithms," in *EMO*, 2003, vol. 2632, pp. 376-390: Springer.

[120] L. Cruz-Reyes, E. Fernandez, C. Gomez, P. Sanchez, G. Castilla, and D. Martinez, "Verifying the Effectiveness of an Evolutionary Approach in Solving Many-Objective Optimization Problems," in *Design of Intelligent Systems Based on Fuzzy Logic, Neural Networks and Nature-Inspired Optimization*: Springer, 2015, pp. 455-464.

[121] A. Zhou, Q. Zhang, and Y. Jin, "Approximating the set of Pareto-optimal solutions in both the decision and objective spaces by an estimation of distribution algorithm," *IEEE transactions on evolutionary computation,* vol. 13, no. 5, pp. 1167-1189, 2009.

[122] K. Deb and H. Jain, "Handling many-objective problems using an improved NSGA-II procedure," in *Evolutionary Computation (CEC), 2012 IEEE Congress on*, 2012, pp. 1-8: IEEE.

[123] K. Sindhya, K. Miettinen, and K. Deb, "A hybrid framework for evolutionary multi-objective optimization," *IEEE Transactions on Evolutionary Computation*, vol. 17, no. 4, pp. 495-511, 2013.

[124] Q. Zhang, H. Li, D. Maringer, and E. Tsang, "MOEA/D with NBI-style Tchebycheff approach for portfolio management," in *Evolutionary Computation (CEC), 2010 IEEE Congress on*, 2010, pp. 1-8: IEEE.

[125] X. Yuan, H. Tian, Y. Yuan, Y. Huang, and R. M. Ikram, "An extended NSGA-III for solution multi-objective hydro-thermal-wind scheduling considering wind power cost," *Energy Conversion and Management*, vol. 96, pp. 568-578, 2015.

[126] W. Mkaouer *et al.*, "Many-objective software remodularization using NSGA-III," *ACM Transactions on Software Engineering and Methodology (TOSEM)*, vol. 24, no. 3, p. 17, 2015.

[127] M. Tavana, Z. Li, M. Mobin, M. Komaki, and E. Teymourian, "Multi-objective control chart design optimization using NSGA-III and MOPSO enhanced with DEA and TOPSIS," *Expert Systems with Applications*, vol. 50, pp. 17-39, 2016.

[128] Y. Yuan, H. Xu, and B. Wang, "An Experimental Investigation of Variation Operators in Reference-Point Based Many-Objective Optimization," in *Proceedings of the 2015 Annual Conference on Genetic and Evolutionary Computation*, 2015, pp. 775-782: ACM.

[129] Y. Yuan, H. Xu, and B. Wang, "An improved NSGA-III procedure for evolutionary many-objective optimization," in *Proceedings of the 2014 Annual Conference on Genetic and Evolutionary Computation*, 2014, pp. 661-668: ACM.

[130] H. Seada and K. Deb, "U-nsga-iii: A unified evolutionary optimization procedure for single, multiple, and many objectives: Proof-of-principle results," in *International Conference on Evolutionary Multi-Criterion Optimization*, 2015, pp. 34-49: Springer.

[131] H. Jain and K. Deb, "An evolutionary many-objective optimization algorithm using reference-point based nondominated sorting approach, part II: handling constraints

and extending to an adaptive approach," *Evolutionary Computation, IEEE Transactions on,* vol. 18, no. 4, pp. 602-622, 2014.

[132] K. Deb, A. Pratap, and T. Meyarivan, "Constrained test problems for multi-objective evolutionary optimization," in *Evolutionary Multi-Criterion Optimization*, 2001, pp. 284-298: Springer.

[133] J. D. Knowles and D. W. Corne, "Approximating the nondominated front using the Pareto archived evolution strategy," *Evolutionary computation,* vol. 8, no. 2, pp. 149-172, 2000.

[134] M. López-Ibáñez, J. Knowles, and M. Laumanns, "On sequential online archiving of objective vectors," in *International Conference on Evolutionary Multi-Criterion Optimization*, 2011, pp. 46-60: Springer.

[135] S. Huband, L. Barone, L. While, and P. Hingston, "A scalable multi-objective test problem toolkit," in *International Conference on Evolutionary Multi-Criterion Optimization*, 2005, pp. 280-295: Springer.

[136] S. Yang, M. Li, X. Liu, and J. Zheng, "A grid-based evolutionary algorithm for many-objective optimization," *IEEE Transactions on Evolutionary Computation,* vol. 17, no. 5, pp. 721-736, 2013.

[137] M. Li, S. Yang, and X. Liu, "Shift-based density estimation for Pareto-based algorithms in many-objective optimization," *IEEE Transactions on Evolutionary Computation,* vol. 18, no. 3, pp. 348-365, 2014.

[138] A. J. N. a. J. J. Durillo, "jMetal 4.5 User Manual," 2014.

[139] D. J. Sheskin, *Handbook of parametric and nonparametric statistical procedures*. crc Press, 2003.

[140] J. Schlaich, R. Bergermann, W. Schiel, and G. Weinrebe, "Design of commercial solar tower systems–utilization of solar induced convective flows for power generation," *solar energy,* vol. 10, p. 1, 2005.

[141] D. Kearney, E. Zarza, G. Cohen, R. Gee, and R. Mahoney, "Advances in Parabolic trough solar power technology," *Advances in Solar Energy,* vol. 16, 2002.

[142] Varun and Siddhartha, "Thermal performance optimization of a flat plate solar air heater using genetic algorithm," *Applied Energy,* vol. 87, no. 5, pp. 1793-1799, 2010.

[143] Y. Thiaux, J. Seigneurbieux, B. Multon, and H. Ben Ahmed, "Load profile impact on the gross energy requirement of stand-alone photovoltaic systems," *Renewable Energy,* vol. 35, no. 3, pp. 602-613, 2010.

[144] H. Yang, L. Lu, and W. Zhou, "A novel optimization sizing model for hybrid solar-wind power generation system," *Solar energy,* vol. 81, no. 1, pp. 76-84, 2007.

[145] Y.-P. Chang, "Optimal the tilt angles for photovoltaic modules in Taiwan," *International Journal of Electrical Power & Energy Systems,* vol. 32, no. 9, pp. 956-964, 2010.

[146] K. Deb, F. Ruiz, M. Luque, R. Tewari, J. M. Cabello, and J. M. Cejudo, "On the sizing of a solar thermal electricity plant for multiple objectives using evolutionary optimization," *Applied Soft Computing,* vol. 12, no. 10, pp. 3300-3311, 2012.

[147] A. Mellit, S. Kalogirou, L. Hontoria, and S. Shaari, "Artificial intelligence techniques for sizing photovoltaic systems: A review," *Renewable and Sustainable Energy Reviews,* vol. 13, no. 2, pp. 406-419, 2009.

[148] S. Sadineni, R. F. Boehm, and R. Hurt, "Spacing analysis of an inclined solar collector field," in *ASME 2008 2nd International Conference on Energy Sustainability collocated with the Heat Transfer, Fluids Engineering, and 3rd Energy Nanotechnology Conferences*, 2008, pp. 417-422: American Society of Mechanical Engineers.

[149] B. Myers, M. Bernardi, and J. C. Grossman, "Three-dimensional photovoltaics," *Applied Physics Letters*, vol. 96, no. 7, p. 071902, 2010.

[150] O. Ekren and B. Y. Ekren, "Size optimization of a PV/wind hybrid energy conversion system with battery storage using simulated annealing," *Applied Energy*, vol. 87, no. 2, pp. 592-598, 2010.

[151] D. Weinstock and J. Appelbaum, "Optimal solar field design of stationary collectors," *Journal of solar energy engineering*, vol. 126, no. 3, pp. 898-905, 2004.

[152] D. Weinstock and J. Appelbaum, "Optimization of solar photovoltaic fields," *Journal of Solar Energy Engineering*, vol. 131, no. 3, p. 031003, 2009.

[153] B. F, R. R, and R. S, "Optimal Photovoltaic Solar Power Farm Design using the Differential Evolution Algorithm," presented at the International Conference on Clean Energy (ICCI'10), , Gazimagusa, N. Cyprus, 2010.

[154] NCDIA. Monthly averaged hourly solar angles relative to the horizon and solar Azimuth angles due south in degrees. [Online]. Available: http://climat.meteo.gc.ca/prods_servs/index_e.html, 2012

[155] NASA. Monthly averaged hourly solar angles relative to the horizon(degrees) and monthly averaged hourly solar azimuth angles(degrees) [Online]. Available: http://eosweb.larc.nasa.gov, 2012

[156] WWW. (2012, August 3). *Solar panels at affordable prices*. Available: http://www.altestore.com/store/SolarPanels/c541/

[157] C. B. Vining, "An inconvenient truth about thermoelectrics," *Nature materials*, vol. 8, no. 2, p. 83, 2009.

[158] A. Z. Sahin and B. S. Yilbas, "Thermodynamic irreversibility and performance characteristics of thermoelectric power generator," *Energy*, vol. 55, pp. 899-904, 2013.

[159] A. Z. Sahin and B. S. Yilbas, "The thermoelement as thermoelectric power generator: Effect of leg geometry on the efficiency and power generation," *Energy Conversion and Management*, vol. 65, pp. 26-32, 2013.

[160] A. Z. Sahin and B. S. Yilbas, "The influence of operating and device parameters on the maximum efficiency and the maximum output power of thermoelectric generator," *International Journal of Energy Research*, vol. 36, no. 1, pp. 111-119, 2012.

[161] C.-C. Wang and C.-I. Hung, "Effect of irreversibilities on the performance of thermoelectric generator investigated using exergy analysis," *Journal of Thermal Science and Technology*, vol. 8, no. 1, pp. 1-14, 2013.

[162] W. He, Y. Su, S. Riffat, J. Hou, and J. Ji, "Parametrical analysis of the design and performance of a solar heat pipe thermoelectric generator unit," *Applied energy*, vol. 88, no. 12, pp. 5083-5089, 2011.

[163] A. Patyk, "Thermoelectric generators for efficiency improvement of power generation by motor generators–environmental and economic perspectives," *Applied energy*, vol. 102, pp. 1448-1457, 2013.

[164] G. Shu, J. Zhao, H. Tian, X. Liang, and H. Wei, "Parametric and exergetic analysis of waste heat recovery system based on thermoelectric generator and organic rankine cycle utilizing R123," *Energy,* vol. 45, no. 1, pp. 806-816, 2012.

[165] D. Wee, "Analysis of thermoelectric energy conversion efficiency with linear and nonlinear temperature dependence in material properties," *Energy conversion and management,* vol. 52, no. 12, pp. 3383-3390, 2011.

[166] S. Kim, "Analysis and modeling of effective temperature differences and electrical parameters of thermoelectric generators," *Applied energy,* vol. 102, pp. 1458-1463, 2013.

[167] M. Chen, H. Lund, L. A. Rosendahl, and T. J. Condra, "Energy efficiency analysis and impact evaluation of the application of thermoelectric power cycle to today's CHP systems," *Applied Energy,* vol. 87, no. 4, pp. 1231-1238, 2010.

[168] R. V. Rao and V. Patel, "Multi-objective optimization of two stage thermoelectric cooler using a modified teaching–learning-based optimization algorithm," *Engineering Applications of Artificial Intelligence,* vol. 26, no. 1, pp. 430-445, 2013.

[169] S. Bélanger and L. Gosselin, "Multi-objective genetic algorithm optimization of thermoelectric heat exchanger for waste heat recovery," *International Journal of Energy Research,* vol. 36, no. 5, pp. 632-642, 2012.

[170] J. Wang, Z. Yan, M. Wang, and Y. Dai, "Thermodynamic analysis and optimization of an ammonia-water power system with LNG (liquefied natural gas) as its heat sink," *Energy,* vol. 50, pp. 513-522, 2013.

[171] Z. Hajabdollahi, F. Hajabdollahi, M. Tehrani, and H. Hajabdollahi, "Thermo-economic environmental optimization of Organic Rankine Cycle for diesel waste heat recovery," *Energy*, vol. 63, pp. 142-151, 2013.

[172] H. Sayyaadi and H. R. Aminian, "Design and optimization of a non-TEMA type tubular recuperative heat exchanger used in a regenerative gas turbine cycle," *Energy*, vol. 35, no. 4, pp. 1647-1657, 2010.

[173] L. Daróczy, G. Janiga, and D. Thévenin, "Systematic analysis of the heat exchanger arrangement problem using multi-objective genetic optimization," *Energy*, vol. 65, pp. 364-373, 2014.

[174] A. Ibrahim, F. Bourennani, S. Rahnamayan, and G. F. Naterer, "Optimal Photovoltaic System Design with Multi-Objective Optimization," *International Journal of Applied Metaheuristic Computing (IJAMC)*, vol. 4, no. 4, pp. 63-89, 2013.

[175] A. Saraswat, A. Saini, and A. K. Saxena, "A novel multi-zone reactive power market settlement model: A pareto-optimization approach," *Energy*, vol. 51, pp. 85-100, 2013.

[176] Y. Li *et al.*, "Parametric study and optimization of a RCCI (reactivity controlled compression ignition) engine fueled with methanol and diesel," *Energy*, vol. 65, pp. 319-332, 2014.

[177] M. G. Ippolito, M. L. Di Silvestre, E. R. Sanseverino, G. Zizzo, and G. Graditi, "Multi-objective optimized management of electrical energy storage systems in an islanded network with renewable energy sources under different design scenarios," *Energy*, vol. 64, pp. 648-662, 2014.

[178] P. Ahmadi, I. Dincer, and M. A. Rosen, "Thermoeconomic multi-objective optimization of a novel biomass-based integrated energy system," *Energy*, vol. 68, pp. 958-970, 2014.

[179] N. Liu, Z. Chen, J. Liu, X. Tang, X. Xiao, and J. Zhang, "Multi-objective optimization for component capacity of the photovoltaic-based battery switch stations: Towards benefits of economy and environment," *Energy*, vol. 64, pp. 779-792, 2014.

[180] J. C. Silva, G. Cruz, C. Vinhal, D. R. Silva, and C. J. Bastos-Filho, "Comparing MOPSO approaches for hydrothermal systems operation planning," in *Computational Intelligence and 11th Brazilian Congress on Computational Intelligence (BRICS-CCI & CBIC), 2013 BRICS Congress on*, 2013, pp. 551-556: IEEE.

[181] X. Shi *et al.*, "Multiple-filled skutterudites: high thermoelectric figure of merit through separately optimizing electrical and thermal transports," *Journal of the American Chemical Society*, vol. 133, no. 20, pp. 7837-7846, 2011.

[182] A. Ibrahim, M. V. Martin, S. Rahnamayan, and K. Deb, "3D-RadVis Antenna: Visualization and Performance Measure for Many-objective Optimization," *Swarm and Evolutionary Computation*, 2017.

[183] A. Ibrahim, M. V. Martin, S. Rahnamayan, and K. Deb, "Fusion-based hybrid many-objective optimization algorithm," in *Evolutionary Computation (CEC), 2017 IEEE Congress on*, 2017, pp. 2372-2381: IEEE.

[184] A. Ibrahim, S. Rahnamayan, M. V. Martin, and K. Deb, "EliteNSGA-III: An improved evolutionary many-objective optimization algorithm," in *Evolutionary Computation (CEC), 2016 IEEE Congress on*, 2016, pp. 973-982: IEEE.

[185] A. Ibrahim, S. Rahnamayan, M. V. Martin, and B. Yilbas, "Multi-objective thermal analysis of a thermoelectric device: Influence of geometric features on device characteristics," *Energy*, vol. 77, pp. 305-317, 2014.

[186] L. v. d. Maaten and G. Hinton, "Visualizing data using t-SNE," *Journal of Machine Learning Research*, vol. 9, no. Nov, pp. 2579-2605, 2008.

APPENDIX

A. Climate Information used in the Photovoltaic System Design Case Study

Table A.1 Monthly average hourly direct normal beam irradiance: Latitude 43.45^{o} / Longitude -79.25^{o}(Kwh/m^2)

Tim	Jan	Feb	Mar	Apr	May	Jun	Jul	Aug	Sep	Oct	Nov	Dec
0:00	0.000	0.000	0.000	0.000	0.000	0.000	0.000	0.000	0.000	0.000	0.000	0.000
1:00	0.000	0.000	0.000	0.000	0.000	0.000	0.000	0.000	0.000	0.000	0.000	0.000
2:00	0.000	0.000	0.000	0.000	0.000	0.000	0.000	0.000	0.000	0.000	0.000	0.000
3:00	0.000	0.000	0.000	0.000	0.000	0.000	0.000	0.000	0.000	0.000	0.000	0.000
4:00	0.000	0.000	0.000	0.000	0.000	0.000	0.000	0.000	0.000	0.000	0.000	0.000
5:00	0.000	0.000	0.000	0.004	0.146	0.158	0.148	0.015	0.000	0.000	0.000	0.000
6:00	0.000	0.000	0.015	0.157	0.336	0.262	0.311	0.208	0.133	0.001	0.000	0.000
7:00	0.000	0.023	0.220	0.263	0.418	0.339	0.378	0.311	0.350	0.163	0.017	0.000
8:00	0.093	0.170	0.342	0.332	0.488	0.389	0.443	0.381	0.409	0.221	0.057	0.065
9:00	0.179	0.256	0.379	0.374	0.460	0.446	0.480	0.410	0.450	0.257	0.104	0.143
10:0	0.262	0.303	0.354	0.405	0.443	0.446	0.506	0.411	0.440	0.332	0.175	0.224
11:0	0.307	0.327	0.328	0.430	0.436	0.453	0.531	0.391	0.412	0.331	0.180	0.244
12:0	0.319	0.350	0.361	0.409	0.418	0.439	0.511	0.404	0.438	0.303	0.214	0.271
13:0	0.311	0.329	0.309	0.382	0.366	0.410	0.441	0.382	0.455	0.290	0.204	0.267
14:0	0.277	0.313	0.286	0.337	0.354	0.364	0.376	0.361	0.405	0.304	0.181	0.180
15:0	0.231	0.312	0.261	0.348	0.307	0.333	0.349	0.348	0.331	0.268	0.090	0.119
16:0	0.114	0.258	0.211	0.305	0.262	0.313	0.343	0.324	0.257	0.175	0.024	0.002
17:0	0.000	0.056	0.134	0.228	0.189	0.275	0.280	0.242	0.150	0.013	0.000	0.000
18:0	0.000	0.000	0.000	0.061	0.092	0.193	0.207	0.139	0.014	0.000	0.000	0.000
19:0	0.000	0.000	0.000	0.000	0.005	0.090	0.074	0.001	0.000	0.000	0.000	0.000
20:0	0.000	0.000	0.000	0.000	0.000	0.000	0.000	0.000	0.000	0.000	0.000	0.000
21:0	0.000	0.000	0.000	0.000	0.000	0.000	0.000	0.000	0.000	0.000	0.000	0.000
22:0	0.000	0.000	0.000	0.000	0.000	0.000	0.000	0.000	0.000	0.000	0.000	0.000
23:0	0.000	0.000	0.000	0.000	0.000	0.000	0.000	0.000	0.000	0.000	0.000	0.000

Table A.2 Monthly average hourly horizontal diffuse irradiance: Latitude 43.45^{o} / Longitude -79.25^{o}(Kwh/m^2)

Time	Jan	Feb	Mar	Apr	May	Jun	Jul	Aug	Sep	Oct	Nov	Dec
0:00	0.0000	0.0000	0.0000	0.0000	0.0000	0.0000	0.0000	0.0000	0.0000	0.0000	0.0000	0.0000
1:00	0.0000	0.0000	0.0000	0.0000	0.0000	0.0000	0.0000	0.0000	0.0000	0.0000	0.0000	0.0000
2:00	0.0000	0.0000	0.0000	0.0000	0.0000	0.0000	0.0000	0.0000	0.0000	0.0000	0.0000	0.0000
3:00	0.0000	0.0000	0.0000	0.0000	0.0000	0.0000	0.0000	0.0000	0.0000	0.0000	0.0000	0.0000
4:00	0.0000	0.0000	0.0000	0.0001	0.0012	0.0079	0.0048	0.0005	0.0000	0.0000	0.0000	0.0000
5:00	0.0000	0.0000	0.0004	0.0086	0.0281	0.0389	0.0322	0.0190	0.0029	0.0000	0.0000	0.0000
6:00	0.0000	0.0017	0.0156	0.0411	0.0701	0.0816	0.0647	0.0591	0.0368	0.0088	0.0003	0.0000
7:00	0.0049	0.0199	0.0483	0.0957	0.1220	0.1354	0.1033	0.1118	0.0786	0.0444	0.0156	0.0013
8:00	0.0280	0.0556	0.0967	0.1378	0.1657	0.1902	0.1443	0.1609	0.1160	0.0921	0.0526	0.0197
9:00	0.0686	0.0960	0.1439	0.1843	0.2215	0.2298	0.1782	0.2155	0.1595	0.1415	0.0986	0.0610
10:00	0.1056	0.1267	0.1752	0.2339	0.2605	0.2803	0.2083	0.2637	0.1977	0.1802	0.1278	0.0943
11:00	0.1282	0.1522	0.2018	0.2314	0.2779	0.3088	0.2373	0.2937	0.2267	0.1920	0.1351	0.1016
12:00	0.1331	0.1699	0.1868	0.2255	0.2909	0.3202	0.2673	0.2943	0.2199	0.2039	0.1316	0.0993
13:00	0.1223	0.1817	0.1875	0.2105	0.2927	0.3171	0.2858	0.2796	0.2015	0.1868	0.1128	0.0892
14:00	0.0936	0.1507	0.1721	0.1915	0.2654	0.2889	0.2783	0.2463	0.1907	0.1427	0.0813	0.0755
15:00	0.0608	0.1040	0.1390	0.1498	0.2040	0.2339	0.2409	0.1998	0.1535	0.1018	0.0460	0.0415
16:00	0.0320	0.0596	0.0930	0.1078	0.1601	0.1715	0.1764	0.1511	0.1008	0.0532	0.0156	0.0073
17:00	0.0063	0.0293	0.0393	0.0597	0.1022	0.1190	0.1194	0.0992	0.0493	0.0103	0.0012	0.0006
18:00	0.0000	0.0032	0.0068	0.0190	0.0475	0.0660	0.0682	0.0461	0.0098	0.0007	0.0000	0.0000
19:00	0.0000	0.0000	0.0002	0.0029	0.0030	0.0245	0.0279	0.0123	0.0009	0.0000	0.0000	0.0000
20:00	0.0000	0.0000	0.0000	0.0000	0.0001	0.0036	0.0038	0.0003	0.0000	0.0000	0.0000	0.0000
21:00	0.0000	0.0000	0.0000	0.0000	0.0000	0.0000	0.0000	0.0000	0.0000	0.0000	0.0000	0.0000
22:00	0.0000	0.0000	0.0000	0.0000	0.0000	0.0000	0.0000	0.0000	0.0000	0.0000	0.0000	0.0000
23:00	0.0000	0.0000	0.0000	0.0000	0.0000	0.0000	0.0000	0.0000	0.0000	0.0000	0.0000	0.0000

Table A.3 Monthly average hourly solar azimuth angles due south (degrees): 43.45^o / Longitude -79.25^o

Time	Jan	Feb	Mar	Apr	May	Jun	Jul	Aug	Sep	Oct	Nov	Dec
0:00	n/a	n/a	n/a	n/a	n/a	n/a	n/a	n/a	n/a	n/a	n/a	n/a
1:00	n/a	n/a	n/a	n/a	n/a	n/a	n/a	n/a	n/a	n/a	n/a	n/a
2:00	n/a	n/a	n/a	n/a	n/a	n/a	n/a	n/a	n/a	n/a	n/a	n/a
3:00	n/a	n/a	n/a	n/a	n/a	n/a	n/a	n/a	n/a	n/a	n/a	n/a
4:00	n/a	n/a	n/a	n/a	n/a	n/a	n/a	n/a	n/a	n/a	n/a	n/a
5:00	n/a	n/a	n/a	n/a	-116.0	-119.5	-119.4	n/a	n/a	n/a	n/a	n/a
6:00	n/a	n/a	n/a	-100.0	-106.1	-109.8	-109.5	-103.8	n/a	n/a	n/a	n/a
7:00	n/a	n/a	-82.8	-89.8	-96.3	-100.4	-99.9	-93.8	-84.1	-75.0	n/a	n/a
8:00	-60.0	-66.0	-72.0	-80.0	-86.1	-90.6	-90.1	-83.3	-74.0	-64.0	-57.0	-55.0
9:00	-49.0	-55.0	-60.0	-67.0	-75.0	-80.0	-79.0	-72.0	-61.0	-51.0	-45.0	-44.0
10:00	-36.0	-42.0	-46.0	-52.0	-60.0	-66.0	-65.0	-57.0	-46.0	-37.0	-32.0	-32.0
11:00	-23.0	-27.0	-29.0	-33.0	-38.0	-44.0	-45.0	-37.0	-27.0	-20.0	-17.0	-18.0
12:00	-7.0	-10.0	-10.0	-8.0	-8.0	-11.0	-15.0	-11.0	-5.0	-1.0	-1.0	-3.0
13:00	8.0	8.0	11.0	18.0	25.0	27.0	21.0	18.0	18.0	17.0	15.0	12.0
14:00	23.0	25.0	31.0	41.0	50.0	54.0	49.0	43.0	38.0	34.0	30.0	26.0
15:00	37.0	40.0	48.0	58.0	68.0	72.0	68.0	61.0	54.0	49.0	43.0	39.0
15:00	49.0	53.0	61.0	72.0	81.0	84.0	81.0	74.0	68.0	61.0	55.0	51.0
17:00	60.0	65.0	73.0	83.0	91.0	95.0	92.0	86.0	79.0	72.0	n/a	n/a
18:00	n/a	n/a	84.0	94.0	101.0	104.0	102.0	96.0	90.0	n/a	n/a	n/a
19:00	n/a	n/a	n/a	n/a	111.0	114.0	111.0	106.0	n/a	n/a	n/a	n/a
20:00	n/a	n/a	n/a	n/a	n/a	n/a	n/a	n/a	n/a	n/a	n/a	n/a
21:00	n/a	n/a	n/a	n/a	n/a	n/a	n/a	n/a	n/a	n/a	n/a	n/a
22:00	n/a	n/a	n/a	n/a	n/a	n/a	n/a	n/a	n/a	n/a	n/a	n/a
23:00	n/a	n/a	n/a	n/a	n/a	n/a	n/a	n/a	n/a	n/a	n/a	n/a

Table A.4 Monthly average hourly solar Angles relative to the horizon (degrees): 43.45^o / Longitude -79.25^o

Time	Jan	Feb	Mar	Apr	May	Jun	Jul	Aug	Sep	Oct	Nov	Dec
0:00	n/a	n/a	n/a	n/a	n/a	n/a	n/a	n/a	n/a	n/a	n/a	n/a
1:00	n/a	n/a	n/a	n/a	n/a	n/a	n/a	n/a	n/a	n/a	n/a	n/a
2:00	n/a	n/a	n/a	n/a	n/a	n/a	n/a	n/a	n/a	n/a	n/a	n/a
3:00	n/a	n/a	n/a	n/a	n/a	n/a	n/a	n/a	n/a	n/a	n/a	n/a
4:00	n/a	n/a	n/a	n/a	n/a	n/a	n/a	n/a	n/a	n/a	n/a	n/a
5:00	n/a	n/a	n/a	n/a	0.3	2.9	0.6	n/a	n/a	n/a	n/a	n/a
6:00	n/a	n/a	n/a	3.5	10.4	12.7	10.4	5.7	n/a	n/a	n/a	n/a
7:00	n/a	n/a	4.9	14.3	21.1	23.2	20.9	16.4	10.8	4.4	n/a	n/a
8:00	1.4	6.9	15.5	25.1	32.0	34.1	31.8	27.2	21.4	14.5	7.3	2.4
9:00	10.1	16.3	25.4	35.6	42.7	44.9	42.6	37.8	31.4	23.6	15.7	10.6
10:00	17.4	24.3	34.1	44.9	52.7	55.3	52.9	47.6	40.1	31.1	22.3	17.2
11:00	22.7	30.3	40.8	52.2	60.9	64.2	61.8	55.6	46.5	36.1	26.7	21.7
12:00	25.4	33.7	44.3	56.0	65.2	69.3	67.2	59.9	49.5	38.0	28.3	23.6
13:00	25.3	33.7	44.1	55.0	63.4	67.7	66.4	59.1	48.2	36.4	26.9	22.6
14:00	22.3	30.6	40.0	49.5	56.7	60.5	60.0	53.5	43.0	31.6	22.6	18.9
15:00	16.8	24.6	33.1	41.2	47.3	50.7	50.6	44.9	35.1	24.3	16.0	12.9
16:00	9.4	16.7	24.2	31.3	36.8	40.1	40.1	34.8	25.5	15.3	7.7	5.2
17:00	0.5	7.3	14.1	20.6	26.0	29.2	29.2	24.0	15.1	5.3	n/a	n/a
18:00	n/a	n/a	3.5	9.8	15.2	18.5	18.4	13.2	4.3	n/a	n/a	n/a
19:00	n/a	n/a	n/a	n/a	4.8	8.3	8.0	2.5	n/a	n/a	n/a	n/a
20:00	n/a	n/a	n/a	n/a	n/a	n/a	n/a	n/a	n/a	n/a	n/a	n/a
21:00	n/a	n/a	n/a	n/a	n/a	n/a	n/a	n/a	n/a	n/a	n/a	n/a
22:00	n/a	n/a	n/a	n/a	n/a	n/a	n/a	n/a	n/a	n/a	n/a	n/a
23:00	n/a	n/a	n/a	n/a	n/a	n/a	n/a	n/a	n/a	n/a	n/a	n/a

B. Sample Non-dominated Solution Set for the Photovoltaic System Design Case Study

Table B.1 The best (IGD) set of non-dominated solution set found by Fusion.

K	H (m)	β $(^o)$	D (m)	γ $(^o)$	E (m)	Q (MWh)	Cost ($)
2	1.81	25.89	2.50	-3.99	0.52	37.60	16701.65
2	1.37	26.91	2.50	-3.99	0.52	28.60	12683.69
2	1.15	27.72	2.50	-3.99	0.69	23.91	10595.16
2	1.09	24.00	2.42	-3.83	1.27	22.75	10087.14
2	1.03	26.92	2.50	-4.00	0.94	21.51	9526.34
2	0.48	26.80	2.50	-3.95	0.75	10.00	4419.81
2	0.37	26.99	2.50	-3.93	0.75	7.68	3393.21
2	0.26	27.52	2.50	-4.00	0.79	5.36	2364.93
2	0.20	27.51	2.50	-3.99	1.06	4.19	1849.76
3	1.94	24.90	2.50	-3.98	1.06	60.46	26936.29
3	1.91	24.64	2.50	-3.99	0.50	59.40	26457.99
3	1.87	24.73	2.50	-3.97	0.91	58.31	25969.20
3	1.79	24.48	2.50	-3.99	0.51	55.70	24796.75
3	1.72	25.45	2.50	-3.98	0.93	53.60	23855.27
3	1.64	25.24	2.50	-3.99	1.10	51.24	22797.12
3	1.61	26.01	2.49	-3.99	0.97	50.21	22335.81
3	1.58	25.24	2.41	-3.95	0.85	49.16	21870.08
3	1.17	24.86	2.01	-4.00	0.91	36.55	16246.25
3	1.06	25.84	2.50	-3.99	0.70	33.07	14665.36
3	1.02	25.74	2.50	-3.99	1.29	31.99	14186.07
3	0.98	26.28	2.50	-4.00	0.69	30.73	13624.19
3	0.80	24.48	2.50	-3.99	0.51	25.01	11080.61
3	0.62	27.67	2.50	-3.99	0.73	19.29	8534.06
3	0.54	25.39	2.50	-4.47	0.70	16.96	7515.75
3	0.51	26.87	2.50	-3.98	0.93	15.84	7006.48
3	0.43	27.36	2.50	-4.00	0.69	13.50	5968.49
3	0.39	26.99	2.33	-3.96	0.94	12.28	5426.14
3	0.35	26.89	2.50	-3.98	0.93	11.14	4924.02
3	0.21	27.36	2.50	-4.00	0.93	6.52	2880.46
4	1.98	24.06	1.58	-3.99	0.77	81.74	36685.64
4	1.96	25.87	1.64	-3.99	1.01	80.63	36195.23
4	1.93	24.80	1.59	-5.10	1.13	79.44	35700.07
4	1.90	24.15	1.69	-3.96	0.87	78.41	35135.33
4	1.87	21.71	1.66	-3.99	0.92	77.35	34666.62
4	1.85	23.20	1.72	-3.99	0.78	76.32	34172.08
4	1.82	23.14	1.73	-4.00	0.67	75.11	33623.63
4	1.79	24.48	1.70	-3.99	0.51	73.85	33062.33
4	1.76	26.32	1.87	-2.43	0.85	72.46	32502.72
4	1.74	24.62	1.88	-3.90	1.07	72.02	32194.25
4	1.71	24.08	1.66	-7.98	0.91	70.36	31578.35
4	1.68	24.89	1.96	-3.99	0.52	69.58	31072.01
4	1.66	30.51	1.94	-7.27	0.89	68.17	30674.93
4	1.62	23.70	1.91	-4.00	0.93	67.24	30024.79
4	1.60	23.23	1.73	-4.00	0.67	66.08	29538.23
4	1.56	24.10	1.97	-3.97	1.20	64.83	28927.39
4	1.54	22.68	2.09	-3.95	0.81	63.76	28441.41

4	1.51	24.55	2.17	-3.99	0.50	62.62	27905.06
4	1.48	24.62	2.18	-4.00	0.86	61.55	27419.48
4	1.38	24.22	2.17	-3.99	0.53	57.27	25498.21
4	1.32	24.52	2.16	-3.99	0.50	54.70	24345.88
4	1.26	27.20	1.75	-3.97	0.57	52.13	23257.63
4	1.14	25.69	2.50	-3.88	0.79	47.66	21166.96
4	1.12	25.75	2.50	-3.89	0.79	46.61	20696.30
4	1.09	25.75	2.50	-4.00	0.51	45.57	20230.62
4	1.07	26.15	2.50	-4.00	0.79	44.56	19778.40
4	1.04	26.11	2.50	-3.97	0.86	43.53	19318.60
4	1.01	26.09	2.50	-4.00	0.50	42.30	18770.16
4	0.99	25.79	2.50	-3.99	1.11	41.14	18251.81
4	0.95	25.86	1.64	-3.99	1.01	39.63	17634.19
4	0.93	25.78	1.97	-4.00	0.51	38.67	17175.78
4	0.85	24.62	2.18	-3.99	0.86	35.48	15744.45
4	0.82	26.32	2.50	-4.00	0.50	34.14	15131.06
4	0.66	26.85	2.50	-3.99	0.73	27.49	12171.77
4	0.63	26.09	2.50	-4.00	0.59	26.18	11590.91
4	0.49	27.28	2.50	-4.00	0.52	20.39	9021.05
4	0.43	27.23	2.50	-4.00	0.68	18.18	8038.00
4	0.21	27.31	2.50	-3.99	0.93	8.85	3908.96
5	1.99	28.51	0.80	-3.99	1.03	100.23	46063.72
5	1.97	26.93	0.81	-4.00	0.93	99.32	45457.26
5	1.94	25.93	0.80	-3.96	0.58	98.17	44841.10
5	1.91	23.41	0.80	-4.00	0.94	97.29	44265.74
5	1.89	22.72	0.81	-3.98	0.94	96.22	43732.82
5	1.87	23.42	0.85	-3.97	0.53	95.15	43221.99
5	1.84	20.25	0.84	-3.98	0.69	94.04	42649.95
5	1.82	21.47	0.83	-4.00	0.91	92.84	42105.81
5	1.80	22.88	0.93	-3.99	0.97	91.70	41515.43
5	1.77	20.69	0.91	-3.99	0.99	90.56	40976.00
5	1.75	22.70	0.98	-3.97	0.50	89.35	40386.59
5	1.73	20.98	0.98	-3.91	1.25	88.47	39965.57
5	1.70	21.55	1.02	-4.00	0.98	87.28	39393.88
5	1.68	21.44	1.04	-3.99	0.93	86.20	38878.44
5	1.66	20.45	0.97	-3.98	0.50	85.02	38388.76
5	1.64	22.92	1.11	-4.00	0.50	84.01	37842.63
5	1.62	21.47	0.89	-4.00	0.91	82.62	37346.85
5	0.57	25.32	1.88	-3.93	0.77	29.69	13161.46
6	2.00	48.21	0.80	-15.99	0.50	109.41	55492.93
6	1.98	47.69	0.80	-15.91	0.50	108.61	54843.47
6	1.95	47.31	0.80	-15.77	0.50	107.44	54077.06
6	1.93	47.19	0.81	-15.80	0.56	106.71	53605.13
6	1.91	46.50	0.82	-15.98	0.51	106.08	52963.25
6	1.89	45.91	0.82	-15.99	0.50	105.32	52351.43
6	1.87	45.73	0.83	-15.87	0.52	104.73	51953.40
6	1.84	43.56	0.80	-15.98	0.53	104.05	50926.76
6	1.81	42.69	0.80	-15.99	0.54	103.17	50215.46
6	1.79	42.30	0.80	-15.99	0.63	102.38	49694.27
6	1.76	41.00	0.80	-15.80	0.74	101.36	48814.29
6	2.00	48.21	0.80	-15.99	0.50	109.18	55368.22
6	1.97	47.76	0.80	-15.82	0.50	108.41	54775.47
6	1.97	47.70	0.80	-15.53	0.50	108.03	54562.89
7	0.20	26.13	1.27	-3.89	0.87	14.63	6474.18

Table B.2 The best (IGD) set of non-dominated solution set found by SMPSO.

K	H (m)	β $(^o)$	D (m)	γ $(^o)$	E (m)	Q (MWh)	Cost ($)
2	0.40	32.24	2.30	-13.89	1.19	8.31	3683.87
2	0.35	29.82	2.33	-10.18	1.19	7.28	3235.37
2	0.54	28.07	2.14	-15.07	1.52	11.34	5019.67
2	0.30	29.67	2.39	-14.01	1.55	6.27	2772.22
2	0.20	28.46	2.50	-15.91	1.64	4.19	1849.76
2	0.45	25.09	2.12	-2.77	1.27	9.32	4128.47
2	0.25	27.21	2.36	-15.56	1.57	5.22	2307.87
2	0.84	25.46	1.85	-13.25	1.40	17.43	7742.50
2	0.89	28.48	1.80	-14.07	1.36	18.49	8211.35
2	0.79	25.50	1.84	-12.60	1.17	16.42	7294.53
2	0.64	28.64	1.88	-5.99	0.95	13.34	5912.24
3	0.33	27.91	2.33	-6.84	1.52	10.32	4567.42
3	0.66	24.22	1.93	-6.38	1.47	20.62	9159.72
3	0.46	24.77	2.27	-2.56	1.37	14.34	6360.58
3	0.49	31.01	2.17	-6.92	1.10	15.35	6813.03
4	0.30	29.12	2.04	-6.66	1.37	12.34	5466.72
4	0.73	26.13	1.94	-15.92	1.28	30.33	13469.57
4	0.76	27.41	1.96	-12.94	1.39	31.41	13971.21
4	0.65	25.16	1.81	-15.26	0.79	26.98	11984.86
4	0.70	27.25	2.01	-13.61	1.42	29.20	12978.10
4	0.57	23.17	2.12	-10.71	1.44	23.76	10575.54
4	0.62	24.53	2.27	-16.72	1.58	25.92	11527.06
5	1.50	24.62	1.26	-5.67	0.80	77.29	34756.51
5	1.94	25.07	0.80	-5.74	0.63	98.12	44811.11
5	1.97	28.02	0.83	-5.79	0.53	99.08	45467.58
5	1.20	25.03	1.56	-4.56	1.10	62.03	27739.72
5	1.70	22.63	1.02	-1.90	0.83	86.98	39374.19
5	0.90	24.35	1.68	-5.70	1.19	46.68	20794.45
5	1.26	23.76	1.46	-6.73	1.07	64.91	29065.62
5	1.83	23.25	0.89	-4.81	0.68	93.27	42370.41
5	1.07	24.73	1.67	-3.55	1.26	55.62	24831.85
5	1.74	23.21	1.00	-6.67	0.63	89.00	40295.30
5	1.89	24.46	0.80	-5.34	0.70	95.58	43594.84
5	1.86	23.58	0.83	-4.89	0.71	94.38	42965.20
5	2.00	28.55	0.80	-5.89	0.50	100.50	46244.11
5	1.24	25.00	1.48	-5.71	0.97	63.97	28620.99
5	1.72	24.49	1.00	-5.88	0.69	88.01	39852.45
5	1.48	23.93	1.26	-5.94	0.88	76.27	34273.69
5	1.40	22.64	1.35	-5.19	1.28	72.13	32364.27
5	1.12	23.59	1.72	-3.88	0.79	57.90	25805.82
5	0.48	24.81	2.24	-4.19	1.57	24.84	11021.55
5	1.38	25.28	1.42	-5.60	1.23	71.13	31891.65
5	1.46	24.37	1.30	-5.68	0.91	75.25	33801.06
5	1.14	23.42	1.65	-5.85	1.24	58.93	26313.24
5	1.91	25.51	0.83	-5.89	0.56	96.80	44182.27
5	0.73	25.33	1.99	-12.27	1.40	37.87	16860.70
5	0.86	27.71	1.77	-5.24	1.18	44.53	19831.91
5	0.79	27.54	1.82	-4.95	1.19	41.13	18303.02
5	0.84	26.04	1.82	-4.61	1.31	43.39	19312.91

5	1.42	24.03	1.36	-6.89	0.73	73.16	32836.71
5	1.44	23.99	1.31	-15.32	0.82	74.17	33326.84
5	1.18	23.96	1.56	-5.31	1.09	61.01	27271.87
5	1.79	22.86	0.94	-1.99	0.68	90.97	41285.26
5	0.62	25.59	2.04	-14.11	1.45	32.51	14439.29
5	1.68	21.79	1.04	-2.40	1.20	86.00	38893.45
5	0.65	25.91	2.04	-6.86	1.45	33.59	14916.12
5	0.71	27.86	2.09	-12.66	1.46	36.83	16382.54
5	0.81	26.43	1.84	-5.05	1.42	42.25	18795.44
5	0.88	25.84	1.77	-5.80	1.33	45.63	20309.29
5	0.69	27.29	1.98	-3.13	1.52	35.76	15900.08
5	0.42	27.22	2.20	-8.31	1.34	21.72	9631.01
5	0.38	28.52	2.15	-7.64	1.74	19.57	8679.15
5	1.01	25.21	1.75	-4.84	1.29	52.21	23275.67
5	0.77	26.40	1.89	-15.76	1.26	40.08	17816.04
5	1.36	23.94	1.44	-6.57	0.71	70.04	31395.91
5	1.55	23.98	1.22	-4.16	0.78	79.41	35761.39
5	1.30	24.19	1.52	-3.90	1.41	67.07	29975.72
5	0.96	23.59	1.68	-6.88	1.27	49.90	22257.26
5	1.05	26.77	1.70	-4.80	1.20	54.48	24316.68
5	0.92	26.04	1.82	-4.67	1.36	47.75	21267.02
5	1.59	24.03	1.18	-3.92	0.74	81.72	36773.92
5	0.94	25.62	1.80	-5.82	0.86	48.85	21753.16
5	1.57	24.17	1.14	-1.12	0.67	80.47	36343.39
5	0.54	26.07	2.15	-13.52	1.39	28.11	12478.90
5	1.76	24.81	0.98	-3.56	0.73	89.91	40794.44
5	1.81	23.60	0.91	-4.83	0.69	92.16	41841.28
5	1.32	26.40	1.50	-4.88	1.35	68.00	30475.11
5	0.75	27.26	1.88	-6.48	1.30	38.99	17338.92
5	0.44	28.31	2.21	-11.15	1.55	22.77	10113.23
5	1.53	22.82	1.20	-7.38	0.75	78.30	35293.98
5	1.62	24.75	1.16	-2.21	0.81	82.79	37390.99
5	0.67	26.41	1.99	-14.86	1.40	34.69	15405.28
5	1.66	22.74	1.08	-3.58	0.66	85.05	38418.12
5	1.28	25.19	1.46	-5.64	1.02	65.96	29530.87
5	1.10	24.87	1.57	-4.88	1.06	56.73	25337.96
5	1.03	26.07	1.72	-3.84	1.30	53.38	23774.52
5	1.22	22.72	1.54	-5.66	1.12	62.99	28173.66
5	1.16	26.85	1.59	-5.57	1.11	59.94	26792.78
5	0.98	24.47	1.68	-5.41	1.26	51.04	22754.35
5	1.34	26.26	1.47	-5.42	0.95	68.94	30898.82
5	1.64	23.42	1.10	-4.43	0.67	83.97	37908.52
6	1.83	43.72	0.80	-9.77	0.50	102.42	50668.28
6	1.84	43.86	0.80	-14.23	0.50	104.12	51138.70
6	1.78	41.90	0.80	-17.48	0.53	101.94	49450.40
6	1.99	48.03	0.80	-12.47	0.50	108.84	55294.18
6	2.00	48.32	0.80	-13.26	0.50	109.05	55492.93
6	1.91	45.98	0.80	-10.65	0.50	106.03	53043.76
6	1.89	46.22	0.80	-17.42	0.50	104.98	52449.51
6	1.95	47.79	0.80	-12.55	0.50	106.65	54031.37

Table B.3 The best (IGD) set of non-dominated solution set found by GDE3.

K	H (m)	β $(^o)$	D (m)	γ $(^o)$	E (m)	Q (MWh)	Cost ($)
2	0.40	32.24	2.30	-13.89	1.19	8.31	3683.87
2	0.35	29.82	2.33	-10.18	1.19	7.28	3235.37
2	0.54	28.07	2.14	-15.07	1.52	11.34	5019.67
2	0.30	29.67	2.39	-14.01	1.55	6.27	2772.22
2	0.20	28.46	2.50	-15.91	1.64	4.19	1849.76
2	0.45	25.09	2.12	-2.77	1.27	9.32	4128.47
2	0.25	27.21	2.36	-15.56	1.57	5.22	2307.87
2	0.84	25.46	1.85	-13.25	1.40	17.43	7742.50
2	0.91	26.41	2.50	-4.00	1.09	19.06	8436.36
2	1.62	27.29	2.50	-4.00	1.09	33.72	14969.79
2	0.20	27.52	2.50	-4.00	1.00	4.19	1849.76
2	0.25	27.52	2.50	-4.00	0.50	5.22	2304.07
2	1.80	26.24	2.50	-4.00	0.50	37.42	16621.65
2	0.20	27.52	2.50	-4.00	0.99	4.19	1849.76
2	1.25	22.98	1.70	-4.00	1.33	26.07	11590.57
3	0.33	27.91	2.33	-6.84	1.52	10.32	4567.42
3	0.66	24.22	1.93	-6.38	1.47	20.62	9159.72
3	1.35	24.24	2.50	-4.00	1.10	42.26	18779.22
3	0.89	24.24	2.50	-4.00	0.92	28.00	12413.21
3	0.47	27.23	2.50	-4.00	0.94	14.86	6571.93
3	1.53	27.29	2.50	-4.00	0.99	47.77	21250.17
3	0.20	27.52	2.50	-4.00	0.58	6.28	2774.65
3	1.57	28.69	2.50	-4.00	1.00	48.77	21717.42
3	1.48	28.69	2.50	-4.00	0.94	46.08	20507.34
3	1.31	28.69	2.50	-4.00	0.94	40.94	18200.51
3	1.11	28.69	2.50	-4.00	1.18	34.65	15383.69
4	0.30	29.12	2.04	-6.66	1.37	12.34	5466.72
4	0.73	26.13	1.94	-15.92	1.28	30.33	13469.57
4	0.76	27.41	1.96	-12.94	1.39	31.41	13971.21
4	0.65	25.16	1.81	-15.26	0.79	26.98	11984.86
4	0.20	27.48	2.50	-4.00	0.94	8.38	3699.53
4	1.65	24.19	1.92	-4.00	0.95	68.52	30600.44
4	1.73	23.86	1.80	-4.00	1.13	71.68	32052.70
4	1.76	24.14	1.72	-4.00	0.67	72.85	32601.34
4	1.33	25.57	1.70	-4.00	0.87	54.99	24538.36
4	1.25	22.98	1.70	-4.00	1.33	51.97	23181.14
4	1.79	22.94	1.60	-4.00	0.50	73.78	33056.18
4	1.92	22.94	1.60	-4.00	0.91	79.13	35486.92
4	0.97	22.34	1.69	-4.00	0.86	40.22	17912.33
4	1.97	22.34	1.50	-4.00	1.01	81.17	36450.03
5	1.50	24.62	1.26	-5.67	0.80	77.29	34756.51
5	1.94	25.07	0.80	-5.74	0.63	98.12	44811.11
5	1.97	28.02	0.83	-5.79	0.53	99.08	45467.58
5	1.20	25.03	1.56	-4.56	1.10	62.03	27739.72
5	1.70	22.63	1.02	-1.90	0.83	86.98	39374.19
5	0.90	24.35	1.68	-5.70	1.19	46.68	20794.45
5	1.26	23.76	1.46	-6.73	1.07	64.91	29065.62

5	1.83	23.25	0.89	-4.81	0.68	93.27	42370.41
5	1.74	23.21	1.00	-6.67	0.63	89.00	40295.30
5	1.89	24.46	0.80	-5.34	0.70	95.58	43594.84
5	1.86	23.58	0.83	-4.89	0.71	94.38	42965.20
5	2.00	28.55	0.80	-5.89	0.50	100.50	46244.11
5	1.24	25.00	1.48	-5.71	0.97	63.97	28620.99
5	1.72	24.49	1.00	-5.88	0.69	88.01	39852.45
5	1.48	23.93	1.26	-5.94	0.88	76.27	34273.69
5	1.40	22.64	1.35	-5.19	1.28	72.13	32364.27
5	1.12	23.59	1.72	-3.88	0.79	57.90	25805.82
5	0.48	24.81	2.24	-4.19	1.57	24.84	11021.55
5	1.38	25.28	1.42	-5.60	1.23	71.13	31891.65
5	1.46	24.37	1.30	-5.68	0.91	75.25	33801.06
5	1.14	23.42	1.65	-5.85	1.24	58.93	26313.24
5	1.91	25.51	0.83	-5.89	0.56	96.80	44182.27
5	0.73	25.33	1.99	-12.27	1.40	37.87	16860.70
5	0.86	27.71	1.77	-5.24	1.18	44.53	19831.91
5	0.79	27.54	1.82	-4.95	1.19	41.13	18303.02
5	0.84	26.04	1.82	-4.61	1.31	43.39	19312.91
5	1.42	24.03	1.36	-6.89	0.73	73.16	32836.71
5	1.44	23.99	1.31	-15.32	0.82	74.17	33326.84
5	1.18	23.96	1.56	-5.31	1.09	61.01	27271.87
5	1.79	22.86	0.94	-1.99	0.68	90.97	41285.26
5	0.62	25.59	2.04	-14.11	1.45	32.51	14439.29
5	1.68	21.79	1.04	-2.40	1.20	86.00	38893.45
5	0.65	25.91	2.04	-6.86	1.45	33.59	14916.12
5	0.71	27.86	2.09	-12.66	1.46	36.83	16382.54
5	0.81	26.43	1.84	-5.05	1.42	42.25	18795.44
5	0.88	25.84	1.77	-5.80	1.33	45.63	20309.29
5	0.69	27.29	1.98	-3.13	1.52	35.76	15900.08
5	0.42	27.22	2.20	-8.31	1.34	21.72	9631.01
5	0.38	28.52	2.15	-7.64	1.74	19.57	8679.15
5	1.01	25.21	1.75	-4.84	1.29	52.21	23275.67
5	0.77	26.40	1.89	-15.76	1.26	40.08	17816.04
5	1.36	23.94	1.44	-6.57	0.71	70.04	31395.91
5	1.98	27.22	0.80	-4.00	0.98	99.70	45673.64
5	1.67	20.89	0.94	-4.00	0.50	85.45	38601.39
5	1.71	20.53	0.89	-4.00	0.94	87.24	39464.24
5	1.86	22.69	0.86	-4.00	0.50	94.58	42917.87
5	1.76	20.66	0.91	-4.00	0.67	90.06	40751.68
5	1.80	20.56	0.89	-4.00	0.89	91.83	41582.80
5	1.62	21.63	1.09	-4.00	0.69	83.16	37458.65
6	1.83	43.72	0.80	-9.77	0.50	102.42	50668.28
6	1.84	43.86	0.80	-14.23	0.50	104.12	51138.70
6	1.78	41.90	0.80	-17.48	0.53	101.94	49450.40
6	1.99	48.03	0.80	-12.47	0.50	108.84	55294.18
6	2.00	48.32	0.80	-13.26	0.50	109.05	55492.93
6	1.91	45.98	0.80	-10.65	0.50	106.03	53043.76
6	1.89	46.22	0.80	-17.42	0.50	104.98	52449.51
6	0.25	27.37	1.65	-4.00	0.73	15.92	7041.82

Table B.4 The best (IGD) set of non-dominated solution set found by SPEA2.

K	H (m)	β $(^o)$	D (m)	γ $(^o)$	E (m)	Q (MWh)	Cost ($)
2	1.64	24.85	2.47	-4.00	0.87	34.17	15171.13
2	0.29	30.50	2.35	-4.00	0.77	6.10	2697.94
2	1.77	24.17	2.42	-3.96	0.61	36.87	16382.17
2	1.94	23.27	0.84	-5.50	0.81	39.81	17929.76
2	1.87	24.44	2.31	-4.00	0.67	38.93	17307.38
2	1.55	27.49	2.50	-3.94	0.78	32.23	14307.52
2	0.25	30.50	2.50	-3.99	0.72	5.22	2307.95
2	0.20	26.21	2.50	-5.82	0.59	4.19	1849.76
3	1.91	25.98	0.82	-3.94	0.65	58.30	26447.32
3	0.40	24.44	2.31	-4.00	0.88	12.43	5501.25
3	0.43	25.18	1.06	-4.00	0.73	13.53	6000.20
3	0.24	24.05	1.86	-4.00	0.72	7.40	3273.88
3	1.70	18.33	2.48	-3.09	0.71	52.67	23635.33
3	0.26	26.78	2.48	-5.54	0.73	8.31	3672.96
3	1.53	21.03	2.35	-4.28	0.79	47.65	21287.54
3	1.43	22.50	2.50	-3.99	0.54	44.64	19862.36
3	1.56	23.84	1.84	-3.99	0.82	48.42	21593.12
3	1.78	21.30	2.46	-7.45	0.91	55.15	24678.55
3	1.86	24.44	2.31	-4.00	0.67	58.00	25850.50
3	2.00	28.78	2.50	-4.00	0.72	62.13	27746.42
3	1.64	24.87	2.47	-3.94	0.87	51.15	22756.69
3	0.29	24.07	2.35	-4.00	0.77	9.15	4046.91
3	1.41	22.50	2.50	-15.99	0.94	43.74	19498.45
3	0.65	24.00	2.38	-5.34	0.75	20.37	9037.48
3	1.98	31.43	2.46	-3.99	0.75	61.39	27519.69
3	1.83	24.41	2.48	-4.00	0.60	56.89	25334.21
3	1.91	25.30	2.46	-4.00	0.77	59.48	26502.78
3	1.60	18.33	1.09	-3.09	0.70	49.18	22189.86
3	1.80	25.15	2.49	-4.00	0.52	56.13	24989.85
3	1.95	28.56	2.49	-3.99	0.76	60.74	27111.93
3	1.74	25.15	2.49	-4.00	0.52	54.18	24115.51
3	0.46	23.30	2.50	-3.99	0.54	14.26	6315.01
3	0.58	23.99	2.50	-4.00	0.55	18.21	8061.68
3	0.37	26.24	2.46	-4.00	0.88	11.54	5098.50
3	0.32	28.06	2.46	-3.99	0.64	9.97	4404.12
3	0.95	22.95	2.37	-3.99	0.57	29.55	13120.58
3	0.34	26.25	2.50	-4.00	1.27	10.76	4752.44
3	1.60	25.81	2.35	-4.00	0.65	50.02	22260.71
3	0.78	28.29	2.35	-3.92	0.81	24.36	10795.67
3	1.46	24.81	2.38	-5.34	0.75	45.56	20286.03
4	1.76	28.49	1.88	-3.99	0.72	72.77	32622.44
4	1.12	24.44	2.23	-3.96	0.51	46.70	20757.82
4	0.37	24.99	1.79	-4.00	0.88	15.36	6798.00
4	0.87	27.41	1.76	-3.99	0.78	36.15	16071.86
4	1.69	26.16	1.85	-4.00	0.71	69.73	31241.29
4	0.60	23.86	1.78	-4.00	0.67	25.20	11179.77
4	1.52	23.81	1.80	-3.99	0.71	63.10	28175.45

4	0.79	25.92	2.38	-3.99	0.56	33.14	14691.28
4	1.71	25.36	1.88	-3.99	0.72	70.64	31573.69
4	1.66	24.40	1.98	-4.00	0.72	68.81	30720.78
4	0.42	26.85	2.34	-3.92	0.67	17.45	7717.99
4	1.78	27.63	1.84	-4.00	0.73	73.68	33017.95
4	1.85	27.57	1.81	-4.00	0.78	76.20	34172.92
4	0.84	23.09	2.47	-4.00	0.54	34.96	15515.25
4	1.63	23.87	1.84	-4.00	0.56	67.53	30168.55
4	0.99	24.08	1.87	-3.96	0.61	41.04	18247.51
4	1.60	27.56	1.81	-4.00	0.78	66.33	29680.99
4	1.57	23.86	1.79	-3.95	1.15	65.18	29118.69
4	1.82	24.39	1.77	-4.00	0.72	75.34	33720.84
4	1.56	23.84	1.84	-4.00	0.58	64.48	28790.83
4	1.73	23.57	1.85	-3.95	0.71	71.66	32031.76
4	1.80	23.86	1.79	-3.95	1.15	74.43	33301.74
5	1.94	28.55	0.82	-3.99	0.65	97.83	44899.64
5	0.52	25.60	1.24	-4.00	0.74	26.84	11921.86
5	0.43	26.58	2.49	-3.99	0.73	22.73	10052.90
5	0.83	22.97	1.03	-8.81	1.22	42.84	19185.94
5	0.50	26.21	0.88	-4.00	0.54	26.02	11584.57
5	1.50	20.46	1.07	-4.00	0.75	76.95	34641.03
5	0.59	23.86	0.94	-4.00	0.67	30.44	13563.41
5	0.37	26.24	2.46	-4.00	0.88	19.22	8497.50
5	0.53	27.36	1.78	-4.00	0.75	27.68	12269.84
5	1.89	23.63	0.84	-3.99	0.72	95.99	43630.77
5	1.66	20.49	0.95	-4.00	0.54	85.17	38467.20
5	0.42	36.68	2.49	-14.30	0.85	21.52	9621.79
5	1.96	28.62	0.84	-3.99	0.78	98.69	45291.52
5	1.73	20.32	0.95	-3.93	0.62	88.53	40017.57
5	0.32	23.12	2.41	-4.59	0.51	16.53	7333.05
5	1.56	24.08	1.11	-3.96	1.19	79.98	36013.48
5	0.45	26.85	2.35	-4.00	0.67	23.57	10428.07
5	0.80	25.43	1.87	-3.99	0.80	41.88	18599.40
5	1.76	21.67	0.90	-4.00	0.81	89.99	40730.14
5	1.62	21.64	1.10	-4.00	0.93	82.98	37367.65
5	1.70	20.49	0.95	-4.00	0.51	87.24	39420.56
5	1.60	20.33	1.11	-4.00	0.65	82.00	36928.06
5	1.78	21.30	0.91	-4.00	1.14	90.88	41130.92
5	1.82	23.36	0.91	-3.98	0.86	92.63	41986.36
5	1.80	23.82	0.90	-3.94	0.64	91.80	41627.20
5	1.58	21.59	1.11	-4.00	0.87	80.98	36449.73
5	0.60	24.46	1.78	-4.00	0.67	31.50	13974.71
5	1.64	22.47	1.08	-3.99	0.70	83.99	37846.39
5	1.69	26.21	1.11	-4.00	0.65	86.31	39003.16
5	1.91	22.82	0.80	-4.00	0.77	97.03	44122.88
5	1.52	21.17	1.18	-4.28	0.79	77.88	35073.91
5	1.86	20.16	0.81	-4.00	0.92	94.87	43053.46
5	1.84	20.32	0.82	-4.04	0.73	93.61	42558.88
5	1.53	22.53	1.21	-3.95	1.15	78.98	35482.90
5	1.97	28.62	0.84	-3.99	0.78	99.34	45598.70

Table B.5 The best (IGD) set of non-dominated solution set found by NSGA-III.

K	H (m)	β $(^o)$	D (m)	γ $(^o)$	E (m)	Q (MWh)	Cost ($)
2	1.95	24.64	2.47	-4.00	0.80	40.64	18062.81
2	1.89	25.34	2.50	-4.00	0.60	39.44	17525.46
2	1.84	26.24	2.49	-4.00	0.94	38.22	16980.39
2	1.78	25.70	2.42	-3.98	0.76	37.03	16448.13
2	1.72	26.00	2.49	-4.00	0.77	35.79	15889.58
2	1.42	27.39	2.49	-10.85	0.83	29.60	13170.26
2	0.33	27.52	1.97	-4.00	1.01	6.80	3008.61
2	0.26	25.34	2.50	-4.00	0.52	5.48	2419.00
2	0.20	27.97	2.50	-4.00	0.57	4.19	1849.76
3	1.98	25.70	2.46	-4.00	0.74	61.78	27536.98
3	1.95	25.15	2.50	-4.00	0.92	60.63	27011.34
3	1.91	24.75	2.50	-3.98	0.76	59.49	26498.95
3	1.87	24.56	2.49	-4.00	0.54	58.31	25973.14
3	1.84	24.95	2.47	-4.00	0.79	57.19	25470.59
3	1.80	25.33	2.43	-4.00	0.51	56.02	24948.45
3	1.76	25.42	2.50	-3.93	0.84	54.86	24422.29
3	1.72	25.16	2.50	-4.00	1.11	53.72	23907.00
3	1.68	25.44	2.50	-4.00	0.80	52.45	23336.54
3	1.65	25.33	2.49	-4.00	0.83	51.34	22840.65
3	1.61	24.63	2.49	-4.00	0.55	50.19	22325.21
3	1.42	25.65	2.45	-3.94	0.92	44.24	19661.36
3	1.38	25.44	2.46	-4.00	0.92	43.03	19121.03
3	1.11	25.20	2.50	-4.00	1.10	34.59	15344.56
3	1.07	25.42	2.50	-4.00	0.79	33.34	14786.68
3	0.83	25.65	2.50	-4.00	0.61	25.94	11493.12
3	0.26	28.34	2.49	-4.00	0.78	8.11	3580.95
4	1.99	23.41	1.51	-4.00	1.16	81.93	36794.53
4	1.93	24.27	1.64	-3.96	0.92	79.69	35736.61
4	1.90	23.29	1.66	-4.00	0.61	78.60	35228.34
4	1.88	22.68	1.66	-4.00	1.02	77.46	34711.55
4	1.85	23.62	1.71	-4.00	0.52	76.39	34207.58
4	1.82	23.59	1.77	-4.00	0.59	75.32	33705.54
4	1.79	23.79	1.81	-4.00	0.84	74.15	33169.02
4	1.77	23.62	1.83	-4.00	0.54	73.14	32707.52
4	1.74	23.79	1.84	-4.00	0.79	71.96	32171.56
4	1.71	23.69	1.91	-4.00	0.58	70.87	31666.28
4	1.68	25.68	1.95	-4.00	1.01	69.71	31142.79
4	1.66	26.02	2.01	-4.00	1.03	68.58	30623.66
4	1.63	24.72	2.02	-4.00	0.56	67.46	30103.51
4	1.60	23.47	2.01	-4.00	1.11	66.36	29612.77
4	1.57	24.71	1.92	-4.00	0.84	65.24	29119.77
4	1.54	23.90	2.09	-4.00	0.59	64.06	28565.66
4	1.52	23.75	2.02	-4.00	0.54	62.89	28049.17
4	1.18	24.59	2.49	-4.00	0.94	49.03	21780.03
4	1.15	25.33	2.49	-4.00	1.17	47.84	21246.40
4	1.12	25.99	2.50	-4.00	0.53	46.66	20717.76
4	1.09	26.22	2.50	-4.00	0.62	45.49	20195.16

4	1.01	25.08	2.47	-4.00	0.56	41.91	18600.48
4	0.77	26.13	2.50	-4.00	0.88	32.15	14245.52
4	0.68	26.25	2.09	-4.00	0.87	28.42	12597.82
4	0.56	26.74	2.49	-4.00	0.84	23.46	10380.27
4	0.38	26.87	2.47	-4.00	0.53	15.86	7013.51
4	0.32	27.20	2.47	-4.00	0.54	13.30	5877.03
4	0.29	26.36	0.84	-4.00	0.58	11.95	5299.95
4	0.26	27.15	2.49	-4.00	0.54	10.72	4734.63
4	0.22	27.39	2.44	-4.00	0.92	9.40	4154.63
5	1.98	28.18	0.81	-4.00	0.68	99.90	45854.13
5	1.95	26.25	0.81	-4.00	0.84	98.88	45189.56
5	1.93	25.32	0.82	-4.00	0.79	97.95	44670.72
5	1.90	23.29	0.81	-3.98	0.62	96.83	44035.43
5	1.88	23.57	0.83	-4.00	0.95	95.86	43578.91
5	1.87	25.48	0.85	-4.00	0.70	94.79	43161.10
5	1.84	20.82	0.85	-4.00	0.53	93.68	42469.57
5	1.82	25.42	0.92	-4.00	0.58	92.66	42074.19
5	1.79	20.22	0.85	-4.00	0.79	91.55	41485.46
5	1.77	21.23	0.92	-4.00	0.58	90.39	40890.74
5	1.72	21.02	0.97	-4.00	1.03	88.25	39870.97
5	1.70	23.57	1.05	-4.00	0.86	87.17	39346.00
5	1.68	23.55	1.07	-4.00	0.98	86.16	38865.68
5	1.66	21.61	1.04	-4.00	0.51	85.08	38367.75
5	1.64	21.35	1.08	-4.00	0.54	84.01	37854.09
5	1.62	21.35	1.08	-4.00	0.54	82.95	37369.35
5	1.57	21.55	1.10	-4.00	0.52	80.74	36344.77
5	0.59	26.92	2.30	-4.00	0.51	30.89	13680.64
5	0.52	28.46	1.73	-4.00	0.55	27.18	12053.36
5	0.47	28.24	2.45	-4.00	0.59	24.72	10940.55
5	0.42	27.56	2.49	-4.00	0.56	22.22	9826.19
5	0.40	26.46	2.50	-4.00	0.89	20.94	9260.21
5	0.38	27.58	2.49	-4.00	0.76	19.73	8722.67
5	0.35	27.51	2.50	-4.00	0.78	18.42	8141.56
5	0.33	26.64	2.50	-4.00	0.69	17.12	7567.50
5	1.98	27.87	0.81	-4.00	0.93	99.56	45668.96
5	1.95	26.25	0.81	-4.00	0.84	98.88	45189.56
5	1.89	23.57	0.83	-4.00	0.93	95.97	43626.73
5	1.87	26.36	0.81	-4.00	0.90	94.48	43136.25
6	1.95	47.32	0.81	-15.89	0.50	107.63	54150.55
6	1.93	47.32	0.82	-15.63	0.53	106.59	53563.57
6	1.85	44.12	0.80	-16.00	0.58	104.48	51346.15
6	1.83	43.65	0.81	-15.72	0.53	103.86	50860.55
6	1.79	42.75	0.81	-15.83	0.56	102.31	49777.21
6	1.75	40.49	0.80	-15.83	0.55	101.28	48635.04
6	1.74	40.44	0.81	-3.98	0.76	100.30	48238.92
6	1.95	47.32	0.81	-15.96	0.50	107.41	54032.15
6	1.93	47.32	0.82	-15.89	0.51	106.65	53605.96
6	1.85	44.19	0.80	-16.00	0.53	104.41	51336.67
6	1.81	43.38	0.80	-16.13	0.51	102.45	50176.11
6	1.75	40.49	0.80	-15.83	0.55	101.28	48635.04

C. Uniformly Distributed Non-dominated Solutions Extracted from the Thermoelectric Problem with and without the Shape Factor using the FNFR Scheme

Table C.1 Fifteen uniformly distributed non-dominated solutions extracted from solutions assembled during 25 runs of the Fusion algorithm using the FNFR scheme

$\dot{W}\ (Watts)$	$\eta(\%)$	$T_1(K)$	$T_2(K)$	$R_L(\Omega)$	$A_p(m^2)$	$A_n(m^2)$	$L_p(m)$	$L_n(m)$
0.14784	18.438	600	273	0.1	8.10×10^{-3}	1.19×10^{-4}	3.92×10^{-3}	2.43×10^{-3}
0.16838	18.299	600	273	0.1	1.59×10^{-4}	1.48×10^{-4}	4.00×10^{-3}	3.94×10^{-3}
0.18818	17.903	600	273	0.1	1.18×10^{-4}	1.52×10^{-4}	3.40×10^{-3}	2.47×10^{-3}
0.20672	17.300	600	273	0.1	1.28×10^{-4}	9.51×10^{-3}	1.84×10^{-3}	2.16×10^{-3}
0.22390	16.538	600	273	0.1	1.75×10^{-4}	1.60×10^{-4}	2.61×10^{-3}	2.50×10^{-3}
0.23982	15.648	600	273	0.1	1.95×10^{-4}	2.41×10^{-4}	3.26×10^{-3}	2.39×10^{-3}
0.25442	14.659	600	273	0.1	2.45×10^{-4}	3.42×10^{-4}	3.87×10^{-3}	2.57×10^{-3}
0.26796	13.591	600	273	0.1	3.00×10^{-4}	2.77×10^{-4}	2.71×10^{-3}	2.61×10^{-3}
0.28035	12.475	600	273	0.1	3.44×10^{-4}	3.42×10^{-4}	2.76×10^{-3}	2.59×10^{-3}
0.29174	11.317	600	273	0.1	3.32×10^{-4}	3.34×10^{-4}	2.34×10^{-3}	2.05×10^{-3}
0.30261	10.097	600	273	0.1	5.01×10^{-4}	2.26×10^{-4}	1.31×10^{-3}	2.57×10^{-3}
0.31272	8.845	600	273	0.1	4.70×10^{-4}	2.17×10^{-4}	1.00×10^{-3}	2.03×10^{-3}
0.32207	7.564	600	273	0.1	3.63×10^{-4}	3.49×10^{-4}	1.25×10^{-3}	1.31×10^{-3}
0.33109	6.252	600	273	0.1	3.81×10^{-4}	3.33×10^{-4}	1.00×10^{-3}	1.00×10^{-3}
0.33949	4.920	600	273	0.1	5.01×10^{-4}	4.56×10^{-4}	1.00×10^{-3}	1.00×10^{-3}

(a) Multi-objective optimization without shape factor

$\dot{W}\ (Watts)$	$\eta(\%)$	$T_1(K)$	$T_2(K)$	S	$L(m)$	$R_L(\Omega)$	$A_0(m^2)$
0.14774	18.418	600	273	0.00000	1.00×10^{-3}	0.1	3.19×10^{-5}
0.17078	18.243	600	273	0.00000	4.00×10^{-3}	0.1	1.58×10^{-4}
0.19314	17.745	600	273	0.12527	3.03×10^{-3}	0.1	2.21×10^{-4}
0.21427	16.973	600	273	0.10810	3.56×10^{-3}	0.1	2.68×10^{-4}
0.23402	15.974	600	273	0.22611	3.02×10^{-3}	0.1	3.73×10^{-4}
0.25233	14.792	600	273	0.33924	1.80×10^{-3}	0.1	3.19×10^{-4}
0.26917	13.470	600	273	0.17295	1.95×10^{-3}	0.1	1.11×10^{-4}
0.28469	12.032	600	273	0.07045	2.58×10^{-3}	0.1	3.61×10^{-4}
0.29898	10.504	600	273	0.10253	2.19×10^{-3}	0.1	3.90×10^{-4}
0.31216	8.903	600	273	0.37309	2.31×10^{-3}	0.1	2.96×10^{-4}
0.32428	7.251	600	273	0.34323	3.30×10^{-3}	0.1	2.97×10^{-4}
0.33553	5.551	600	273	0.51045	2.11×10^{-3}	0.1	2.96×10^{-4}
0.34596	3.813	600	273	0.49305	3.45×10^{-3}	0.1	3.10×10^{-4}
0.35566	2.048	600	273	0.65929	3.82×10^{-3}	0.1	3.18×10^{-4}
0.36469	0.258	600	273	0.99984	3.99×10^{-3}	0.1	9.27×10^{-5}

(b) Multi-objective optimization with shape factor.

Table C.2 Fifteen uniformly distributed non-dominated solutions extracted from solutions assembled during 25 runs of the SMPSO algorithm using the FNFR scheme

$\dot{W}\ (Watts)$	$\eta(\%)$	$T_1(K)$	$T_2(K)$	$R_L(\Omega)$	$A_p(m^2)$	$A_n(m^2)$	$L_p(m)$	$L_n(m)$
0.14731	18.438	600	273	0.1	1.05×10^{-4}	1.18×10^{-4}	3.90×10^{-3}	3.16×10^{-3}
0.16808	18.302	600	273	0.1	1.19×10^{-4}	1.23×10^{-4}	3.33×10^{-3}	2.97×10^{-3}
0.18764	17.916	600	273	0.1	1.34×10^{-4}	1.05×10^{-4}	2.42×10^{-3}	2.74×10^{-3}
0.20628	17.317	600	273	0.1	5.73×10^{-3}	6.35×10^{-3}	1.20×10^{-3}	1.00×10^{-3}
0.22354	16.551	600	273	0.1	2.52×10^{-4}	1.39×10^{-4}	2.29×10^{-3}	3.59×10^{-3}
0.23958	15.663	600	273	0.1	2.42×10^{-4}	2.51×10^{-4}	3.42×10^{-3}	2.96×10^{-3}
0.25421	14.675	600	273	0.1	3.81×10^{-4}	3.52×10^{-4}	4.00×10^{-3}	4.00×10^{-3}
0.26766	13.617	600	273	0.1	2.76×10^{-4}	2.79×10^{-4}	2.73×10^{-3}	2.42×10^{-3}
0.28038	12.472	600	273	0.1	2.84×10^{-4}	2.82×10^{-4}	2.33×10^{-3}	2.10×10^{-3}
0.29209	11.285	600	273	0.1	3.24×10^{-4}	3.08×10^{-4}	2.10×10^{-3}	2.03×10^{-3}
0.30283	10.073	600	273	0.1	3.19×10^{-4}	2.97×10^{-4}	1.68×10^{-3}	1.66×10^{-3}
0.31275	8.821	600	273	0.1	4.93×10^{-4}	4.96×10^{-4}	2.22×10^{-3}	2.18×10^{-3}
0.32232	7.543	600	273	0.1	4.69×10^{-4}	4.55×10^{-4}	1.69×10^{-3}	1.61×10^{-3}
0.33113	6.247	600	273	0.1	3.85×10^{-4}	3.44×10^{-4}	1.00×10^{-3}	1.04×10^{-3}
0.33951	4.915	600	273	0.1	5.01×10^{-4}	4.57×10^{-4}	1.00×10^{-3}	1.00×10^{-3}

(a) Multi-objective optimization without shape factor

$\dot{W}\ (Watts)$	$\eta(\%)$	$T_1(K)$	$T_2(K)$	S	$L(m)$	$R_L(\Omega)$	$A_0(m^2)$
0.14773	18.418	600	273	0.10841	3.84×10^{-3}	0.1	2.23×10^{-4}
0.17080	18.243	600	273	0.21254	2.18×10^{-3}	0.1	2.33×10^{-4}
0.19339	17.738	600	273	0.00000	2.50×10^{-3}	0.1	1.22×10^{-4}
0.21465	16.956	600	273	0.11764	2.46×10^{-3}	0.1	1.92×10^{-4}
0.23453	15.945	600	273	0.11970	3.06×10^{-3}	0.1	2.73×10^{-4}
0.25277	14.760	600	273	0.32998	2.82×10^{-3}	0.1	4.90×10^{-4}
0.26967	13.423	600	273	0.13853	4.00×10^{-3}	0.1	5.01×10^{-4}
0.28509	11.992	600	273	0.16438	2.04×10^{-3}	0.1	8.95×10^{-5}
0.29936	10.458	600	273	0.29149	2.18×10^{-3}	0.1	2.18×10^{-4}
0.31247	8.863	600	273	0.05357	2.19×10^{-3}	0.1	4.92×10^{-4}
0.32452	7.217	600	273	0.16551	3.22×10^{-3}	0.1	7.25×10^{-5}
0.33565	5.531	600	273	0.50000	1.86×10^{-3}	0.1	2.51×10^{-4}
0.34620	3.773	600	273	0.98156	1.00×10^{-3}	0.1	3.13×10^{-4}
0.35583	2.015	600	273	0.59770	3.86×10^{-3}	0.1	2.60×10^{-4}
0.36490	0.216	600	273	0.50493	3.96×10^{-3}	0.1	1.96×10^{-5}

(b) Multi-objective optimization with shape factor.

Table C.3 Fifteen uniformly distributed non-dominated solutions extracted from solutions assembled during 25 runs of the GDE3 algorithm using the FNFR scheme

$\dot{W}\ (Watts)$	$\eta(\%)$	$T_1(K)$	$T_2(K)$	$R_L(\Omega)$	$A_p(m^2)$	$A_n(m^2)$	$L_p(m)$	$L_n(m)$
0.14767	18.438	600	273	0.1	1.33×10^{-4}	1.13×10^{-4}	3.72×10^{-3}	4.00×10^{-3}
0.16848	18.296	600	273	0.1	1.52×10^{-4}	1.25×10^{-4}	3.45×10^{-3}	3.71×10^{-3}
0.18833	17.901	600	273	0.1	1.27×10^{-4}	1.35×10^{-4}	3.05×10^{-3}	2.62×10^{-3}
0.20706	17.291	600	273	0.1	2.34×10^{-4}	1.99×10^{-4}	3.78×10^{-3}	4.00×10^{-3}
0.22401	16.536	600	273	0.1	2.76×10^{-4}	2.51×10^{-4}	4.00×10^{-3}	4.00×10^{-3}
0.23984	15.645	600	273	0.1	2.64×10^{-4}	7.53×10^{-3}	1.00×10^{-3}	3.28×10^{-3}
0.25453	14.637	600	273	0.1	3.67×10^{-4}	3.03×10^{-4}	3.60×10^{-3}	3.66×10^{-3}
0.26789	13.583	600	273	0.1	2.76×10^{-4}	2.81×10^{-4}	2.83×10^{-3}	2.34×10^{-3}
0.28041	12.471	600	273	0.1	4.47×10^{-4}	3.33×10^{-4}	2.72×10^{-3}	3.33×10^{-3}
0.29194	11.300	600	273	0.1	4.51×10^{-4}	5.01×10^{-4}	3.41×10^{-3}	2.83×10^{-3}
0.30275	10.075	600	273	0.1	1.98×10^{-4}	1.70×10^{-4}	1.00×10^{-3}	1.00×10^{-3}
0.31275	8.841	600	273	0.1	4.24×10^{-4}	3.12×10^{-4}	1.46×10^{-3}	1.81×10^{-3}
0.32233	7.539	600	273	0.1	2.99×10^{-4}	2.60×10^{-4}	1.00×10^{-3}	1.00×10^{-3}
0.33122	6.231	600	273	0.1	3.67×10^{-4}	3.49×10^{-4}	1.00×10^{-3}	1.00×10^{-3}
0.33966	4.891	600	273	0.1	5.01×10^{-4}	4.63×10^{-4}	1.00×10^{-3}	1.00×10^{-3}

(a) Multi-objective optimization without shape factor

$\dot{W}\ (Watts)$	$\eta(\%)$	$T_1(K)$	$T_2(K)$	S	$L(m)$	$R_L(\Omega)$	$A_0(m^2)$
0.14774	18.418	600	273	0.09934	4.00×10^{-3}	0.1	2.17×10^{-4}
0.17122	18.237	600	273	0.12463	2.24×10^{-3}	0.1	1.28×10^{-4}
0.19336	17.738	600	273	0.12274	3.68×10^{-3}	0.1	2.66×10^{-4}
0.21478	16.950	600	273	0.00000	2.68×10^{-3}	0.1	1.61×10^{-4}
0.23470	15.935	600	273	0.00000	2.34×10^{-3}	0.1	1.73×10^{-4}
0.25313	14.735	600	273	0.00000	2.35×10^{-3}	0.1	2.13×10^{-4}
0.27009	13.391	600	273	0.00000	2.12×10^{-3}	0.1	2.37×10^{-4}
0.28572	11.929	600	273	0.00000	1.39×10^{-3}	0.1	1.94×10^{-4}
0.30001	10.385	600	273	0.15987	3.63×10^{-3}	0.1	1.24×10^{-4}
0.31331	8.754	600	273	0.29779	3.27×10^{-3}	0.1	2.80×10^{-4}
0.32549	7.078	600	273	0.30335	2.81×10^{-3}	0.1	1.97×10^{-4}
0.33667	5.369	600	273	0.23532	2.17×10^{-3}	0.1	6.82×10^{-5}
0.34709	3.616	600	273	0.64323	2.34×10^{-3}	0.1	3.29×10^{-4}
0.35678	1.833	600	273	0.53123	1.99×10^{-3}	0.1	9.68×10^{-5}
0.36592	0.003	600	273	0.92887	4.00×10^{-3}	0.1	1.00×10^{-6}

(b) Multi-objective optimization with shape factor.

Table C.4 Fifteen uniformly distributed non-dominated solutions extracted from solutions assembled during 25 runs of the SPEA2 algorithm using the FNFR scheme

$\dot{W}\ (Watts)$	$\eta(\%)$	$T_1(K)$	$T_2(K)$	$R_L(\Omega)$	$A_p(m^2)$	$A_n(m^2)$	$L_p(m)$	$L_n(m)$
0.14755	18.438	600	273	0.1	9.41×10^{-5}	1.14×10^{-4}	3.75×10^{-3}	2.83×10^{-3}
0.16873	18.291	600	273	0.1	1.36×10^{-4}	1.50×10^{-4}	3.98×10^{-3}	3.42×10^{-3}
0.18863	17.891	600	273	0.1	1.00×10^{-4}	1.57×10^{-4}	3.59×10^{-3}	2.03×10^{-3}
0.20752	17.273	600	273	0.1	1.93×10^{-4}	1.78×10^{-4}	3.31×10^{-3}	3.33×10^{-3}
0.22479	16.496	600	273	0.1	8.24×10^{-5}	1.67×10^{-4}	2.62×10^{-3}	1.20×10^{-3}
0.24050	15.599	600	273	0.1	2.26×10^{-4}	1.67×10^{-4}	2.18×10^{-3}	2.82×10^{-3}
0.25502	14.618	600	273	0.1	3.15×10^{-4}	2.01×10^{-4}	2.26×10^{-3}	3.28×10^{-3}
0.26864	13.534	600	273	0.1	1.39×10^{-4}	1.34×10^{-4}	1.29×10^{-3}	1.20×10^{-3}
0.28129	12.381	600	273	0.1	2.43×10^{-4}	2.27×10^{-4}	1.86×10^{-3}	1.75×10^{-3}
0.29301	11.184	600	273	0.1	4.02×10^{-4}	1.51×10^{-4}	1.03×10^{-3}	2.44×10^{-3}
0.30349	9.988	600	273	0.1	2.12×10^{-4}	2.35×10^{-4}	1.34×10^{-3}	1.07×10^{-3}
0.31352	8.737	600	273	0.1	3.01×10^{-4}	3.16×10^{-4}	1.47×10^{-3}	1.25×10^{-3}
0.32296	7.444	600	273	0.1	3.98×10^{-4}	2.82×10^{-4}	1.08×10^{-3}	1.29×10^{-3}
0.33189	6.128	600	273	0.1	4.14×10^{-4}	4.77×10^{-4}	1.39×10^{-3}	1.07×10^{-3}
0.34033	4.775	600	273	0.1	5.01×10^{-4}	4.92×10^{-4}	1.00×10^{-3}	1.00×10^{-3}

(a) Multi-objective optimization without shape factor

$\dot{W}\ (Watts)$	$\eta(\%)$	$T_1(K)$	$T_2(K)$	S	$L(m)$	$R_L(\Omega)$	$A_0(m^2)$
0.14775	18.418	600	273	0.06635	2.83×10^{-3}	0.1	1.21×10^{-4}
0.17104	18.240	600	273	0.06920	3.65×10^{-3}	0.1	1.79×10^{-4}
0.19334	17.739	600	273	0.14315	1.38×10^{-3}	0.1	8.88×10^{-5}
0.21499	16.941	600	273	0.14235	3.57×10^{-3}	0.1	3.07×10^{-4}
0.23484	15.926	600	273	0.29329	2.22×10^{-3}	0.1	3.14×10^{-4}
0.25319	14.730	600	273	0.14433	2.89×10^{-3}	0.1	1.38×10^{-4}
0.27010	13.390	600	273	0.08266	3.12×10^{-3}	0.1	4.56×10^{-5}
0.28573	11.928	600	273	0.14876	2.86×10^{-3}	0.1	1.04×10^{-4}
0.30004	10.379	600	273	0.23556	1.92×10^{-3}	0.1	1.32×10^{-4}
0.31324	8.762	600	273	0.26694	3.96×10^{-3}	0.1	2.80×10^{-4}
0.32543	7.085	600	273	0.10411	2.60×10^{-3}	0.1	2.30×10^{-5}
0.33659	5.382	600	273	0.28315	3.12×10^{-3}	0.1	1.41×10^{-4}
0.34701	3.629	600	273	0.30773	3.97×10^{-3}	0.1	1.36×10^{-4}
0.35690	1.810	600	273	0.92203	1.85×10^{-3}	0.1	2.61×10^{-4}
0.36592	0.003	600	273	0.99122	3.75×10^{-3}	0.1	1.02×10^{-6}

(b) Multi-objective optimization with shape factor.

Table C.5 Fifteen uniformly distributed non-dominated solutions extracted from solutions assembled during 25 runs of the NSGAIII algorithm using the FNFR scheme

$\dot{W}\ (Watts)$	$\eta(\%)$	$T_1(K)$	$T_2(K)$	$R_L(\Omega)$	$A_p(m^2)$	$A_n(m^2)$	$L_p(m)$	$L_n(m)$
0.14773	18.438	600	273	0.1	1.23×10^{-4}	8.45×10^{-3}	2.78×10^{-3}	3.70×10^{-3}
0.16745	18.311	600	273	0.1	1.35×10^{-4}	1.01×10^{-4}	2.78×10^{-3}	3.37×10^{-3}
0.18914	17.879	600	273	0.1	1.04×10^{-4}	1.14×10^{-4}	2.55×10^{-3}	2.12×10^{-3}
0.20756	17.271	600	273	0.1	1.35×10^{-4}	1.53×10^{-4}	2.90×10^{-3}	2.30×10^{-3}
0.22490	16.486	600	273	0.1	2.27×10^{-4}	1.84×10^{-4}	2.85×10^{-3}	3.33×10^{-3}
0.24081	15.581	600	273	0.1	1.63×10^{-4}	1.10×10^{-4}	1.43×10^{-3}	2.02×10^{-3}
0.25516	14.596	600	273	0.1	1.28×10^{-4}	2.21×10^{-4}	2.58×10^{-3}	1.28×10^{-3}
0.26866	13.522	600	273	0.1	3.71×10^{-4}	1.79×10^{-4}	1.78×10^{-3}	3.13×10^{-3}
0.28125	12.386	600	273	0.1	1.42×10^{-4}	2.42×10^{-4}	1.98×10^{-3}	1.03×10^{-3}
0.29297	11.188	600	273	0.1	2.00×10^{-4}	1.54×10^{-4}	1.03×10^{-3}	1.23×10^{-3}
0.30380	9.952	600	273	0.1	4.32×10^{-4}	3.74×10^{-4}	2.06×10^{-3}	2.23×10^{-3}
0.31387	8.688	600	273	0.1	4.41×10^{-4}	2.60×10^{-4}	1.15×10^{-3}	1.89×10^{-3}
0.32327	7.402	600	273	0.1	4.51×10^{-4}	3.46×10^{-4}	1.23×10^{-3}	1.54×10^{-3}
0.33221	6.050	600	273	0.1	4.84×10^{-4}	3.35×10^{-4}	1.03×10^{-3}	1.16×10^{-3}
0.34043	4.753	600	273	0.1	5.01×10^{-4}	4.99×10^{-4}	1.00×10^{-3}	1.00×10^{-3}

(a) Multi-objective optimization without shape factor

$\dot{W}\ (Watts)$	$\eta(\%)$	$T_1(K)$	$T_2(K)$	S	$L(m)$	$R_L(\Omega)$	$A_0(m^2)$
0.14779	18.418	600	273	0.15388	2.50×10^{-3}	0.1	1.95×10^{-4}
0.17057	18.247	600	273	0.12988	3.96×10^{-3}	0.1	2.77×10^{-4}
0.19137	17.796	600	273	0.19012	3.36×10^{-3}	0.1	3.07×10^{-4}
0.21432	16.971	600	273	0.10385	2.90×10^{-3}	0.1	1.06×10^{-4}
0.23454	15.944	600	273	0.03155	3.99×10^{-3}	0.1	1.33×10^{-5}
0.25316	14.732	600	273	0.28888	2.84×10^{-3}	0.1	4.46×10^{-4}
0.27018	13.383	600	273	0.19628	1.64×10^{-3}	0.1	2.29×10^{-4}
0.28573	11.927	600	273	0.19138	2.91×10^{-3}	0.1	1.66×10^{-4}
0.30006	10.380	600	273	0.25053	2.47×10^{-3}	0.1	1.89×10^{-4}
0.31325	8.761	600	273	0.21236	3.90×10^{-3}	0.1	1.81×10^{-4}
0.32539	7.091	600	273	0.36205	2.19×10^{-3}	0.1	2.12×10^{-4}
0.33641	5.410	600	273	0.39256	2.96×10^{-3}	0.1	2.49×10^{-4}
0.34646	3.726	600	273	0.33919	3.95×10^{-3}	0.1	1.68×10^{-4}
0.35734	1.725	600	273	0.81936	2.94×10^{-3}	0.1	3.14×10^{-4}
0.36592	0.003	600	273	0.98007	3.98×10^{-3}	0.1	1.01×10^{-6}

(b) Multi-objective optimization with shape factor.